



Simulation numérique d'écoulements turbulents de gaz dense

Luca Sciacovelli

► To cite this version:

Luca Sciacovelli. Simulation numérique d'écoulements turbulents de gaz dense. Mécanique des matériaux [physics.class-ph]. Ecole nationale supérieure d'arts et métiers - ENSAM; Politecnico di Bari. Dipartimento di Ingegneria Meccanica e Gestionale (Italia), 2016. Français. NNT : 2016ENAM0061 . tel-01498552

HAL Id: tel-01498552

<https://pastel.hal.science/tel-01498552>

Submitted on 30 Mar 2017

HAL is a multi-disciplinary open access archive for the deposit and dissemination of scientific research documents, whether they are published or not. The documents may come from teaching and research institutions in France or abroad, or from public or private research centers.

L'archive ouverte pluridisciplinaire **HAL**, est destinée au dépôt et à la diffusion de documents scientifiques de niveau recherche, publiés ou non, émanant des établissements d'enseignement et de recherche français ou étrangers, des laboratoires publics ou privés.

École doctorale n° 432 : Sciences des métiers de l'ingénieur

Doctorat ParisTech

T H È S E

pour obtenir le grade de docteur délivré par

l'École Nationale Supérieure d'Arts et Métiers

Spécialité “mécanique et matériaux”

présentée et soutenue publiquement par

Luca SCIACOVELLI

le 13 Décembre 2016

Numerical simulation of dense gas turbulent flows

Directeur de thèse : **Paola CINNELLA**
Co-Directeur de thèse : **Francesco GRASSO**
Co-Directeur de thèse : **Michele NAPOLITANO**

Jury

M. Pierre SAGAUT, Professeur, Université d'Aix-Marseille
M. Christophe CORRE, Professeur, École Centrale de Lyon
M. Jörn SESTERHENN, Professeur, Technische Universität Berlin
M. Paola CINNELLA, Professeur, Arts et Métiers ParisTech
M. Francesco GRASSO, Professeur, Conservatoire National des Arts et Métiers
M. Michele NAPOLITANO, Professeur, Politecnico di Bari
M. Rene PECNIK, Professeur, Delft University of Technology

Président
Rapporteur
Rapporteur
Examineur
Examineur
Examineur
Examineur



UNIVERSITÉ
FRANCO
ITALIENNE



Doctorat ParisTech

THÈSE

pour obtenir le grade de docteur délivré par

l'École Nationale Supérieure d'Arts et Métiers

Spécialité “mécanique et matériaux”

présentée et soutenue publiquement par

Luca SCIACOVELLI

le 13 Décembre 2016

Numerical simulation of dense gas turbulent flows*

Directeur de thèse : **Paola CINNELLA**

Co-encadrement de la thèse : **Francesco GRASSO**

Co-encadrement de la thèse : **Michele NAPOLITANO**

**Thèse en cotutelle entre Arts et Métiers ParisTech et le Politecnico di Bari (Italie),
co-financé par une bourse Vinci pour la mobilité de l'Université Franco-Italienne*

Contents

Contents	i
List of Figures	iii
List of Tables	x
Riassunto esteso	1
Résumé étendu	11
1 Introduction	21
1.1 Dense gas dynamics	22
1.2 State of the art	24
1.3 Compressible turbulence	26
1.4 Outline	30
2 Governing equations and numerical methods	33
2.1 Governing Equations	33
2.1.1 Working Fluid	34
2.1.2 Thermodynamic models	35
2.1.3 Transport Properties	40
2.1.4 Comparisons of the EoS	43
2.2 Numerical methods	48
2.2.1 Approximation of centered fluxes	49
2.2.2 Numerical stabilization terms	51
2.2.3 Shock-capturing methods	53
2.2.4 Time integration methods	56
2.3 Description of the CFD codes	57
2.3.1 Scalability tests	59
2.4 Preliminary validations	62
3 Decay of dense-gas inviscid compressible homogeneous isotropic turbulence	65
3.1 Definitions	65
3.2 Initial and boundary conditions	67
3.3 Assessment of the numerical strategy	68
3.4 Results	73
3.4.1 Influence of the initial compressibility ratio	73
3.4.2 Influence of the initial peak wavenumber	74
3.4.3 Influence of the specific heat ratio	75
3.4.4 Dense gas simulations	78

4	Small scale dynamics of dense-gas homogeneous isotropic turbulence	93
4.1	General statistics	93
4.1.1	Influence of the thermodynamic and transport property models	95
4.1.2	Influence of the fluid type	100
4.1.3	Mach number effects	100
4.2	Small-scale features	107
4.2.1	Local flow topology	107
4.2.2	Contribution of flow structures to dissipation	114
4.2.3	Enstrophy generation mechanisms	121
5	Supersonic dense-gas turbulent channel flow	131
5.1	Numerical experiments of compressible channel flows	131
5.1.1	Setup and definitions	131
5.1.2	Validations	133
5.1.3	Description of the computed cases	133
5.2	Influence of dense-gas effects on flow properties	135
5.2.1	Global flow properties	135
5.2.2	Scalings and first-order statistics	140
5.2.3	Second-order statistics of the thermodynamic and transport properties	145
5.3	Influence of dense-gas effects on turbulence structure	148
5.3.1	Reynolds stresses and anisotropies	148
5.3.2	Turbulent kinetic energy budgets	154
5.3.3	Near-wall turbulent structures	156
6	Conclusions and Perspectives	163
6.1	Future work	166
6.2	Acknowledgement	166
	Appendices	167
A	Basic thermodynamics relations	169
B	Computation of saturation curves	171
C	Jacobian matrix for dense gases	173
D	Shock-detection algorithm	175
	Bibliography	177
	List of Acronyms	191
	List of Symbols	193

List of Figures

2.1	Comparison of viscosity laws for air (a) and relative error of power-law w.r.t. Sutherland law.	41
2.2	Iso-contours of reduced temperature T/T_c in the Clapeyron Diagram for fluid PP11, modelled by means of PFG (top panel), VDW (central panel) and MAH (bottom panel) EoS.	44
2.3	Iso-contours of normalized speed of sound $c/\sqrt{p_c v_c}$ in the Clapeyron Diagram for fluid PP11, modelled by means of PFG (top panel), VDW (central panel) and MAH (bottom panel) EoS.	45
2.4	Iso-contours of dynamic viscosity μ in the Clapeyron Diagram for fluid PP11, modelled by means of VDW (top panel) and MAH (bottom panel) EoS.	46
2.5	Iso-contours of specific heat ratio $\gamma = c_p/c_v$ (top panel) and Prandtl number Pr (bottom panel) in the Clapeyron diagram for fluid PP11, modelled by means of MAH EoS.	47
2.6	Iso-contours of reduced temperature T/T_c in the Clapeyron diagram for fluids D6 (top, SWN EoS) and R245fa (bottom, SWP EoS).	47
2.7	Behaviour of standard finite-difference schemes in the wavenumber space. (a) modified wavenumber $k^*\Delta x$ as a function of actual wavenumber $k\Delta x$ and (b) dispersion error in logarithmic scales.	50
2.8	Behaviour of optimized finite-difference schemes in the wavenumber space. (a) modified wavenumber $k^*\Delta x$ as a function of actual wavenumber $k\Delta x$ and (b) dispersion error in logarithmic scales.	51
2.9	Behaviour of selective standard filters in the wavenumber space. The transfer function of the filter as a function of wavenumber $k\Delta x$ is plotted in normal (a) and logarithmic (b) scales, respectively.	54
2.10	Behaviour of selective standard filters in the wavenumber space. The transfer function of the filter as a function of wavenumber $k\Delta x$ is plotted in normal (a) and logarithmic (b) scales, respectively.	54
2.11	Left panel: decomposition of the computational Cartesian domain into subdomains by means of the MPI_CART functionalities. Right panel: interfaces exchanged among neighbours in the three directions, each one composed of 5 plans.	58
2.12	Weak efficiency scalability (a) and speedup as a function of the number of processing units, for different values of grid points per processing unit.	60
2.13	Weak efficiency scalability (a) and speedup as a function of the number of processing units, for different values of grid points per processing unit.	61
2.14	Results for test case DG1. Profiles of reduced density (a), reduced pressure (b), fundamental derivative (c), velocity and Mach number (d). Grid: 400 cells, $t^* = 0.15$	63
2.15	Test case DG2. Profiles of reduced density (a), reduced pressure (b), fundamental derivative (c) and velocity (d).	63

3.1	Comparison between the present results for CHIT decay at $M_{t_0} = 0.2$ and $\chi_0 = 0$ using the 9th-order scheme and Jameson's second-order scheme and those of Garnier <i>et al.</i> (1999) based on a 5th-order modified ENO scheme (MENO) and Jameson's schemes. Time histories of the turbulent kinetic energy (a), enstrophy (b), pseudo-Taylor microscale (c), and spectrum of the turbulent kinetic energy at $t = 10$ (d).	68
3.2	Comparison of the present results for a 9th-order accurate scheme with those provided by Garnier <i>et al.</i> (1999) using a 4th-order ENO scheme, for different choices of the initial conditions.	69
3.3	Influence of grid resolution for a PFG CHIT simulation. The working fluid is a perfect gas with $\gamma = 1.4$, and the initial turbulent Mach number is $M_{t_0} = 0.8$. Panels a-c show the time histories of the normalized r.m.s. density (a), the pseudo Taylor microscale (b) and the normalized enstrophy (c); panels d-e show the turbulent kinetic energy spectrum (d) and the p.d.f. of velocity divergence (e) at $t = 2.5$	70
3.4	Influence of grid resolution for a DG CHIT simulation. Here, the working fluid is PP11, modelled as a polytropic VDW gas, and the initial turbulent Mach number is $M_{t_0} = 0.8$. Panel a shows the time history of the normalized enstrophy; panels b-c show the turbulent kinetic energy spectrum (b) and the p.d.f. of velocity divergence (c) at $t = 2.5$	71
3.5	Comparison of Euler-based and Navier-Stokes-based results for PFG. Panels a-d show the time histories of the normalized r.m.s. density (a), the normalized r.m.s. sound speed (b), the turbulent kinetic energy (c) and the normalized r.m.s. velocity divergence (d) at various Reynolds numbers.	73
3.6	Comparison of Euler-based and Navier-Stokes-based results for PFG simulations. (a) Turbulent kinetic energy spectrum and (b) p.d.f. of the normalized velocity divergence evaluated at $t = 2.5$ at various Reynolds numbers.	74
3.7	Influence of the artificial dissipation coefficients k_2 and k_{10} (256^3 grid, $M_{t_0} = 0.8$, perfect gas with $\gamma = 1.4$). Panels a-b show the time histories of the normalized turbulent kinetic energy (a), the normalized enstrophy (b). Panels c-d show the turbulent kinetic energy spectrum (c) and the p.d.f. of velocity divergence (d) at $t = 2.5$	75
3.8	Influence of the initial compressibility ratio χ_0 . The working fluid is a perfect gas with $\gamma = 1.4$. Panels a-d show the time histories of the normalized r.m.s. density (a), normalized r.m.s. sound speed (b), time history of the normalized enstrophy (c), and p.d.f. of local Mach number at $t = 2.5$ (d).	76
3.9	Influence of the initial peak wavenumber k_0 . The working fluid is a perfect gas with $\gamma = 1.4$. Panels a-d show the time histories of the normalized r.m.s. density (a), normalized r.m.s. velocity divergence (b), turbulent Mach number (c), and turbulent kinetic energy spectrum at $t = 2.5$ (d).	77
3.10	PFG simulations: influence of the specific heat ratio. Time evolution of the r.m.s. of the density (a), the pressure (b), the sound speed (c), and the rescaled values of p_{rms} (d) and c_{rms} (e) according to equations (3.13) and (3.11), respectively.	79
3.11	PFG simulations: influence of the specific heat ratio. Time evolutions of the turbulent Mach number (a), turbulent kinetic energy (b), normalized r.m.s. of the vorticity (c), normalized r.m.s. of the dilatation (d), kinetic energy spectrum (e) and p.d.f. of the local Mach number at $t = 2.5$ (f)	80
3.12	Representation in the $p - v$ plane of the initial thermodynamic conditions used for the dense gas simulations with the VDW model (isocontours of reduced temperature).	81
3.13	PFG and DG simulations. Kinetic energy spectra at $t = 2.5$ at various initial turbulent Mach numbers.	81

3.14	PFG and DG simulations. Time evolution of the r.m.s. density (a), turbulent Mach number (b), average speed of sound (c) and r.m.s. speed of sound (d).	82
3.15	PFG and DG simulations. Time histories of the average (panel a) and r.m.s. (panel b) fundamental derivative of gas dynamics for the dense gas at various initial turbulent Mach numbers.	83
3.16	Representation in the $p - v$ diagram of the thermodynamic states at $t = 2.5$ for various initial turbulent Mach numbers. Each symbol represents the thermodynamic conditions computed at a given mesh points at various initial Mach numbers. The spread of thermodynamic states (approximately distributed along an isentropic curve) increases with the Mach number, due to compressibility effects.	83
3.17	Instantaneous iso-contours ($t = 2.5$) of Γ (top), c/c_0 (middle), and ρ/ρ_0 (bottom) along a mesh plane for a dense-gas computation at $M_{t_0} = 1$	84
3.18	PFG and DG simulations. Time evolution of the r.m.s. divergence of the velocity field normalized with the initial vorticity at various initial turbulent Mach numbers.	84
3.19	Instantaneous iso-contours of the normalized velocity divergence $\theta/\theta_{\text{rms}}$ for $M_{t_0} = 1$ at time $t = 1$ (a), $t = 3$ (b), and $t = 5$ (c). Results for the perfect gas case are represented on the left, dense gas on the right. Red regions correspond to strong compressions ($\theta/\theta_{\text{rms}} < -3$), green regions to strong expansions ($\theta/\theta_{\text{rms}} > 3$).	85
3.20	Snapshots at $t = 2.5$ of the isosurfaces $\theta/\theta_{\text{rms}} = 3$ (a) and of the iso-surfaces $\theta/\theta_{\text{rms}} = -3$ (b), coloured by the local Mach number, for perfect (left panel) and dense gas (right panel) simulations at $M_{t_0} = 1$	86
3.21	P.d.f.s of the normalized velocity divergence scaled by $M_{t_0}^2$ for $M_{t_0} = 0.2$ (a), $M_{t_0} = 0.5$ (b), $M_{t_0} = 0.8$ (c), and $M_{t_0} = 1$ (d) ($t = 2.5$). The vertical dashed lines indicate the values $\theta/\theta_{\text{rms}} = \pm 3$	88
3.22	Contours of the joint probability density function (log scale) of the fundamental derivative of gas dynamics Γ with the scaled normalized local velocity divergence $\theta/\theta_{\text{rms}} M_{t_0}^2$ at the initial turbulent Mach numbers $M_{t_0} = 0.2$ (a), $M_{t_0} = 0.5$ (b), $M_{t_0} = 0.8$ (c), and $M_{t_0} = 1$ (d).	89
3.23	Probability density function of the normalized sound speed conditioned on $\theta/\theta_{\text{rms}}$ at $M_{t_0} = 1$	90
3.24	Probability density functions of the local Mach number at various initial turbulent Mach numbers.	90
3.25	Total probability density function of the local Mach number (a) and the normalized local vorticity (b), and p.d.f. conditioned on strong compressions ($\theta/\theta_{\text{rms}} < -2$) and strong expansions ($\theta/\theta_{\text{rms}} > 2$) for $M_{t_0} = 1$ at time $t = 2.5$	91
4.1	Isocontours of the reduced temperature in the Clapeyron diagram for PP11 using Martin-Hou (a), and Van der Waals (b) model. Three iso- Γ lines are also represented. The black dashed line denotes the critical isotherm. White circles are the initial thermodynamic conditions chosen for the MAH and VDW cases. The red circle in panel (a) denotes the PP11-MAH-IC2 initial condition. White and red dash-dotted lines are used to highlight the corresponding initial isentropes.	94
4.2	Grid resolution of the dense gas computations. Time history of the ratios of the Kolmogorov length scale to the mesh size, $\eta/\Delta x$	95
4.3	Time histories of the normalized turbulent kinetic energy (left), and normalized enstrophy (right) for various dense gas simulations at $M_{t_0} = 1$	96
4.4	Time histories of the r.m.s. pressure (a), r.m.s. temperature (b) and r.m.s. speed of sound (c) for various dense gas simulations at $M_{t_0} = 1$	96

4.5	Time histories of the mean (left) and r.m.s. (right) values of the fundamental derivative of gas dynamics at $M_{t_0} = 1$	97
4.6	Distributions of thermodynamic states in the Clapeyron diagram, for PP11-MAH (a) and PP11-VDW (b) at $M_{t_0} = 1$ ($t = 2$). For PP11-MAH two initial thermodynamic conditions are considered, namely, IC1 (black symbols) and IC2 (red symbols). . . .	97
4.7	Time histories of normalized mean viscosity (left) and Eckert number (right) at $M_{t_0} = 1$	98
4.8	P.d.f.s of the normalized speed of sound (a), local Mach number (b), and normalized dilatation (c) for $M_{t_0} = 1$ ($t = 2$).	98
4.9	Pressure ratio p_{sh} vs density ratio ρ_{sh} in a direction normal to the extracted shocklets at $t = 2$ for Air (left panel) and PP11-PFG (right panel). The solid line denotes the ideal relation	99
4.10	Time histories of the normalized turbulent kinetic energy (a), and premultiplied kinetic energy spectrum (b) and p.d.f. of the velocity divergence (c) at $t = 2$	101
4.11	Time histories of the mean fundamental derivative of gas dynamics (a), normalized r.m.s. values of density (b), temperature (c) and speed of sound (d).	102
4.12	Time histories of the normalized turbulent kinetic energy (a), normalized enstrophy (b) and compensated turbulent kinetic energy spectra at $t = 2$ (c) for air (left panels) and PP11-MAH-IC1 (right panels) at various Mach numbers.	103
4.13	P.d.f.s of the velocity differences for $M_{t_0} = 0.5$ (a) and $M_{t_0} = 1$ (b) for air (left panels) and PP11-MAH-IC1 (right panels) at $t = 2$	104
4.14	Time histories of the r.m.s. temperature (a), r.m.s. pressure (b), r.m.s. density (c), and maximum to minimum density ratio (d), for air (left panels) and PP11-MAH-IC1 (right panels) at various Mach numbers.	105
4.15	Time histories of normalized sound speed (a), r.m.s. sound speed (b), turbulent Mach number (c), and r.m.s. dilatation normalized with the initial r.m.s. vorticity (d), for air (left panels) and PP11-MAH-IC1 (right panels) at various Mach numbers. . . .	106
4.16	Distribution of the thermodynamic states in the Clapeyron diagram at $t = 2$ for PP11-MAH-IC1 at various M_{t_0} . White symbols: $M_{t_0} = 0.5$; red symbols: $M_{t_0} = 0.8$; black symbols: $M_{t_0} = 1$	107
4.17	Time history of the average (a) and r.m.s. (b) fundamental derivative of gas dynamics at various M_{t_0}	107
4.18	Time histories of the normalized average viscosity (a), Eckert number (b) for air (left panels) and PP11-MAH-IC1 (right panels) at various Mach numbers. The Prandtl number (c) is reported only for PP11, being constant and equal to 0.7 for air. . . .	108
4.19	Time histories of the velocity gradient skewness (a) and flatness (b), for air (left panels) and PP11-MAH-IC1 (right panels) at various Mach numbers.	109
4.20	Local topologies for incompressible flows. Extracted from Ooi <i>et al.</i> (1999)	110
4.21	Volume fractions (%) occupied by flow regions characterized by different normalized dilatation intervals as a function of M_{t_0} ($t = 2$).	112
4.22	Iso-contours (-4 to 0, spacing equal to 1) of the \log_{10} of the joint p.d.f. of the scaled second and third invariants of the anisotropic part of the velocity gradient at $M_{t_0} = 1$ ($t = 2$) for air (panel a), PP11-MAH-IC1 (panel b) and PP11-MAH-IC2 (panel c). Left column: total joint p.d.f. Central column: p.d.f. conditioned on strong compressions (regions with $\theta/\theta_{rms}M_{t_0}^2 \in [-\infty, -2]$). Right column: p.d.f. conditioned on strong expansions (regions with $\theta/\theta_{rms}M_{t_0}^2 \in [2, \infty]$). The bold solid isoline denotes the iso-contour -3.	114

4.23	Iso-contours (-4 to 0, spacing equal to 1) of the \log_{10} of the joint p.d.f. of the scaled second and third invariants of the anisotropic part of the velocity gradient at $M_{t_0} = 1$ ($t = 2$) conditioned on the local type of structure for air (panel a), PP11-MAH-IC1 (panel b) and PP11-MAH-IC2 (panel c). Left column: eddy regions. Central column: shear regions. Right column: convergence regions.	115
4.24	Fractional contribution of the various flow structures to $\langle V \rangle^+$ (a) and $\langle V \rangle^-$ (b) at various M_{t_0} ($t = 2$). Left column: incompressible structures; center column: compressed structures; right column: expanding structures.	116
4.25	Fractional contribution of the various flow structures to the solenoidal dissipation $\langle Q_W \rangle^+$ (a) and $\langle Q_W \rangle^-$ (b), at various M_{t_0} ($t = 2$). Left column: incompressible structures; center column: compressed structures; right column: expanding structures.	117
4.26	Fractional contribution of the various flow structures to the total dissipation $-\langle Q_{S^*} \rangle^+$ (a) and $-\langle Q_{S^*} \rangle^-$ (b) at various M_{t_0} ($t = 2$). Left column: incompressible structures; central column: compressed structures; right column: expanding structures.	118
4.27	Fractional contribution of the various flow structures to the dilatational dissipation $\langle Q_P \rangle^+$ (a) and $\langle Q_P \rangle^-$ (b) at various M_{t_0} ($t = 2$). Left column: incompressible structures; central column: compressed structures; right column: expanding structures.	119
4.28	Influence of the initial thermodynamic state on the fractional contribution of the various flow structures to the dilatational dissipation $\langle Q_P \rangle^+$ (a) and $\langle Q_P \rangle^-$ (b) at various M_{t_0} ($t = 2$). Left column: incompressible structures; central column: compressed structures; right column: expanding structures.	120
4.29	Volume fractions of the various flow structures conditioned with respect to strong compression regions (a) and strong expansion regions (b) at various M_{t_0} ($t = 2$).	120
4.30	Normalized conditional volume-integrated data at $M_{t_0} = 1$ ($t = 2$). (a) Volume fraction \mathcal{V} ; (b) \mathcal{Q}_W ; (c) \mathcal{Q}_{S^*} ; (d) \mathcal{Q}_P	121
4.31	Strong compressions $\theta/\theta_{\text{rms}} = -3$ (left panels) and strong expansions $\theta/\theta_{\text{rms}} = 3$ (right panels) for air (a), PP11-MAH-IC1 (b) and PP11-MAH-IC2 (c) coloured with the local type of structure. Blue: eddy; white: shear; red: convergence.	122
4.32	Iso-surfaces of $\log_{10}(\Delta /\langle Q_W \rangle^3) = 3$, conditioned on eddy-type structures (left panels) and convergence regions (right panels) for air (a), PP11-MAH-IC1 (b) and PP11-MAH-IC2 (c), coloured with the local dilatation $\theta/\theta_{\text{rms}}$	123
4.33	Distribution of the averages of the vortex stretching vector $\omega_i V_i^T$ (left column), $\omega_i V_i^D$ (central column), and $\omega_i V_i^S$ (right column) conditioned on the dilatation for air (a) and PP11-MAH-IC1 (b) at $M_{t_0} = 1$ ($t = 2$).	124
4.34	P.d.f. and p.d.f.s conditioned on dilatation levels of the eigenvalues ratios λ_2^*/λ_1^* (left) and λ_2^*/λ_3^* (right) of the deviatoric strain rate tensor at $M_{t_0} = 1$ ($t = 2$) for air (a) and PP11-MAH-IC1 (b).	125
4.35	P.d.f. and p.d.f.s conditioned on dilatation levels of the normalized eigenvalues ($\beta_k = \lambda_k/\sqrt{\sum_i \lambda_i^2}$) of the strain rate tensor S_{ij} for air (a) and PP11-MAH-IC1 (b) ($M_{t_0} = 1$; $t = 2$).	126
4.36	Conditional averages of squares of cosines of angles between density gradient direction \mathbf{n} and the strain rate eigenvectors $\mathbf{\Lambda}_k$ for air (a), PP11-MAH-IC1 (b) and PP11-MAH-IC2 (c) at $M_{t_0} = 1$ ($t = 2\tau$).	126
4.37	P.d.f.s and conditional p.d.f.s of the cosines of the angles between the vorticity $\boldsymbol{\omega}$ and the strain rate eigenvectors $\mathbf{\Lambda}_k$ for air (a) and PP11-MAH-IC1 (b) at $M_{t_0} = 1$ ($t = 2$).	127

4.38	Conditional averages of enstrophy production associated with the three strain rate eigenvectors at $M_{t_0} = 1$ (at $t = 2$) for air (a), PP11-MAH-IC1 (b) and PP11-MAH-IC2 (c).	128
4.39	Conditional average of the normalized vorticity magnitude at $M_{t_0} = 1$ ($t = 2$).	128
4.40	Total and conditional p.d.f. of the normalized vorticity magnitude. Air (a); PP11-MAH-IC1 (b); PP11-MAH-IC2 (c)	128
5.1	Validations for the subsonic channel flow case. Lines, present simulation; symbols, data from Kim <i>et al.</i> (1987) . (a) Law of the wall; (b) r.m.s. velocity fluctuations; (c) turbulent kinetic energy budget.	134
5.2	Validations for the supersonic channel flow case. Lines, present simulation; symbols, data from Coleman <i>et al.</i> (1995) . (a) Profiles of mean quantities; (b) r.m.s. velocity fluctuations.	135
5.3	Evolutions of M_B (a) and \bar{T}_{cl}^+ (b) as a function of \bar{M}_{cl} for different cases.	136
5.4	Evolution of Re_τ^* as a function of Re_τ for different cases.	139
5.5	Evolutions of C_f (a) and Nu_B (b) as a function of Re_{D_h} for different cases.	140
5.6	Scalings for the law of the wall for air (top) and PP11 (bottom). (a,d) Classical incompressible scaling u^+ ; (b,e) Van Driest transformation u_{VD} ; (c,f) Trettel-Larsson transformation u_{TL} in semi-local coordinates.	141
5.7	Profiles of density $\bar{\rho}^+$, temperature \bar{T}^+ and pressure \bar{p}/\bar{p}_w for cases air (top) and PP11 (bottom).	142
5.8	Mean profiles of the speed of sound \bar{c}/\bar{c}_w and of the Mach number \bar{M} for air (a,b) and PP11 (c,d) flows.	143
5.9	Mean profiles of the viscosity $\bar{\mu}/\bar{\mu}_w$, the friction Reynolds number Re_τ^* and the Reynolds number \bar{Re} for air (a,b,c) and PP11 (d,e,f) flows.	144
5.10	Mean profiles of the Prandtl number \bar{Pr} (a), specific heat at constant pressure \bar{c}_p/R (b) for PP11, and Eckert number \bar{Ec} (c) for air and PP11.	145
5.11	Profiles of the normalised r.m.s. density (a,d), temperature (b,e), and pressure (c,f) for air flows (top row) and PP11 flows (bottom row).	146
5.12	Profiles of normalised r.m.s. viscosity for air (a) and PP11 (b) flows.	146
5.13	Profiles of the correlation coefficients $C_{\rho'\rho'}$ (a,e), $C_{\rho'u'}$ (b,f), $C_{\rho'v'}$ (c,g) and $C_{u'v'}$ (d,h) for air (top row) and PP11 (bottom row) flows.	147
5.14	Distribution of $p - v$ states of an instantaneous flow field for PP11 in a Clapeyron diagram.	149
5.15	Profiles of the turbulent Mach number M_t for air (a) and PP11 (b) and of the fundamental derivative of gas dynamics $\bar{\Gamma}$ for PP11 (c).	150
5.16	Reynolds stresses in the streamwise (a, e), wall-normal (b, f) and spanwise (c, g) directions and Reynolds shear stresses (d, h) for air (top row) and PP11 (bottom row) flows with semi-local scaling.	151
5.17	Reynolds stresses in the streamwise (a, e), wall-normal (b, f) and spanwise (c, g) directions and Reynolds shear stresses (d, h) for air (top row) and PP11 (bottom row) flows with outer scaling.	151
5.18	Profiles of the streamwise (a,e), wall-normal (b,f), spanwise (c,g) and shear (d,h) Reynolds stress anisotropies for air (top row) and PP11 (bottom row) flows.	152
5.19	Evolutions of non-dimensional shear rate Sk/ϵ (a,c) and gradient Mach number M_g (b,d) profiles for air (top row) and PP11 (bottom row) flows.	152
5.20	Comparisons of turbulent kinetic energy budgets for cases AM3R12 (dashed lines) and PM3R12 (solid lines) normalised by $\tau_w u_B/h$ (a), $\bar{\rho}_w u_\tau^4/\bar{\nu}_w$ (b) and $\tau_w^2/\bar{\mu}(y)$ (c).	154

5.21	Profiles of the turbulent production P_k , the turbulent dissipation ε_k and the ratio of production to dissipation $P_k/\varepsilon_k - 1$ for air (top row) and PP11 (bottom row) flows.	155
5.22	Isosurfaces of normalised Q -criterion $Q(h/u_B)^2 = 1$ coloured with normalised stream-wise velocity $\sqrt{\rho}u/\sqrt{\tau_w}$. Top: AM3R7, centre: PM1R3, bottom: PM3R7.	156
5.23	$\sqrt{\rho}u''/\sqrt{\tau_w}$ fluctuations at $y^* \approx 12$ for AM3R7 (top) and PM1R3 (bottom).	157
5.24	$\sqrt{\rho}u''/\sqrt{\tau_w}$ fluctuations at $y^* \approx 50$ for AM3R7 (top) and PM1R3 (bottom).	157
5.25	$\sqrt{\rho}u''/\sqrt{\tau_w}$ fluctuations at $y^* \approx 200$ for AM3R7 (top) and PM1R3 (bottom).	158
5.26	Pressure fluctuations p'^+ at $y^* \approx 12$ for AM3R7 (top) and PM1R3 (bottom).	159
5.27	Density fluctuations ρ'^+ at $y^* \approx 12$ for AM3R7 (top) and PM1R3 (bottom).	159
5.28	Premultiplied energy spectra for cases AM3R7 (top) and PM1R3 (bottom).	160
5.29	Joint p.d.f.s of $\sqrt{\rho}u''/\sqrt{\tau_w}$ and $\sqrt{\rho}v''/\sqrt{\tau_w}$ for air (top) and PP11 (bottom).	160
5.30	Probability weighted Reynolds shear stress $\rho u''v''/\tau_w P(\sqrt{\rho}u''/\sqrt{\tau_w}, \sqrt{\rho}v''/\sqrt{\tau_w})$ for air (top) and PP11 (bottom).	161
B.1	Panel a: isotherms computed by means of the VDW EoS. Panel b: example of Maxwell reconstruction algorithm for the isotherm $\bar{T} = 0.9T_c$	171

List of Tables

2.1	Thermodynamic properties of the fluids under investigation.	35
2.2	Coefficients η_i for the computation of the ideal specific heat in the ideal limit, equation (2.29).	38
2.3	Coefficients n_i for the computation of the residual part of the Span–Wagner EoS, equations (2.31) and (2.32).	39
2.4	Parameters for evaluating the functions A_i of equation (2.47) for the computation of the dense-gas viscosity.	42
2.5	Parameters for evaluating the functions B_i of equation (2.54) for the computation of the dense-gas thermal conductivity.	43
2.6	Centered component \mathcal{H} and dissipation term \mathcal{D} of the numerical flux $\mathcal{F} = \mathcal{H} - \mathcal{D}$ of the schemes of Lerat & Corre (2003) up to 9-th order.	52
2.7	Coefficients c_j (with $c_{1-j} = c_j$) of the conservative form of the adaptive nonlinear selective filtering method for the standard (Fo2) and optimized second order (Fopt).	56
2.8	Comparison of the restitution times per iteration per grid point for the two codes and the different thermodynamic models.	59
2.9	Weak scalability test from 16 to 16384 processing units. The efficiencies for five different distributions of grid points per core are shown.	60
2.10	Strong scalability test from 16 to 16384 processing units. Workloads A and B consist of 16.8 and 537 millions of grid points, respectively.	61
2.11	Riemann problem data for the dense-gas shock tube.	62
3.1	Cases considered to study the influence of the artificial dissipation coefficients.	74
3.2	PFG simulations: influence of the specific heat ratio. Values of the specific heat ratio (γ), specific heat coefficient at constant volume (c_v) and at constant pressure (c_p), and fundamental derivative of gas dynamics Γ	76
3.3	Volume fraction occupied by flow regions with different dilatation levels at time $t = 2.5$	78
3.4	Initial thermodynamic conditions used for the dense gas simulations using the PFG and VDW equations of state.	81
3.5	Volume fraction occupied by compression and expansion regions at time $t = 2.5$	87
3.6	Volume fraction occupied by flow regions characterized by different Γ values, conditioned on dilatation levels (dense gas simulations at $M_{t_0} = 1$, $t = 2.5$).	87
4.1	Summary of the thermodynamic models and initial thermodynamic conditions used in the study.	94
4.2	Classification of turbulent regions in three-dimensional compressible flow according to Kevlahan <i>et al.</i> (1992).	111
4.3	Percentage of focal/non focal structures according to dilatation levels (at nondimensional time $t = 2$). PP11-IC1 and PP11-IC2 refer to MAH EoS.	112
5.1	Parameters used for the DNS of the selected test cases.	133
5.2	Results of the DNS computations of the selected test cases.	133
5.3	Line styles for some of the DNS cases considered.	135

5.4	Numerical parameters and DNS results for air and PP11.	137
5.5	DNS results for air and PP11 cases.	138
5.6	Contributions to the skin friction coefficient according to the compressible extension of the FIK identity of Gomez <i>et al.</i> (2009) for different cases.	153
5.7	Values of y^* and λ^* for the peak values of the spectra shown in figure 5.28	158
A.1	Derivation of Maxwell relations from the fundamental laws of thermodynamics. . . .	169

Riassunto esteso

Introduzione

La comprensione fisica della dinamica della turbolenza nei flussi di gas denso è rilevante per molti sistemi ingegneristici come, ad esempio, gallerie del vento ad alto numero di Reynolds ([Anderson, 1991](#)), processi e trasporto di sostanze chimiche ([Kirillov, 2004](#)), cicli per produzione e conversione d'energia ([Brown & Argrow, 2000](#)) e refrigerazione ([Zamfirescu & Dincer, 2009](#)). Con il termine gas denso (DG) ci si riferisce a fluidi monofase con complessità molecolare tale che la derivata fondamentale della gasdinamica $\Gamma := 1 + \frac{\rho}{c} \frac{\partial c}{\partial \rho} \Big|_s$ (dove ρ è la densità, p la pressione, s l'entropia e c la velocità del suono), che misura il tasso di variazione della velocità del suono in trasformazioni isentropiche, è minore di uno (o addirittura negativa, [Thompson, 1971](#)) in un determinato intervallo di condizioni termodinamiche prossime alla curva di saturazione. In tali condizioni, la velocità del suono aumenta nelle espansioni isentropiche e diminuisce nelle compressioni isentropiche, contrariamente a ciò che accade nei classici casi di gas perfetto. I gas densi esibiscono i fenomeni più interessanti per una famiglia di composti pesanti poliatomici, chiamata fluidi di Bethe–Zel'dovich–Thompson (BZT, [Thompson, 1971](#)): tali fluidi esibiscono una regione termodinamica nella fase vapore, prossima alla curva di coesistenza liquido/vapore e chiamata “zona di inversione” [Cramer & Kluwick \(1984\)](#), in cui il valore di Γ è negativo. In queste condizioni, la teoria prevede la creazione di effetti di comprimibilità non classici in regime di flussi transonici o supersonici, come ad esempio urti di espansione, onde miste (urto/fascio), o decomposizione dell'urto ([Cramer & Kluwick, 1984](#); [Cramer, 1991a](#)). Inoltre, la variazione d'entropia attraverso un urto debole è molto inferiore per gas densi con $\Gamma \ll 1$ rispetto al gas perfetto, portando a perdite d'urto ridotte. Solitamente, le simulazioni numeriche di flussi di gas denso di interesse ingegneristico sono basate sulle ben conosciute equazioni RANS (Reynolds-Averaged Navier–Stokes equations), che necessitano di essere accoppiate con un idoneo modello per il tensore degli stress di Reynolds. L'accuratezza dei modelli RANS per flussi di gas denso non è stata propriamente verificata finora, a causa della mancanza di dati di riferimento sperimentali e numerici. La creazione di una banca dati di simulazioni numeriche dirette (DNS) completa e affidabile è dunque necessaria per quantificare le eventuali carenze dei modelli di turbolenza esistenti e per sviluppare e calibrare modelli migliorati. In aggiunta, le simulazioni DNS possono permettere lo studio e la comprensione dell'influenza dei fluidi in uso sull'evoluzione della turbolenza comprimibile. Per i gas densi, infatti, il modello di gas perfetto (PGF) perde la sua validità e si rende necessario l'utilizzo di equazioni di stato (EoS) più complesse per prendere in conto il loro insolito comportamento termodinamico. Inoltre, in regime di gas denso la viscosità dinamica μ e la conduttività termica κ dipendono, oltre che dalla temperatura, anche dalla densità tramite complesse relazioni di trasporto. Analogamente, l'approssimazione di numero di Prandtl ($Pr = \mu c_p / \kappa$, dove c_p è il calore specifico a pressione costante) quasi costante non è più valida. In questo riassunto esteso verranno presentati recenti risultati DNS relativi a due classiche configurazioni di flussi turbolenti, ossia il decadimento della turbolenza omogenea isotropa comprimibile (CHIT), e il flusso turbolento attraverso un canale piano (TCF), rispettivamente rappresentativi di turbolenza libera e confinata da pareti, e saranno sottolineati le principali differenze rispetto alla più classica turbolenza di gas perfetto.

Table 0.1. Proprietà termofisiche del PP11: peso molecolare (\mathcal{M}), temperatura critica (T_c), densità critica (ρ_c), pressione critica (p_c), fattore di comprimibilità critico (Z_c), fattore acentrico (ω_{ac}), momento di dipolo della fase gassosa (ξ), temperatura di ebollizione (T_b), rapporto del calore specifico nel limite di gas diluito valutato alla temperatura critica sulla costante del gas ($c_v(T_c)/R$) e esponente della legge per il calore specifico nel limite di gas diluito (n).

\mathcal{M}	T_c	ρ_c	p_c	Z_c	ω_{ac}	ξ	T_{eb}	$c_v(T_c)/R$	n
g mol ⁻¹	K	kg m ⁻³	MPa	-	-	D	K	-	-
624.11	650.2	627.14	1.46	0.2688	0.4963	0.0	488.15	97.3	0.5776

Equazioni di governo e metodo numerico

In questo studio si restringe l'attenzione su flussi di gas in regime monofase governati dalle equazioni di Navier–Stokes tridimensionali comprimibili. Il comportamento del gas è modellato tramite l'equazione termica di Martin–Hou (MAH, [Martin & Hou, 1955](#)), che fornisce una descrizione realistica del gas e dell'estensione della sua zona di inversione. Tale equazione, che implica l'utilizzo di cinque termini viriali e il soddisfacimento di dieci vincoli termodinamici, è ragionevolmente accurata per il fluido di interesse e richiede una quantità minima di informazioni sperimentali. Per modellare le variazioni del calore specifico nel limite di gas ideale con la temperatura, si utilizza una legge esponenziale del tipo $c_{v\infty} = c_{v\infty}(T_c)(T/T_c)^n$, dove n è un parametro dipendente dal fluido considerato. In aggiunta alla EoS, occorre specificare dei modelli termofisici per esprimere la viscosità dinamica e la conduttività termica alla temperatura e pressione del gas. Nelle seguenti simulazioni, le proprietà di trasporto seguono il modello di Chung–Lee–Starling ([Chung et al., 1988](#)), che contiene un termine di correzione per la regione di gas denso. Per i casi di aria, il classico modello di gas perfetto politropico è usato con una legge esponenziale nella temperatura per la viscosità, $\mu = \mu_{\text{ref}}(T/T_{\text{ref}})^{0.7}$, e un'assunzione di Prandtl costante, $Pr = 0.7$. Il fluido di lavoro è il perfluoro-perhydrophenanthrene (formula chimica $\text{C}_{14}\text{F}_{24}$), chiamato da qui in avanti col suo nome commerciale PP11. Le proprietà termodinamiche del PP11 sono fornite in tabella 0.1. Questo fluido è stato spesso considerato negli studi sui gas densi in letteratura poichè esibisce una zona di inversione relativamente ampia e, di conseguenza, può portare all'apparizione di effetti non classici.

Le derivate spaziali nelle equazioni di governo sono approssimate per mezzo di schemi alle differenze finite ottimizzati. In particolare, i termini convettivi sono approssimati con differenze finite ottimizzate al quarto ordine con una molecola di calcolo su undici punti per ogni direzione ([Bogey & Bailly, 2004](#)), e i termini viscosi con differenze finite standard al quarto ordine centrate. L'algoritmo prevede anche l'uso di un filtro selettivo al sesto ordine ottimizzato su undici punti, applicato in ogni direzione al fine di rimuovere le oscillazioni maglia a maglia nelle regioni di flusso senza discontinuità. Per assicurare robustezza numerica per flussi comprimibili in presenza di shock, si impiega una strategia basata sul filtraggio adattativo selettivo non lineare ([Bogey et al., 2009](#)). In ultimo, l'integrazione temporale è effettuata tramite uno schema di tipo Runge-Kutta a sei passi a basso stoccaggio, ottimizzato nello spazio delle frequenze.

Decadimento della turbolenza omogenea isotropa comprimibile

Il problema del decadimento della turbolenza omogenea isotropa è risolto su un dominio cubico $[0, 2\pi]^3$, nelle cui tre direzioni cartesiane si impone una condizione al contorno di periodicità. Lo spettro dell'energia cinetica turbolenta iniziale è del tipo Passot-Pouquet, ossia $E(k) = Ak^4 \exp[-2(k/k_0)^2]$, dove k_0 è il numero d'onda di picco e A è una costante che dipende dalla

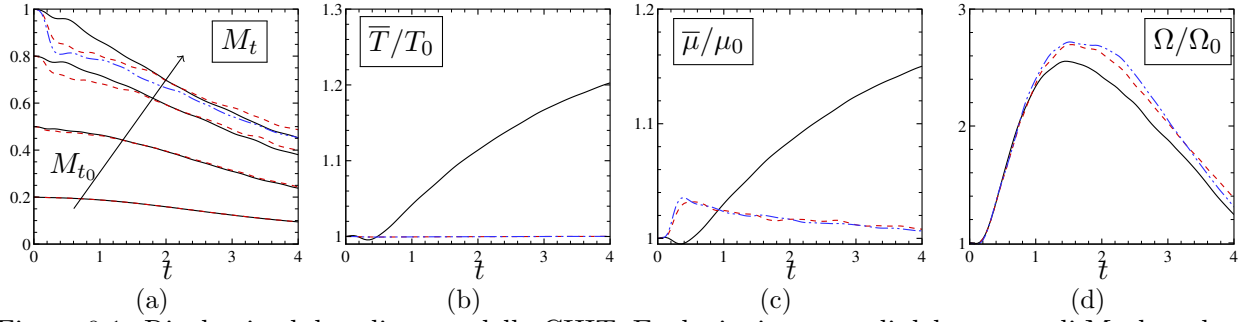


Figure 0.1. Risultati sul decadimento della CHIT. Evoluzioni temporali del numero di Mach turbolento M_t per vari M_{t_0} (a). Pannelli da (b) a (d): temperatura media normalizzata T/T_0 , viscosità normalizzata $\bar{\mu}/\mu_0$ ed enstrofia normalizzata Ω/Ω_0 a $M_{t_0} = 1$. —: Aria; - - -: PP11 IC1; - · - · -: PP11 IC2.

quantità iniziale di energia cinetica immessa nel dominio. Il campo iniziale di velocità è puramente solenoidale e gli r.m.s. delle variabili termodinamiche sono fissati a zero. Il decadimento della turbolenza comprimibile è governato dal numero di Mach turbolento $M_t = \sqrt{u_i^2}/\bar{c}$ e dal numero di Reynolds $Re_\lambda = u'\lambda\bar{\rho}/\bar{\mu}$, basato sulla microscala di Taylor λ . Si è effettuata una serie di simulazioni numeriche dirette di CHIT di gas denso per diversi valori del numero di Mach turbolento iniziale, cioè $M_{t_0} = 0.2, 0.5, 0.8$ e 1 . Il numero di Reynolds iniziale è fissato a $Re_\lambda = 200$ e il numero d'onda di picco iniziale k_0 è uguale a 2 per tutte le simulazioni. Il decadimento è simulato sino a $t = 4$ (essendo t una scala di tempo adimensionalizzata rispetto al large eddy turnover time iniziale). Tutte le simulazioni sono state effettuate su una griglia regolare cartesiana di 512^3 . Nei casi più severi (cioè per $M_{t_0} = 1$), la più piccola scala adimensionale risolta $k_{max}\eta$ (con k_{max} il numero d'onda più grande e $\eta = (\bar{\mu}^3/\bar{\rho}^2\bar{\epsilon})^{1/4}$ la scala di lunghezza di Kolmogorov, Jagannathan & Donzis, 2016) è sempre maggiore di $\approx 6.5 - 7$, e la scala di Kolmogorov è discretizzata con almeno due punti di griglia, assicurando una soddisfacente risoluzione in tutti i casi.

Le simulazioni di gas denso sono riportate per due differenti condizioni dello stato termodinamico iniziale, corrispondenti ad un punto nella regione di gas denso ($\rho_0/\rho_c = 1.618$, $p_0/p_c = 1.02$, $T_0/T_c = 1.01$, $\Gamma_0 = 0.1252$, condizione IC1) ed una nella zona di inversione ($\rho_0/\rho_c = 1.618$, $p_0/p_c = 0.98$, $T_0/T_c = 1.001$, $\Gamma_0 = -0.093$, condizione IC2), per cui il flusso può esibire effetti BZT. Poiché l'entropia può solo aumentare durante l'evoluzione, nessun effetto BZT può apparire per la prima scelta di condizioni termodinamiche. I risultati sono sistematicamente confrontati con quelli per un gas perfetto diatomico (aria). Gli effetti di comprimibilità sono analizzati comparando le evoluzioni temporali delle principali statistiche del flusso per le simulazioni con aria e gas denso a vari M_{t_0} (figura 0.1a). Le soluzioni PFG e DG sono praticamente sovrapposte a $M_{t_0} = 0.2$ e deviano progressivamente con l'aumento di M_{t_0} , a causa della differente comprimibilità e delle proprietà di trasporto dei due fluidi. Per brevità, in seguito l'analisi è ristretta al caso più rappresentativo, cioè $M_{t_0} = 1$. La temperatura media (figura 0.1b) aumenta significativamente col tempo per PFG, e la viscosità (figura 0.1c) ha lo stesso comportamento. Al contrario, per i casi DG la temperatura rimane approssimativamente costante a causa dei ben più alti calori specifici, e l'evoluzione temporale della viscosità (che dipende dalle variazioni di densità) mostra un picco all'inizio del decadimento per poi diminuire, comportandosi in modo opposto al PFG. L'energia cinetica turbolenta normalizzata K/K_0 (non mostrata per brevità) e l'enstrofia Ω/Ω_0 (figura 0.1d) sono simili per PFG e DG. Si osserva un picco di enstrofia per $t \approx 1.4 - 1.5$, che è leggermente superiore per il gas denso, a causa della viscosità media più bassa rispetto all'aria. L'evoluzione delle principali statistiche è molto simile per le due condizioni IC1 e IC2 scelte per il gas denso.

Le evoluzioni temporali della quantità termodinamiche fluttuanti sono mostrate in figura 0.2 (rigo

superiore). Il rapporto istantaneo tra densità massima e minima aumenta durante la fase iniziale supersonica, guidata dal meccanismo di vortex stretching e caratterizzata dalla produzione di forti gradienti di velocità, raggiungendo un massimo per un tempo adimensionale compreso tra 1 e 2. Per il gas denso, il valore massimo è comunque circa 2.5 volte inferiore a quello di gas perfetto, a causa della formazione di shocklet più deboli. Successivamente il rapporto diminuisce ed entrambi i fluidi esibiscono un comportamento simile. Analogamente, le fluttuazioni di pressione (figura 0.2b) nel gas denso sono circa 5 volte inferiori per il PP11, indipendentemente dalla scelta dello stato termodinamico iniziale. Gli r.m.s. della velocità del suono, invece, sono più alti in gas denso. Per tale fluido, infatti $c = c(\rho, T)$ segue essenzialmente le variazioni di densità (essendo la temperatura circa costante per tutto il decadimento). Tale comportamento è profondamente differente da quello osservato in gas perfetto, per cui la velocità del suono aumenta a causa del riscaldamento per attrito. Le evoluzioni temporali del valore medio ed r.m.s. della derivata fondamentale della gasdinamica sono anche riportate per il PP11 per varie condizioni iniziali. Il valore medio $\bar{\Gamma}$ (figura 0.2d) segue le variazioni di densità. Sia per IC1 che IC2, lo sviluppo iniziale dei modi comprimibili aumenta il Γ medio, che rimane comunque sotto 1 durante l'intera evoluzione (implicando che la velocità del suono tende a decrescere nelle regioni di compressione) e poi diminuisce. Le fluttuazioni r.m.s. di Γ arrivano circa ad 1 a $t \approx 1$; ciò significa che, per flussi ad alto numero di Mach, i valori puntuali di Γ sono ampiamente distribuiti attorno al valore medio e possono essere localmente molto più alti di 1 o, per IC2, più bassi di 0. Nonostante il differente comportamento locale di Γ , le statistiche macroscopiche del flusso sono poco influenzate e tendono a comportarsi similmente per entrambi le condizioni iniziali.

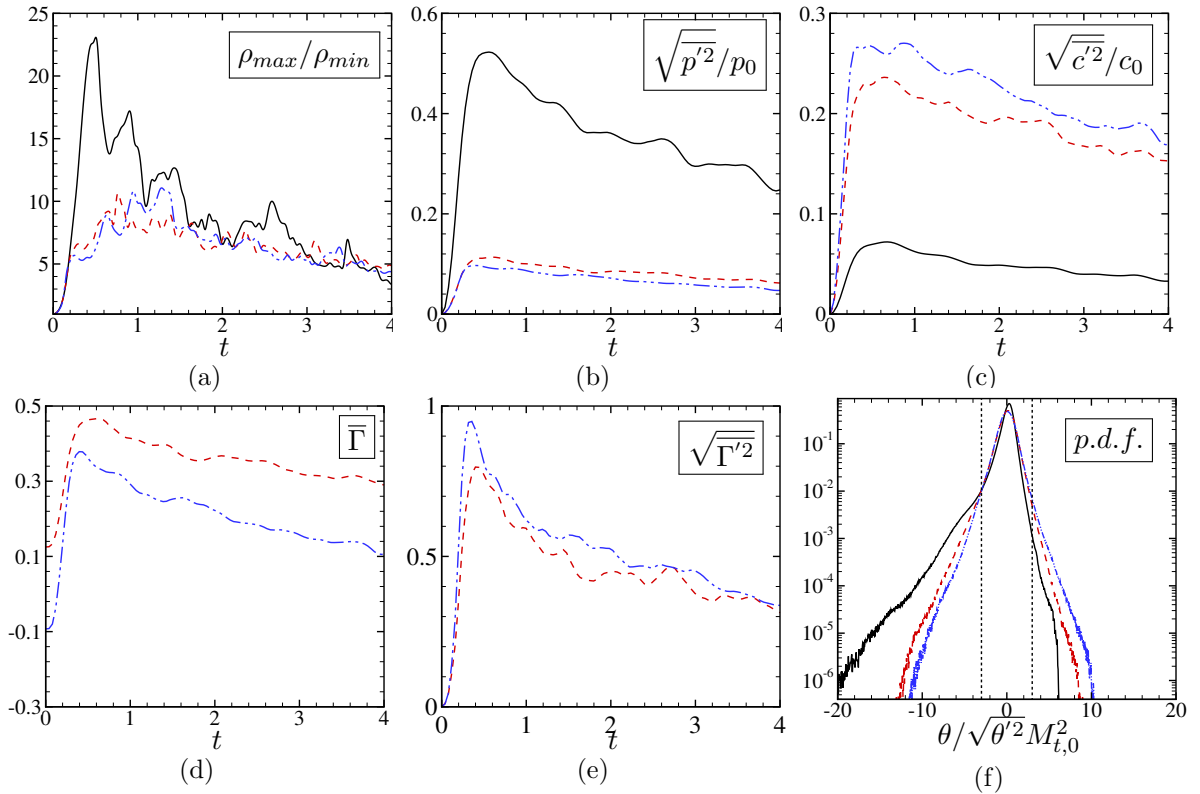


Figure 0.2. CHIT a $M_{t_0} = 1$. Da (a) a (c): evoluzioni temporali del rapporto tra densità massima e minima ρ_{max}/ρ_{min} , r.m.s. della pressione $\sqrt{p'^2}/p_0$ e r.m.s. della velocità del suono $\sqrt{c'^2}/c_0$; da (d) a (f): evoluzioni temporali della media $\bar{\Gamma}$ e r.m.s. $\sqrt{\Gamma'^2}$ della derivata fondamentale, e p.d.f. della dilatazione normalizzata $\theta/\sqrt{\theta'^2}M_{t,0}^2$ al tempo adimensionale $t = 2$. Legenda come in figura 0.1.

La figura 0.3 mostra la distribuzione degli stati termodinamici del flusso nel diagramma di Clapeyron al tempo $t = 2$, per la condizione IC1 a vari M_{t_0} e per IC2 a $M_{t_0} = 1$. Tutti gli stati tendono ad essere distribuiti lungo l'isentropica iniziale, essendo la viscosità e le perdite d'urto basse. La regione termodinamica spazzata dagli stati $p - v$ durante il decadimento aumentano all'aumentare di M_{t_0} . Per $M_{t_0} = 1$, il piccolo cambio delle condizioni termodinamiche iniziali cambia drasticamente la pressione massima raggiunta. Il volume specifico, infatti, è limitato inferiormente (limite superiore per la densità, rispettivamente) dal valore corrispondente alla transizione liquido/gas, quando il flusso è sottoposto a forti compressioni. D'altra parte, le forti espansioni sono favorite dal comportamento di gas denso, poichè la velocità del suono aumenta e la comprimibilità diminuisce. Le regioni a differente dilatazione sono classificate in base al livello locale di dilatazione normalizzata $\theta/\sqrt{\theta'^2 M_{t_0}^2}$ (Sciacovelli *et al.*, 2016a). In particolare, regioni con $0 < |\theta/\sqrt{\theta'^2 M_{t_0}^2}| < 2$ sono catalogate come deboli espansioni/compressioni, mentre $|\theta/\sqrt{\theta'^2 M_{t_0}^2}| > 2$ denota forti moti di espansione/compressione. Inoltre, comunemente si considera che si possono ottenere shocklets per $\theta/\sqrt{\theta'^2 M_{t_0}^2} < -3$ (Samtaney *et al.*, 2001). Le differenze nel diagramma di Clapeyron sono confermate dalla funzione di densità di probabilità (p.d.f.) della dilatazione normalizzata mostrata in figura 0.2f. Il gas denso esibisce una p.d.f. ben più simmetrica rispetto al gas perfetto, che è caratterizzata da una lunga coda sinistra, in accordo con risultati simili in letteratura (Wang *et al.*, 2012b). Il maggior bilanciamento tra le code destra e sinistra della p.d.f. nei casi di gas denso sono dovute al significativo indebolimento o soppressione degli shock di compressione nelle regioni dove Γ è prossima o inferiore a zero; d'altra parte, le espansioni sono favorite, portando ad una coda destra più pesante. Tale comportamento è più evidente per IC2, a causa della possibilità dell'esistenza di effetti BZT che portano alla comparsa di shocklet di espansione. A $t = 2$, approssimativamente la metà dell'intero volume è caratterizzato da stati termodinamici racchiusi all'interno della zona di inversione. Tra questi stati, circa il 36% consistono in regioni di debole dilatazione e circa il 6% di regione di forte espansione. Globalmente, le forti compressioni diminuiscono dal 3% al 2% mentre le forti espansioni aumentano da 1.7% a 2.6%.

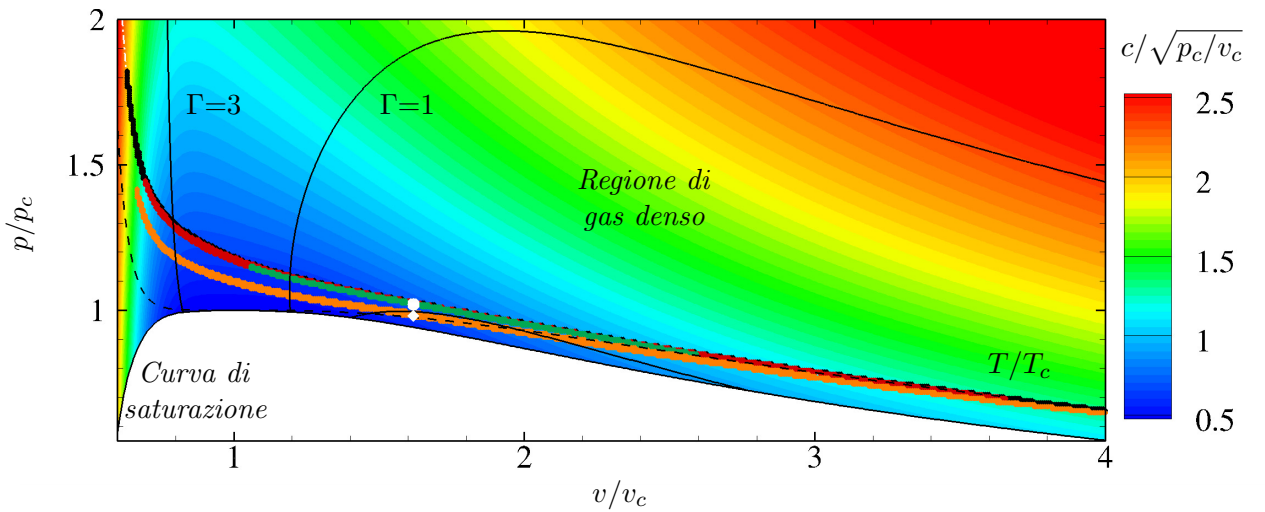


Figure 0.3. Distribuzione degli stati termodinamici nel diagramma di Clapeyron per il PP11 a $t = 2$ per differenti valori di M_{t_0} e delle condizioni termodinamiche iniziali, con isovalori della velocità del suono normalizzata. I simboli bianchi denotano le condizioni iniziali: \circ PP11 IC1, \diamond PP11 IC2. Per la condizione IC1: \bullet $M_{t_0} = 0.5$, \bullet $M_{t_0} = 0.8$, \bullet $M_{t_0} = 1$. Per la condizione IC2: \bullet $M_{t_0} = 1$.

Flusso in un canale piano supersonico turbolento

In tale sezione si analizza nel dettaglio la configurazione di flusso attraverso un canale piano supersonico turbolento (TCF). Condizioni periodiche sono imposte nelle direzioni streamwise (x) e spanwise (z), mentre sulle pareti superiore ed inferiore si applicano condizioni di no-slip con temperatura costante. Al fine di controbilanciare l'attrito viscoso e mantenere una portata massica costante, una forza di volume costante è applicata nella direzione streamwise (Gerolymos & Vallet, 2014). Nel seguito, i pedici $(\cdot)_B$, $(\cdot)_w$ e $(\cdot)_{cl}$ denotano valori mediati nel tempo e nello spazio (sulla sezione trasversale del canale), alla parete ed al centro del canale, rispettivamente; $\overline{(\cdot)}$ indica una media di Reynolds e $(\cdot)'$ la fluttuazione di Reynolds; analogamente, $\widetilde{(\cdot)}$ e $(\cdot)''$ denotano media e fluttuazione di Favre. Le condizioni del flusso sono definite imponendo il numero di Reynolds bulk $Re_B := \frac{\bar{\rho}_B \tilde{u}_B h}{\bar{\mu}_w}$, e il numero di Mach bulk $M_B := \frac{\tilde{u}_B}{\bar{c}_w}$. Poiché alle pareti si applicano condizioni isoterme, si ha $\bar{T}_w = T_w = \text{const.}$ Per il modello di PFG, fissare una temperatura di parete permette di fissare conseguentemente la velocità del suono e le proprietà di trasporto a parete. Per i casi di gas denso, queste quantità dipendono sia dalla temperatura che dalla densità, e dunque i loro valori cambiano durante la simulazioni poiché $\bar{\rho}_w$ non può essere fissata a priori. Per tale ragione, bisogna utilizzare un procedimento iterativo al fine di ottenere i numeri di Reynolds e Mach prescritti. E' stato effettuato uno studio parametrico per vari numeri di Reynolds ($Re_B = 3000, 7000$ e 12000) e per due numeri di Mach ($M_B = 1.5$ e 3.0). Il dominio computazionale ha dimensioni $L_x \times L_y \times L_z = 8\pi h \times 2h \times 2\pi h$ (essendo h la semi altezza del canale); le griglie computazionali selezionate assicurano una risoluzione spaziale comparabile ad altre DNS di TCF (Coleman *et al.*, 1995; Huang *et al.*, 1995; Lechner *et al.*, 2001; Foysi *et al.*, 2004; Gerolymos & Vallet, 2014), ossia $\Delta x^* \in [5, 16]$, $\Delta y_w^* \in [0.5, 0.8]$, $\Delta y_{cl}^* \in [2, 6]$, $\Delta z^* \in [2, 6]$. Il numero di punti di griglia totale varia tra $3.3 \cdot 10^7$ e $1.2 \cdot 10^9$ per i differenti casi. I principali parametri numerici e i risultati globali delle DNS sono riassunti nella tabella 0.2. Le quantità asteriscate si riferiscono allo scaling semi-locale inizialmente proposto da Huang *et al.* (1995) per flussi comprimibili, che corregge il classico scaling di parete con quantità valutate localmente. In particolare, $y^* = \frac{\bar{\rho}(y)u_\tau^* y}{\bar{\mu}(y)}$ e $Re_\tau^* = Re_\tau \sqrt{\frac{\bar{\rho}_{cl}}{\bar{\rho}_w} \frac{\bar{\mu}_w}{\bar{\mu}_{cl}}}$, con $u_\tau^* := \sqrt{\frac{\bar{\tau}_w}{\bar{\rho}(y)}}$ la velocità d'attrito semi-locale. Tale scaling misto (recentemente analizzato in Patel *et al.*, 2015)) ha dimostrato di fornire risultati piuttosto soddisfacenti nello scalare i momenti del primo e del secondo ordine (Foysi *et al.*, 2004) ottenuti per un ampio range di M_B . Ricordiamo che in caso di un flusso incomprimibile, $Re_\tau^* = Re_\tau$.

La figura 0.4 mostra i profili della velocità longitudinale trasformata alla Van-Driest in funzione dello scaling parietale. La velocità di Van-Driest è introdotta in letteratura per migliorare lo scaling nel buffer layer e nella regione esterna degli strati limiti comprimibili prendendo in considerazione le variazioni della densità media. Nonostante il considerevole miglioramento ottenuto rispetto al classico scaling incomprimibile (con la velocità d'attrito u_τ), i profili si scostano dalla legge logaritmica incomprimibile $(\ln y^+)/0.4 + 5.5$ all'aumentare del M_B . Al contrario, per il PP11 si ottengono risultati piuttosto soddisfacenti per tutti i numeri di Mach considerati. Ciò conferma che il gas denso tende a comportarsi similmente ad un liquido con proprietà variabili. Per aria, la temperatura media \tilde{T}^+ aumenta rapidamente con M_B a causa dell'importante riscaldamento da attrito, in particolare per il più basso Re_B (pannello b). Per il PP11, a causa degli alti calori specifici del fluido \tilde{T}^+ è circa costante in tutto il canale per tutte le scelte di numeri di Mach e Reynolds (pannello f), e la temperatura alla mezzeria del canale differisce di meno del 1% da \tilde{T}_w . Il disaccoppiamento degli effetti termici e dinamici nel gas denso porta a minori variazioni di densità nel canale. Per l'aria, la densità al centro del canale è fino al 60% inferiore rispetto a $\bar{\rho}_w$ (per $M_B = 3$) mentre per il PP11 si osservano variazioni al di sotto del 20%. I pannelli (c) e (d) mostrano i profili della viscosità normalizzata $\bar{\mu}/\bar{\mu}_w$. Tale quantità segue le variazioni di temperatura per aria, così che $\bar{\mu}_{cl}/\bar{\mu}_w \approx 2$ per il caso AM3R3. Per il PP11, la viscosità mostra un comportamento

Table 0.2. Parametri numerici e risultati delle DNS per i casi di aria e PP11.

	air				PP11			
M_B	1.50		3.0		1.50		3.0	
Re_B	3000	7000	7000	12000	3000	7000	7000	12000
Name	AM1R3	AM1R7	AM3R7	AM3R12	PM1R3	PM1R7	PM3R7	PM3R12
Line	---	---	---	---	---	---	---	---
N_x	512	768	1024	1536	512	768	768	1280
N_y	256	384	512	768	256	384	384	768
N_z	256	512	768	1024	256	512	512	1024
Re_τ	218.7	466.5	627	1017	191.3	401.6	425.1	692.8
Re_τ^*	147.1	314.8	199.7	324.7	196.4	412.1	492.1	800.2
Δx_c^*	7.2	10.3	4.9	5.3	9.7	13.5	16.1	15.7
Δz_c^*	3.6	5.7	1.6	2.0	4.8	5.1	6.1	4.9
$\Delta y_{c,w}^*$	0.52	0.79	0.25	0.26	0.79	0.66	0.79	0.8
Δy_{cl}^*	2.2	5.5	1.8	2.0	2.7	5.0	6.0	4.3
\overline{M}_{cl}	1.5	1.47	2.18	2.16	1.62	1.60	2.61	2.58
\overline{Re}_{cl}	2740	6319	4035	6903	3659	8423	10256	17635
$\overline{T}_{cl}/\overline{T}_w$	1.39	1.39	2.59	2.58	1.00	1.00	1.01	1.01
$\overline{\rho}_w/\overline{\rho}_B$	1.36	1.37	2.49	2.51	1.05	1.05	1.25	1.25

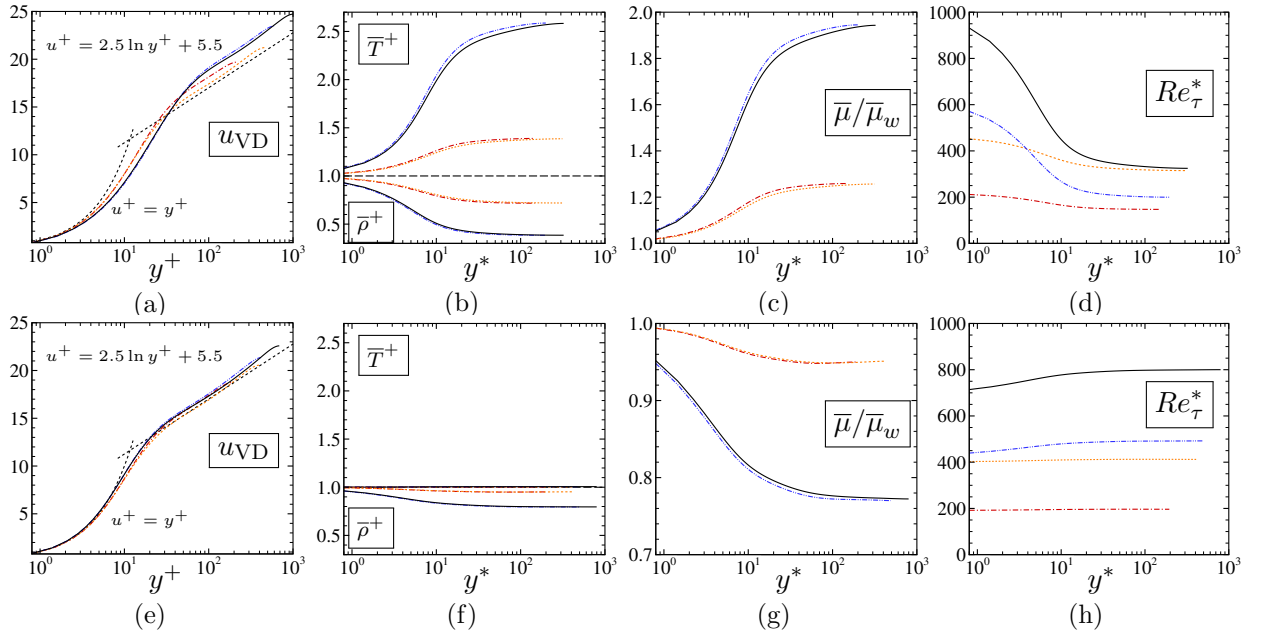


Figure 0.4. Da sinistra a destra: trasformazione di Van-Driest della velocità (u_{VD}) in funzione di y^+ , profili di temperatura e densità normalizzati rispetto ai valori a parete (\overline{T}^+ e $\overline{\rho}^+$) in funzione di y^* , viscosità normalizzata ($\overline{\mu}/\overline{\mu}_w$), e numero di Reynolds d'attrito semi-locale (Re_τ^*) in funzione di y^* . Linea superiore: aria; linea inferiore: PP11. Legenda come in tabella 0.2.

simile al liquido per le condizioni termodinamiche considerate e assume valori inferiori in mezzeria. Differentemente dai liquidi, comunque, ciò non è dovuto all'aumento della temperatura, ma alla diminuzione della densità. Tale differenze motivano il comportamento opposto del numero di Reynolds d'attrito per i due fluidi (pannelli d e h). Per l'aria, Re_τ^* diminuisce rapidamente fino al buffer layer e più lentamente fino in mezzeria. Per un dato Re_B , numeri di Mach più alti aumentano i

gradienti di temperatura portando ad una caduta del Re_τ^* nell'inner layer. Per il PP11, Re_τ^* aumenta monotonicamente fino al buffer layer; in seguito, il suo valore è approssimativamente costante. Gli effetti di gas denso diventano più evidenti per alti M_B , poiché gli stati termodinamici locali sono distribuiti su un range più ampio. In generale, si ottiene $Re_\tau^* < Re_\tau$ per l'aria (comportamento di tipo gas) e $Re_\tau^* > Re_\tau$ per il PP11 (comportamento di tipo liquido). Nella regione parietale, Re_τ^* è $\approx 20\%$ inferiore per il PP11 (comportando un coefficiente d'attrito minore), mentre è fino a due volte più alto al centro del canale, che è quindi caratterizzato da strutture turbolente in proporzione più piccole. Nonostante il comportamento di tipo liquido di alcune proprietà di gas denso, gli effetti di comprimibilità non sono soppressi. Al contrario, il numero di Mach in mezzeria è da 20 a 30% più alto nel gas denso rispetto all'aria, per la quale il riscaldamento per attrito riduce il numero di Mach local rispetto al numero di Mach bulk.

La distribuzione degli stati termodinamici $p - v$ per il caso PM3R12 è riportata in figura 0.5 in funzione della distanza da parete in scaling semi-locale. Nel diagramma sono rappresentati gli isovalori del numero di Prandtl locale. Muovendosi dalla parete alla mezzeria, gli stati spazzano una regione termodinamica più piccola, mentre l'entropia media tende ad aumentare. Si osserva che, poiché il flusso non attraversa mai la linea di transizione, non si possono registrare effetti BZT. Inoltre, il numero di Mach turbolento massimo, approssimativamente 0.5 nel buffer layer, è abbastanza basso da poter trascurare l'influenza della comprimibilità sulla turbolenza. D'altra parte, il numero di Prandtl subisce variazioni importanti (in particolare nella regione di parete), per cui la classica assunzione di Prandtl costante si rivela piuttosto inaccurata per predire la giusta evoluzione di flussi di gas denso caratterizzata da una temperatura di parete prossima a quella critica.

La figura 0.6 mostra gli r.m.s. di densità, delle tensioni di Reynolds e della tensione di shear $\overline{\rho u_i'' u_j''}^+ = \tau_w^{-1} \overline{\rho u_i'' u_j''}$ in scaling semi-locale, e il rapporto tra la produzione e la dissipazione di energia cinetica turbolenta. I profili degli r.m.s. di densità per il gas denso ed il gas perfetto (pannelli a ed e) mostrano delle importanti differenze. Alcuni risultati presenti in letteratura (Gerolymos & Vallet, 2014) hanno mostrato che per casi di aria, $\mathcal{O}(\bar{T}^{-1} \sqrt{\bar{T}^2}) = \mathcal{O}(\bar{\rho}^{-1} \sqrt{\bar{\rho}^2}) = \mathcal{O}(\bar{p}^{-1} \sqrt{\bar{p}^2})$, indipendentemente dalla coordinata y^* e dai numeri di Mach e Reynolds. Lo stesso comportamento è stato osservato nella turbolenza omogenea isotropa, sia forzata (Donzis & Jagannathan, 2013) che libera. I risultati correnti per aria sono in accordo con la letteratura; la densità r.m.s. e

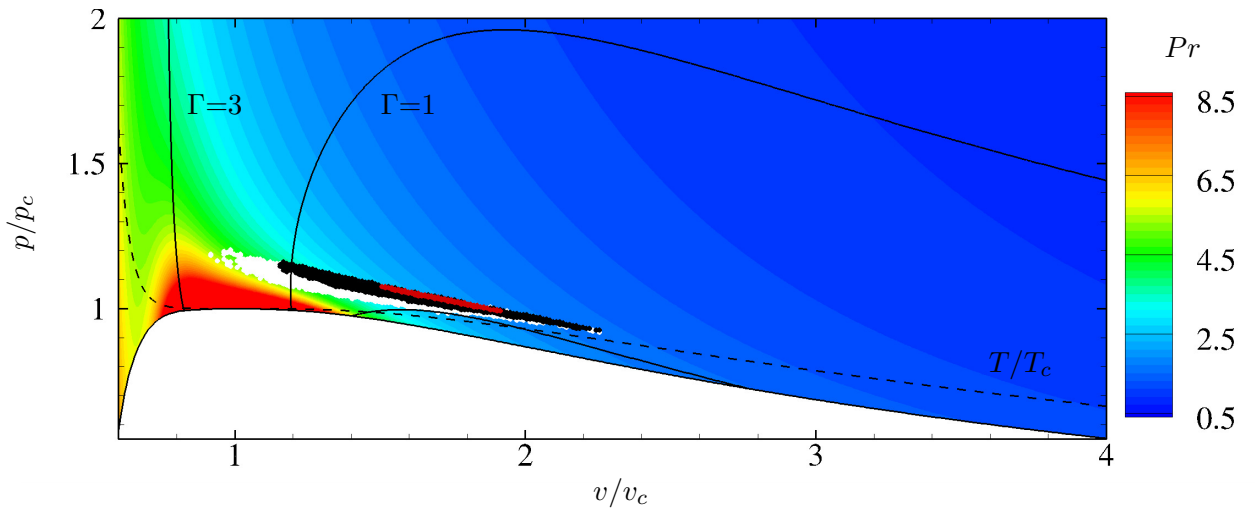


Figure 0.5. Distribuzione degli stati termodinamici istantanei nel diagramma di Clapeyron per il caso PM3R12 (fluido PP11) per differenti distanze dalla parete, con isocontours del numero di Prandtl Pr . ○: $y^* \approx 10$, ●: $y^* \approx 50$, ●: $y^* \approx 800$ (mezzeria).

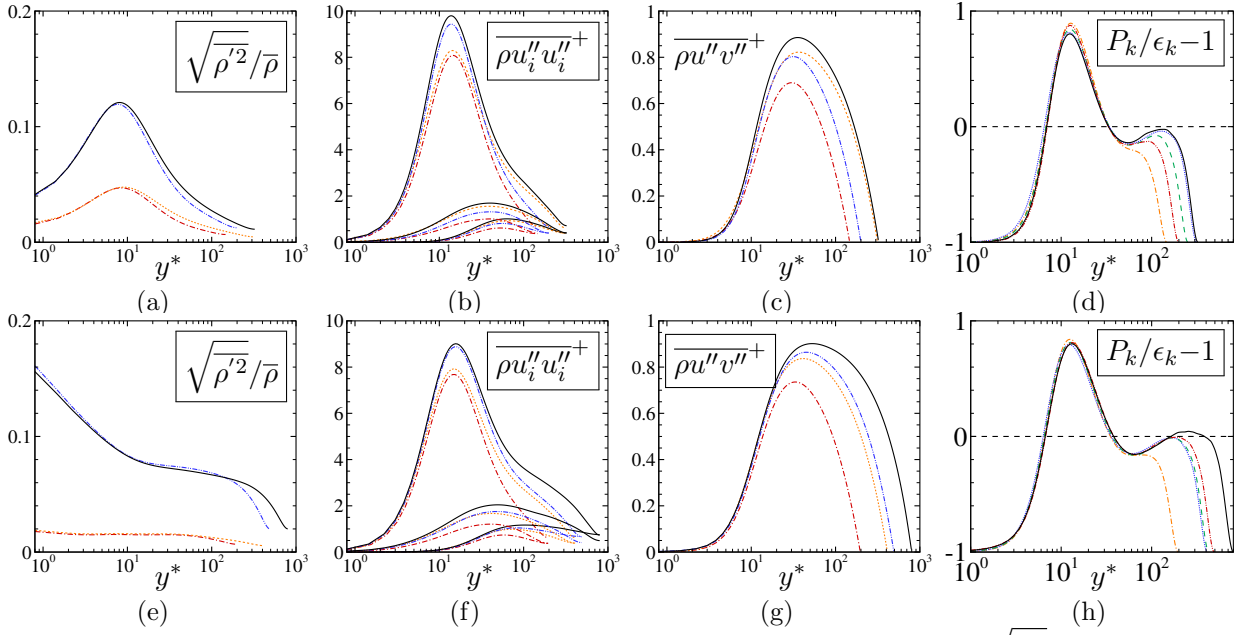


Figure 0.6. Da sinistra a destra: profili y^* dei valori r.m.s. della densità ($\sqrt{\rho'^2/\bar{\rho}}$), tensioni di Reynolds normali ($\overline{\rho u'' u''^+}$) e di taglio ($\overline{\rho u'' v''^+}$) e rapporto produzione su dissipazione dell'energia cinetica turbolenta ($P_k/\epsilon_k - 1$). Rigo superiore: aria; rigo inferiore: PP11. Legenda come in tabella 0.2.

le fluttuazioni di temperatura sono più alte nel buffer layer, con un picco localizzato a $y^* \approx 10$, mentre le fluttuazioni di pressione (non mostrate) sono approssimativamente costanti fino alla zona logaritmica. Per il PP11, le fluttuazioni relative di densità e pressione sono dello stesso ordine di quelle ottenute per flussi d'aria, mentre le fluttuazioni di temperatura (non riportate) sono quasi due ordini di grandezza inferiori. Nonostante ciò, $\overline{\rho'^2}$ diminuisce monotonicamente dalla parete in mezziera, come suggerito dalla dispersione inferiore degli stati $p - v$), rimanendo approssimativamente costante nella zona logaritmica. Tale comportamento è dovuto al fatto che, poiché la densità media diminuisce con la coordinata normale alla parete, la comprimibilità del fluido è inferiore (essendo lo stato termodinamico medio più lontano dalla regione critica) e le fluttuazioni di densità diminuiscono. In media, le fluttuazioni relative di densità sono più piccole di quelle osservate per aria a $M_B = 1.5$, mentre si ottiene il risultato opposto per $M_B = 3$. In altri termini, le fluttuazioni di densità crescono più rapidamente con M_B nel PP11 rispetto all'aria. L'ipotesi di Morkovin resta tuttavia valida, anche per il numero di Mach più alto.

Nonostante le importanti differenze nel comportamento termodinamico, i profili degli stress di Reynolds sono simili per entrambi i fluidi. In particolare, i profili di gas denso sono simili a quelli osservati in altri studi di TCF a basso Mach con proprietà di trasporto variabili (Patel *et al.*, 2015). Il comportamento di tipo liquido della viscosità porta ad un aumento degli stress di Reynolds in direzione trasversale al flusso e normale alla parete e degli stress di shear, rispetto alla corrispondente evoluzione incomprimibile, mentre le tensioni in direzione longitudinale diminuiscono, e tale comportamento è tanto più evidente quando più alto è il numero di Mach (pannelli f e g). Si osserva l'evoluzione opposta per l'aria (pannelli b e c). Ad esempio, il caso AM1R7 ($Re_\tau^* \approx 315$) è caratterizzato da un numero di Reynolds semi-locale più alto del caso AM3R7 ($Re_\tau^* \approx 200$); tuttavia, essendo la viscosità (che dipende unicamente dalla temperatura) molto più alta nell'intero canale per l'ultimo caso, $\overline{\rho v'' v''}$, $\overline{\rho w'' w''}$ e $\overline{\rho u'' v''}$ sono più basse rispetto al caso AM1R7.

Infine, i pannelli d e h mostrano i profili del rapporto dei termini di produzione e dissipazione P_k/ϵ_k

del budget di energia cinetica turbolenta. Lo scaling semi-locale, costruito con $\tau_w^2/\bar{\mu}(y)$, fornisce risultati ben migliori dello scaling con variabili bulk (Lechner *et al.*, 2001) $\tau_w \bar{u}_B/h$ e dello scaling parietale $\bar{\rho}_w u_\tau^4/\bar{\nu}_w$. Studi precedenti (Sarkar, 1995) hanno sottolineato che l'effetto principale della comprimibilità è una riduzione sia di produzione che di dissipazione dell'energia cinetica turbolenta; tale comportamento è confermato per entrambi i fluidi. Tutti i casi di aria e PP11 esibiscono il classico picco di produzione nell'inner region, collocato approssimativamente a $y^* \approx 12$. Per il caso di PP11 a Reynolds più alto, un secondo picco di produzione è osservato nell'outer region, analogamente ai flussi incomprimibili ad alto Re . Ciò è dovuto al comportamento di tipo liquido della viscosità nel PP11, che porta a valori di dissipazione inferiori avvicinandosi verso la mezzzeria del canale.

Conclusioni

In questo lavoro si sono effettuate simulazioni numeriche dirette del decadimento della turbolenza omogenea isotropa comprimibile (CHIT) e di flussi di canale piano turbolento supersonico (TCF) di gas denso. Per entrambi le configurazioni si sono effettuati studi parametrici rispetto ai numeri di Mach e Reynolds caratteristici del problema. I risultati sono stati sistematicamente confrontati a quelli ottenuti con aria. Nelle simulazioni di CHIT si sono osservate importanti differenze per flussi con alti numeri di Mach turbolento iniziale. I trend differenti per i valori r.m.s. delle quantità termodinamiche e delle proprietà di trasporto modificano significativamente l'evoluzione della turbolenza. Nel gas denso, gli effetti di comprimibilità, e specificatamente gli eddy shocklets, sono più deboli. Si osserva inoltre una tendenza alla simmetrizzazione della p.d.f. della divergenza della velocità normalizzata, a causa dell'indebolimento degli shocklets di compressione e all'intensificazione delle onde di rarefazione, portando alla possibile formazione di eddy shocklets di rarefazione per fluidi BZT in idonee condizioni di funzionamento. Per il TCF, il classico scaling y^+ basato sulla velocità d'attrito si rivela non idoneo per sovrapporre i profili delle grandezze termodinamiche e le tensioni di Reynolds quando alti M_B vengono considerati, e dunque bisogna utilizzare scaling che prendano in conto le variazioni delle proprietà del fluido. Lo scaling semi-locale, basato su un misto di quantità termodinamiche a parete e locali, si rivela la scelta più idonea per le tensioni di Reynolds ed i singoli termini dell'equazione dell'energia cinetica turbolenta. Tuttavia, il numero di Mach turbolento massimo raggiunto è approssimativamente 0.5, nonostante l'elevato valore del numero di Mach bulk, e dunque la struttura della turbolenza è poco influenzata dagli effetti di comprimibilità. Inoltre, l'accoppiamento tra il campo cinetico e termico è molto piccolo per fluidi densi caratterizzati da elevati valori dei calori specifici, contrariamente all'aria che invece subisce un significativo riscaldamento per attrito, tipico di flussi altamente comprimibili. Per tali ragioni, per il PP11 molte delle quantità di interesse seguono un'evoluzione simile a quella osservata in turbolenza incomprimibile. Per le condizioni termodinamiche di riferimento considerate, le proprietà di trasporto hanno un comportamento simile al liquido e i numeri di Reynolds reali si rivelano essere molto più alti rispetto ai casi di aria. Ovviamente, la comprimibilità può diventare importante se numeri di Reynolds e Mach più elevati fossero considerati.

Le simulazioni numeriche riportate nella tesi sono state effettuate per il PP11, ma alcune simulazioni preliminari sono state effettuate per altri perfluorocarburi (come ad esempio il PP9 ed il PP10) che hanno mostrato un comportamento simile. Alcune analisi preliminari sono state fatte anche per dei silossani (in particolare, D5 e D6) e dei refrigeranti (R245fa e R134a). Si ricorda anche che alcune simulazioni per un gas BZT modellato con l'equazione di stato di Van der Waals (non riportate nel sommario ma presenti nella tesi) hanno mostrato un comportamento qualitativamente simile. Ciò suggerisce che, benché l'importanza degli effetti di gas denso osservati dipenda dall'estensione della regione di gas denso per un dato fluido e dalla presenza (o no) di una zona di inversione, ci si aspetta che il comportamento qualitativo sia simile anche per altri gas densi.

Résumé étendu

Introduction

La compréhension physique de la dynamique de la turbulence pour des écoulements de gaz dense est importante pour plusieurs domaines en ingénierie, comme les souffleries à haut Reynolds (Anderson, 1991), le transport et le traitement des produits chimiques (Kirillov, 2004), les cycles pour la conversion d'énergie (Brown & Argrow, 2000) et la réfrigération (Zamfirescu & Dincer, 2009). Les gaz denses (DG) sont des fluides mono-phases avec une complexité moléculaire telle que la dérivée fondamentale de la dynamique des gaz $\Gamma := 1 + \frac{\rho}{c} \frac{\partial c}{\partial \rho} \Big|_s$ (avec ρ la masse volumique, p la pression, s l'entropie, et c la vitesse du son), qui mesure le taux de variation de la vitesse du son dans les transformations isentropiques, est inférieure à l'unité (ou même négative, Thompson, 1971) dans une gamme de conditions thermodynamiques proches de la courbe de saturation. Dans ces conditions, la vitesse du son augmente dans les détentes isentropiques et diminue dans les compressions isentropiques, contrairement aux gaz parfaits. On s'attend à ce que les gaz denses montrent les phénomènes les plus intéressants pour une famille de composés polyatomiques lourds, nommés fluides Bethe–Zel'dovich–Thompson (BZT, Thompson, 1971), qui présentent une région de valeurs de Γ négatives (appelée “zone d'inversion”, Cramer & Kluwick, 1984) dans la phase vapeur proche de la courbe de coexistence liquide/vapeur. La théorie prédit que des effets de compressibilité non classiques peuvent se produire dans les régimes d'écoulements transsoniques et supersoniques, comme par exemple des ondes de choc de raréfaction ou des ondes mixtes choc/fan (Cramer & Kluwick, 1984; Cramer, 1991a). En plus, le changement d'entropie à travers un choc faible est beaucoup plus faible que d'habitude pour des gaz denses avec $\Gamma \ll 1$, conduisant à des pertes de choc réduites.

Les simulations numériques des écoulements turbulents de gaz dense d'intérêt technique sont basées sur les bien connues équations RANS (Reynolds-Averaged Navier–Stokes equations), qui doivent être complétées par un modèle pour le tenseur de contraintes de Reynolds. L'exactitude des modèles RANS pour les écoulements de gaz dense n'a pas été correctement évaluée jusqu'à maintenant, en raison de l'absence de données de référence expérimentales et numériques. La création de bases de données DNS fiables et complètes est donc nécessaire pour quantifier les carences des modèles de turbulence existants et pour développer et étalonner des modèles améliorés. De plus, les simulations DNS peuvent améliorer notre compréhension des modifications apportées à la turbulence compressible due au fluide utilisé. En effet, pour les gaz denses, le modèle de gaz parfait (PGF) n'est plus valable, et des équations d'état plus complexes (EoS) doivent être utilisées pour prendre en compte leur comportement thermodynamique particulier. En outre, dans le régime de gaz dense, la viscosité dynamique μ et la conductivité thermique κ dépendent de la température et de la pression à travers des relations complexes. De même, l'approximation de nombre de Prandtl presque constant ($Pr = \mu c_p / \kappa \approx \text{const}$) n'est plus valide. Dans ce qui suit, nous présentons des résultats récents de DNS pour la décroissance de la turbulence isotrope homogène compressible (CHIT), et du canal plan turbulent (TCF), représentant respectivement des exemples de turbulence libre et pariétale, et nous mettons en évidence les différences les plus frappantes par rapport à la turbulence des gaz parfaits.

Table 0.1. Propriétés thermophysiques du PP11: poids moléculaire (\mathcal{M}), température critique (T_c), densité critique (ρ_c), pression critique (p_c), facteur de compressibilité critique (Z_c), facteur acentrique (ω), moment dipolaire (d.m.), température d'ébullition (T_b), rapport de la chaleur spécifique à volume constante sur la constante du gaz ($c_v(T_c)/R$) évalué à la température critique et exposant de la loi de puissance pour la chaleur spécifique dans la limite idéale (n).

\mathcal{M}	T_c	ρ_c	p_c	Z_c	ω_{ac}	ξ	T_{eb}	$c_v(T_c)/R$	n
g mol ⁻¹	K	kg m ⁻³	MPa	-	-	D	K	-	-
624.11	650.2	627.14	1.46	0.2688	0.4963	0.0	488.15	97.3	0.5776

Équations et méthode numérique

Dans cet étude, nous considérons des écoulements de gaz en régime mono-phase, régis par les équations de Navier-Stokes tridimensionnelles compressibles. Le comportement du gaz est modélisé par l'équation d'état thermique de Martin-Hou (MAH) (Martin & Hou, 1955), qui fournit une description réaliste du comportement du gaz et de l'extension de la zone d'inversion. Cette équation, impliquant cinq termes viriales et satisfaisant dix contraintes thermodynamiques, est raisonnablement précise pour le fluide d'intérêt et requiert un minimum d'informations expérimentales. Une loi de puissance de type $c_{v\infty} = c_{v\infty}(T_c)(T/T_c)^n$ est utilisée pour modéliser les variations de la chaleur spécifique à basse densité avec la température, où n est un paramètre dépendant du fluide. En plus de l'EoS, des modèles thermodynamiques reliant la viscosité dynamique et la conductivité thermique à la température et à la pression du gaz doivent être spécifiés. Dans les calculs suivants, les propriétés de transport suivent le modèle de Chung-Lee-Starling (Chung *et al.*, 1988), qui contient un terme de correction pour la région de gaz dense. Pour les cas d'air, le modèle de gaz parfait polytropique classique est utilisé avec une loi de puissance dépendant de la température pour la viscosité, $\mu = \mu_{ref}(T/T_{ref})^{0.7}$, et une hypothèse de Prandtl constant, $Pr = 0.7$. Le fluide de travail est le perfluoro-perhydrophénanthrène (formule chimique C₁₄F₂₄), appelé ci-après avec le nom commercial PP11. Les propriétés thermodynamiques du PP11 sont fournies dans la table 0.1. Ce fluide a été souvent utilisé dans la littérature de gaz dense car il présente une zone d'inversion relativement large et peut par conséquent conduire à l'apparition d'effets non classiques.

Les dérivées spatiales dans les équations de Navier-Stokes sont approchées avec des schémas aux différences finies optimisés. Plus précisément, les termes convectifs sont approximés par des différences finies optimisées au quatrième ordre avec un stencil à onze points dans chaque direction de maillage Bogey & Bailly (2004), et les termes visqueux par des différences finies standard au quatrième ordre centrées. L'algorithme prévoit aussi l'application dans chaque direction d'un filtre sélectif optimisé de sixième ordre utilisant également un stencil à onze points pour supprimer les oscillations maille à maille. Afin d'assurer la robustesse du calcul pour les écoulements compressibles avec chocs, une stratégie de filtrage sélectif non linéaire adaptatif est utilisée Bogey *et al.* (2009). Enfin, l'intégration temporelle s'effectue au moyen d'un schéma de Runge-Kutta à six pas à stockage réduit optimisé dans l'espace des fréquences Bogey & Bailly (2004).

Décroissance de la turbulence homogène isotrope compressible

Le problème de la décroissance de la CHIT est résolu sur un domaine cubique de $[0, 2\pi]^3$. Conditions aux limites périodiques sont appliquées dans les trois directions cartésiennes. Le spectre d'énergie cinétique turbulent initial est de type Passot-Pouquet type, i.e., $E(k) = Ak^4 \exp[-2(k/k_0)^2]$, où k_0 est le nombre d'onde de pic et A une constante dépendant de la quantité initiale d'énergie

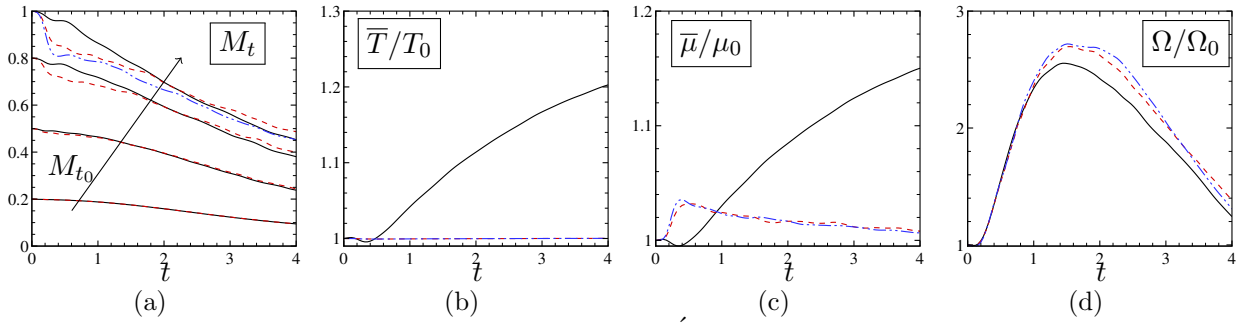


Figure 0.1. Résultats de la décroissance de CHIT. Évolutions temporelles du nombre de Mach turbulent M_t pour différents M_{t_0} (panneau a). (b) à (d): température moyenne normalisée T/T_0 , viscosité normalisée $\bar{\mu}/\mu_0$ et enstrophie normalisée Ω/Ω_0 à $M_{t_0} = 1$. —: Air; - - - -: PP11 IC1; - · - · -: PP11 IC2.

cinétique injectée. Le champ de vitesse initial est purement solénoïdal et les r.m.s. des variables thermodynamiques sont fixées à zéro. La décroissance de la turbulence compressible est régie par le nombre de Mach turbulent $M_t = \sqrt{u_i^2}/\bar{c}$ et le nombre de Reynolds $Re_\lambda = u'\lambda\bar{\rho}/\bar{\mu}$, basé sur la micro-échelle de Taylor λ . Nous avons réalisé des simulations directes de CHIT de gaz dense à différents nombres de Mach turbulent initiaux, i.e. $M_{t_0} = 0.2, 0.5, 0.8$ et 1 . Le nombre de Reynolds initial est fixé à $Re_\lambda = 200$ et le nombre d'onde de pic k_0 est égal à 2 pour toutes les simulations. La décroissance est simulée jusqu'à $t = 4$ (avec t une échelle de temps non dimensionnelle basée sur le temps initial de rotation des gros tourbillons). Toutes les simulations ont été réalisées sur une grille cartésienne régulière de 512^3 . Dans le cas le plus sévère (i.e. $M_{t_0} = 1$), la plus petite échelle non-dimensionnelle résolue $k_{max}\eta$ (étant k_{max} le nombre d'onde le plus grande et $\eta = (\bar{\mu}^3/\bar{\rho}^2\bar{\epsilon})^{1/4}$ l'échelle spatiale de Kolmogorov, Jagannathan & Donzis, 2016) est toujours supérieure à $\approx 6.5 - 7$ et la longueur de Kolmogorov est discrétisée au moins sur 2 points de maillage, qui correspond à une très bonne résolution.

Les simulations de gaz dense sont montrées pour deux choix de l'état thermodynamique initial, correspondant à un point dans la région de gaz dense ($\rho_0/\rho_c = 1.618$, $p_0/p_c = 1.02$, $T_0/T_c = 1.01$, $\Gamma_0 = 0.1252$, appelée IC1) et un à l'intérieur de la zone d'inversion ($\rho_0/\rho_c = 1.618$, $p_0/p_c = 0.98$, $T_0/T_c = 1.001$, $\Gamma_0 = -0.093$, IC2), pour lequel l'écoulement peut présenter des effets BZT. Puisque l'entropie ne peut qu'augmenter pendant l'évolution, aucun effet BZT ne peut apparaître pour le premier choix des conditions thermodynamiques. Les résultats ont été systématiquement comparés à ceux d'un gaz diatomique parfait (air). Les effets de compressibilité sont d'abord étudiés en comparant les évolutions temporelles des statistiques principales de l'écoulement pour les simulations d'air et de gaz dense à divers M_{t_0} (figure 0.1a). Les solutions PFG et DG sont pratiquement superposées à $M_{t_0} = 0.2$ et s'écartent progressivement au fur et à mesure que M_{t_0} augmente, en raison des différentes propriétés de compressibilité et de transport des deux fluides. Nous limitons notre analyse au cas le plus représentatif, c'est-à-dire $M_{t_0} = 1$. La température moyenne (figure 0.1b) augmente significativement au cours du temps pour PFG, et la viscosité (figure 0.1c) suit le même comportement. Au contraire, pour les cas DG, la température reste presque constante en raison de la chaleur spécifique beaucoup plus élevée et l'évolution temporelle de la viscosité (qui dépend des variations de densité) présente un pic au début et décroît ensuite, contrairement au PFG. L'énergie cinétique turbulente normalisée K/K_0 (non montrée pour brièveté) et l'enstrophie Ω/Ω_0 (figure 0.1d) sont similaires pour les cas PFG et DG. Un pic d'enstrophie est observé pour $t \approx 1.4 - 1.5$, ce qui est légèrement plus élevé pour le gaz dense, en raison de la viscosité moyenne plus faible par rapport au PFG. Des comportements similaires sont observés pour IC1 et IC2.

Les évolutions temporelles des grandeurs thermodynamiques fluctuantes sont présentées dans la

figure 0.2 (ligne supérieure). Le rapport de densité instantanée maximum à minimum augmente pendant la phase supersonique initiale, entraîné par des mécanismes d'étirement de tourbillon avec la production de gradients de vitesse forts, atteignant un maximum pour un temps non dimensionnel compris entre 1 et 2. Dans le gaz dense, la valeur maximale est cependant environ 2.5 fois plus faible que dans le gaz parfait dû à la formation de shocklets plus faibles. Ensuite, le rapport décroît et les deux fluides présentent des comportements similaires à des moments ultérieurs. De même, les fluctuations de pression (figure 0.2b) dans le gaz dense sont environ cinq fois plus faibles pour le PP11, indépendamment du choix de l'état thermodynamique initial. Au contraire, les valeurs r.m.s. de la vitesse du son sont plus élevées pour le gaz dense. Pour ce fluide, $c = c(\rho, T)$ suit essentiellement les variations de densité (la température étant presque constante pendant la décroissance). Ce mécanisme est profondément différent de celui observé pour le PFG, où la vitesse du son augmente en raison du réchauffement par frottement. Les évolutions temporelles de la dérivée fondamentale de la dynamique des gaz moyenne et r.m.s sont également rapportées pour PP11 à diverses conditions initiales. La valeur moyenne $\bar{\Gamma}$ (figure 0.2d) suit les variations de densité moyenne. Pour IC1 et IC2, le développement initial des modes compressibles augmente la valeur moyenne de Γ , qui reste cependant inférieure à 1 pendant toute l'évolution (ce qui implique que la vitesse du son tend à diminuer dans les régions des compressions), puis décroît. Les r.m.s. de Γ sont aussi élevée que 1 à $t \approx 1$ signifiant que, pour des écoulements à nombre de Mach élevés, les valeurs de Γ sont largement distribuées autour de la moyenne et peuvent être localement supérieures à 1 ou, pour IC2, inférieures à 0. Malgré le différent comportement local de Γ , les statistiques de

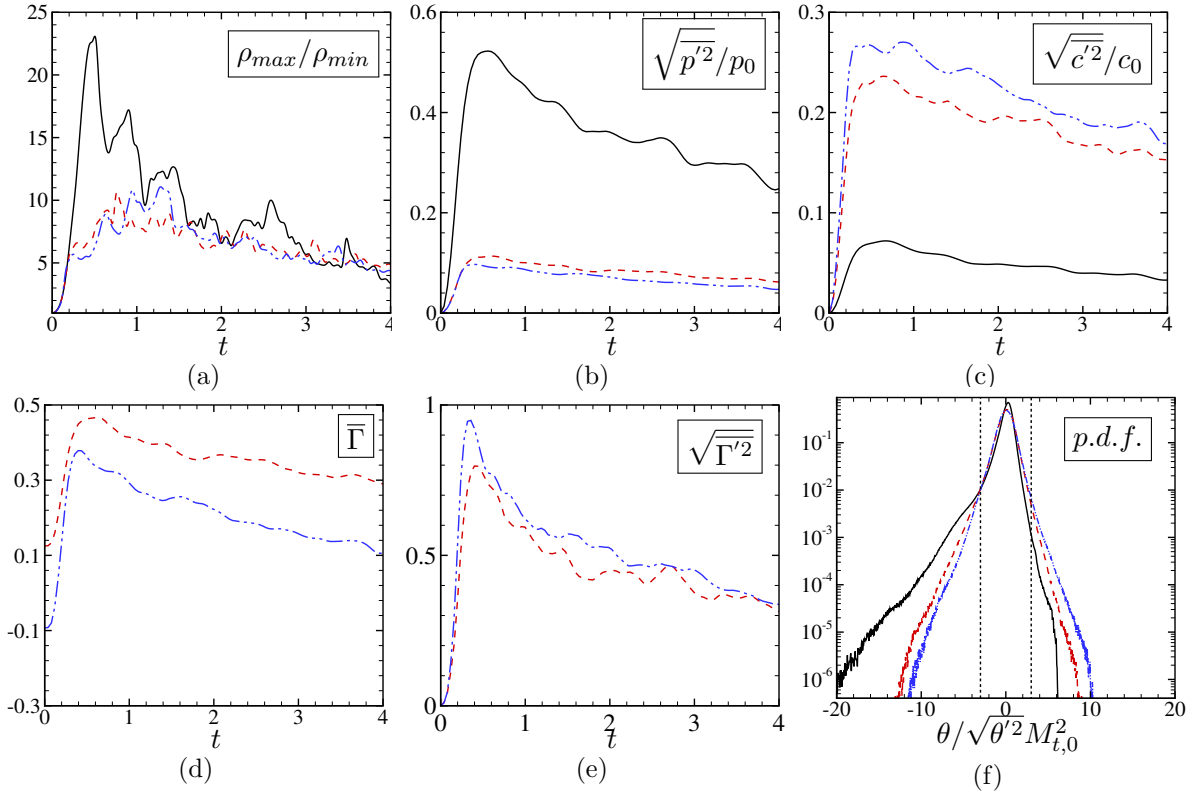


Figure 0.2. CHIT à $M_{t_0} = 1$. (a) à (c): évolutions temporelles du rapport des valeurs maximum et minimum de masse volumique ρ_{max}/ρ_{min} , r.m.s. de pression $\sqrt{p'^2}/p_0$ et r.m.s. de vitesse du son $\sqrt{c'^2}/c_0$; (d) à (f): évolutions temporelles de la moyenne ($\bar{\Gamma}$) et r.m.s. ($\sqrt{\Gamma'^2}$) de la dérivée fondamentale de la dynamique des gaz, et p.d.f. de la dilatation normalisée $\theta/\sqrt{\theta'^2}M_{t,0}^2$ au temps non dimensionnel $t = 2$. Légende en figure 0.1.

l'écoulement macroscopiques sont peu affectées et tendent à se comporter de manière similaire pour les deux conditions initiales.

La figure 0.3 montre la distribution des états thermodynamiques de l'écoulement dans le diagramme $p - v$ à l'instant $t = 2$, pour IC1 à divers M_{t_0} et pour IC2 à $M_{t_0} = 1$. La viscosité et les pertes de choc étant faibles, tous les états ont tendance à se distribuer le long de l'isentrope initiale. La région thermodynamique couverte par les états $p - v$ pendant la décroissance augmente avec M_{t_0} . Pour $M_{t_0} = 1$, la légère modification des conditions thermodynamiques initiales modifie considérablement la pression maximale atteinte. Le volume spécifique, en effet, est limité par une limite inférieure correspondant à la transition liquide/gaz (respectivement, une limite supérieure de densité), car l'écoulement subit de fortes compressions. D'autre part, les fortes détentes sont favorisées par le comportement de gaz dense, puisque la vitesse du augmente et la compressibilité diminue. Les régions de dilatation sont classées selon le niveau local de dilatation normalisée $\theta/\sqrt{\theta'^2}M_{t_0}^2$ (Sciacovelli *et al.*, 2016a). Les régions avec $0 < |\theta/\sqrt{\theta'^2}M_{t_0}^2| < 2$ sont considérées des dilatations/compressions faibles, alors que $|\theta/\sqrt{\theta'^2}M_{t_0}^2| > 2$ indique des mouvements de dilatation/compression forts. De plus, il est communément admis que des chocs de compression peuvent être formés pour $\theta/\sqrt{\theta'^2}M_{t_0}^2 < -3$ (Samtaney *et al.*, 2001). Les différences dans le diagramme de Clapeyron sont confirmées par les fonctions de distribution de probabilité (p.d.f.s) de la dilatation normalisée montrée dans la figure 0.2f. Le gaz dense présente une p.d.f. beaucoup plus symétrique que le gaz parfait, qui se caractérise par une longue queue gauche, conformément à résultats similaires dans la littérature (Wang *et al.*, 2012b). Le plus grand équilibre entre les queues gauche et droite de la p.d.f. pour le gaz dense est dû à l'affaiblissement ou à la suppression significative des chocs de compression dans les régions d'écoulement où Γ est proche ou inférieur à zéro; d'autre part, les détentes sont favorisées, conduisant à une queue droite plus lourde. Ce comportement est plus développé pour IC2, en raison de la possibilité d'effets BZT conduisant à l'apparition de chocs de détente. À $t = 2$, environ la moitié du domaine est caractérisée par des états thermodynamiques enfermés sous la ligne de transition. Parmi ces états, environ 36% se composent de régions de dilatation faible et $\approx 6\%$ de régions de forte détente. Globalement, les fortes régions de compression diminuent de 3% à 2% alors que les fortes détentes passent de 1.7% à 2.6%.

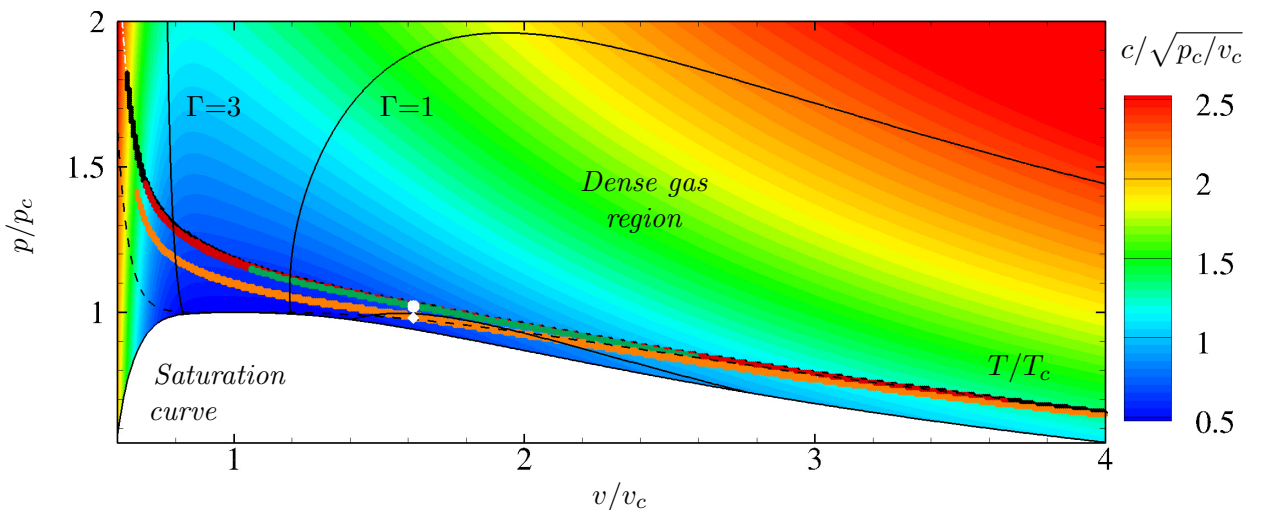


Figure 0.3. Distributions des états thermodynamiques dans le diagramme de Clapeyron pour le PP11 à $t = 2$ pour différents M_{t_0} et différentes conditions initiales, avec iso-valeurs de la vitesse du son normalisée. Les symboles blancs dénotent les conditions initiales: \circ PP11 IC1, \diamond PP11 IC2. Pour la condition IC1: \bullet $M_{t_0} = 0.5$, \bullet $M_{t_0} = 0.8$, \bullet $M_{t_0} = 1$. Pour la condition IC2: \bullet $M_{t_0} = 1$.

Canal plan turbulent supersonique

La configuration de canal plan turbulent supersonique est maintenant considérée. Les conditions périodiques sont appliquées dans les directions longitudinale (x) et transversale (z) par rapport à l'écoulement. Des conditions de paroi isotherme sans glissement sont appliquées sur les parois inférieure et supérieure. Afin d'équilibrer le frottement visqueux et de maintenir le débit massique visé, une force volumique spatiale constante est appliquée dans la direction longitudinale (Gerolymos & Vallet, 2014). Dans ce qui suit, les indices $(\cdot)_B$, $(\cdot)_w$ et $(\cdot)_{cl}$ indiquent les valeurs moyennées en temps et en espace sur la section transversale du canal, à la paroi et sur la ligne médiane, respectivement; $\overline{(\cdot)}$ indique la moyenne de Reynolds et $(\cdot)'$ la fluctuation de Reynolds; de même, $\widetilde{(\cdot)}$ et $(\cdot)''$ indiquent les moyennes et les fluctuations de Favre. Les conditions de l'écoulement sont définies en imposant le nombre de Reynolds bulk $Re_B := \frac{\bar{\rho}_B \tilde{u}_B h}{\bar{\mu}_w}$ et le nombre de Mach bulk $M_B := \frac{\tilde{u}_B}{\tilde{c}_w}$. Puisque des conditions isothermes sont appliquées aux parois, $\bar{T}_w = T_w = \text{const.}$ Pour le modèle PFG, fixer la température de la paroi permet d'imposer la vitesse du son et les propriétés de transport en conséquence. Pour les gaz denses, ces dernières dépendent à la fois de la température et de la densité, et donc leur valeurs changent pendant la simulation car $\bar{\rho}_w$ ne peut pas être fixé a priori. Pour cette raison nous avons utilisé une procédure itérative afin de obtenir les nombres de Mach et Reynolds prescrits. Une étude paramétrique est effectuée à différents nombres de Reynolds ($Re_B = 3000, 7000$ et 12000) et deux nombres de Mach bulk ($M_B = 1.5$ et 3). Le domaine de calcul a dimensions $L_x \times L_y \times L_z = 8\pi h \times 2h \times 2\pi h$ (étant h la demi-hauteur du canal); les grilles de calcul sélectionnées assurent une résolution spatiale comparable à celle d'autres DNS de TCF (Coleman *et al.*, 1995; Huang *et al.*, 1995; Lechner *et al.*, 2001; Foysi *et al.*, 2004; Gerolymos & Vallet, 2014), i.e., $\Delta x^* \in [5, 16]$, $\Delta y_w^* \in [0.5, 0.8]$, $\Delta y_{cl}^* \in [2, 6]$, $\Delta z^* \in [2, 6]$. Le nombre total de points de grille varie entre $3.3 \cdot 10^7 \div 1.2 \cdot 10^9$ pour les différents cas. Les principaux paramètres numériques et les résultats globaux des DNS sont résumés dans le tableau 0.2. Les quantités indiquées se réfèrent à l'échelle semi-locale empirique initialement proposée par Huang *et al.* (1995) pour écoulements compressibles, qui corrige l'échelle de paroi habituelle avec des quantités locales. Plus précisément, $y^* = \frac{\bar{\rho}(y) u_\tau^* y}{\bar{\mu}(y)}$ et $Re_\tau^* = Re_\tau \sqrt{\frac{\bar{\rho}_{cl} \bar{\mu}_w}{\bar{\rho}_w \bar{\mu}_{cl}}}$, avec $u_\tau^* := \sqrt{\frac{\bar{\tau}_w}{\bar{\rho}(y)}}$ la vitesse de frottement semi-locale. Cette échelle mixte (récemment analysée par Patel *et al.*, 2015) donne des résultats tout à fait satisfaisants pour superposer les moments de premier et deuxième ordre (Foysi *et al.*, 2004) obtenus à partir d'une large gamme de M_B . Nous rappelons que dans le cas d'un écoulement incompressible, $Re_\tau^* = Re_\tau$.

Figure 0.4 (panneaux a et e) montre les profils de vitesse longitudinale de Van-Driest dans l'échelle pariétale. La vitesse de Van-Driest est introduite dans la littérature pour améliorer le scaling dans la couche tampon et la région externe des couches limites compressibles en tenant compte des variations de densité moyenne. Malgré une amélioration considérable par rapport à l'échelle classique incompressible (avec vitesse de frottement u_τ), les profils s'écartent de la loi log incompressible $(\ln y^+)/0.4 + 5.5$ lorsque M_B augmente. Au contraire, des résultats tout à fait satisfaisants sont obtenus pour PP11 à tous les nombres de Mach. Dans un certain sens, le gaz dense se comporte de manière similaire à un liquide ayant des propriétés variables. Pour l'air, la température moyenne \tilde{T}^+ croît rapidement avec M_B , en raison de l'augmentation significative du chauffage par frottement, en particulier pour le plus bas Re_B (panneau b). Pour PP11, en raison de la grande chaleur spécifique du fluide, \tilde{T}^+ est presque constante sur le canal pour tout choix des nombres de Mach et de Reynolds (panneau f), et la température au centre du canal diffère moins de 1% par rapport à \tilde{T}_w . Le découplage des effets dynamiques et thermiques dans le gaz dense conduit à de plus faibles variations de densité à travers le canal. Pour l'air, la densité au centre du canal est jusqu'à 60% inférieure à $\bar{\rho}_w$ (à $M_B = 3$) alors que des variations inférieures à 20% sont observées pour le PP11. Les panneaux c et d montrent des profils de la viscosité normalisée $\bar{\mu}/\bar{\mu}_w$. Cette quantité suit

Table 0.2. Paramètres numériques et résultats globaux des DNS pour l'air et PP11.

	air				PP11			
$M_{B,w}$	1.50		3.0		1.50		3.0	
$Re_{B,w}$	3000	7000	7000	12000	3000	7000	7000	12000
Name	AM1R3	AM1R7	AM3R7	AM3R12	PM1R3	PM1R7	PM3R7	PM3R12
Line	---	---	---	---	---	---	---	---
N_x	512	768	1024	1536	512	768	768	1280
N_y	256	384	512	768	256	384	384	768
N_z	256	512	768	1024	256	512	512	1024
Re_τ	218.7	466.5	627	1017	191.3	401.6	425.1	692.8
Re_τ^*	147.1	314.8	199.7	324.7	196.4	412.1	492.1	800.2
Δx_c^*	7.2	10.3	4.9	5.3	9.7	13.5	16.1	15.7
Δz_c^*	3.6	5.7	1.6	2.0	4.8	5.1	6.1	4.9
$\Delta y_{c,w}^*$	0.52	0.79	0.25	0.26	0.79	0.66	0.79	0.8
Δy_{cl}^*	2.2	5.5	1.8	2.0	2.7	5.0	6.0	4.3
\overline{M}_{cl}	1.5	1.47	2.18	2.16	1.62	1.60	2.61	2.58
\overline{Re}_{cl}	2740	6319	4035	6903	3659	8423	10256	17635
$\overline{T}_{cl}/\overline{T}_w$	1.39	1.39	2.59	2.58	1.00	1.00	1.01	1.01
$\overline{\rho}_w/\overline{\rho}_B$	1.36	1.37	2.49	2.51	1.05	1.05	1.25	1.25

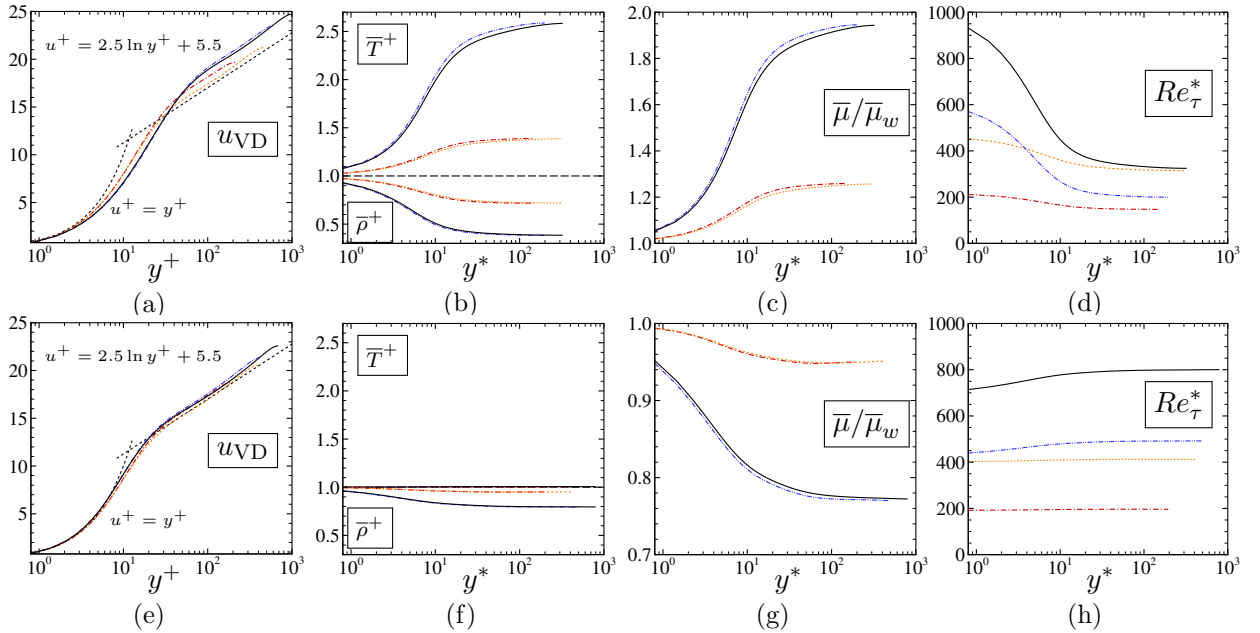


Figure 0.4. De gauche à droite: transformation de Van-Driest vitesse longitudinale (u_{VD}) vs y^+ , température et masse volumique normalisées par rapport aux valeurs de paroi (\overline{T}^+ et $\overline{\rho}^+$) vs y^* , viscosité normalisée ($\overline{\mu}/\overline{\mu}_w$), et nombre de Reynolds de frottement semi-local (Re_τ^*). Ligne supérieure: air; ligne inférieure: PP11. Légende comme en tableau 0.2.

les variations de température pour l'air, ayant $\overline{\mu}_{cl}/\overline{\mu}_w \approx 2$ pour le cas AM3R3. Pour le PP11, la viscosité présente un comportement de type liquide aux conditions thermodynamiques considérées et présente des valeurs plus faibles en centerline. Contrairement aux liquides, cependant, ceci n'est pas dû à une élévation de température, mais à la réduction de la densité. Les différences précédentes expliquent le comportement opposé du nombre de Reynolds de frottement pour les deux fluides

(panneaux d et h). Pour l'air, Re_τ^* diminue rapidement jusqu'à la couche tampon et plus lentement jusqu'à la ligne centrale. Pour un Re_B donné, les nombres de Mach plus élevés augmentent les gradients de température, conduisant à la chute de Re_τ^* dans la région interne. Pour le PP11, Re_τ^* augmente monotoniquement jusqu'à la couche tampon; après, sa valeur est approximativement constante. Les effets de gaz denses deviennent plus évidents à M_B élevés, puisque les états thermodynamiques locaux se répartissent sur une région plus large. En général, $Re_\tau^* < Re_\tau$ pour l'air (comportement de type gaz) et $Re_\tau^* > Re_\tau$ pour PP11 (comportement de type liquide). Dans la région de paroi, Re_τ^* est $\approx 20\%$ inférieur pour le PP11 (conduisant à un coefficient de frottement plus petit), alors qu'il est jusqu'à deux fois plus élevé en centerline, qui est alors caractérisé par des structures turbulentes plus petites. En dépit du comportement liquide de certaines propriétés dans le gaz dense, les effets de compressibilité ne sont pas supprimés. Au contraire, le nombre de Mach de la ligne médiane est de 20 à 30% plus grand dans le gaz dense que dans l'air, où le chauffage par frottement réduit le nombre de Mach local par rapport à la valeur de référence bulk.

La distribution des états thermodynamiques $p-v$ pour le cas PM3R12 est montrée dans la figure 0.5 en fonction de la distance de la paroi en unités semi-locales. Le diagramme est coloré avec le nombre de Prandtl local. En se déplaçant de la paroi à la ligne centrale, une région thermodynamique plus petite est intéressée, alors que l'entropie moyenne tend à augmenter. Nous observons que, puisque l'écoulement ne traverse jamais la ligne de transition, aucun effet BZT n'est impliqué. En outre, le nombre de Mach turbulent maximal, environ 0.5, est suffisamment faible pour négliger l'influence de la compressibilité sur la turbulence. D'autre part, le nombre de Prandtl subit des variations significatives, en particulier dans la région proche de la paroi, ce qui rend l'utilisation d'une hypothèse de Prandtl constante tout à fait inexacte pour prédire l'évolution des écoulements de gaz dense caractérisés par une température de paroi proche de la valeur critique.

La figure 0.6 montre les valeurs r.m.s. de la masse volumique, les contraintes de Reynolds et de shear $\overline{\rho u_i'' u_j''}^+ = \tau_w^{-1} \overline{\rho u_i'' u_j''}$ en échelle semi-locale et le rapport entre production et dissipation de l'énergie cinétique turbulente. Les profils des r.m.s. de la densité pour le gaz dense et le gaz parfait (panneaux a et e) sont profondément différents. Les résultats de référence en littérature (Gerolymos & Vallet, 2014) ont montré que pour les cas d'air, $\mathcal{O}(\bar{T}^{-1} \sqrt{T'^2}) = \mathcal{O}(\bar{\rho}^{-1} \sqrt{\rho'^2}) = \mathcal{O}(\bar{p}^{-1} \sqrt{p'^2})$, indépendamment de la coordonnée y^* et des nombres de Mach et Reynolds considérées. Le même comportement a été observé à la fois pour la CHIT forcée et décroissante. Les résultats actuels

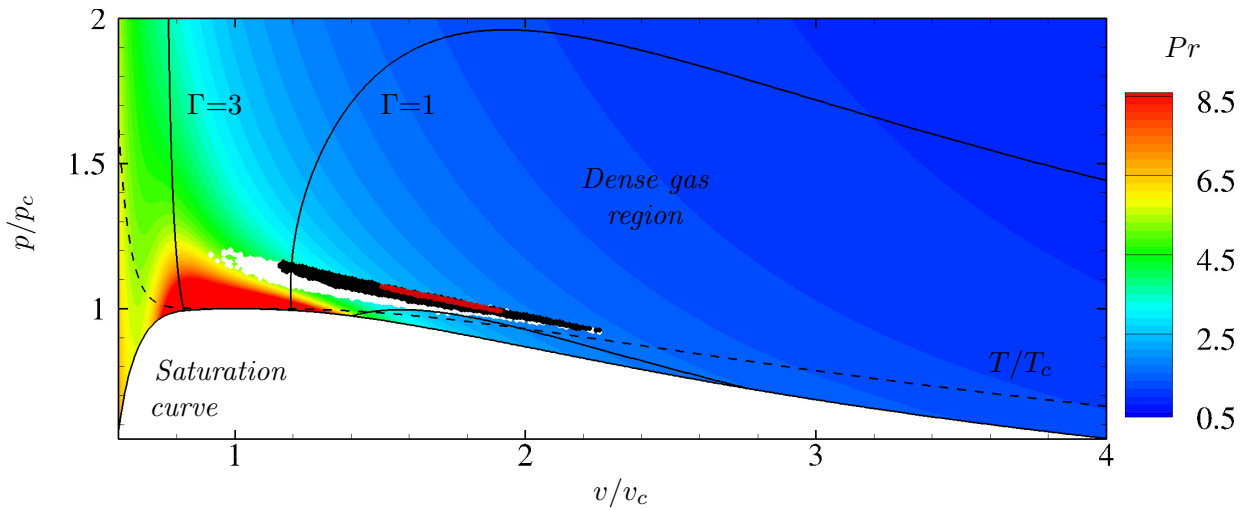


Figure 0.5. Distributions des états thermodynamiques dans le diagramme de Clapeyron pour le cas PM3R12 (fluide PP11) pour différentes distances de la paroi, avec iso-valeurs du nombre de Prandtl Pr . \circ : $y^* \approx 10$, \bullet : $y^* \approx 50$, \bullet : $y^* \approx 800$ (centerline).

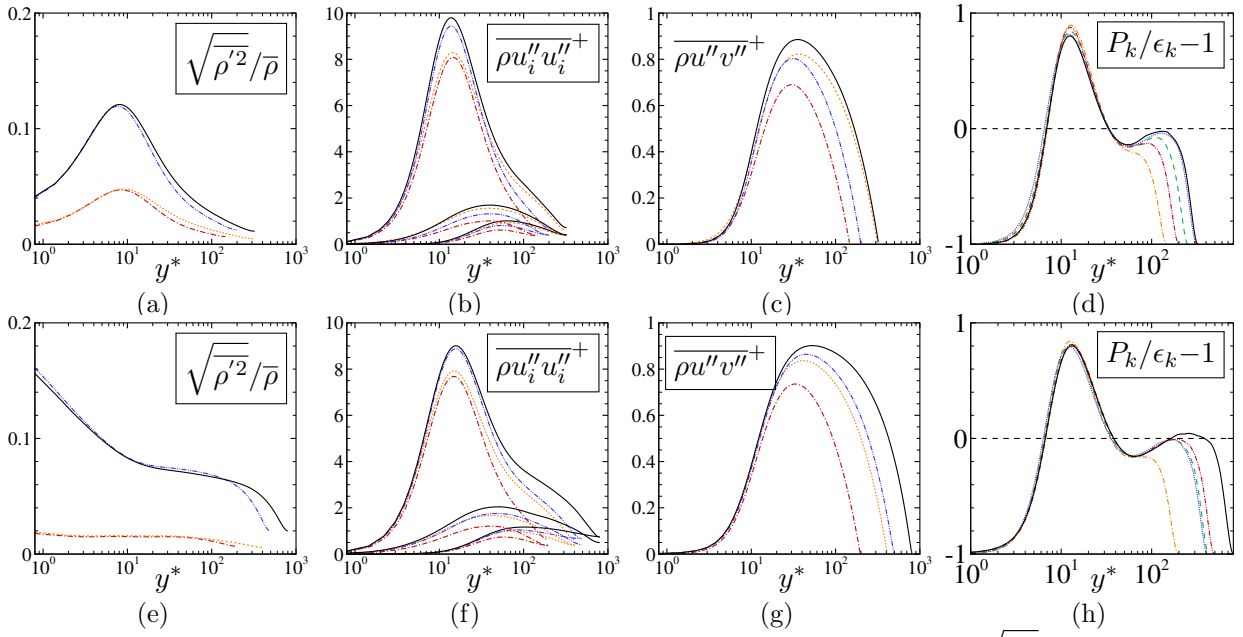


Figure 0.6. De gauche à droite: profils en y^* des fluctuations de densité ($\sqrt{\rho'^2}/\bar{\rho}$), tensions de Reynolds normales ($\overline{\rho u'' u''^+}$) et de cisaillement ($\overline{\rho u'' v''^+}$), et rapport production-dissipation de l'énergie cinétique turbulente ($P_k/\epsilon_k - 1$). Ligne supérieure: air; ligne inférieure, PP11. Légende comme en tableau 0.2.

pour l'air concordent avec les tendances de référence; les r.m.s. de la densité et de la température sont plus élevées dans la couche tampon, avec un pic à $y^* \approx 10$, alors que les fluctuations de pression (non montrées) sont approximativement constantes jusqu'à la région logarithmique. Pour le PP11, la densité relative et les fluctuations de pression sont du même ordre pour les écoulements d'air, alors que les fluctuations de température sont près de deux ordres de grandeur inférieures. Néanmoins, $\bar{\rho}^2$ diminue monotoniquement de la paroi à la centerline (comme le suggère la plus petite dispersion des états $p - v$), restant à peu près constante dans la couche logarithmique. Le comportement observé est dû au fait que, lorsque la densité moyenne diminue avec la coordonnée normale à la paroi, la compressibilité du fluide devient inférieure (l'état thermodynamique moyen s'éloigne de la région du point critique) et les fluctuations de la densité diminuent. En moyenne, les fluctuations relatives de densité sont plus faibles que celles observées pour l'air à $M_B = 1.5$, alors qu'un résultat opposé est obtenu à $M_B = 3$. En autres termes, les fluctuations de densité se développent plus rapidement avec M_B dans le PP11 que dans l'air. Néanmoins, l'hypothèse de Morkovin reste satisfaite, même au plus haut nombre de Mach.

Malgré les évidentes différences du comportement thermodynamique, les profils de contraintes de Reynolds sont similaires pour les deux fluides. Plus précisément, les profils de gaz dense sont en accord avec ceux observés dans d'autres études (Patel *et al.*, 2015) pour le TCF à bas-Mach avec des propriétés de transport dépendant de la température. Le comportement de type liquide de la viscosité conduit à une augmentation des contraintes de Reynolds spanwise, normales à la paroi et de shear par rapport à la correspondante évolution incompressible, alors que celles longitudinales diminuent et cet effet tend à être renforcé lors de l'augmentation du nombre de Mach (panneaux f et g). Un comportement opposé est observé pour l'air (panneaux b et c). Par exemple, le cas AM1R7 ($Re_\tau^* \approx 315$) est caractérisé par un nombre de Reynolds de frottement semi-local plus élevé que le cas AM3R7 ($Re_\tau^* \approx 200$). Néanmoins, étant la viscosité dépendant de la température beaucoup plus élevée dans tout le canal, dans ce dernier cas, $\overline{\rho v'' v''}$, $\overline{\rho w'' w''}$ et $\overline{\rho u'' v''}$ sont inférieurs par

rapport à AM1R7. Enfin, les panneaux d et h montrent les profils du rapport entre la production et le terme de dissipation P_k/ϵ_k du budget turbulent de l'énergie cinétique. L'échelle semi-locale, construite avec $\tau_w^2/\bar{\mu}(y)$, se comporte mieux que l'échelle bulk (Lechner *et al.*, 2001) $\tau_w \bar{u}_B/h$ et l'échelle de paroi $\bar{\rho}_w u_\tau^4/\bar{\nu}_w$. Des travaux précédents (Sarkar, 1995) ont montré que l'effet principal de la compressibilité est une réduction de la production et de la dissipation; ceci est confirmé pour l'air et le PP11. Tous les cas d'air et PP11 présentent le pic de production habituel dans la région intérieure, situé approximativement à $y^* \approx 12$. Pour le cas avec le nombre Reynolds plus élevé avec le PP11, un deuxième pic de production est observé dans la région externe, comme dans le cas d'écoulements incompressibles à haut Reynolds, ce qui n'est pas le cas pour l'air au même Re_B . Cet effet est dû au comportement liquide de viscosité dans PP11, conduisant à une dissipation réduite lors de l'approche à centerline.

Conclusions

Des simulations numériques directes de la décroissance de la turbulence homogène isotrope compressible (CHIT) et du canal plan turbulent supersonique (TCF) de gaz dense ont été réalisées. Des études paramétriques concernant les nombres caractéristiques de Mach et de Reynolds ont été effectuées pour les deux configurations. Les résultats ont été systématiquement comparés à ceux obtenus pour l'air. Dans les simulations CHIT, des différences importantes sont observées pour les cas avec un nombre de Mach turbulent initial élevé. Les différentes évolutions des valeurs moyennes et r.m.s. des grandeurs thermodynamiques et des propriétés de transport modifient fortement l'évolution de la turbulence. Dans le gaz dense, les effets de compressibilité, et en particulier les shocklets de compression, sont plus faibles. Une tendance à la symétrisation est observée pour les p.d.f. de la divergence de la vitesse normalisée, due à l'affaiblissement des chocs de compression et au renforcement des ondes de raréfaction, conduisant éventuellement à la formation de shocklets de raréfaction pour les fluides BZT dans des conditions de fonctionnement convenables. Pour le TCF, le scaling y^+ classique basé sur la vitesse de frottement n'est pas capable de superposer les profils thermodynamiques et les contraintes de Reynolds lorsqu'on considère des valeurs M_B élevées; des scalings corrigés qui prennent en compte les variations des propriétés du fluide doivent être considérés. L'échelle semi-locale, basée sur un mélange des quantités thermodynamiques pariétales et locales, se révèle le choix le plus approprié. Néanmoins, le nombre de Mach turbulent maximal étant environ 0.5, la structure de la turbulence est en effet peu affectée par les effets de compressibilité. De plus, le couplage entre effets dynamiques et thermiques est très faible pour un fluide dense caractérisé par des chaleurs spécifiques élevées, contrairement à l'air qui subit un important chauffage par frottement (typique des écoulements hautement compressibles). Pour ces raisons, pour le PP11, une grande partie des quantités d'intérêt suit une évolution similaire à celle observée dans la turbulence incompressible. Pour les conditions thermodynamiques de référence adoptées, les propriétés de transport ont un comportement de type liquide et les nombres réels de Reynolds se révèlent être beaucoup plus élevés par rapport à l'air. La compressibilité peut devenir importante si l'on considère un nombre plus élevé de Reynolds ou de Mach.

Les simulations numériques montrées ont été réalisées pour le PP11, mais des simulations préliminaires réalisées pour d'autres perfluorocarbones (PP9 et PP10) ont montré un comportement similaire. En plus, les simulations pour un gaz BZT van der Waals présentent un comportement qualitatif similaire. Ceci suggère que, bien que l'amplitude des effets de gaz dense observés dépende de l'extension de la région de gaz dense pour un fluide donné et de la présence (ou non) d'une zone d'inversion, on s'attend à ce que le comportement qualitatif soit semblable pour différents gaz denses.

1 Introduction

Contents

1.1	Dense gas dynamics	22
1.2	State of the art	24
1.3	Compressible turbulence	26
1.4	Outline	30

Dense gas are characterized by complex molecules and moderate to large molecular weights. Due to their molecular complexity, these gases exhibit important deviations from the perfect-gas behaviour over wide ranges of thermodynamic conditions, and namely for pressures and temperatures of the same order of the critical-point value or close to the saturation curve. The nonlinear thermodynamic behaviour of dense gases is governed by the fundamental derivative of gas dynamics, which is defined as

$$\Gamma := \frac{v^3}{2c^2} \left. \frac{\partial^2 p}{\partial v^2} \right|_s = 1 + \frac{\rho}{c} \left. \frac{\partial c}{\partial \rho} \right|_s, \quad (1.1)$$

where ρ is the density, $v := 1/\rho$ the specific volume, p the pressure, s the entropy, and $c = \sqrt{\partial p / \partial \rho|_s}$ the sound speed. The first equality in the preceding definition shows that Γ is related to the curvature of isentropic lines in the $p - v$ plane; according to the second definition, Γ is a measure of the rate of change of the sound speed in isentropic transformations. From (1.1), $\Gamma < 1$ implies $\partial c / \partial \rho|_s < 0$, meaning that the sound speed grows in isentropic expansions and drops in isentropic compressions, unlike the case of perfect gases, where:

$$\Gamma = \frac{\gamma + 1}{2}, \quad (1.2)$$

$\gamma = c_p/c_v$ being the ratio of the isobaric specific heat c_p to the isochoric specific heat c_v . For thermodynamic stability, γ is always greater than unity, hence $\Gamma > 1$ for perfect gases. On the contrary heavy gases, characterized by high c_v/R ratios (R being the gas constant), exhibit extended ranges of density and pressures in which Γ is less than unity, or even negative, whereas the perfect gas behaviour is recovered in the low-density limit. In regions where $\Gamma < 1$, dense gases can exhibit non-classical phenomena, which will be detailed later.

In the last 40 years, the study of dense gases has generated a growing interest in both academic and industry. An increasing number of researchers has been attracted by the peculiar behaviour of these fluids, that have shown to be suitable for a wide range of engineering applications. Dense gases have shown their major benefits in the energy production sector, primarily for turbomachinery applications. Their use as working fluids in Organic Rankine Cycle (ORC) turbines (Brown & Argrow, 2000; Angelino & Colonna, 1998) is exponentially increased over the last 20 years. Whereas a traditional Rankine Cycle operates with water vapour as working medium, ORC turbines use organic fluids such as silicon oils, hydrocarbons or organic refrigerants. Due to their high density, low critical temperature and high specific heats, these fluids are suitable for a number of low temperature applications. Furthermore, the slope of the saturated vapour curve for certain organic fluids reduces – or even deletes – the risk of condensation in the proximity of the turbine outlet, eliminating the need of heating the fluid into the superheated vapor region. As a result, ORC

power systems have become attractive due to their high flexibility and their higher conversion efficiency in the low power range, when compared to other classical systems. ORCs can be used to convert thermal energy in a wide range of different temperatures and for different capacities, make them suitable for a great number of external sources (geothermal reservoirs, solar radiation, biomass combustion, industrial waste heat recovery, ocean thermal gradient and next-generation nuclear reactors). Aside from the studies related to the components optimization and efficiency increase of thermodynamic cycles of ORC systems, huge efforts have been made to improve the fluid dynamic design of rotating equipment for dense gases. The strong non-linearities of the fluid thermophysical properties near the saturation curve, indeed, cause substantial differences with respect to the classical evolutions for steam and air. The lack of experience and experimental data on the physical behaviour of dense gases represent the main limitation in the design of efficient machines, which still nowadays often relies on simplified models or on design strategies developed for air or steam compressors or turbines. ORCs, for instance, use turbo-expanders for medium to high power (from approximately 100kW to several MW) and temperatures ($120 \div 350^\circ\text{C}$), and volumetric (screw and scroll) machinery for low-capacity power systems ($1 \div 100\text{kW}$). An improvement of the fluid dynamic performance of the expander influences directly the power output, hence considerable research has been dedicated to this purpose (Harinck *et al.*, 2013; Casati *et al.*, 2014; Sciacovelli & Cinnella, 2014; Bufi & Cinnella, 2015). Dense gases have been also considered for compressors and turboexpanders for chemical processes and compressors for refrigeration applications (Schnerr & Leidner, 1993; Monaco *et al.*, 1997; Zamfirescu & Dincer, 2009), or even for the development of Stirling engines (Angelino & Invernizzi, 1996, 2000). For an exhaustive review on ORC technology, applications and future outlooks one should refer to Colonna *et al.* (2015) and references therein. Apart from the energy production sector, dense gases have been widely considered for wind tunnel design. The idea of using dense gases in wind tunnel design is rather old (Wagner & Schmidt, 1978), and several conceptual studies have shown suitable applications for hypersonic and transonic wind tunnels (Anderson, 1991; Anders *et al.*, 1999; Korte, 2000). In 2014, the Variable Density Turbulence Tunnel (Bodenschatz *et al.*, 2014) has been built at the Max Planck Institute in Göttingen (Germany). This new-generation facility allow to perform experimental studies on high-Reynolds number turbulent flows, mainly thanks to the use of sulfur hexafluoride (SF_6), a non flammable dense fluid. SF_6 , indeed, has the advantage that at atmospheric pressure it is five times denser than air, and it reaches a density of about 1/10 of water at 15 bars – a pressure much lower than the 100 bars needed to bring air to the same density.

1.1 Dense gas dynamics

The study of compressible flows in this so-called dense-gas regime requires the use of thermodynamic models able to take into account real-gas effects. Van der Waals (1873) was the first to introduce an Equation of State (EoS) with the capability of predicting the real-gas behaviour, by considering the so-called co-volume occupied by the molecules (i.e., the volume which had to be excluded from the space that the fluid has in order to compress or expand itself), and the two-body inter-molecular collisions. Under specific thermodynamic conditions, the Van der Waals (VDW) EoS shows that fluids composed of polyatomic molecules can exhibit phenomena that both quantitatively and qualitatively differ from the ideal-gas behaviour. Among the others, the most interesting ones concern the admissibility of shock waves. In ideal gases, only compression shock waves and expansions fans are allowed to occur, in compliance with the statement of the second law of thermodynamics. In dense gases, under certain circumstances, expansion shock waves and compression fans become admissible (Zemplen, 1905; Rayleigh, 1910), whereas the former are forbidden. An exhaustive review of these nonclassical phenomena is given in Menikoff & Plohr (1989).

Hayes (1958) and Landau & Lifshitz (1959) showed that the admissibility of the type of shock wave is dependent on the magnitude of the variation of the speed of sound with isentropic density perturbations, i.e., on the fundamental derivative of gas dynamics. The adjective “fundamental” derives from the fact that Γ governs the nonlinear behaviour of any substance. For instance, this parameter has been introduced to study expansion and compression waves arising in compressible flows (Thompson, 1971; Menikoff & Plohr, 1989; Cramer, 1991b), isentropic flows through nozzles (Bober & Chow, 1990; Cramer & Fry, 1993), Fanno flows (Cramer *et al.*, 1994) or Rayleigh flows (Cramer, 2006). As shown by Bethe (1942), the entropy change across a weak shock can be written as:

$$\Delta s = -\frac{c^2 \Gamma}{v^3} \frac{(\Delta v)^3}{6T} + \mathcal{O}((\Delta v)^4), \quad (1.3)$$

with T the absolute temperature and $\Delta(\bullet) = (\bullet)_2 - (\bullet)_1$, $(\bullet)_1$ and $(\bullet)_2$ representing the pre- and post-shock values, respectively. When $\Gamma \ll 1$, Δs is much weaker than usual, leading to reduced shock losses. Moreover, if Γ is negative, $\Delta s > 0$ only if $\Delta v > 0$, meaning that expansion shocks are admissible according to the second principle of thermodynamics¹. The behaviour of the critical isotherm in the $p - v$ plane can be considered to explain the negative values for Γ . It is known, indeed, that

1. at the critical point, $\left. \frac{\partial p}{\partial v} \right|_T = \left. \frac{\partial^2 p}{\partial v^2} \right|_T = 0$;
2. the critical isotherm has a positive concavity in the ideal-gas limit;
3. the isothermal compressibility coefficient $\beta_T := -\frac{1}{v} \left. \frac{\partial v}{\partial p} \right|_T$, is positive for any substance in any phase.

The critical isotherm must therefore exhibit a region, located in the interval $v \geq v_c$ (subscript $(\bullet)_c$ referring to critical point values), in which it exhibits a negative concavity. Moreover, for fluids characterized by sufficiently complex molecules, also isentropes can display an interval of negative concavity, due to their large isochoric heat capacity (when $c_v/R \rightarrow \infty$, isentropes and isotherms collapse). This was shown for the first time by Bethe (1942) and Zel’dovich (1946) by means of the VDW model. A rigorous description of what “sufficiently complex” means for fluid modelled with the VDW EoS is given in Colonna & Guardone (2006).

Because of the pioneering work of Bethe, Zel’dovich and Thompson in the field of nonclassical gas dynamics, i.e., the study of compressible wave fields in the dense-gas thermodynamic regime of a molecularly complex substance, substances that exhibit a region of $\Gamma < 0$ in the single-phase dense-gas regime are known as Bethe-Zel’dovich-Thompson (BZT) fluids (Cramer, 1991a), and phenomena related to the presence of an inversion zone (i.e., a thermodynamic region with $\Gamma < 0$, Cramer & Kluwick, 1984) are referred to as BZT effects.

A second important consideration is that in the dense gas regime, the dynamic viscosity μ and the thermal conductivity κ depend both on temperature and pressure through complex relationships. In this respect, the dense gas regime is a transition between two qualitatively different behaviours, namely, the one of liquids, whose viscosity tends to decrease with increasing temperature, and that of dilute gases, for which it increases with T . Similarly, the classical approximation of nearly

¹It should be noted that expansion shocks can also be generated for solids undergoing a polymorphic phase transition (Zel’dovich & Raizer, 1965) because of the discontinuity of isentropes at the phase boundary. These have indeed been observed, for instance, for solid-solid phase transition of iron (Ivanov & Novikov, 1961) or in fused silica (Barker & Hollenbach, 1970). Similarly, for certain thermodynamic states located on the vapour- and liquid saturation lines of a retrograde fluid, Γ can tend to $-\infty$ (Bethe, 1942), so that nonclassical phenomena related to mixed nonlinearity may occur, as evaporation expansions shock waves (Thompson *et al.*, 1986, 1987).

constant Prandtl number ($Pr = \mu c_p / \kappa \approx \text{const}$) is no longer valid. Since the thermal conductivity varies as the viscosity with temperature and pressure, the behaviour of Pr tends to be controlled by variations of c_p . Hence, in regions where c_p becomes large, strong variations of Pr can be observed, contrary to what occurs in perfect gases. Nevertheless, if the immediate vicinity of the thermodynamic critical point is excluded from considerations, the Prandtl number remains of order one. In contrast the Eckert number ($Ec = u_{\text{ref}}^2 / (2c_p T_{\text{ref}})$, with u_{ref} and T_{ref} a reference velocity and temperature respectively), which is a measure of the sensitivity to friction heating, is significantly lower due to the heat capacities much larger than those of gases of less molecular complexity. Hence, the coupling between the dynamic and thermal boundary layers is much weaker than in flows of standard gases like air (Schlichting & Gersten, 2003).

The VDW EoS is the simplest gas model accounting for dense gas effects, including the qualitative features of BZT flows, but it is not very accurate for thermodynamic conditions close to saturation, and largely over-predicts the extent of the inversion zone (Thompson & Lambrakis, 1973). A more accurate representation of the fluid properties can be achieved by using more complex cubic EoS like the Peng-Robinson-Stryjek-Vera (Stryjek & Vera, 1986), virial-expansion-EoS like the Martin-Hou (Martin & Hou, 1955), or multiparameter models based, e.g., on Helmholtz' free energy (Lemmon & Span, 2006). Concerning the transport properties, good predictions are obtained by means of the Chung-Lee-Starling laws (Chung *et al.*, 1984, 1988), which consider several fluid-specific parameters and contains correction terms for the behaviour in the dense-gas region.

Depending on the thermodynamic conditions considered, these compounds may exhibit other effects than dense gas ones. For instance, serious attention has been paid to supercritical fluids (i.e., fluids operating at temperatures and pressures higher than the values of its critical point) for their peculiar physics properties (Eckert, 1996; Gorelli *et al.*, 2006; Simeoni *et al.*, 2010; McMillan & Stanley, 2010; Bolmatov *et al.*, 2013; Brazhkin *et al.*, 2013), for which they have been employed in countless engineering applications, such as in the food industry (Brunner, 2005), cosmetic and pharmaceutical industries (Kaiser *et al.*, 2001), chemical, wood and waste treatment industries (Kiran, 1995), and many others (Brunner, 2010; Stahl *et al.*, 2012; McHugh & Krukoniš, 2013). It should be noted that the term “supercritical” refers to a particular phase of matter rather than a specific family of fluids. Studies involving supercritical behaviour of thermodynamic properties are usually carried out using light fluids that do not exhibit dense gas effects. Nevertheless, dense gases share a common behaviour when temperatures and pressures higher than the critical ones are considered, as it will be shown later.

Lastly, we point out that we will not consider critical-point effects. It is known that in the neighbourhood of the critical point, several thermodynamic parameters undergo rapid variations, representing a challenge for experimentalist and theoreticians. The behaviour of systems near the critical point is described by the Renormalization group theory (Wilson, 1983), that classifies all the fluids in term of universality classes. Fluids sharing the same class exhibit a common asymptotic behaviour through the critical region, which is well described by means of exponential power laws having universal exponents. Nevertheless, to represent the thermodynamic properties in this region, one should use scaled fundamental equations (Sengers & Sengers, 1986), valid only in the critical zone and which would provide discontinuous solutions when coupled with equations for the outer region. Hence, we will not consider the critical region in our analysis.

1.2 State of the art

Considerable progress has been made in the past 30 years about the study of inviscid dense gas flows. These have been extensively studied analytically, with focus on the generation of non-classical compressibility effects like expansion shocks, sonic and double-sonic shocks, and shock splitting (Thompson & Lambrakis, 1973; Cramer & Kluwick, 1984; Cramer & Sen, 1987; Cramer, 1989*a,b*;

Menikoff & Plohr, 1989; Cramer, 1991a; Cramer & Tarkenton, 1992; Cramer & Fry, 1993; Rusak & Wang, 1997; Wang & Rusak, 1999; Rusak & Wang, 2000), both for one-dimensional unsteady and two-dimensional steady configurations. Concerning viscous flows of dense gases, analytical studies were carried out to investigate the dissipative structure of shock waves and the impact of dense gas effects on laminar boundary layers and laminar shock/boundary layer interactions (Cramer & Crickenberger, 1991; Cramer & Park, 1999; Kluwick, 2004; Kluwick & Wrabel, 2004; Kluwick & Meyer, 2010, 2011). These studies pointed out that it is possible to greatly reduce or even suppress the separation induced by shock/boundary layer interactions for some optimal choice of the operating thermodynamic state.

Dense gases have reached mature stages regarding their exploitation in several engineering fields and the theoretical study of their behaviour; nevertheless, reliable experimental measurements are still difficult to obtain. This is even more problematic considering experimental evidence of nonclassical gas-dynamic effects. Most attempts of constructing dense gas shock tubes or nozzle experiments aiming at getting experimental proofs of the existence of non classical shock waves are at the preliminary design stage yet. For single-phase gases close to saturation conditions, the formation of a rarefaction shock wave was observed experimentally by Borisov *et al.* (1983) and Kutateladze *et al.* (1987); however, the interpretation of such results has been challenged by several authors (Cramer & Sen, 1986; Fergason *et al.*, 2001). More recently, dense gas shock tubes and test rigs have been devised by Fergason *et al.* (2001), Colonna *et al.* (2008a) and Spinelli *et al.* (2010). Spinelli *et al.* (2013) illustrates the simulation and the construction of a Test Rig for Organic Vapors (TROVA), build at the Politecnico di Milano to investigate expansions of organic vapor streams, representative of the conditions in an ORC turbine. They show preliminary results using the siloxane MDM and the hydrofluorocarbon R245fa. Mathijssen *et al.* (2015) describes the commissioning of the Flexible Asymmetric Shock Tube (FAST) facility, built at Delft University of Technology, whose objective is to carry out measurements of the velocity of waves propagating in dense gases in the non-ideal regime. They conducted preliminary experiments on rarefaction waves by means of the siloxane D₆ at temperatures up to 300 °C, providing values of the speed of sound within 1.6% of the predictions of the state-of-the-art thermodynamic model. More experiments are planned closer to the saturation line, where Γ attains its minimum. Further experiments on BZT fluids could allow to gain insight into their actual behaviour, and to exploit such nonclassical phenomena in technical applications operating in the dense-gas regime or in transonic or supersonic conditions.

Even though huge efforts are being made from experimentalists to reproduce physics in the Non-Ideal Compressible Fluid Dynamics (NICFD) regime, performing dense gas measurements in turbulent flows is undoubtedly beyond the possibilities given by current technologies. In this context, Computational Fluid Dynamics (CFD) is a powerful tool to investigate fundamental aspects of non-ideal fluid flow behaviour. Computations of inviscid dense gas flows have been presented, among others, by Argrow (1996), Brown & Argrow (1998) and Cinnella & Congedo (2005). Cinnella & Congedo (2007) performed the first numerical simulation of turbulent dense gas flows. Specifically, they investigated compressible turbulent boundary layers and transonic turbulent flows around airfoils by using the Reynolds-Averaged Navier–Stokes (RANS) equations closed by standard turbulence models. The simulations were carried out under a set of working assumptions, namely: (a) the flow conditions being sufficiently far from the thermodynamic critical point, dramatic variations of the fluid specific heats and compressibility coefficients, as well as density fluctuations were neglected; (b) the compressible RANS equations supplemented by an eddy viscosity turbulence model were supposed to provide an adequate description of the mean flow for the configurations under study; (c) the turbulent heat transfer was modelled though a “turbulent Fourier law”, by introducing a turbulent Prandtl number, assumed to be roughly constant and $\mathcal{O}(1)$ throughout the flow, as commonly done in perfect gas flows. More recently, several other authors have carried

out RANS simulations of turbulent dense gas flows, in particular for turbomachinery applications (Harinck *et al.*, 2010a,b, 2013; Pasquale *et al.*, 2013; Sciacovelli & Cinnella, 2014; Wheeler & Ong, 2013, 2014). However, the accuracy of RANS models for these flows has not been properly assessed up to now, due to the lack of reference data either experimental, either numerical.

High-fidelity numerical dataset as those provided by Direct Numerical Simulation (DNS) represent an effective tool for getting insight into the physics of turbulent dense gas flows. In DNS, the computational mesh size and time step must be such that all the relevant spatial and temporal scales of the turbulence – from the smallest dissipative scale up to the integral one – are adequately resolved, without any turbulence model. Therefore, the computational cost of a DNS rapidly grows with the Reynolds number (the number of the degrees of freedom of turbulence growing faster than $\mathcal{O}(Re^{11/4})$, see Garnier *et al.*, 2009), and their use for practical or industrial cases become unfeasible even on the most powerful computers currently available. Nevertheless, they play a crucial role in both understanding compressible turbulence dynamics and calibration of turbulent closure models. In the literature, DNS have been carried out for low-Mach-number turbulent flows of light supercritical fluids like carbon dioxide and nitrogen, with focus on heat-transfer properties, the so-called piston effect and dissipation effects in mixing layers (Zappoli *et al.*, 1990; Okong'o & Bellan, 2002; Bae *et al.*, 2005; Okong'o & Bellan, 2010; Tanahashi *et al.*, 2011). Selle & Schmitt (2010) have studied the influence of supercritical initial conditions on the decay of homogeneous turbulence for nitrogen, assumed to obey a cubic EoS, even though their analysis is limited to the study of the kinetic energy decay evolution at low turbulent Mach number ($M_{t_0} = 0.1$). At these conditions compressibility effects are absent and the authors conclude that real gas thermodynamic effects have a negligible influence on the turbulence dynamics. Battista *et al.* (2014) extended the low-Mach Navier-Stokes equations for reactive perfect gas flows to a generic real-gas equation of state. They analysed the turbulent mixing of slightly supercritical fluids at low Mach number by means of the VDW EoS, and found differences in the ligament structures. Nevertheless, to the author knowledge, the influence of dense-gas effects on highly-compressible turbulence has never been assessed, and represents an open research field.

1.3 Compressible turbulence

The starting point of the research on compressible turbulence is represented by the simulation of the decay of Compressible Homogeneous Isotropic Turbulence (CHIT), a well-documented configuration allowing a detailed study of turbulent features. Much of the numerical work on CHIT is restricted to low or moderate Taylor-based Reynolds numbers Re_λ (generally $Re_\lambda < 500$, see Wang *et al.*, 2012b; Donzis & Jagannathan, 2016), restricting severely the range of scales in the inertial range undergoing a cascade mechanism unimpeded by dissipative processes (Porter *et al.*, 1998). Addressing high Reynolds numbers is more difficult as the turbulent Mach number of the simulation increases. Dissipative processes are, of course, fundamental at the smallest scales, where the turbulent kinetic energy is converted into heat. For high Reynolds number incompressible isotropic decaying turbulence, Lesieur (2008) identified two distinct stages: in the first stage, viscous effects are negligible, worm-like structures due to sheet roll-up develop, and vortex stretching causes a large increase of enstrophy; in the second stage of the decay the energy, transferred to the smallest scales by means of the energy cascade mechanism, starts to be dissipated by viscosity. The transition from the first to the second stage corresponds to a peak in the time history of the total enstrophy, since no smaller structures can be created in the second phase and the existing ones are destroyed due to viscous effects. Lesieur then concludes that the initial stages of the decay are well represented by an inviscid model.

Euler-based turbulent simulations have been largely employed in the literature to investigate the behaviour of high Reynolds number supersonic turbulent flows, such as wakes of objects moving at

supersonic speed or those encountered in the interstellar medium. High-resolution numerical simulations of both forced and decaying inviscid supersonic turbulence have been performed by [Porter *et al.* \(1992b,a, 1994, 1998, 1999, 2002\)](#); [Sytime *et al.* \(2000\)](#), who provided information about the spectra, intermittency, energy transfers and scaling exponents for structure functions of velocity, density and entropy. For decaying turbulence, the impact of dilatational modes on the different temporal phases has been addressed by [Kritsuk *et al.* \(2007\)](#), who performed large-scale 3D simulations of supersonic inviscid turbulence. They measured the velocity scaling exponents and the slope of velocity power spectrum, founding substantial differences with respect to incompressible turbulence and proposed an extension of Kolmogorov's theory taking into account compressibility effects. [Benzi *et al.* \(2008\)](#) performed high-resolution numerical simulations of homogeneous isotropic inviscid weakly-compressible turbulence. They showed that the scaling properties of the velocity field in the inertial range were in excellent agreement with those observed in direct numerical simulations of the Navier-Stokes equations. One important result of the studies cited above is that the dynamics of the inertial range is independent not only of viscosity but also of the detailed dynamics of the dissipative mechanism. As a consequence, the latter does not affect the statistical properties in the inertial range. Similar considerations have led several investigators to model the small-scale dissipative processes using hyperviscosity algorithms (e.g. [Lamorgese *et al.*, 2005](#); [Cook & Cabot, 2005](#)).

For perfect gases at sufficiently high turbulent Mach numbers, turbulence is strongly affected by randomly distributed spatially varying shocks and other compressibility effects. [Erlebacher & Sarkar \(1993\)](#) carried out direct numerical simulations of compressible homogeneous shear flow turbulence and highlighted the differences of behaviour of the solenoidal and irrotational strain rate tensors. [Samtaney *et al.* \(2001\)](#) presented DNS of decaying CHIT for initial turbulent Mach numbers in the range $0.1 \div 0.5$ and $50 < Re_\lambda < 200$. They highlighted that a new phenomenon produced by compressibility is the appearance of random shocklets, which form during the main part of the decay, and developed an algorithm to extract and quantify the shocklet statistics from the DNS fields. The shock thickness statistics were found to scale with the Kolmogorov length. The existence of eddy shocklets was suggested by earlier simulations ([Lee *et al.*, 1991](#); [Passot & Pouquet, 1987](#)), which assessed their role in expediting the energy exchanges between turbulent kinetic energy and internal energy, as well as their influence on kinetic energy decay. The responsible mechanisms were identified as the pressure-dilatation and the dilatation dissipation terms, whose modelling has interested many authors in the 1990s ([Sarkar *et al.*, 1991](#); [Zeman, 1990, 1991](#); [Zeman & Blaisdell, 1991](#)). More recently, the statistical properties of decaying CHIT were analyzed by [Pirozzoli & Grasso \(2004\)](#) for various turbulent Mach numbers. Those authors discussed the influence of compressibility on the time evolution of mean turbulence properties and on the statistical properties and dynamics of turbulent structures. Specifically, they found that the joint probability density function of the second and third invariants of the anisotropic part of the deformation rate tensor has a universal tear-drop shape, as in incompressible turbulence. They furthermore confirmed that, due to the competing mechanisms of vortex stretching and viscous dissipation, the enstrophy obeys a two-stage evolution; however, at high turbulent Mach numbers, compressibility effects associated with the occurrence of shocklets, become important. The effects of local compressibility on the statistical properties and structures of velocity gradients for forced CHIT at high turbulent Mach number were studied by [Wang *et al.* \(2012b\)](#). Those authors showed in particular that strong local compression motions enhance the enstrophy production by vortex stretching, while strong local expansion motions suppress enstrophy through the same mechanism. [Jagannathan & Donzis \(2016\)](#) also studied stochastically forced CHIT at various Reynolds and Mach numbers. They suggested that for turbulent Mach number above a critical value of about 0.3, dilatational effects strongly influence the flow behaviour. Specifically, strong compressions are found to be ten times more likely to occur than strong expansions at high Mach numbers. This

results in significant changes in the dynamics of energy exchanges. Furthermore, the probability distribution of local dilatation develops long negative tails (thus leading to a negative skewness).

The study of homogeneous turbulence provides useful insights on both turbulence dynamics and developments of RANS models. Nevertheless, the majority of compressible engineering flows are characterized by the presence of solid walls. Wall turbulence includes several phenomena that are absent in CHIT, such as the mean shear or variations of mean density. The coupling between turbulence and state variables is a problem of fundamental interest and has been discussed notably for high-speed flows, where compressibility effects come into play, or in the context of strong variations of properties where the temperature can no longer be considered as a passive scalar.

The question of the effects of compressibility on the structure of wall-bounded turbulence is tightly related to variations of the density, temperature, viscosity, and thermal conductivity, leading to variations of the Reynolds and Mach numbers across the flow. [Chu & Kovasznay \(1958\)](#) proposed a general decomposition into vorticity, acoustic and entropic modes and analyzed systematically their interactions up to the second order. The effects of variable transport properties on heat transfer or large-scale coherent structures can then be viewed as interactions between vorticity and entropy modes. For supersonic wall-bounded flows, the main lesson learned from previous studies is that the vortical motions are weakly affected by variations of mean properties and the large-scale organisation of wall turbulence remains close to the one that has been extensively described for incompressible wall-bounded turbulence ([Spina *et al.*, 1994](#)). The nonlinear coupling with acoustic or entropy modes ([Chu & Kovasznay, 1958](#)) does not generate substantial sources of the vorticity mode. This passive character of compressible wall turbulence is well summarized by Morkovin's hypothesis ([Morkovin, 1962](#)), i.e., that compressibility only influences the turbulence through variations in mean density, whereas the density fluctuations have a negligible effect. Compressibility only modulates the turbulence through variations in the mean values of thermodynamic quantities. Since the flow dynamics essentially follows an incompressible pattern, a lot of studies have focused on the incompressible-compressible correspondence. Indeed, since no universal theory for wall-bounded compressible flows is available so far, the incompressible limit remains an interesting reference to quantify the alteration of turbulence structure. In particular, efforts have been made to extend conventional scaling laws for constant property flows to compressible conditions ([Bradshaw, 1977](#)).

The first DNS of compressible turbulent channel flow of a perfect gas have been performed by [Coleman *et al.* \(1995\)](#) and [Huang *et al.* \(1995\)](#). They considered a plane channel flow between two (cooled) isothermal walls for two values of the bulk Mach number, namely 1.5 and 3. They found that the flow is influenced by the strong wall-normal gradients of the mean density and confirmed the validity of the Morkovin's hypothesis ([Morkovin, 1962](#)), i.e., that compressibility only influences the turbulence through variations in mean density, whereas the density fluctuations have a negligible effect. Data were further analysed by [Huang *et al.* \(1995\)](#), who introduced a semi-local scaling where local thermodynamic properties for density and viscosity replace wall values to collapse turbulent statistics. The agreement with incompressible data is improved for mean streamwise velocity profiles compared to the Van Driest transformation ([Van Driest, 1951](#)) often used for turbulent boundary layers with adiabatic walls. [Lechner *et al.* \(2001\)](#) reproduced the DNS of [Coleman *et al.* \(1995\)](#) at $M=1.5$ and $Re=3000$ and studied scatter plots to analyse sweeps and ejections in the wall layer. They reported a slight change in Reynolds stresses anisotropy compared to the incompressible case. [Foysi *et al.* \(2004\)](#) investigated turbulent channel flow with isothermal walls using DNS with Mach numbers up to 3.5 and Reynolds numbers based on friction velocity (Re_τ) up to 1030. They focused on the behaviour of pressure fluctuations and also found that turbulent stresses are mainly affected by mean property variation so that the semi-local scaling is well suited for comparison with incompressible cases. [Morinishi *et al.* \(2004\)](#) complemented the study of [Coleman *et al.* \(1995\)](#) by investigating the influence of the thermal condition at the wall.

They performed DNS of compressible channel flows between both adiabatic and isothermal walls at Mach number 1.5. [Tamano & Morinishi \(2006\)](#) considered the asymmetric case of a channel with a cold and a hot wall, either adiabatic or isothermal. Heat transfers can reduce compressibility effects but remain of little entity, and Morkovin hypothesis is still applicable. [Brun *et al.* \(2008\)](#) performed large-eddy simulations of fully developed channel flows with specific focus on wall modelling. They proposed a variant of the semi-local scaling for both amplitude and distance and arrive at the same conclusions as [Huang *et al.* \(1995\)](#) or [Morinishi *et al.* \(2004\)](#). [Wei & Pollard \(2011\)](#) studied the influence of the Mach number, $M=0.2$, 0.7 and 1.5 , at constant bulk Reynolds number and proposed budgets of transport properties. [Gerolymos & Vallet \(2014\)](#) performed a series of DNS and derived transport equations to study in detail the variance of thermodynamic fluctuations. [Trettel & Larsson \(2016\)](#) gave a theoretical framework to the semi-local scaling of [Huang *et al.* \(1995\)](#) showing that the scaling of the wall distance is important to take into account the variable mean properties. A good match with incompressible distributions is found for a wide range of Reynolds and Mach numbers. Recently, [Modesti & Pirozzoli \(2016\)](#) carried out an extensive DNS database increasing the bulk Reynolds number up to $Re = 34\,000$. They applied the different scalings proposed in previous studies and showed that the transformation of [Trettel & Larsson \(2016\)](#) very well reproduces the behaviour of the mean velocity profile by matching the friction Reynolds number based on semi-local quantities.

In terms of coherent motions in the wall layer, [Coleman *et al.* \(1995\)](#) identified an enhanced coherence of near-wall streaks when compared to the incompressible references. Greater streak elongation was also reported for supersonic boundary layers with cooled walls, whereas a tendency towards shorter streaks is noted for heated walls ([Duan *et al.*, 2010](#); [Lagha *et al.*, 2011](#)). [Morinishi *et al.* \(2004\)](#) noted that streaks do not become more coherent if the semi-local scaling is used instead of wall units to non-dimensionalize the lengths. This was confirmed later by [Patel *et al.* \(2015\)](#) for low-Mach number flows with variable properties.

Given the importance of mean density and viscosity variations, other studies have considered turbulent channel flow with variable properties without compressibility effects due to high speed. Some studies have investigated heat transfers in turbulent channel flow by treating temperature as a passive scalar. For instance, [Teitel & Antonia \(1993\)](#) considered the influence of different thermal wall conditions and noted the importance of the value of the Prandtl number for heat transfers. [Nicoud & Poinso \(1999\)](#) investigated by DNS the effects of variable density and molecular viscosity on a channel flow between two isothermal walls for different temperature ratios or viscosity laws. Low-Mach simulations are used and support Van Driest scaling for mean velocity profiles and semi-local scaling for Reynolds stresses. Several works have investigated the effects of temperature-dependent properties using a nonlinear coupling algorithm ([Bae *et al.*, 2005](#); [Li *et al.*, 2008](#); [Sewall & Tafti, 2008](#); [Zonta *et al.*, 2012](#)). In all of these studies the viscosity, density and thermal conductivity vary with the temperature. [Zonta *et al.* \(2012\)](#) considered temperature gradients in water channel flow and examined the turbulent kinetic energy budgets. [Lee *et al.* \(2013\)](#) showed that the viscosity stratification and associated wall heating can alter the ejections and sweeps events in an incompressible turbulent boundary layer. [Bae *et al.* \(2005\)](#) studied the turbulent heat transfer mechanisms of supercritical carbon dioxide (CO_2) performing DNS in heated vertical tubes. They focused on the well-known heat transfer deterioration phenomenon in supercritical flows. [Li *et al.* \(2008\)](#) investigated the same fluid in a long plane channel by imposing wall temperature variations in the streamwise direction, i.e. considering heating and cooling regions at the beginning and at the end of the channel, respectively. They found that the effects of density fluctuations, particularly near the pseudo-critical temperature, on turbulent kinetic energy cannot be ignored, and that the different temperature values cause a modulation of the near-wall turbulent structures. [Patel *et al.* \(2015\)](#) conducted numerical experiments by imposing different distributions for the fluid properties to investigate separately the effects of mean density or viscosity gradients in low-Mach-number

turbulent channel flow. They showed that various laws bearing similarities either with liquid-like or gas-like behaviour can be taken into account for turbulent statistics by using the semi-local scaling introduced in the compressible regime. In particular, a good similarity was observed for an equivalent friction Reynolds number constructed with semi-local quantities.

Understanding how the peculiar variations of the thermodynamic and transport properties typical of dense gases influence the behaviour of wall-bounded turbulent flows is of primal importance for providing a correct description of friction drag and heat fluxes in many applications, and to develop suitable models for predicting them. Measurements of dense gas flows are hardly available due to the difficulty of conducting measurements of this kind of flows. Most of the facilities presently under development are thought to provide average pressure and temperature profiles and, in some cases, flow visualizations, but are not expected to provide a detailed description of the turbulence structure, at least in the short term.

1.4 Outline

In this work, we investigate the influence of dense gas effects on the structure of compressible turbulence. The final purpose is the creation of reliable and complete DNS databases needed to quantify the deficiencies of existing turbulence models and allow the development and calibration of improved models.

Simulations are performed for PP11, a heavy fluorocarbon representative of the family of dense gases, modelled by means of the simple Van Der Waals and the more complex Martin-Hou EoS. The influence of the EoS is assessed and the results are systematically compared with canonical perfect-gas cases. We consider also fluids of other dense-gas families usually employed for industrial and experimental applications, namely, two siloxanes (D_5 and D_6) and two refrigerants (R134a and R245fa).

The thesis is organized as follows. Chapter 2 describes the governing equations, the thermodynamic models, the fluids under investigation and the numerical strategy adopted for the simulations. Some preliminary validations for shock-tube dense gas test-cases are shown.

As a natural starting point, we select a configuration that has been well documented for perfect gases, namely, the decay of highly-compressible HIT in a periodic box, which may exhibit eddy shocklets. For this kind of flow, the peculiar behaviour of the speed of sound when Γ is close or less than zero is expected to modify the turbulence structure significantly. Specifically, for turbulent flows of BZT fluids, non-classical eddy shocklets may appear, leading to significant changes in the probability distribution functions of several flow properties. In decaying CHIT, the turbulent Mach number decreases with time. As a consequence, dense gas effects are expected to have an impact most of all on the initial stages of the decay, which are dominated by large to medium scales of turbulence. Since we are mainly interested in high-Reynolds number flows typical of dense-gas industrial applications, in chapter 3 we first show inviscid CHIT simulations, focusing on the behaviour of the scales in the inertial range and on the evolution of integral quantities. PP11 is modelled by means of the Van der Waals equation, and results are compared to perfect gas configurations. A sensitivity analysis is carried out in order to quantify the influence of the shape of the initial turbulent kinetic energy spectrum, the value of the artificial viscosity coefficients and the value of the specific heat ratio. Afterwards, the viscous case is considered in chapter 4, in order to investigate the influence of the peculiar behaviour of the thermodynamic quantities and the transport properties on the small-scale dynamics. The local flow topology, the fractional contribution of the different flow structures to dissipation and the mechanisms of enstrophy generation are analyzed in detail. Chapter 5 focuses on turbulent configurations in presence of mean shear, namely, a supersonic turbulent plane channel flow. The validity of the Morkovin's hypothesis and of the classical literature scalings is assessed, and the differences in the first- and second-order

profiles of thermodynamic and turbulent quantities are highlighted. Moreover, an investigation on the modifications in the turbulent kinetic energy budgets and in the near-wall structures is carried out.

Parametric studies on the characteristic Reynolds and Mach numbers are performed for both the configurations and the fluids, and their effect on the dynamics and structures of turbulence is discussed. Lastly, conclusions and future works are drawn in chapter 6.

2 Governing equations and numerical methods

Contents

2.1	Governing Equations	33
2.1.1	Working Fluid	34
2.1.2	Thermodynamic models	35
2.1.3	Transport Properties	40
2.1.4	Comparisons of the EoS	43
2.2	Numerical methods	48
2.2.1	Approximation of centered fluxes	49
2.2.2	Numerical stabilization terms	51
2.2.3	Shock-capturing methods	53
2.2.4	Time integration methods	56
2.3	Description of the CFD codes	57
2.3.1	Scalability tests	59
2.4	Preliminary validations	62

The mathematical framework and the informatics tools used in this thesis are hereafter reported. Section 2.1 describes the governing equations, the thermodynamic models and the working fluids under investigation. The numerical strategy is proposed in section 2.2, with a focus on spatial discretization and shock-capturing methods. Afterwards, the CFD codes used for the simulations and preliminary validations on a shock-tube test case are presented in sections 2.3 and 2.4, respectively.

2.1 Governing Equations

We consider flows of gases in the single-phase regime, governed by the compressible Navier-Stokes equations that are written in differential form

$$\begin{aligned}
 \frac{\partial \rho}{\partial t} + \frac{\partial(\rho u_j)}{\partial x_j} &= 0 \\
 \frac{\partial \rho u_i}{\partial t} + \frac{\partial(\rho u_i u_j)}{\partial x_j} &= -\frac{\partial p}{\partial x_i} + \frac{\partial \tau_{ij}}{\partial x_j} \\
 \frac{\partial \rho \mathcal{E}}{\partial t} + \frac{\partial((\rho \mathcal{E} + p)u_j)}{\partial x_j} &= \frac{\partial(\tau_{ij}u_i - q_j)}{\partial x_j}
 \end{aligned} \tag{2.1}$$

with u_i the components of the velocity vector ($i \in \{1, 2, 3\}$), ρ the density and p the pressure. The specific total energy \mathcal{E} is given by

$$\mathcal{E} := e + \frac{1}{2}u_i u_i, \tag{2.2}$$

where e is the specific internal energy. The viscous stress tensor τ_{ij} is completely dependent on motion and derives from the momentum transport mechanisms at the molecular level. To express

its formulation, it is convenient to decompose the velocity gradient tensor $A_{ij} := \partial u_i / \partial x_j$ into its symmetric and antisymmetric parts, denoted as S_{ij} (strain-rate tensor) and W_{ij} (rotation-rate tensor), respectively:

$$A_{ij} = S_{ij} + W_{ij}, \quad (2.3)$$

$$S_{ij} = \frac{1}{2}(A_{ij} + A_{ji}) = \frac{1}{2}\left(\frac{\partial u_i}{\partial x_j} + \frac{\partial u_j}{\partial x_i}\right), \quad W_{ij} = \frac{1}{2}(A_{ij} - A_{ji}) = \frac{1}{2}\left(\frac{\partial u_i}{\partial x_j} - \frac{\partial u_j}{\partial x_i}\right). \quad (2.4)$$

We will consider only Newtonian fluids, for which τ_{ij} depends linearly on S_{ij} . Moreover, S_{ij} can be decomposed into a traceless symmetric part (the shear-rate tensor) and a pure diagonal component (expansion-rate tensor):

$$S_{ij} = \frac{1}{3}S_{kk}\delta_{ij} + (S_{ij} - \frac{1}{3}S_{kk}\delta_{ij}), \quad (2.5)$$

where δ_{ij} denotes the Kronecker delta. The most general form of τ_{ij} is a linear combination of these two tensors, namely

$$\tau_{ij} = \zeta S_{kk}\delta_{ij} + \mu \left(2S_{ij} - \frac{2}{3}S_{kk}\delta_{ij} \right) = 2\mu S_{ij} + \vartheta S_{kk}\delta_{ij}, \quad (2.6)$$

where μ , ϑ and $\zeta := \vartheta + 2/3\mu$ are respectively the first (shear, or dynamic), the second and the bulk viscosity coefficients. According to the Stokes' hypothesis which assumes that the bulk viscosity can be neglected with respect to the shear viscosity, one obtains $\zeta = \vartheta + 2/3\mu \approx 0$ and the viscous stress tensor becomes

$$\tau_{ij} = 2\mu S_{ij} - \frac{2}{3}\mu S_{kk}\delta_{ij}. \quad (2.7)$$

Finally, q_j represents the heat flux, modelled by means of Fourier's law:

$$q_j = -\kappa \frac{\partial T}{\partial x_j} \quad (2.8)$$

where κ is the thermal conductivity of the fluid. It should be noted that by setting $\mu = 0$ and $\kappa = 0$ in system (2.1), the inviscid compressible Euler equations are recovered.

In order to close the system, a thermodynamic model relating the pressure with the conservative variables is needed, i.e. an equation of state of the type

$$p = p(\rho, e) \quad (2.9)$$

as well as constitutive laws for the transport properties μ and κ .

2.1.1 Working Fluid

In the following simulations, we consider the perfluoro-perhydrophenanthrene, (chemical formula $C_{14}F_{24}$), called hereafter PP11 (commercial name); its thermodynamic properties are provided in table 2.1. This fluid has been often used in the literature since it exhibits a wide inversion zone and, as a consequence, significant dense-gas effects. For such a complex gas, the specific heat ratio γ varies with the temperature. However, since the flow conditions investigated in this work are characterized by small temperature variations, when we use the polytropic (i.e. calorically perfect) assumption – for perfect gas and Van der Waals models – we assume hereafter an equivalent γ value of 1.0125, which is representative of heavy fluorocarbons (Brown & Argrow, 1998). Other fluids considered in this work are air, always modelled as a diatomic perfect gas ($R = 287.04 \text{ J kg}^{-1} \text{ K}^{-1}$ and $\gamma = 1.4$), the siloxanes D5 (decamethylcyclopentasiloxane) and D6 (dodecamethylcyclohexasiloxane), and the refrigerants R134a (1,1,1,2-tetrafluoroethane) and R245fa

Table 2.1. Thermodynamic properties of the fluids under investigation: molecular weight (\mathcal{M}), critical temperature (T_c), critical density (ρ_c), critical pressure (p_c), critical compressibility factor (Z_c), acentric factor (ω_{ac}), dipole moment of the gas phase (ξ), boiling temperature (T_{eb}) and ratio of ideal-gas specific heat at constant volume over the gas constant ($c_v(T_c)/R$) at the critical point.

	\mathcal{M}	T_c	ρ_c	p_c	Z_c	ω_{ac}	ξ	T_{eb}	$c_v(T_c)/R$
	g mol ⁻¹	K	kg m ⁻³	MPa	-	-	D	K	-
PP11	624.11	650.2	627.14	1.46	0.2688	0.4963	0.0	488.15	97.3
D5	370.77	619.23	292.57	1.161	0.274	0.658	1.349	484.05	83.0
D6	444.92	645.78	279.09	0.961	0.285	0.736	1.559	518.11	105.9
R245fa	134.05	427.16	516.09	3.651	0.267	0.3776	1.549	288.29	16.45
R134a	102.03	374.18	508.0	4.056	0.262	0.327	2.058	247.06	16.3

(1,1,2,2,3-pentafluoropropane). The thermodynamic properties of these fluids are also reported in table 2.1.

2.1.2 Thermodynamic models

For gases that are not perfect, it is generally not possible to write an explicit relation for the pressure as a function of ρ and e , as in equation (2.9). For this reason, system (2.1) must be supplemented by a thermal and a caloric EoS, respectively:

$$p = p(\rho, T), \quad (2.10)$$

$$e = e(\rho, T). \quad (2.11)$$

The caloric EoS depends on the thermal eos via the following compatibility relation:

$$e = e_{\text{ref}} + \int_{T_{\text{ref}}}^T c_v^{id}(T') dT' - \int_{\rho_{\text{ref}}}^{\rho} \left[T \left. \frac{\partial p}{\partial T} \right|_{\rho} - p \right] \frac{d\rho'}{\rho'^2}, \quad (2.12)$$

where the subscript $(\cdot)_{\text{ref}}$ indicates a reference state, the superscript $(\cdot)'$ denotes auxiliary integration variables and $c_v^{id}(T)$ is the isochoric specific heat in the ideal-gas limit. The derivation of this relation is reported in appendix A. Given the thermal EoS and the law for $c_v^{id}(T)$ or $c_p^{id}(T)$, the fundamental derivative of gas dynamics can be obtained analytically as follows:

$$\Gamma = \frac{v^3}{2c^2} \left\{ \left. \frac{\partial^2 p}{\partial v^2} \right|_T - 3 \frac{T}{c_v} \left. \frac{\partial p}{\partial T} \right|_v \left. \frac{\partial^2 p}{\partial v \partial T} \right|_{v,T} + \left[\frac{T}{c_v} \left. \frac{\partial p}{\partial T} \right|_v \right]^2 \left[3 \left. \frac{\partial^2 p}{\partial T^2} \right|_v + \frac{1}{T} \left. \frac{\partial p}{\partial T} \right|_v \left[1 - \frac{T}{c_v} \left. \frac{\partial c_v}{\partial T} \right|_v \right] \right] \right\}. \quad (2.13)$$

The complete derivation of equation (2.13) from the definition of Γ can be found in Colonna & Silva (2003).

Perfect gas model

In the Perfect Gas (PFG) model the fluid is considered simultaneously thermally and calorically perfect. Equations (2.10)–(2.11) then become:

$$p = \rho RT, \quad (2.14)$$

$$e = c_v T, \quad (2.15)$$

with $c_v = R/(\gamma - 1) = \text{constant}$, and $R = \mathcal{R}/\mathcal{M}$ (being $\mathcal{R} = 8.314472 \text{ J K}^{-1} \text{ mol}^{-1}$ the universal gas constant and \mathcal{M} the molecular weight). In this case it exists a direct relation between the pressure and the conservative variables, i.e. $p = (\gamma - 1)\rho e$. Furthermore, the fundamental derivative of gas dynamics takes the simple form shown in equation (1.2), namely:

$$\Gamma = \frac{\gamma + 1}{2}. \quad (2.16)$$

Since, for thermodynamic stability reasons, γ is always greater than 1, then Γ is also greater than 1 everywhere, and the PFG EoS is not able to predict dense gas effects.

Van der Waals model

The Van der Waals thermal equation of state (Van der Waals, 1873) models the gas molecules as rigid spheres of given radius and subject to inter-particle attractive forces. Such EoS captures the qualitative aspects of dense gas dynamics without the complexities and computational overhead associated to more complex thermodynamic models. By assuming a polytropic (calorically perfect) gas, equations (2.10)–(2.11) become:

$$p = \frac{RT}{v - b} - \frac{a}{v^2}, \quad (2.17)$$

$$e = c_v T - \frac{a}{v}, \quad (2.18)$$

with:

$$a = \frac{9p_c v_c^2}{8Z_c}, \quad b = \frac{v_c}{3}, \quad (2.19)$$

where $Z_c = p_c v_c / RT_c$ is the critical compressibility factor and $(\bullet)_c$ denotes critical-point values. For VDW gases, the value of Z_c is univocally determined by thermodynamic constraints at the liquid/vapour critical point, and is found to be equal to $3/8$ (for PFG one obviously has $Z_c = 1$). When the VDW EoS is cast in dimensionless form by introducing the reduced thermodynamic values $p_r = p/p_c$, $T_r = T/T_c$ and $\rho_r = \rho/\rho_c$, it is found to be invariant for all fluids. Physically, the invariance derives from the principle of corresponding states (De Boer, 1948), which states that if two fluids have the same reduced pressure, volume and temperature, they will respond to thermodynamic perturbations roughly in the same way, even if their measurable physical characteristics may differ significantly. Consequently, the only free parameters for the VDW EoS are the gas constant R and the equivalent specific heat ratio γ . As for PFG, it is possible to derive an explicit relationship for the pressure in terms of density ρ and internal energy e , i.e.,

$$p = \frac{(\gamma - 1)\rho e + a\rho^2}{1 - b\rho} - a\rho^2. \quad (2.20)$$

For a polytropic VDW gas, the fundamental derivative of gas dynamics writes:

$$\Gamma = \frac{1}{2} \left(\frac{\gamma(\gamma+1)RT}{(1-b\rho)^3} - 6a\rho \right) \bigg/ \left(\frac{\gamma RT}{(1-b\rho)^2} - 2a\rho \right) \quad (2.21)$$

A region of negative values of the fundamental derivative appears if the specific heat ratio is in the range $1 < \gamma \leq 1.06$ (Thompson & Lambrakis, 1973). As a consequence, VDW represents the simplest thermodynamic model that is able to account for BZT effects.

Martin-Hou model

The Martin-Hou (MAH) thermal equation of state (Martin & Hou, 1955) ensures high accuracy with a minimum amount of experimental information, thus providing a realistic description of the gas behaviour and of the inversion zone size. In its derivation it is assumed that for any compound, four properties are necessary to provide its complete characterization, namely, the critical temperature, pressure and volume, and one point on the vapor-pressure curve. The point of the vapor-pressure curve gives the slope m of the critical isometric on the pressure-temperature diagram. The Martin-Hou thermal equation reads:

$$p = \frac{RT}{v-b} + \sum_{i=2}^5 \frac{A_i + B_i T + C_i e^{-kT/T_c}}{(v-b)^i} \quad (2.22)$$

where $b = v_c \left(1 - \frac{\beta}{Z_c}\right)$ is a constant, with $\beta = -31,883Z_c^2 + 20.533Z_c$ and $k = 5.475$. The conditions that the equation of state has to verify are

- 1) $pv = RT$ as $p \rightarrow 0$,
- 2)-5) $\left. \frac{\partial p}{\partial v} \right|_T = \left. \frac{\partial^2 p}{\partial v^2} \right|_T = \left. \frac{\partial^3 p}{\partial v^3} \right|_T = \left. \frac{\partial^4 p}{\partial v^4} \right|_T = 0$ at the critical point,
- 6) $\left. \frac{\partial Z}{\partial p_r} \right|_{T_r} = -(1 - Z_c)$ at $T_r = T_p \approx 0.8$ as $p_r \rightarrow 0$,
- 7) $\left. \frac{\partial Z}{\partial p_r} \right|_{T_r} = 0$ at $T_r = T_{\text{boy}}$ as $p_r \rightarrow 0$,
- 8) $\left. \frac{\partial^2 p}{\partial T^2} \right|_v = 0$ at $v = v_c$,
- 9) $\left. \frac{\partial p}{\partial T} \right|_v = m = -a_c p_c / T_c$ at $v = v_c$.

In the preceding relations, T_{boy} is the absolute temperature at Boyle point, given by

$$T_{\text{boy}} = -0.6492324 \times 10^{-3} T_c^2 + 2.505308 T_c + 9.654291; \quad (2.23)$$

T_p is the absolute temperature for which the slope at $p_r = 0$ of the isotherm on the compressibility chart equals the slope of the line joining the critical point and the point ($Z = 1, p_r = 0$), given by the relation

$$\frac{T_c}{T_p} = -0.6751 Z_c + 0.9869, \quad (2.24)$$

Table 2.2. Coefficients η_i for the computation of the ideal specific heat in the ideal limit, equation (2.29).

η_i	D5	D6	R134a	R245fa
1	-4.197260×10^6	-4.197257	2.791385	3.494300
2	2.238870×10^{-1}	2.238867×10^{-1}	2.903363×10^{-2}	3.957406×10^{-2}
3	-1.687900×10^{-4}	-1.687900×10^{-4}	-1.523713×10^{-5}	-1.609372×10^{-5}
4	6.013600×10^{-8}	6.013610×10^{-8}	5.668392×10^{-9}	-0.205304×10^{-9}

and a_c is the Riedel parameter,

$$a_c = \frac{(0.315\psi_b - \log \frac{1.01325}{p_c})}{0.0838\psi_b - \log T_{eb}}; \quad (2.25)$$

with T_{eb} the boiling temperature and $\psi_b = f(T_{eb}) = -35 + 36T_{eb}^{-1} + 42 \log T_{eb} - T_{eb}^6$. These constraints set the values of the coefficients A_i , B_i , and C_i , whose values (not reported here for brevity) are shown in [Martin & Hou \(1955\)](#). Finally, to compute the caloric EoS, a law for the variations of the low-density specific heat must be provided. In our case we consider a power law of the form:

$$c_v^{id}(T) = c_v^{id}(T_c) \left(\frac{T}{T_c} \right)^{n_c}, \quad (2.26)$$

where n_c is a parameter that depends on the gas used (for PP11, $n_c = 0.5776$, see [Cramer, 1991a](#)).

Span-Wagner model

The Span-Wagner model is formulated in the terms of the free Helmholtz energy $a(T, v) = e(T) - Ts(T, v)$. For the sake of clarity, we introduce only for this section the classical notations $\tau = T_c/T$ and $\delta = v_c/v$, denoting the inverse of the reduced temperature and the reduced specific volume, respectively. As initially proposed by [Setzmann & Wagner \(1989\)](#), the free Helmholtz energy, expressed in reduced form, is split into an ideal and a real part:

$$\frac{a(T, \rho)}{RT} = \frac{a^{id}(T, \rho) + a^{real}(T, \rho)}{RT} = \alpha(\tau, \delta) = \alpha^{id}(\tau, \delta) + \alpha^{real}(\tau, \delta), \quad (2.27)$$

where α^{id} describes the behaviour of the hypothetical ideal gas at given values of temperature and density and α^{real} describes the residual behaviour of the real fluid. All thermodynamic properties can be calculated by combinations of derivatives of α^{id} and α^{real} with respect to τ and δ . The ideal component is computed as

$$\alpha^{id}(\tau, \delta) = \frac{h_{\text{ref}}^{id}\tau}{RT_c} - \frac{s_{\text{ref}}^{id}}{R} - 1 + \ln \frac{\delta\tau_{\text{ref}}}{\delta_{\text{ref}}\tau} - \frac{\tau}{R} \int_{\tau_{\text{ref}}}^{\tau} \frac{c_p^{id}}{\tau^2} d\tau + \frac{1}{R} \int_{\tau_{\text{ref}}}^{\tau} \frac{c_p^{id}}{\tau} d\tau \quad (2.28)$$

where the subscript $(\cdot)_{\text{ref}}$ denotes arbitrary reference values. The arbitrary values for the enthalpy h_{ref}^{id} and the entropy s_{ref}^{id} are chosen according to recommendations of the International Union for Pure and Applied Chemistry (IUPAC). The computation of α^{id} requires an auxiliary equation for the ideal-gas isobaric heat capacity $c_p^{id}(T)$; in this work, $c_p^{id}(T)$ is approximated as a polynomial

Table 2.3. Coefficients n_i for the computation of the residual part of the Span–Wagner EoS, equations (2.31) and (2.32).

n_i	D5	D6	R134a	R245fa
1	1.40844725	1.69156186	1.0663189	1.2904
2	-2.29248044	-3.37962568	-2.4495970	-3.2154
3	0.42851607	0.38609039	$0.44645718 \times 10^{-1}$	0.50693
4	-0.73506382	$0.64598995 \times 10^{-1}$	$0.75656884 \times 10^{-1}$	0.93148×10^{-1}
5	0.16103808	0.10589012	$0.20652089 \times 10^{-3}$	0.27638×10^{-3}
6	$0.29643278 \times 10^{-3}$	$0.45456825 \times 10^{-4}$	0.42006912	0.71458
7	0.82412481	0.74169279	0.76739111	0.87252
8	0.15214274	$-0.88102648 \times 10^{-1}$	$0.17897427 \times 10^{-2}$	-0.15077×10^{-1}
9	-0.68495890	-0.17373336	-0.36219746	-0.40645
10	$-0.55703624 \times 10^{-1}$	-0.10951368	$-0.67809370 \times 10^{-1}$	-0.11701
11	$0.13055391 \times 10^{-1}$	$-0.62695695 \times 10^{-1}$	-0.10616419	-0.13062
12	$-0.31853761 \times 10^{-1}$	$0.37459986 \times 10^{-1}$	$-0.18185791 \times 10^{-1}$	-0.22952×10^{-1}

function of the temperature:

$$c_p^{id}(T) = \eta_0 + \eta_1 T + \eta_2 T^2 + \eta_3 T^3 \quad (2.29)$$

where the coefficients η_i depend on the substance under consideration and are given in table 2.2. The residual part is assumed to be a linear combination of dimensionless density and temperature terms, in the form

$$\alpha^{real}(\tau, \delta) = \sum_{m=1}^{M_1} a_m \delta^{i_m} \tau^{j_m} + \sum_{m=M_1+1}^{M_2} a_m \delta^{i_m} \tau^{j_m} \exp(-\delta^{k_m}) \quad (2.30)$$

where a_m is the coefficient for each term, i_m , j_m and k_m are exponents on τ , δ and exponential δ terms, respectively, and M_1 and M_2 are the numbers of different type of terms. Decision and regression algorithms are used to determine the number of polynomial and exponential terms and the values of the parameters. This functional form has been widely used to produce several state-of-the-art EoS, such as those for fluids CO₂ (Span & Wagner, 1996) or R134a (Tillner-Roth & Dieter Baehr, 1994).

For many industrial fluids for which the quantity and quality of available thermodynamic data are not sufficient to develop a reference EoS, it is possible to adopt the short technical multiparameter EoS proposed by Span & Wagner (2003a) and Span & Wagner (2003b). This kind of EoS, also expressed in the Helmholtz explicit functional form, conserves the same formulation for the ideal part, whereas the residual part is written in the more compact form:

$$\begin{aligned} \alpha^{real}(\tau, \delta) = & n_1 \delta \tau^{0.25} & + n_2 \delta \tau^{1.125} & + n_3 \delta \tau^{1.5} & + \\ & n_4 \delta^2 \tau^{1.375} & + n_5 \delta^3 \tau^{0.25} & + n_6 \delta^7 \tau^{0.875} & + \\ & n_7 \delta^2 \tau^{0.625} \exp^{-\delta} & + n_8 \delta^5 \tau^{1.75} \exp^{-\delta} & + n_9 \delta \tau^{3.625} \exp^{-\delta^2} & + \\ & n_{10} \delta^4 \tau^{3.625} \exp^{-\delta^2} & + n_{11} \delta^3 \tau^{14.5} \exp^{-\delta^3} & + n_{12} \delta^4 \tau^{12.0} \exp^{-\delta^3}, \end{aligned} \quad (2.31)$$

obtaining the Span-Wagner for Non-polar fluids (SWN) EoS, and

$$\begin{aligned} \alpha^{real}(\tau, \delta) = & n_1 \delta \tau^{0.25} + n_2 \delta \tau^{1.25} + n_3 \delta \tau^{1.5} + \\ & n_4 \delta^3 \tau^{0.25} + n_5 \delta^7 \tau^{0.875} + n_6 \delta \tau^{2.375} + \\ & n_7 \delta^2 \tau^{2.0} \exp^{-\delta} + n_8 \delta^5 \tau^{2.125} \exp^{-\delta} + n_9 \delta \tau^{3.5} \exp^{-\delta^2} + \\ & n_{10} \delta \tau^{6.5} \exp^{-\delta^2} + n_{11} \delta^4 \tau^{4.75} \exp^{-\delta^2} + n_{12} \delta^2 \tau^{12.5} \exp^{-\delta^3}, \end{aligned} \quad (2.32)$$

obtaining the Span-Wagner for Polar fluids (SWP) EoS. Finally, the thermal and caloric equations read

$$\frac{p}{\rho RT} = 1 + \delta \left. \frac{\partial \alpha^{real}}{\partial \delta} \right|_{\tau}, \quad (2.33)$$

$$\frac{e}{RT} = \tau \left(\left. \frac{\partial \alpha^{id}}{\partial \tau} \right|_{\delta} + \left. \frac{\partial \alpha^{real}}{\partial \tau} \right|_{\delta} \right). \quad (2.34)$$

The coefficients n_i of the residual part of the EoS are fluid-specific and are reported in table 2.3 for the fluids of interest in this work. Namely, the coefficients for the siloxanes, modelled by means of the SWN EoS, are taken from Colonna *et al.* (2006) for D5 and Colonna *et al.* (2008b) for D6. For the refrigerants (modelled by means of the SWP EOS), the values are taken from (Span & Wagner, 2003b) and (Lemmon & Span, 2006) for R134a and R245fa, respectively.

2.1.3 Transport Properties

Calorically perfect gases

Since in the PFG and VDW models no fluid-specific parameter is considered, aside from the molecular weight and the equivalent specific heat ratio in the low density limit, they cannot be combined with accurate dense-gas laws for the transport properties. Instead, a simple temperature-dependent power law

$$\frac{\mu}{\mu_{ref}} = \left(\frac{T}{T_{ref}} \right)^{0.7} \quad (2.35)$$

is used to account for variations of viscosity with the temperature. This power-law has been preferred to the well-known Sutherland law (Sutherland, 1893) since the parameter needed to compute the latter (the so-called Sutherland temperature) is available only for a restricted group of fluids. Figure 2.1 shows the comparison of the viscosity laws and the relative error of the power-law for air. The influence of the viscosity law has been found to be negligible for the configurations under investigation, the relative error being always lower than 2% for the range of temperature considered in this work. Additionally, a constant Prandtl assumption $Pr = \mu c_p / \kappa = 0.7$ is used to model the thermal conductivity.

Dense gases

For dense gases, transport properties are generally considered to depend only on the temperature. Nevertheless, when $1 < T/T_c < 1.5$ and when $p > p_c$, pressure has a strong effect on viscosity and thermal conductivity. This effect is usually taken into account by applying correction factors in the formula used to estimate the diluted-gas properties (i.e., the values of viscosity and thermal conductivity in the ideal-gas limit). In the following, we describe the formulation derived by Chung *et al.* (1984, 1988).

Dynamic viscosity. The Chapman-Enskog theory describes the integral relations for the transport properties when the interactions between colliding molecules are described by a potential

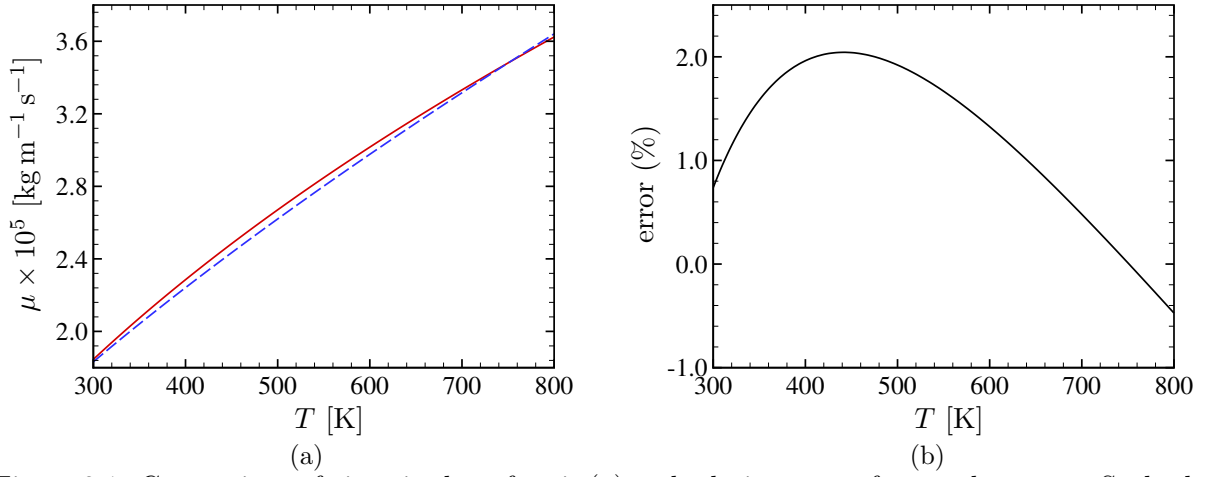


Figure 2.1. Comparison of viscosity laws for air (a) and relative error of power-law w.r.t. Sutherland law (b). For panel a, —: Sutherland law, - - -: power law.

energy function. In general terms, the first-order solution for the dilute gas viscosity can be written as:

$$\mu_0 = \frac{26.69(\mathcal{M}T)^{1/2}}{\sigma^2\Omega_v(T)} \quad (2.36)$$

where \mathcal{M} is the molecular weight, T the temperature, $\Omega_v(T)$ the temperature dependence of the collision integral and $\sigma(v_c)$ the collision diameter. In the derivation of equation (2.36), Ω_v is obtained as a function of a dimensionless temperature T^* , defined as (Poling *et al.*, 2001):

$$T^* = \frac{k_B T}{\epsilon} \quad (2.37)$$

where k_B is Boltzmann's constant ($k_B = 1.38064852 \times 10^{-23} \text{ J K}^{-1}$) and ϵ is the potential energy parameter. Neufeld *et al.* (1972) proposed the following empirical equation:

$$\Omega_v = \frac{A}{T^{*B}} + \frac{C}{\exp(DT^*)} + \frac{E}{\exp(FT^*)} + GT^{*B} \sin(ST^{*W} - H) \quad (2.38)$$

with $A = 1.16145$, $B = 0.14874$, $C = 0.52487$, $D = 0.77320$, $E = 2.16178$, $F = 2.43787$, $G = -6.436 \times 10^{-4}$, $H = 7.27371$, $S = 18.0323$ and $W = -0.76830$.

The method of Chung *et al.* (1984, 1988) starts from equation (2.36) with $\epsilon/k_B = T_c/1.2593$ and $\sigma = 0.809v_c^{1/3}$ (being T_c and v_c the critical temperature and volume, respectively). Furthermore, they multiply the right-hand side of equation (2.36) by a factor F_c in order to account for molecular shapes and polarities of dilute gases. The final result for the dilute-gas viscosity μ_0 reads:

$$\mu_0 = 40.785 \frac{F_c(\mathcal{M}T)^{1/2}}{v_c^{2/3}\Omega_v}, \quad (2.39)$$

with

$$F_c = 1 - 0.2756\omega_{ac} + 0.059035\xi_r^4 + \varpi. \quad (2.40)$$

In equation (2.40), ω_{ac} is the acentric factor, ξ_r is the reduced dipole moment, which reads

$$\xi_r = 131.3 \frac{\xi}{(v_c T_c)^{1/2}}, \quad (2.41)$$

Table 2.4. Parameters for evaluating the functions A_i of equation (2.47) for the computation of the dense-gas viscosity.

i	a_0	a_1	a_2	a_3
1	6.32402	5.04119×10^1	-5.16801×10^1	1.18902×10^3
2	0.12102×10^{-3}	-0.11536×10^{-2}	-0.62571×10^{-2}	0.37283×10^{-1}
3	5.28346	2.54209×10^2	-1.68481×10^1	3.89827×10^3
4	6.62263	3.80957×10^1	-8.46414	3.14178×10^1
5	1.97454×10^1	7.63034	-1.43544×10^1	3.15267×10^1
6	-1.89992	-1.25367×10^1	4.98529	-1.81507×10^1
7	2.42745×10^1	3.44945	-1.12913×10^1	6.93466×10^1
8	0.79716	1.11764	0.12348×10^{-1}	-4.11661
9	-0.23816	0.67695×10^{-1}	-0.81630	4.02528
10	0.68629×10^{-1}	0.34793	0.59256	-0.72663

being ξ the dipole moment (measured in Debeye), and ϖ is an empirically determined association parameter, computed as (Chung *et al.*, 1988):

$$\varpi = 0.0682 + 4.704 \frac{[\text{number of -OH groups}]}{\mathcal{M}}. \quad (2.42)$$

The last three terms of equation (2.40), hence, take into account the molecular structure effect of polyatomic molecules, the polar effect, and the hydrogen-bonding effect, respectively. For nonpolar fluids one has $\xi_r = 0$ and $\varpi = 0$.

In order to take into account dense-gas effects, the dense-gas viscosity μ is written as the sum of two terms:

$$\mu = \mu_k + \mu_p \quad (2.43)$$

being μ_k a modified dilute-gas viscosity and μ_p a correction term; specifically,

$$\mu_k = \mu_0 \left[\frac{1}{G} + A_6 Y \right] \quad (2.44)$$

$$\mu_p = 36.44 \times 10^{-6} \frac{(\mathcal{M} T_c)^{1/2}}{v_c^{2/3}} A_7 Y^2 G \exp [A_8 + A_9 (T^*)^{-1} + A_{10} (T^*)^{-2}]. \quad (2.45)$$

In equations (2.44) and (2.45), $Y = \rho v_c / 6$ is a density-dependent term, G is a nonlinear function written as

$$G = \frac{A_1 [1 - \exp(-E_4 Y)] / Y + A_2 X \exp(A_5 Y + A_3 X)}{A_1 A_4 + A_2 + A_3}, \quad X = \frac{1 - 0.5Y}{(1 - Y)^3}, \quad (2.46)$$

and parameters A_1 to A_{10} are linear functions of ω_{ac} , ξ_r and ϖ :

$$A_i = a_0(i) + a_1(i)\omega + a_2(i)\xi_r^4 + a_3(i)\varpi, \quad i \in \{1, \dots, 10\}. \quad (2.47)$$

Values for the coefficients a_0 , a_1 , a_2 and a_3 are given in table 2.4. One should note that at very low densities, Y approaches zero, X and G approach unity and the dense gas term becomes negligible, and equation (2.45) reduces to equation (2.36).

Thermal conductivity. The dense-gas thermal conductivity is derived, in a similar way, as the

Table 2.5. Parameters for evaluating the functions B_i of equation (2.54) for the computation of the dense-gas thermal conductivity.

i	b_0	b_1	b_2	b_3
1	2.41657	0.74824	-0.91858	1.21721×10^2
2	-0.50924	-1.50936	-4.99912×10^1	6.99834×10^1
3	6.61069	5.62073	64.7599	2.70389×10^1
4	1.45425×10^1	-8.91387	-5.63794	7.43435×10^1
5	0.79274	0.82019	-0.69369	6.31734
6	-5.86340	1.28005×10^1	9.58926	-6.55292×10^1
7	8.11710×10^1	1.14158×10^2	-6.08410×10^1	4.66775×10^2

sum of a dilute-gas component and a correction term. The dilute-gas component κ_0 is written as

$$\kappa_0 = 7.452 \frac{\mu_0 \Psi_\kappa}{\mathcal{M}} \quad (2.48)$$

with

$$\Psi_\kappa = 1 + \alpha_\kappa \frac{0.215 + 0.28288\alpha_\kappa - 1.061\beta_\kappa + 0.26665\delta_\kappa}{0.6366 + \beta_\kappa\delta_\kappa + 1.061\alpha_\kappa\beta_\kappa} \quad (2.49)$$

Here, $\beta_\kappa = 0.7682 - 0.7109\omega_{ac} + 1.3168\omega_{ac}^2$ is a fluid-dependent parameter, whereas $\alpha_\kappa = c_v^{id}(T)/R - 3/2$ and $\delta_\kappa = 2 + 10.5(T/T_c)^2$ are temperature-dependent functions. The term β_κ is an empirical correlation for the contribution of the internal degrees of freedom of the molecule, and is applied only for nonpolar materials. For polar substances β_κ is specific for each compound, and Chung *et al.* (1984) list values for a few materials. If the compound is polar and β is not available, a default value of $\beta_\kappa = 0.758$ is used. The parameter δ_κ represents instead the number of collisions required to interchange a quantum of rotational energy with a quantum translational energy. Using the same approach as for viscosity, the dense-gas thermal conductivity κ is computed as:

$$\kappa = \kappa_k + \kappa_p, \quad (2.50)$$

with

$$\kappa_k = \kappa_0 \left[\frac{1}{H} + B_6 Y \right], \quad \kappa_p = 3.039 \times 10^{-4} \sqrt{\frac{T}{\mathcal{M}}} \frac{1}{v_c^{2/3}} B_7 Y^2 H, \quad (2.51)$$

where

$$Y = \frac{\rho v_c}{6}, \quad (2.52)$$

$$H = \frac{B_1 [1 - \exp(-B_4 Y)] / Y + B_2 X \exp(B_5 Y + B_3 X)}{B_1 B_4 + B_2 + B_3}, \quad X = \frac{1 - 0.5Y}{(1 - Y)^3}, \quad (2.53)$$

$$B_i = b_0(i) + b_1(i)\omega_{ac} + b_2(i)\xi_r^4 + b_3(i)\varpi, \quad i \in \{1, \dots, 7\}. \quad (2.54)$$

Values for b_0 , b_1 , b_2 and b_3 are given in table 2.5.

2.1.4 Comparisons of the EoS

In order to emphasize the importance of a suitable thermodynamic model for the prediction of the actual thermodynamic behaviour of a specific substance, we plot the prediction of some thermodynamic parameters of interest for the same fluid (PP11) according to the EoS considered in the study. Figure 2.2 shows the isocontours of the reduced temperature in a Clapeyron diagram (i.e.

in the $p - v$ thermodynamic plane) for PFG (top), VDW (center) and MAH (bottom panel) EoS. In all the diagrams, the dashed line represents the critical isotherm, $T/T_c = 1$. Two isolines of Γ are plotted (solid lines), respectively $\Gamma = 1$ (denoting the beginning of the dense gas region, which extends downwards up to the saturation curve) and $\Gamma = 0$ line (which marks the passage from the dense gas region to the BZT zone).

The most striking difference is related to the saturation curve: the PFG EoS is of course unable to predict its presence, due to the monotonicity of the isotherms. In the VDW case, a different shape is obtained with respect to MAH EoS, the curve being much less flatter in the critical region. We recall that saturation curves are computed by means of the Maxwell reconstruction; the algorithm is described in appendix B. Moreover, VDW largely overestimates the extension of both the dense

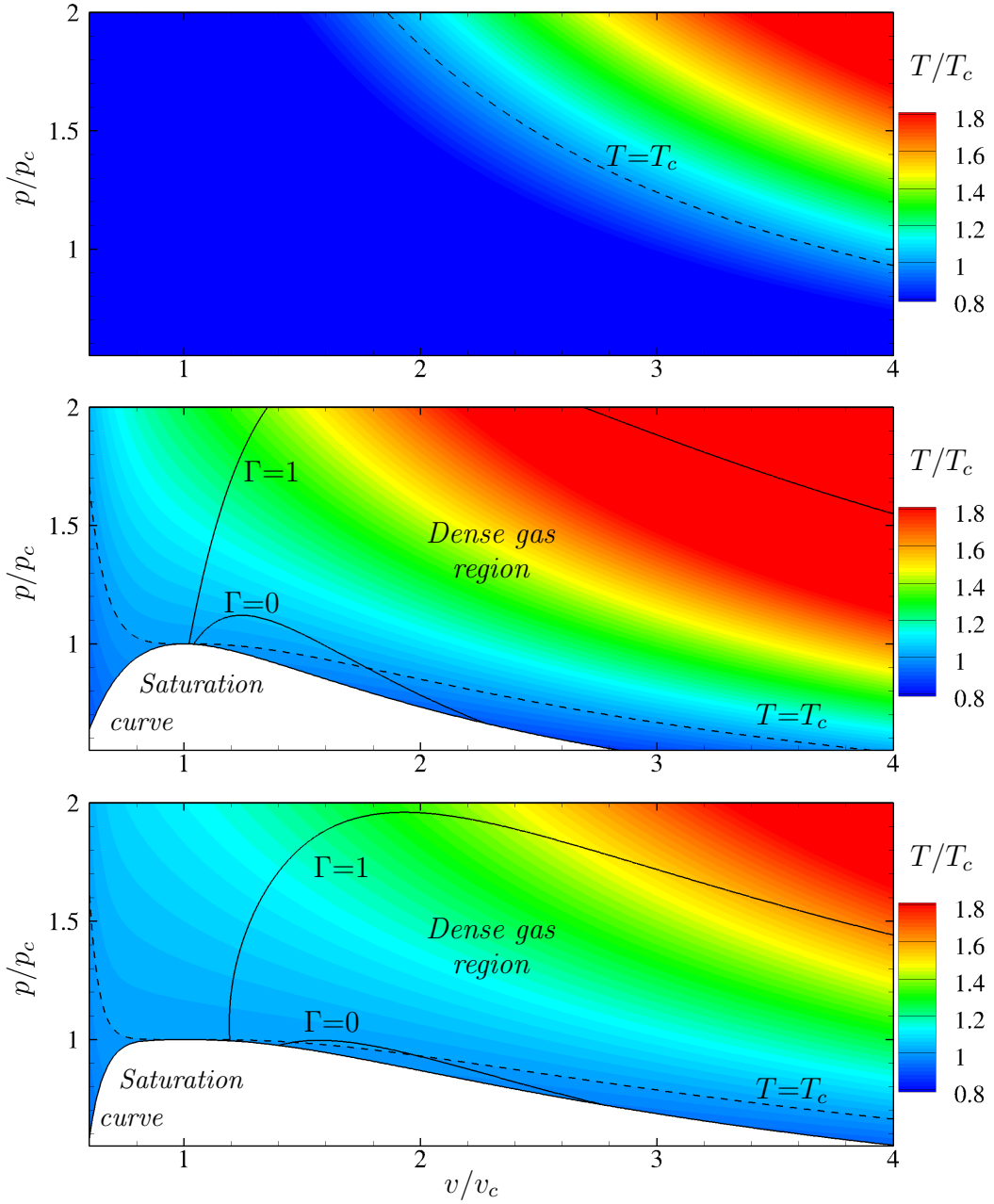


Figure 2.2. Iso-contours of reduced temperature T/T_c in the Clapeyron Diagram for fluid PP11, modelled by means of PFG (top panel), VDW (central panel) and MAH (bottom panel) EoS.

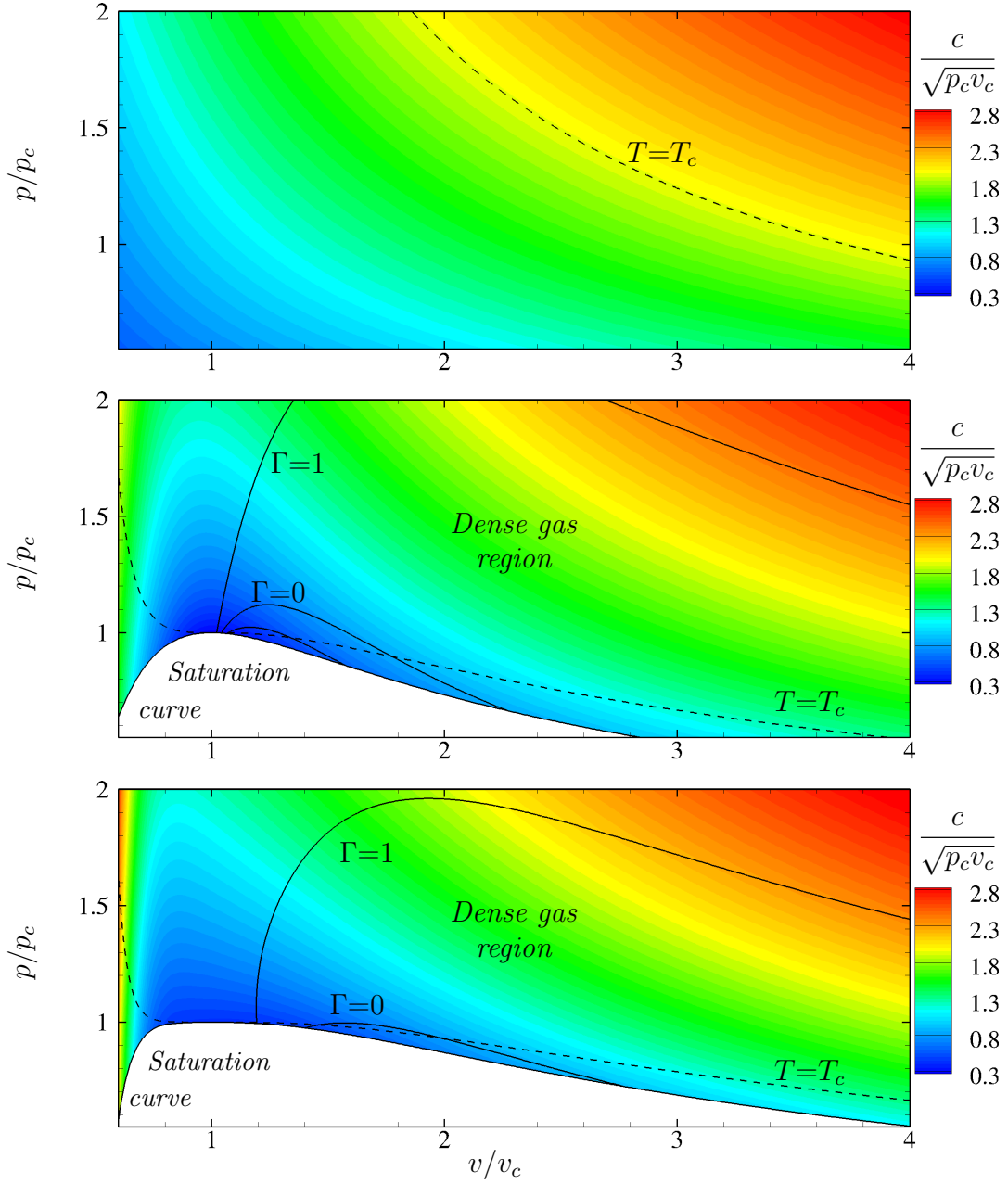


Figure 2.3. Iso-contours of normalized speed of sound $c/\sqrt{p_c v_c}$ in the Clapeyron Diagram for fluid PP11, modelled by means of PFG (top panel), VDW (central panel) and MAH (bottom panel) EoS.

gas and BZT regions. Figures 2.3 and 2.4 show the contours of the normalized speed of sound and viscosity for the different EoS. The critical region strongly influences the speed of sound value c , which goes to zero approaching the critical point for both VDW and MAH equations. Nevertheless, c increases abruptly (as well as Γ) when entering the compressed liquid region; this behaviour is expected to lead to substantial changes (w.r.t. PFG) when strong compressions occur in turbulent flows. Similarly, the dynamic viscosity predicted by the Chung-Lee law exhibit a strong density dependence; note that for $v \gg v_c$ the same viscosity value is recovered. Furthermore, figure 2.5 shows the local values of the equivalent specific heat ratio ($\gamma = c_p/c_v$) and the Prandtl number, highlighting the importance of the caloric component. For PFG and VDW cases, γ is constant due

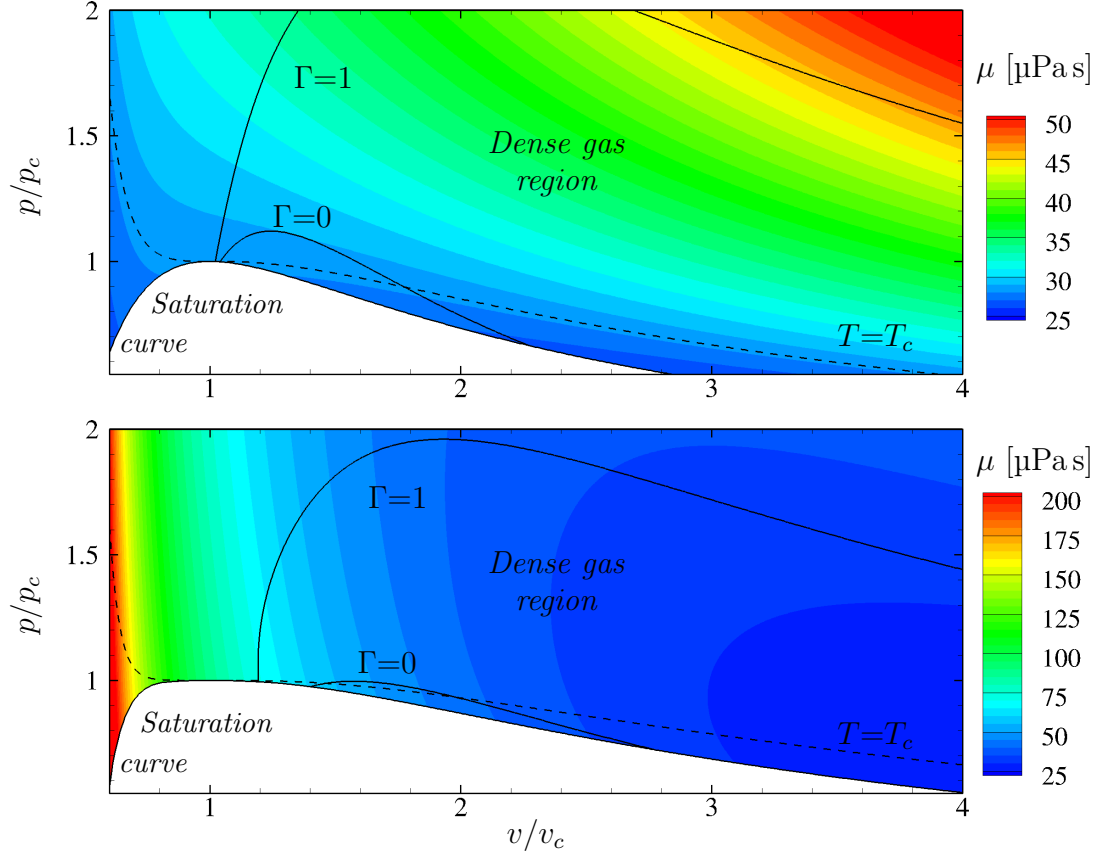


Figure 2.4. Iso-contours of dynamic viscosity μ in the Clapeyron Diagram for fluid PP11, modelled by means of VDW (top panel) and MAH (bottom panel) EoS.

to the polytropic assumption. In the low-density limit, the value of γ is similar to the typical one for perfluorocarbons (i.e., $\gamma \approx 1.0125$), whereas the Prandtl number is of the order of unity for any thermodynamic condition. Deviations become important approaching the critical region, in which these quantities rapidly increase.

Lastly, figure 2.6 shows, as an example, the isocontours of the reduced temperature for two fluids of different families, namely, the siloxane D6 and the refrigerant R245fa.

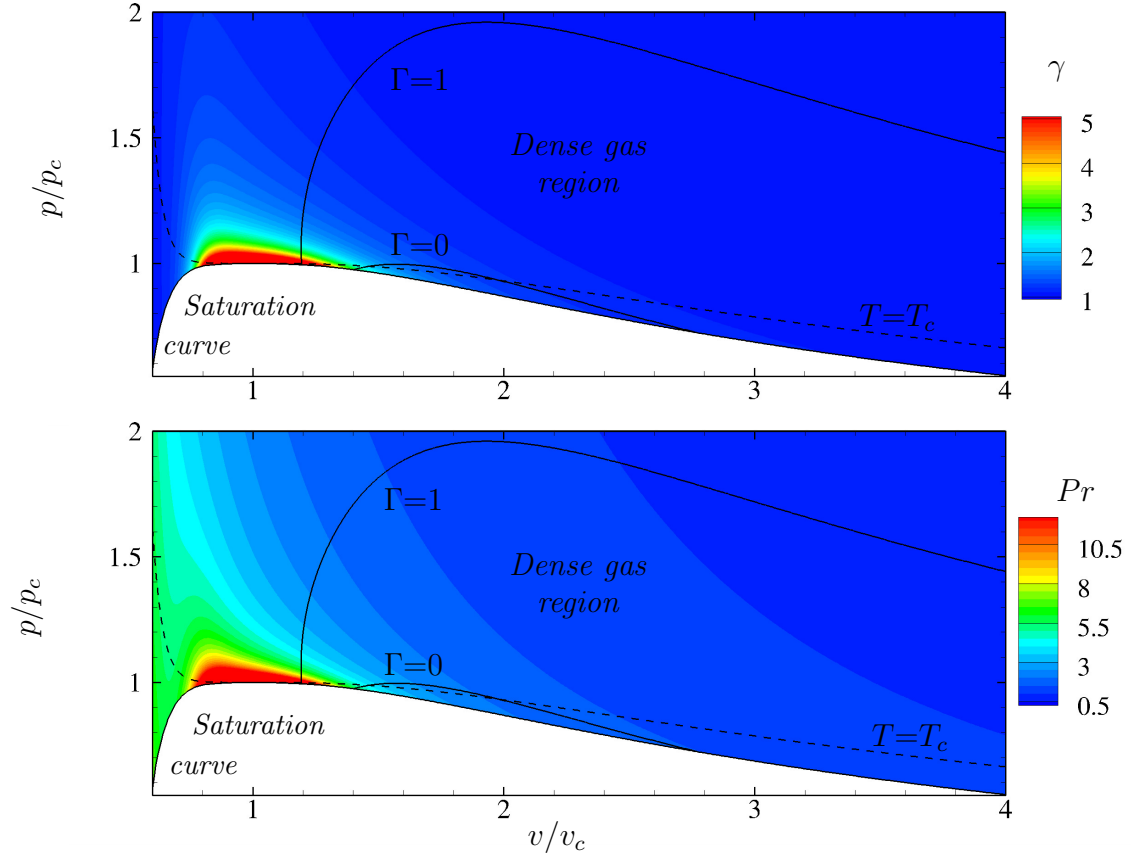


Figure 2.5. Iso-contours of specific heat ratio $\gamma = c_p/c_v$ (top panel) and Prandtl number Pr (bottom panel) in the Clapeyron diagram for fluid PP11, modelled by means of MAH EoS.

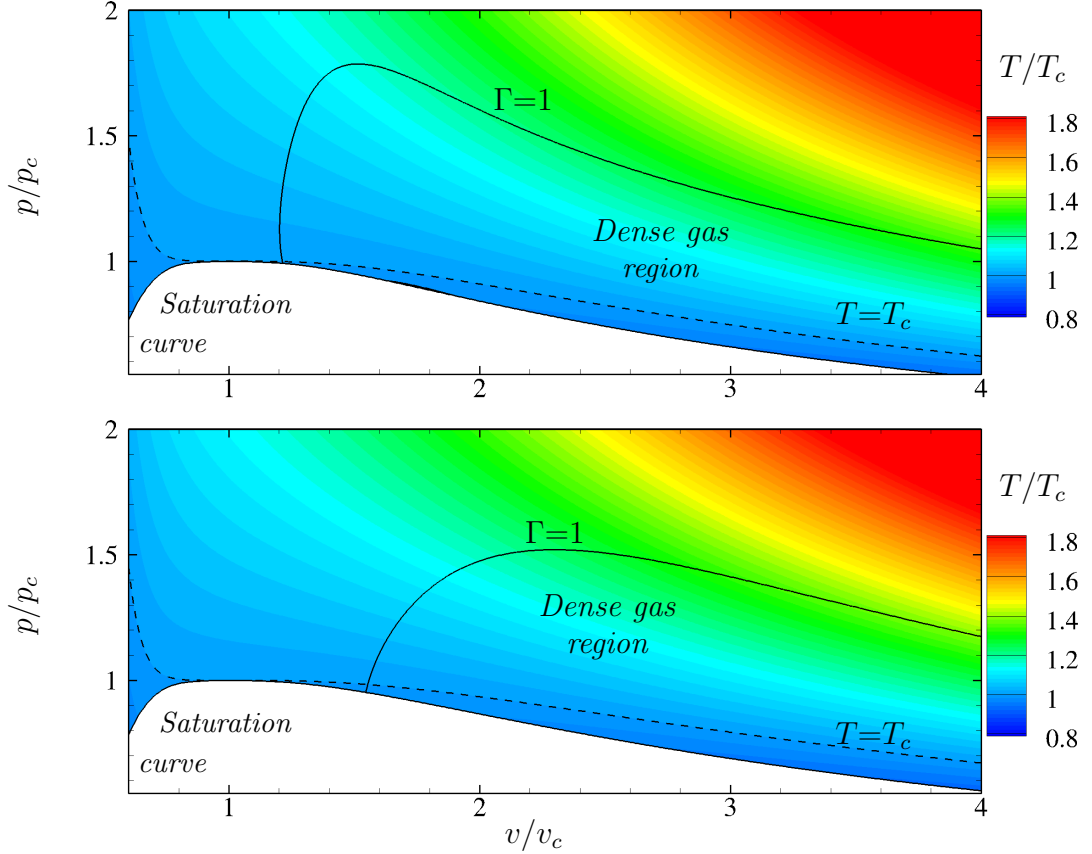


Figure 2.6. Iso-contours of reduced temperature T/T_c in the Clapeyron diagram for fluids D6 (top, SWN EoS) and R245fa (bottom, SWP EoS).

2.2 Numerical methods

The Navier–Stokes equations are discretized by means of high-order finite-difference numerical schemes, ensuring low discretization errors. To describe the methods, it is convenient to cast system (2.1) in flux form:

$$\frac{\partial \mathbf{U}}{\partial t} + \frac{\partial(\mathbf{F}_e - \mathbf{F}_v)}{\partial x} + \frac{\partial(\mathbf{G}_e - \mathbf{G}_v)}{\partial y} + \frac{\partial(\mathbf{H}_e - \mathbf{H}_v)}{\partial z} = 0 \quad (2.55)$$

where $\mathbf{U} = [\rho, \rho u, \rho v, \rho w, \rho E]^T$ is the state vector containing the conservative variables; \mathbf{F} , \mathbf{G} and \mathbf{H} are the fluxes along, respectively, the x , y and z direction, split in an inviscid (convective) and viscous (diffusive) part, $(\bullet) = (\bullet)_e - (\bullet)_v$. Specifically, the inviscid fluxes read:

$$\mathbf{F}_e = [\rho u, \rho u^2 + p, \rho uv, \rho uw, (\rho E + p)u]^T, \quad (2.56)$$

$$\mathbf{G}_e = [\rho v, \rho uv, \rho v^2 + p, \rho vw, (\rho E + p)v]^T, \quad (2.57)$$

$$\mathbf{H}_e = [\rho w, \rho uw, \rho vw, \rho w^2 + p, (\rho E + p)w]^T, \quad (2.58)$$

and the viscous ones:

$$\mathbf{F}_v = [0, \tau_{xx}, \tau_{xy}, \tau_{xz}, u\tau_{xx} + v\tau_{xy} + w\tau_{xz} - q_x]^T, \quad (2.59)$$

$$\mathbf{G}_v = [0, \tau_{xy}, \tau_{yy}, \tau_{yz}, u\tau_{xy} + v\tau_{yy} + w\tau_{yz} - q_y]^T, \quad (2.60)$$

$$\mathbf{H}_v = [0, \tau_{xz}, \tau_{yz}, \tau_{zz}, u\tau_{xz} + v\tau_{yz} + w\tau_{zz} - q_z]^T. \quad (2.61)$$

The viscous fluxes are discretized by means of standard fourth-order centered derivatives on a five-point stencil. For the inviscid fluxes, instead, two different families of high-order finite-difference numerical schemes have been used, namely, a Directional Non-Compact (DNC) scheme initially developed in [Lerat & Corre \(2003\)](#) and a Dispersion-Relation Preserving (DRP) scheme introduced by [Tam & Webb \(1993\)](#). For the sake of clarity, in the following we consider the 1D case, all the considerations being easily extended to three-dimensional cases. We defined the following 1D problem

$$\frac{\partial w}{\partial t} + \frac{\partial f(w)}{\partial x} = 0, \quad (2.62)$$

being t the time, x the spatial coordinate, $w = w(x, t)$ the state vector, $f = f(w)$ the physical flux. Only for this section, we define two discrete spatial operators, namely, the basic difference $\delta(\bullet)_j := (\bullet)_{j+\frac{1}{2}} - (\bullet)_{j-\frac{1}{2}}$, and the cell average operator $\mu(\bullet)_{j+\frac{1}{2}} := \frac{1}{2}((\bullet)_{j+1} + (\bullet)_j)$. Considering a Cartesian grid $x_j = j\Delta x$ (with Δx the grid step), a semi-discrete conservative approximation of equation (2.62) writes:

$$(w_t)_j + \frac{(\delta \mathcal{F})_j}{\Delta x} = 0, \quad (2.63)$$

where $\mathcal{F}_{j+\frac{1}{2}}$ is the numerical flux at cell interface $j + \frac{1}{2}$. \mathcal{F} can be written as the sum of a high-order, centered, non-dissipative component, \mathcal{H} , and a dissipative part, \mathcal{D} :

$$\mathcal{F}_{j+\frac{1}{2}} = (\mathcal{H} - \mathcal{D})_{j+\frac{1}{2}}. \quad (2.64)$$

The numerical dissipation term plays a crucial role, especially for high-Reynolds number turbulence, in order to prevent numerical instabilities due to the accumulation of the aliasing errors resulting from discrete evaluation of the nonlinear convective terms ([Phillips, 1959](#)). Instead of introducing dissipation terms, numerical stability can be ensured, for instance, by explicitly filtering the solution or by adopting energy-consistent schemes. Moreover, some modifications are needed when dealing

with flow discontinuities. A throughout review of numerical methods suitable for both smooth and shocked flows is reported in Pirozzoli (2011).

For the two aforementioned numerical strategies used in this work, we will first present the derivation of the high-order centered fluxes, then we will consider the construction of the dissipative term. Lastly, the shock-capturing corrections introduced for DNC and DRP schemes are presented.

2.2.1 Approximation of centered fluxes

Standard finite differences (DNC schemes)

DNC schemes are constructed by means of standard centered finite differences, for which the order is determined by the truncation error of the corresponding Taylor expansion. Generally, a spatial derivative $\partial f / \partial x$ is discretized with a centered approximation by:

$$\frac{\partial f}{\partial x}(x_0) = \frac{1}{\Delta x} \sum_{j=-N}^N a_j [f(x_0 + j\Delta x)] = \frac{1}{\Delta x} \sum_{j=1}^N a_j [f(x_0 + j\Delta x) - f(x_0 - j\Delta x)] \quad (2.65)$$

with $a_j = -a_{-j}$. It is possible to derive higher-order approximations of the first derivative by successive corrections of the leading truncation error term. We cancel the terms of the Taylor expansion of f up to order Δx^{2N-1} (included):

$$\begin{aligned} f(x_0 + j\Delta x) &= f(x_0) + j\Delta x f'(x_0) + \frac{(j\Delta x)^2}{2!} f''(x_0) + \frac{(j\Delta x)^3}{3!} f'''(x_0) + \frac{(j\Delta x)^4}{4!} f^{(4)}(x_0) + \dots \\ f(x_0 - j\Delta x) &= f(x_0) - j\Delta x f'(x_0) + \frac{(j\Delta x)^2}{2!} f''(x_0) - \frac{(j\Delta x)^3}{3!} f'''(x_0) + \frac{(j\Delta x)^4}{4!} f^{(4)}(x_0) + \dots \end{aligned}$$

obtaining

$$\frac{\partial f}{\partial x}(x_0) = \frac{1}{\Delta x} \sum_{j=1}^N a_j \left[2j\Delta x f'(x_0) + \frac{2j^3\Delta x^3}{3!} f'''(x_0) + \frac{2j^5\Delta x^5}{5!} f^{(5)}(x_0) + \frac{2j^7\Delta x^7}{7!} f^{(7)}(x_0) + \dots \right] \quad (2.66)$$

The coefficients a_j are then solutions of the following system:

$$\left\{ \begin{array}{l} \sum_{j=1}^N 2ja_j = 1 \\ \sum_{j=1}^N j^3 a_j = 0 \\ \vdots \\ \sum_{j=1}^N j^{2N-1} a_j = 0 \end{array} \right. \quad N \text{ relations} \rightarrow \text{order } 2N \quad (2.67)$$

In the end, the general expression of \mathcal{H} is:

$$\mathcal{H} = \left(I + \sum_{j=1}^{N-1} (-1)^j a_j \delta^{2j} \right) \mu f \quad (2.68)$$

which gives a centered approximation of order $2N$ using $2N + 1$ points in each direction.

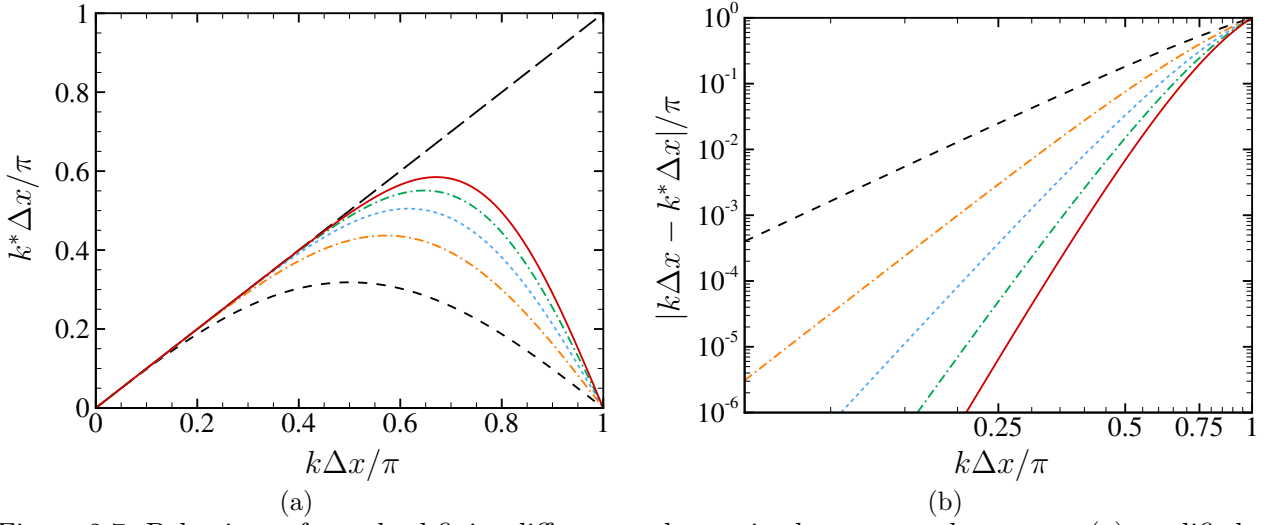


Figure 2.7. Behaviour of standard finite-difference schemes in the wavenumber space. (a) modified wavenumber $k^*\Delta x$ as a function of actual wavenumber $k\Delta x$ and (b) dispersion error in logarithmic scales. -----: order 2, -.-.-.: order 4,: order 6, -.-.-.-.: order 8, —: order 10, -----: exact.

We consider in the following the 10-th order scheme, which uses a 11-points stencil. By computing the Fourier transform of equation (2.65), we define a modified wavenumber of the finite-difference scheme k^* :

$$k^*\Delta x = 2 \sum_{j=1}^N a_j \sin(jk\Delta x) \quad (2.69)$$

The dispersion error is given by $|k^*\Delta x - k\Delta x|/\pi$. The effective wavenumber of the standard schemes and their dispersion errors are reported in figure 2.7.

Optimized finite differences (DRP schemes)

DRP schemes have been developed in the context of aeroacoustic simulations. Differently from the DNC schemes, in which the objective is to maximise the spatial order with respect to the corresponding Taylor expansion, DRP schemes are built by optimizing the dispersion error in the Fourier space. Namely, the minimum of the following function

$$E = \int_{\ln(k\Delta x)_l}^{\ln(k\Delta x)_h} |k^*\Delta x - k\Delta x| d(\ln(k\Delta x)) \quad (2.70)$$

is computed, i.e., $\frac{\partial E}{\partial a_j} = 0$. The upper and lower limits $(k\Delta x)_l$ et $(k\Delta x)_h$ of the integral of equation (2.70) have to be fixed. In order to create an optimized scheme on $2N + 1$ points of order $2M$ (with $M < N$), one has to verify the M relations that cancel the terms of the Taylor expansion up to Δx^{2M-1} , then it is possible to add $M - N$ relations $\partial E / \partial a_j = 0$ (for $j = 1, \dots, M - N$) in order to obtain a system of N equations with N unknowns a_j . In this work, we consider the DRP11

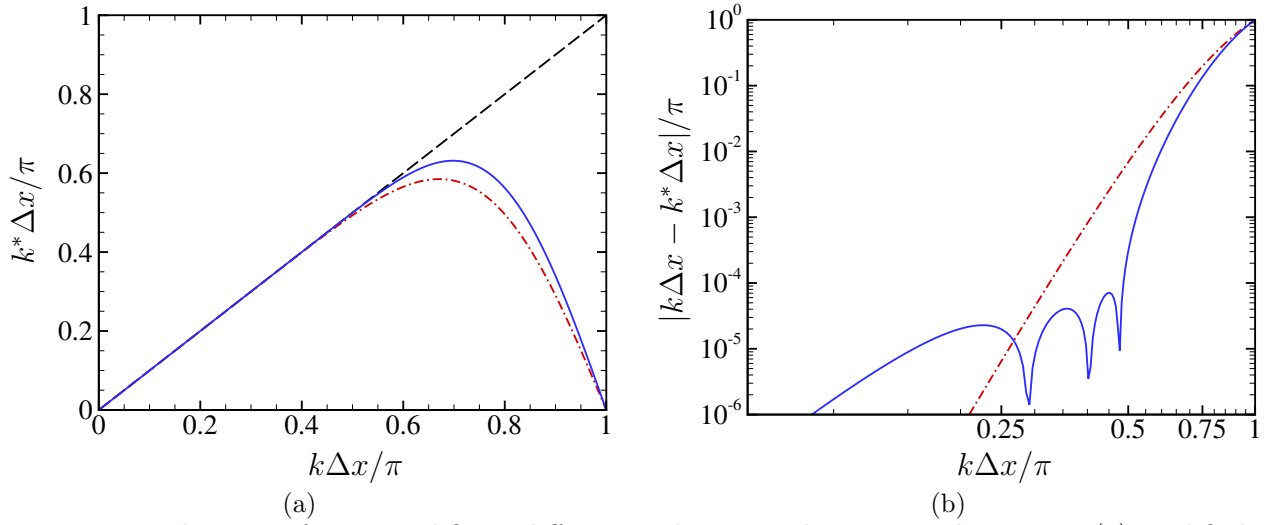


Figure 2.8. Behaviour of optimized finite-difference schemes in the wavenumber space. (a) modified wavenumber $k^*\Delta x$ as a function of actual wavenumber $k\Delta x$ and (b) dispersion error in logarithmic scales. ---: DNC9, —: DRP11, ----: exact.

scheme with a 11-points stencil ($N = 5$), for which we have to resolve the system

$$\left\{ \begin{array}{l} \sum_{j=1}^N 2ja_j = 1 \\ \sum_{j=1}^N j^3 a_j = 0 \\ \frac{\partial E}{\partial a_i} = 0 \quad \text{with } i = 1, 2, 3 \end{array} \right. \quad (2.71)$$

with $(k\Delta x)_l = \pi/16$ and $(k\Delta x)_h = \pi/2$. The coefficients are given in [Bogey & Bailly \(2004\)](#).

The results of the optimization procedure are clearly visible in figure 2.8, where the dispersion error of the 11-points optimized scheme is definitely lower with respect to the classic standard scheme (DNC9) for wavenumber values in $\pi/4 < k\Delta x < \pi/2$.

2.2.2 Numerical stabilization terms

Central finite difference schemes are zero-dissipative and cannot damp unresolved grid-to-grid oscillations (i.e., $k\Delta x = \pi$) and, in the end, lead to numerical instabilities. To avoid these high-frequency oscillations one can, for instance, introduce dissipation terms or adopt filtering techniques.

Dissipative flux

A convenient way of introducing dissipation in schemes of the DNC family has been proposed by [Lerat & Corre \(2003\)](#), which introduce a directional matrix dissipation term that leads to a global odd-order accurate, dissipative dominant, space approximation. In their development, the dissipation term naturally arises by recursively applying an upwind correction to the second-order central scheme, up to the desired order of accuracy. The upwind correction terms involve the numerical flux of a first-order upwind scheme, generally Roe's scheme. For smooth flow fields, the resulting schemes are equivalent to MUSCL schemes ([Van Leer, 1979](#)) based on a high-order extrapolation of the physical fluxes. The first order scheme of this family corresponds to the Roe

Table 2.6. Centered component \mathcal{H} and dissipation term \mathcal{D} of the numerical flux $\mathcal{F} = \mathcal{H} - \mathcal{D}$ of the schemes of Lerat & Corre (2003) up to 9-th order.

Order	\mathcal{H}	\mathcal{D}
1	μf	$\frac{1}{2} Q \delta w$
3	$(I - \frac{1}{6}\delta^2)\mu f$	$\frac{1}{12} Q \delta^3 w$
5	$(I - \frac{1}{6}\delta^2 + \frac{1}{30}\delta^4)\mu f$	$\frac{1}{60} Q \delta^5 w$
7	$(I - \frac{1}{6}\delta^2 + \frac{1}{30}\delta^4 - \frac{1}{140}\delta^6)\mu f$	$\frac{1}{280} Q \delta^7 w$
9	$(I - \frac{1}{6}\delta^2 + \frac{1}{30}\delta^4 - \frac{1}{140}\delta_1^6 + \frac{1}{630}\delta^8)\mu f$	$\frac{1}{1260} Q \delta^9 w$

scheme (Roe, 1981). The high-order centered component \mathcal{H} and the dissipation term \mathcal{D} of the numerical flux \mathcal{F} of Lerat & Corre (2003) schemes up to the 9-th order of accuracy are listed in table 2.6. In the dissipation term, $(Q)_{j+\frac{1}{2}} = Q(w_j, w_{j+1})$ is the Roe matrix. When an ideal-gas equation of state is considered, Q is uniquely determined. If a complex equation of state is taken into account, the Roe matrix has to be modified since generally it will depend on three independent variables, namely the velocity u and two thermodynamic variables, and is no longer uniquely determined. Different types of linearization can be performed; a review of the techniques available in literature is found in Guardone & Vigevano (2002) and Cinnella (2006). The “simplified” approach described in Cinnella (2006) has been implemented in the CFD code; the Jacobian matrices for perfect and dense gas cases are reported in appendix C.

To simplify the scheme implementation and reduce the computational cost for dense gas flows, the Roe matrix Q can be replaced by its spectral radius. This leads to a scalar dissipation term, and the resulting schemes correspond to higher-order versions of Rusanov’s first-order scheme.

Selective filtering methods

A selective centered (non-dispersive) filter is able to damp the highest frequencies without affecting the physical solution. The filtered quantity f^{filt} reads:

$$f^{\text{filt}}(x_0) = f(x_0) - \sigma_d D_f(x_0) \quad \text{with} \quad D_f(x_0) = \sum_{j=-N}^N d_j f(x_0 + j\Delta x) \quad (2.72)$$

where $0 < \sigma_d < 1$ is a coefficient used to adjust the filter strength. The damping function of the centered filter is:

$$D_k(k\Delta x) = d_0 + \sum_{j=1}^N 2d_j \cos(jk\Delta x) \quad (2.73)$$

As shown for the high-order centered schemes, filters are also built by means of an optimization process.

Standard filters. As usual, by means of Taylor expansions we obtain

$$\begin{aligned} D_f(x_0) &= d_0 f(x_0) + \sum_{j=1}^N d_j [f(x_0 + j\Delta x) + f(x_0 - j\Delta x)] \\ &= d_0 f(x_0) + \sum_{j=1}^N d_j \left[2f(x_0) + j^2 \Delta x^2 f''(x_0) + \frac{2j^4 \Delta x^4}{4!} f^{(4)}(x_0) + \frac{2j^6 \Delta x^6}{6!} f^{(6)}(x_0) + \dots \right] \end{aligned}$$

In order to construct a standard high-order filter of order $2N-1$, the terms of the Taylor expansions up to Δx^{2N-1} (included) are canceled. The $N+1$ coefficients d_j are solutions of the system

$$\left\{ \begin{array}{l} d_0 + 2 \sum_{j=1}^N d_j = 0 \\ \sum_{j=1}^N j^2 d_j = 0 \\ \vdots \\ \sum_{j=1}^N j^{2N-2} d_j = 0 \end{array} \right. \quad \begin{array}{l} \text{In the Fourier space,} \\ N \text{ relations} + \end{array} \quad \left(\begin{array}{ll} D_k(0) = 0 & \Rightarrow d_0 + 2 \sum_{j=1}^N d_j = 0 \\ D_k(\pi) = 1 & \Rightarrow d_0 + 2 \sum_{j=1}^N (-1)^j d_j = 1 \end{array} \right)$$

The damping functions of the standard filters are reported in figure 2.9.

Optimized filters. Following the same procedure of the optimized scheme, the following dissipation error is minimized:

$$E = \int_{\ln(\pi/16)}^{\ln(\pi/2)} D_k(k\Delta x) d(\ln(k\Delta x)) \quad (2.74)$$

The coefficients of the optimized 11-points filters are given in [Bogey et al. \(2009\)](#). This filter is compared with the tenth-order standard filter in figure 2.10. One should note that the dissipation error is lower for the optimized filter with respect to the standard tenth-order filter for values of $k\Delta x$ between $\pi/4$ and $\pi/2$, but it is slightly higher for lower wavenumbers. In order to limit its effects, it is possible to reduce the filtering width or call the selective filtering procedure less frequently (e.g., at the end of each Runge-Kutta iteration instead of each sub-step). Unless differently stated, in this work we use $\sigma_d = 0.1$.

2.2.3 Shock-capturing methods

Both DNC and DRP schemes are conservative by construction, but not Total Variation Diminishing (TVD), therefore it is not possible to produce non-oscillatory shock profiles. Apart from switching to different numerical schemes (such as WENO, see for instance [Liu et al., 1994](#); [Jiang & Shu, 1995](#)), possible ways to circumvent this problem are the introduction of artificial viscosity models, or the use of hybrid schemes with nonlinear filtering. The two latter techniques are described below.

Adaptive nonlinear artificial dissipation

This technique is used in this work to enable shock-capturing abilities when using the DNC scheme. An artificial dissipation based on the one proposed in [Jameson et al. \(1981\)](#) and extended to high order by [Kim & Lee \(2001\)](#) has been used. It consists in a blending of a second-order term and a high-order one, depending on the order of the centered approximation. Thus, the dissipative flux

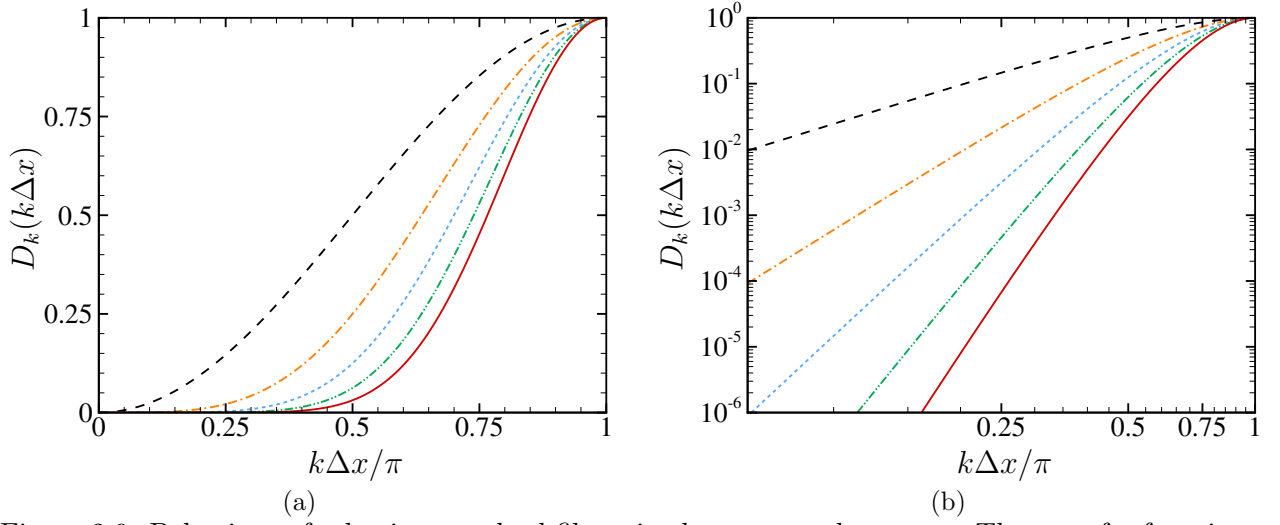


Figure 2.9. Behaviour of selective standard filters in the wavenumber space. The transfer function of the filter as a function of wavenumber $k\Delta x$ is plotted in normal (a) and logarithmic (b) scales, respectively. -----: order 2, ----: order 4,: order 6, -.-.-: order 8, —: order 10.

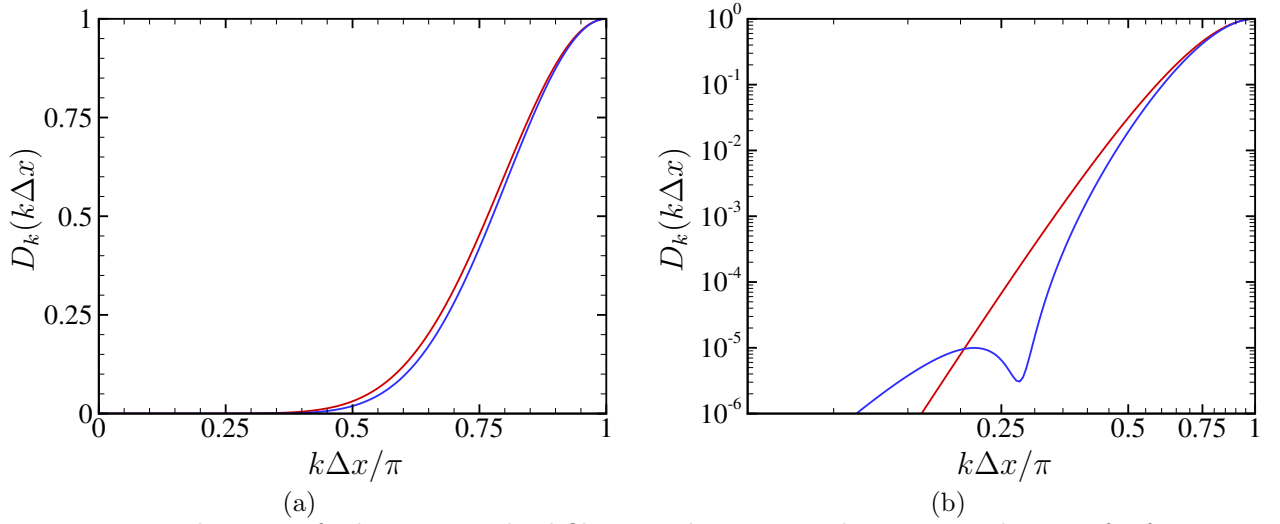


Figure 2.10. Behaviour of selective standard filters in the wavenumber space. The transfer function of the filter as a function of wavenumber $k\Delta x$ is plotted in normal (a) and logarithmic (b) scales, respectively. —: order 10, —: optimized 11-points filter.

for the DNC9 scheme reads:

$$\mathcal{D}_{j+\frac{1}{2}} = |\lambda|_{j+\frac{1}{2}} [\epsilon_{j+\frac{1}{2}}^{(2)} (\delta\omega)_{j+\frac{1}{2}} - \epsilon_{j+\frac{1}{2}}^{(10)} (\delta^9\omega)_{j+\frac{1}{2}}], \quad (2.75)$$

being $|\lambda|_{j+\frac{1}{2}}$ the approximation at a cell face of the spectral radius of the Jacobian matrix,

$$\epsilon_j^{(2)} = k_2 \Psi_{j+\frac{1}{2}}, \quad \epsilon_{j+\frac{1}{2}}^{(2)} = \max(\epsilon_j^{(2)}, \epsilon_{j+1}^{(2)}), \quad \epsilon_{j+\frac{1}{2}}^{(10)} = \max[0, (k_{10} - \epsilon_{j+\frac{1}{2}}^{(2)})] \quad (2.76)$$

the nonlinear dissipation functions, k_2 and k_{10} some adjustable constants and

$$\Psi_j = \frac{|p_{j+1} - 2p_j + p_{j-1}|}{p_{j+1} + 2p_j + p_{j-1}} \quad (2.77)$$

the well-known pressure-based shock sensor of [Jameson *et al.* \(1981\)](#). The use of a scalar dissipation term allows to simplify the implementation of complex equations of state and greatly reduces the computational cost. However, [Garnier *et al.* \(1999\)](#) and [Ducros *et al.* \(1999\)](#) showed that a Jameson-like dissipation is not recommended for its high damping at the small scales. Hence, in order to be able to deal with flow discontinuities while preserving fine-scale structures, [Ducros *et al.* \(1999\)](#) proposed a sensor based on local properties of the flow:

$$\Phi = \frac{\theta^2}{\theta^2 + \omega^2 + \epsilon_c} \quad (2.78)$$

being $\theta = \nabla \cdot \mathbf{u}$ the velocity divergence, $\omega = \|\boldsymbol{\omega}\| = \|\nabla \times \mathbf{u}\|$ the vorticity and ϵ_c a small real constant used to prevent the denominator to become zero. The sensor acts in a very localized fashion. It becomes $\mathcal{O}(1)$ in high-divergence regions and tends to zero in vortex-dominated regions, thus allowing capturing flow discontinuities sharply while minimizing the effect of numerical dissipation on vortical structures. It is applied to the second order term of the Jameson artificial viscosity, which becomes:

$$\epsilon_{j+1/2}^{(2)} = k_2 |\lambda(A)|_{j+\frac{1}{2}} \Psi_{j+\frac{1}{2}} \Phi_{j+\frac{1}{2}} \quad \text{with} \quad \Psi_{j+\frac{1}{2}} \Phi_{j+\frac{1}{2}} = \max(\Psi_j \Phi_j, \Psi_{j+1} \Phi_{j+1}) \quad (2.79)$$

This allows to perform a shock-capturing treatment and to achieve a better resolution in shock-free regions. Note that, when $k_2 = 0$ and $k_{10} = \frac{1}{1260}$, the preceding method degenerates to the ninth-order accurate upwind scheme.

Adaptive nonlinear selective filtering

The adaptive nonlinear selective filtering is similar to the artificial viscosity model, but the damping term is replaced by a signal processing operation at each time integration. This technique exploits an algebraic algorithm which is theoretically able to treat flow discontinuities, as shown in [Bogey *et al.* \(2009\)](#). The filter is applied at each time integration after the selective filtering procedure. In conservative form, the filtered variable $(\bullet)^f$ reads:

$$f_j^f = f_j - (\sigma_{j+\frac{1}{2}}^f D_{j+\frac{1}{2}}^f - \sigma_{j-\frac{1}{2}}^f D_{j-\frac{1}{2}}^f) \quad (2.80)$$

where the filter width $0 < \sigma^f < 1$ is dynamically adjusted as a function of the flow variables, and the damping functions $D_{j+\frac{1}{2}}^f$ et $D_{j-\frac{1}{2}}^f$ are computed through the following interpolations:

$$D_{j+\frac{1}{2}}^f = \sum_{m=1-n}^n c_m f_{j+m} \quad \text{and} \quad D_{j-\frac{1}{2}}^f = \sum_{m=1-n}^n c_m f_{j+m-1} \quad (2.81)$$

The coefficients c_m are determined starting from the non conservative form of the filter ($f_j^f = f_j - (\sigma_j^f \sum_{m=-n}^n D_{j+1}^f)$) and are given in table 2.7 for the standard and the optimized 2nd order filters, Fo2 and Fopt, respectively. Two sensors can be used to trigger the filter, namely, a pressure- and a dilatation-based sensor. We consider only the latter which is more suitable to distinguish shocks and turbulent fluctuations. Moreover, it has embedded information such as the local speed of sound (important for dense gases) and grid step Δx . The value of the shock sensor is thus:

$$r_j^d = \frac{\frac{1}{2}[(D\theta_j - D\theta_{j+1})^2 + (D\theta_j - D\theta_{j-1})^2]}{c_j^2/\Delta x^2} + \epsilon \quad (2.82)$$

Table 2.7. Coefficients c_j (with $c_{1-j} = c_j$) of the conservative form of the adaptive nonlinear selective filtering method for the standard (Fo2) and optimized second order (Fopt).

	Fo2	Fopt
c_1	-1/4	-0.210383
c_2	0	0.039617

being ϵ a small constant used to prevent numerical divergence, c_j the speed of sound at the j -th point, Δ the grid spacing, θ the local dilatation and $D\theta_j$ extracted starting from a second-order filter: $D\theta_j = (-\theta_{j+1} + 2\theta_j - \theta_{j-1})/4$. Alternatively, a pressure-based formulation can be used, in which

$$r_j^p = \frac{\frac{1}{2}[(Dp_j - Dp_{j+1})^2 + (Dp_j - Dp_{j-1})^2]}{p_i^2} + \epsilon. \quad (2.83)$$

Lastly, the filter width is computed as:

$$\sigma_j^f = \frac{1}{2} \left[1 - \frac{r_{th}}{r_j} + \left| \left(1 - \frac{r_{th}}{r_j} \right) \right| \right] \quad (2.84)$$

where r_j is the dilatation- or pressure-based filter chosen and r_{th} is the threshold parameter governing the filter sensitivity. Its value is generally $10^{-6} < r_{th} < 10^{-4}$; lower values of r_{th} lead to bigger sensitivity and thus to the application of the filter on a wider region. The filtering amplitudes in the conservative form are approximated by:

$$\sigma_{j+\frac{1}{2}}^f = \frac{1}{2}(\sigma_{j+1}^f + \sigma_j^f) \quad \text{and} \quad \sigma_{j-\frac{1}{2}}^f = \frac{1}{2}(\sigma_{j-1}^f + \sigma_j^f) \quad (2.85)$$

2.2.4 Time integration methods

In this work a class of explicit Runge-Kutta (RK) algorithms is considered. Given the equation $\partial \mathbf{U} / \partial t = \mathbf{F}(\mathbf{U}, t)$, the general form of a RK method with p subiterations reads:

$$\mathbf{U}^{n+1} = \mathbf{U}^n + \Delta t \sum_{i=1}^p b_i \mathbf{K}^i \quad \text{with} \quad \mathbf{K}^i = \mathbf{F} \left(\mathbf{U}^n + \sum_{j=1}^{i-1} a_{ij} \mathbf{K}^j, t^n + c_i \Delta t \right) \quad (2.86)$$

where $c_i = \sum_{j=1}^{i-1} a_{ij}$ ($i \in \{1, \dots, p\}$). The most famous scheme is the one proposed by [Runge \(1895\)](#) and [Kutta \(1901\)](#), whose Butcher tableau reads:

c_i	a_{ij}	0	0	0	0
	b_i	1/2	1/2	0	0
		1/2	0	1/2	0
		1	0	0	1
		1/6	1/3	1/3	1/6

In order to obtain low-stockage schemes, we impose $b_p = 1$ et $b_i = 0$ for $i = 1, \dots, p-1$ ([Hu et al., 1996](#)). The only non-zero a_{ij} are a_{ii-1} . The scheme reads:

$$\mathbf{U}^{n+1} = \mathbf{U}^n + b_p \mathbf{K}^p \quad \text{with} \quad \mathbf{K}^i = \Delta t \mathbf{F}(\mathbf{U}^n + \alpha_{i-1} \mathbf{K}^{i-1}, t^n + c_i \Delta t). \quad (2.87)$$

where $\alpha_i = a_{ii-1}$ and $\alpha_0 = 0$. For the fourth-order, we obtain the following coefficients:

c_i	a_{ij}	0	0		
	b_i	1/4	1/4		
		1/3	0	1/3	
		1/2	0	0	1/2
			0	0	0
					1

This scheme is fourth-order for linear problems and second-order for nonlinear ones.

In order to increase the numerical efficiency and ensure low dispersion and dissipation errors, we consider also the six-step RK algorithm described in [Bogey & Bailly \(2004\)](#). Similarly to the spatial discretization, the coefficients are the results of an optimization procedure. Specifically, they chose to minimize the following function:

$$\int_{\ln(\pi/16)}^{\ln(\pi/2)} (1 - |G_{RK}(\omega\Delta t)|) d(\ln(\omega\Delta t)) + \int_{\ln(\pi/16)}^{\ln(\pi/2)} (|\omega^* \Delta t - \omega\Delta t|/\pi) d(\ln(\omega\Delta t)), \quad (2.88)$$

with the constraints: $1 - |G_{RK}| > 0$ and $\partial[\ln(1 - |G_{RK}|)]/\partial[\ln(\omega\Delta t)] \geq -5$; G_{RK} denotes the effective amplification factor of the scheme. The details of the optimization procedure, as well as the values of the coefficients are given in [Bogey & Bailly \(2004\)](#). For the numerical simulations presented in this thesis, we will use the optimized RK algorithm.

2.3 Description of the CFD codes

In this work, two different CFD codes developed at DynFluid Laboratory have been used.

The first one is the Dynamic High-order Laboratory (DynHoLab), which combines the interpreted, object-oriented Python language, and the compiled, fast Fortran language. This allows to shorten the development time thanks to a flexible and modular Python environment, preserving the high performances of compiled languages. Thanks to project like *numpy* (numerical libraries), *scipy* (mathematics, science and engineering libraries), *matplotlib* (plotting library), *sage* (mathematics software) and many others, Python – being moreover a free and open-source software – represents a very good choice to develop a CFD kernel. DynHoLab is organized as a Python package, in the sense that every component of the code can be imported by other programs to be re-used. The most time consuming methods are written in Fortran and converted into Python libraries by using the wrapper *f2py*. The data-structure chosen for DynHoLab is a CGNS-tree, which provides a full hierarchical structure to store the data. This data-structure has been developed by a consortium (ADAPCO, ANSYS, Boeing, NASA, ONERA, Rolls-Royce, Stanford University, Tecplot, US Air Force, ..) with the purpose of creating a general, portable and extensible standard for the storage and retrieval of CFD analysis data. DynHoLab is a multi-purpose CFD code based on a finite-volume formulation able to handle complex geometries (including overlapping grids) and carry out RANS, LES and DNS simulations. The code is equipped with a variety of high-order space-discretization and time-integration methods. A thorough discussion on the structure of the code, the development strategy, the physical and numerical models implemented and a series of validation test cases can be found in [Outtier et al. \(2013\)](#) and [Outtier \(2014\)](#). This code has been used to perform numerical simulations of decaying compressible homogeneous isotropic turbulence, presented in chapters 3 and 4, as well as for cross validations with solution provided by the second code on the configurations discussed on chapter 5. It will represent the basis for upcoming studies of turbulent dense gas flow around turbine blades.

Since, however, the main objective of this thesis is to perform parametric DNS studies of turbulent flows in simple Cartesian configurations and given the high cost required by such simulations, we chose to use a dedicated faster code, based on finite-difference schemes. This code, also developed at the DynFluid Laboratory, is named MULTiscale Solver in Computational Aeroacoustics (MUSICA).

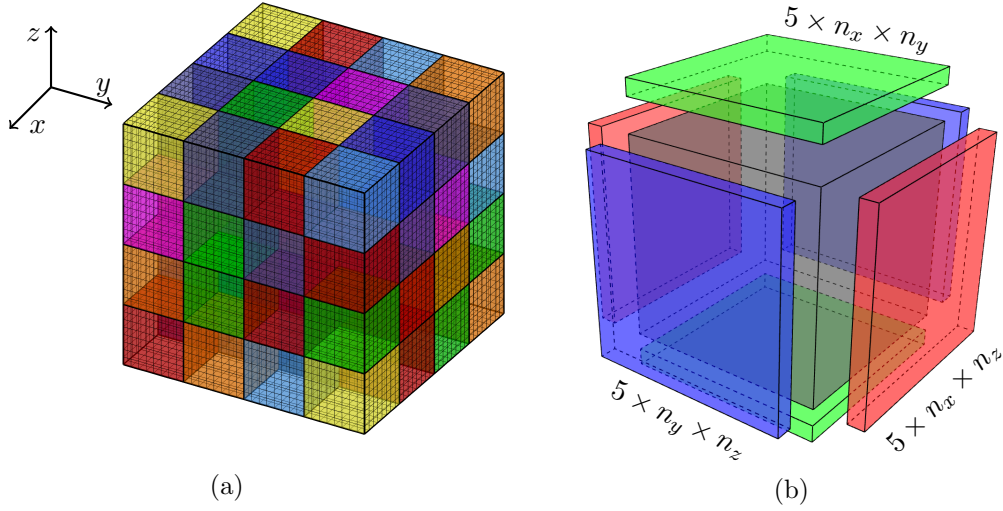


Figure 2.11. Left panel: decomposition of the computational Cartesian domain into subdomains by means of the `MPI_CART` functionalities. Right panel: interfaces exchanged among neighbours in the three directions, each one composed of 5 plans.

MUSICA is completely written in Fortran, ensuring fast computations and an efficient memory management. Differently from DynHoLab, MUSICA is not a modular code, but rather an ensemble of solvers sharing a common core structure, dedicated to specific configurations. The code has been employed, for instance, for aeroacoustics computations (Gloerfelt & Berland, 2013) and large-eddy simulations of compressible flows (Aubard *et al.*, 2013).

MUSICA takes advantage of the MPI libraries to enable data communication among different processors. Since we are dealing with single-block structures meshes, the code has been parallelized by means of the `MPI_CART` functionalities. The cartesian communicator automatically distributes the processors on a three-dimensional grid topology which is used to map the entire computational domain. Each processor is given an equal fraction of the entire domain, ensuring a perfect repartition of the computational work (figure 2.11a). The data exchange among the processors is carried out by means of non-blocking communications `ISEND/IRECV`. The passage from blocking to non-blocking communications is needed in order to overcome the problems related to a saturation of the performances when more than 1024 processors were used. Being the numerical discretization completely explicit, each processor communicates only with its own neighbours in the three directions (figure 2.11b). Each exchanged interface is composed of 5 planes, corresponding to the stencil of the spatial scheme. Given the the size of the computational domains, The input-output `MPI_IO` routines have been implemented in order to ensure high efficiency when big files are read/written from thousands of processors. Particular attention has been paid to the portability of the code, in order to allow a transparent passage from big-endian to little-endian machines and vice versa.

In order to perform dense gas simulations, both codes have been significantly modified. The computation of thermodynamic properties has been externalized in a Fortran module; this allows to implement any complex equation of state without changing the code kernel. The module contains a set of functions which compute the thermal and caloric equations of state, the sound speed and the pressure partial derivatives with respect to density and internal energy, written as a function of density and temperature. A Newton–Raphson algorithm has been implemented whenever an iterative procedure is required (i.e., for the calculation of temperature from density and internal energy). To speed up the the Newton cycles, the solution at the previous iteration is taken as initial guess. Since these functions are called at least once for each grid point and each Runge–Kutta step, the computational overhead due to the externalization has been examined. It is shown

Table 2.8. Comparison of the restitution times per iteration per grid point for the two codes and the different thermodynamic models.

Code	EoS	time [μ s]
DynHoLab	PFG	18.5
	PFG	5.42
	VDW	5.97
MUSICA	MAH	8.89
	SWP/SWN	21.4

to be negligible for complex EoS (such as MAH and SW models), due to the much higher number of operations to be performed inside the function. For simpler EoS (such as PFG and VDW), instead, it is slightly more important, but the use of aggressive optimizations and inlining techniques removes almost completely the overhead.

In table 2.8 we provide a comparison of the values of the CPU time per iteration and per grid point obtained by running a reference CHIT test-case with the two different codes and by means of different equations of state. As previously stated, considering the PFG EoS, MUSICA is approximately 3.5 times faster than DynHoLab. This is mainly due to the fact that DynHoLab is a multipurpose code, written in a mix of Python and Fortran languages in a finite volume formulation. Conversely, MUSICA is a dedicated solver, completely written in Fortran and in a finite differences formulation. Popescu *et al.* (2005) showed that writing the finite-volume version of the DRP scheme requires more than twice the number of operations needed in the finite-difference one. This is hence the main reason for the different performances between the code, (the cost of the Python layer for DynHoLab being negligibly small when big simulations are performed). Lastly, one should note that the perfect gas and Van der Waals EoS have approximately the same computational cost, whereas the Martin–Hou and Span–Wagner equation are respectively 1.5 and 4 times slower with respect to the perfect gas case.

2.3.1 Scalability tests

The scalability of DynHoLab is extensively described in Outtier (2014). Since the code used for the most computationally expensive simulations is MUSICA, we present hereafter some of the tests performed with the latter. The scalability study has been carried out on the same supercomputers on which the computations have been successively performed. The computational hours have been granted from the Institute for Development and Resources in Intensive Scientific Computing (IDRIS), mainly on Turing (IBM Blue Gene/Q, 98304 processors Power A2 64-bit, 1.258 Pflop/s of peak performance) and ADA (IBM x3750-M4, 10624 processors Intel Sandy Bridge E5-4650, 233 Tflop/s of peak performance). In the following we will show the scalability test on Turing, given the restriction on the maximum number of processors available on ADA. Since the tests are performed on a channel flow configuration, the different boundary conditions in the three directions can influence the overall performance. Nevertheless, this allows us to have a prediction of the computational time in actual runs – which is the aim of these tests.

There are commonly two ways to characterize the parallel performance of a code, that are referred to as strong scalability and weak scalability. In the weak scalability, we consider a fixed problem size assigned to each processing element, and additional elements are used to solve a larger total problem (e.g., one that wouldn't fit in RAM on a single node). Linear scaling is achieved if the run time stays constant while the workload is increased in direct proportion with the number of processor units. Programs that employ mainly nearest-neighbour communication patterns (as

Table 2.9. Weak scalability test from 16 to 16384 processing units. The efficiencies for five different distributions of grid points per core are shown.

N_{proc}	# blocks	$E_{\text{weak}}^{16}(N)$				
		64^3	48^3	32^3	24^3	16^3
16	$4 \times 2 \times 2$	100	100	100	100	100
32	$4 \times 2 \times 4$	100	100	100	100	100
64	$4 \times 4 \times 4$	100	100	99.5	97.1	95.2
128	$8 \times 4 \times 4$	99.9	99.8	99.1	95.8	93.5
256	$8 \times 4 \times 8$	99.8	99.7	99.1	95.2	91.8
512	$8 \times 8 \times 8$	97.4	97.1	96.5	91.2	87.6
1024	$16 \times 8 \times 8$	97.3	97.1	96.4	91.0	87.5
2048	$16 \times 8 \times 16$	97.0	96.6	95.3	89.7	86.1
4096	$32 \times 8 \times 16$	96.8	96.2	94.9	89.3	85.2
8192	$32 \times 8 \times 32$	96.1	95.7	94.1	88.3	84.4
16384	$32 \times 8 \times 64$	95.9	95.5	93.8	87.5	83.6

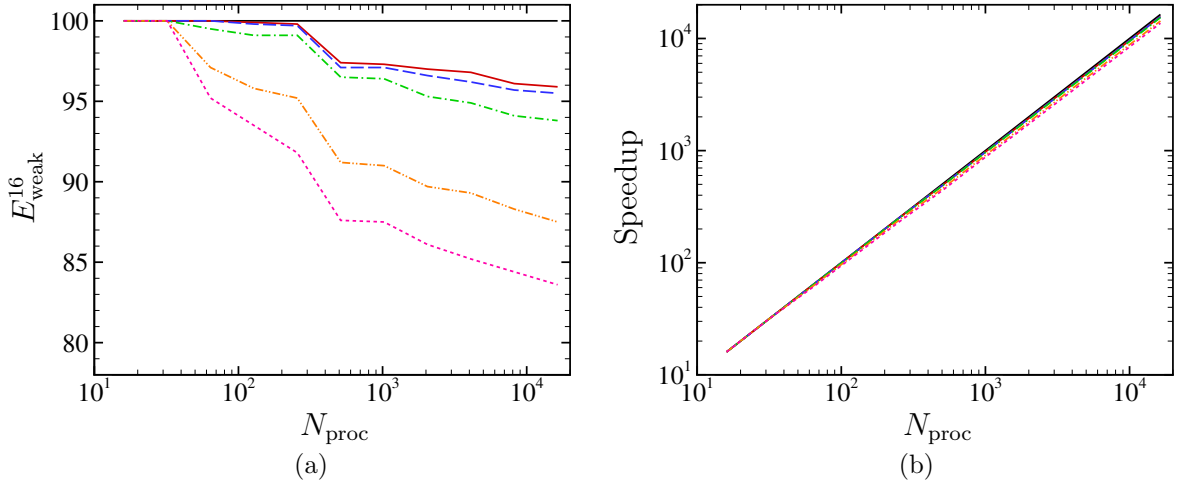


Figure 2.12. Weak efficiency scalability (a) and speedup as a function of the number of processing units, for different values of grid points per processing unit. —: ideal, —: 64^3 , - - - : 48^3 , - . . : 32^3 , . . . : 24^3 , . . . : 16^3 .

for the code in use) should have a good weak scalability, because the communication overhead is approximately constant regardless of the number of processors. The goal of this test is to find the smallest workload to be given to each unit ensuring good performance even for high core numbers. We consider five different distributions of grid points per core, namely, 64^3 , 48^3 , 32^3 , 24^3 and 16^3 points per core. Table 2.9 shows the efficiencies obtained in the different cases, for a core count going from 16 to 16384. The weak scaling efficiency is given as

$$E_{\text{weak}}^B(N) = \frac{t_B}{t_N} \times 100 \quad (\%), \quad (2.89)$$

where t_B is the amount of time to complete B work units with B processing elements (value taken as baseline), and t_N is the time to complete N of the same work units with N processing elements. Usually, the time of a single core is taken as baseline, but in this study we consider $B = 16$,

Table 2.10. Strong scalability test from 16 to 16384 processing units. Workloads A and B consist of 16.8 and 537 millions of grid points, respectively.

N_{proc}	# grid/proc (A)	E_{strong}^{16}	# grid/proc (B)	E_{strong}^{512}
16	$256 \times 32 \times 128$	100	—	—
32	$128 \times 32 \times 128$	99.2	—	—
64	$128 \times 32 \times 64$	98.9	—	—
128	$64 \times 32 \times 64$	98.2	—	—
256	$64 \times 32 \times 32$	97.5	—	—
512	$32 \times 32 \times 32$	95.1	$256 \times 32 \times 128$	100
1024	—	93.6	$128 \times 32 \times 128$	98.4
2048	—	92.4	$128 \times 32 \times 64$	97.2
4096	—	90.1	$64 \times 32 \times 64$	95.5
8192	—	88.5	$64 \times 32 \times 32$	93.1
16384	—	85.4	$32 \times 32 \times 32$	89.8

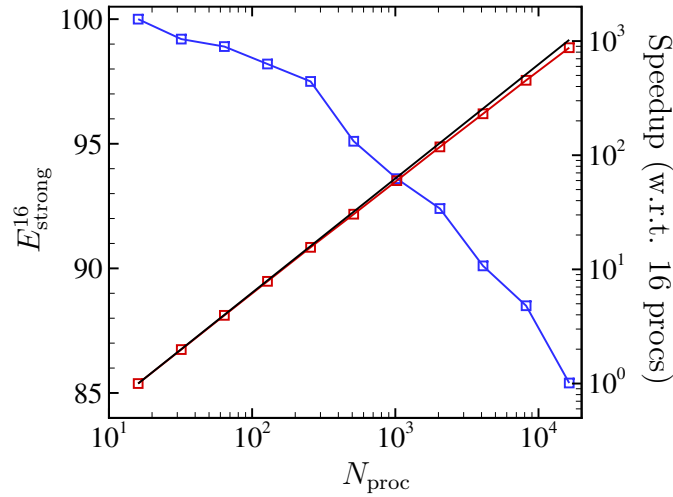


Figure 2.13. strong scalability efficiency (left y -axis) and speedup normalized with respect to 16 cores (right y -axis) as a function of the number of processing units. —: E_{strong}^{16} , —: ideal speedup, — actual speedup.

that is, the smallest possible allocation allowed on Turing. As shown in figure 2.12, very good overall efficiencies are obtained and the speedup is close to the ideal one. Using work units of 24^3 or less, important efficiency drops are observed, hence we will consider 32^3 as the minimal number of grid points to be assigned per core. One should note that, by disabling the few collective communications needed in the code (as, for instance, to compute the forcing term for the channel flow configuration), the performance degradation decreases and a minimum efficiency of 95% is reached for work units $\geq 32^3$ (figures not shown).

In the strong scalability, the problem size (workload) is fixed and the number of processing elements is increased (the problem is said to be CPU-bounded). The goal is to find a compromise that allows the computation to complete in a reasonable amount of time, without wasting much time for the parallel overhead due to the increase of communications. This test is particularly severe because the weight of the communications rapidly increase whereas the total work unit does not change.

Table 2.11. Riemann problem data for the dense-gas shock tube.

Case	ρ_l	u_l	p_l	Γ_l	ρ_r	u_r	p_r	Γ_r
DG1	1.818	-0.5	0.1	0.679	0.1	0.5	0.1	0.679
DG2	0.879	0	1.09	-0.031	0.562	0	0.885	-4.016×10^{-2}

The strong scaling efficiency, computed as

$$E_{\text{strong}} = \frac{Bt_B}{Nt_N} \times 100 \quad (\%), \quad (2.90)$$

is shown in table 2.10 and figure 2.13. The smallest work unit is chosen on the basis of the weak scalability (32^3). Being the total workload too big for small numbers of working units (the RAM per core being limited to 1GB), the study is performed for two different workloads (A and B in the table) and the efficiencies of workload A for $N_{\text{proc}} > 512$ are extrapolated assuming the same proportionality of workload B. The overall performance is shown to be quite satisfactory.

These results should be seen as the worst-case scenario for two reasons. First, both the scalability efficiencies are expected to be sensibly higher for the CHIT configuration due to the homogeneity of the (periodic) boundary conditions. Secondly, since tests were performed with a perfect gas model, higher efficiencies are expected if a dense gas is considered, due to the much higher computational costs of these models.

2.4 Preliminary validations

Different dense-gas shock tube simulations have been performed in order to compare the numerical strategies and validate the implementation of dense gas models in the CFD codes. In the following, we consider two classical configurations with a Van der Waals gas having $\gamma = 1.0125$.

These cases have been initially studied by Argrow (1996), and then used for validation from Guardone & Vigeveno (2002) and Cinnella (2006), which developed simplified linearization procedures in order to extend the Roe's scheme to real gas flow computations. The initial conditions for the two cases, named DG1 and DG2 (as in the references cited above), are reported in table 2.11. We run the 1D computations by using the 3D DynHoLab and MUSICA codes, and by setting periodicity conditions in two of the space directions. Case DG1 represents a Riemann problem where both the left and the right states lie within the $\Gamma > 0$ region. The solution is characterized by a left-running rarefaction wave, a middle contact discontinuity and a right-running compression wave. The left-running wave starts as a rarefaction fan in the positive Γ region; then, the transition line is crossed and it becomes a rarefaction shock for states with $\Gamma < 0$. For case DG2, both the initial left and right states lie within the negative Γ region. During the evolution, the fundamental derivative remains negative everywhere, and the flow behaviour is exactly opposite with respect to "classical" Riemann problems in common fluids. Specifically, the solution presents a left-running rarefaction shock, a middle contact discontinuity, and a right-running compression fan. The overall computed numerical solution is again in very good agreement with the reference, even if some small oscillations are generated near the rarefaction wave and the contact discontinuity.

Figure 2.14 shows the profiles of reduced density, pressure, fundamental derivative, velocity and Mach at $t^* = 0.15$ for case DG1, obtained for a 400-cells grid and both a DRP11 scheme ($r_{th} = 10^{-5}$) and a DNC9 scheme ($k_2 = 1$). Results are compared with those of Cinnella (2006). Both the solutions are in good agreement with the reference. Similar results are obtained for case DG2 (figure 2.15, $t^* = 0.45$). The numerical damping introduced by the Jameson sensor is much lower

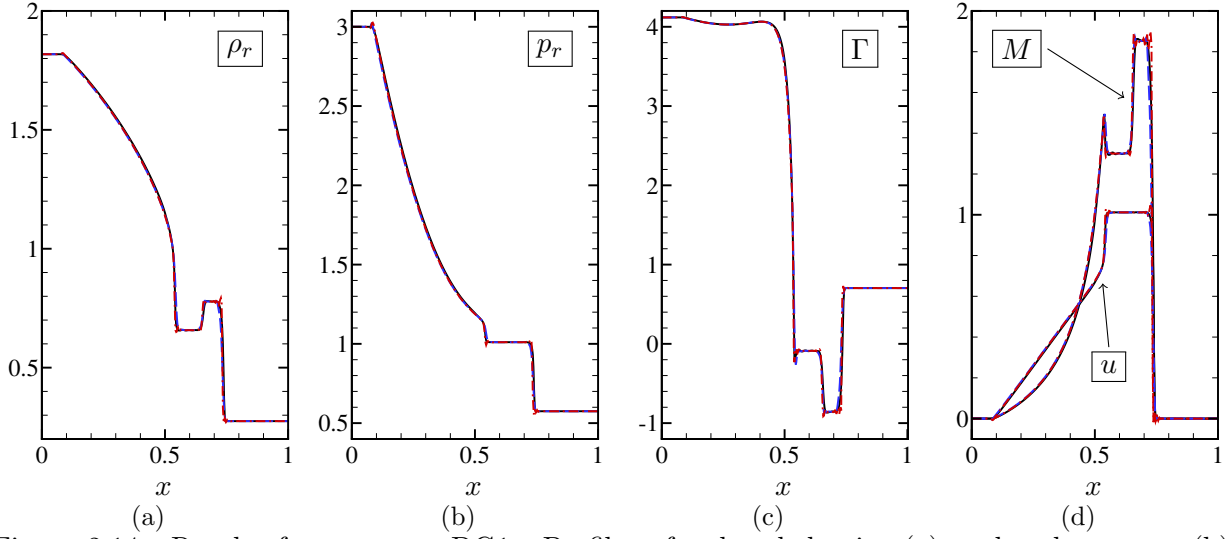


Figure 2.14. Results for test case DG1. Profiles of reduced density (a), reduced pressure (b), fundamental derivative (c), velocity and Mach number (d). Grid: 400 cells, $t^* = 0.15$. ---: DRP11 ($r_{th} = 10^{-5}$); -.-: DNC9 ($k_2 = 1$); —: Cinnella (2006).

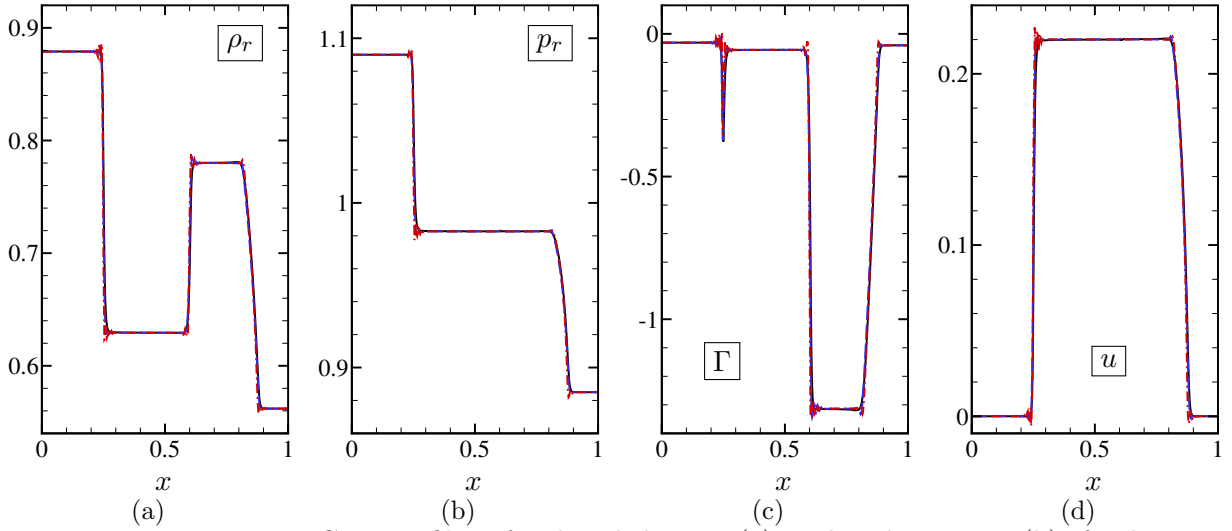


Figure 2.15. Test case DG2. Profiles of reduced density (a), reduced pressure (b), fundamental derivative (c) and velocity (d). Grid: 400 cells, $t^* = 0.45$. ---: DRP11 ($r_{th} = 10^{-5}$); -.-: DNC9 ($k_2 = 1$); —: Cinnella (2006).

with respect to that of the low-order filter of Bogey-Bailly, resulting in a higher oscillatory profile. The different behaviour of the two approaches relies essentially on the different definitions of the shock sensors (equations (2.83) and (2.77), respectively).

One should consider that shock tubes are severe test cases in which the capability of numerical schemes to appropriately resolve strong discontinuities is tested. In the following, hence, we retain the less dissipative DNC9 for the computation of CHIT decay, characterized by the presence of shocklets, i.e. weak, highly unsteady shock waves. For channel flow computations, instead, we retain the DRP11 scheme without any shock correction term, which is slightly less costly. We have verified for some cases that DNC9 produces virtually identical solutions.

Chapter Summary

The governing equations, the numerical methods and the CFD codes considered in this work have been presented.

- Governing equations:
 - Several thermodynamic models are considered in order to study dense gases, namely, the Van der Waals, the Martin–Hou and the Span–Wagner equations of state. The Chung–Lee laws are used to model the dense gas transport properties.
 - The analysis focuses on the perfluorocarbon PP11; other dense fluids considered are the siloxanes D5 and D6 and the refrigerants R134a and R245fa.
- Numerical methods:
 - Centered fluxes approximated by means of DNC and DRP high-order schemes
 - Numerical stabilization performed by means of filtering methods build similarly to centered fluxes
- CFD codes:
 - DynHoLab: multipurpose, flexible and modular code, used to perform CHIT computations
 - MUSICA: dedicated solver for wall-bounded flows, used for TCF simulations
 - Implementation of dense-gas routines and analysis of MPI scalability capabilities for both codes
 - Preliminary validations by means of reference dense-gas shock-tube cases.

3 Decay of dense-gas inviscid compressible homogeneous isotropic turbulence

Contents

3.1	Definitions	65
3.2	Initial and boundary conditions	67
3.3	Assessment of the numerical strategy	68
3.4	Results	73
3.4.1	Influence of the initial compressibility ratio	73
3.4.2	Influence of the initial peak wavenumber	74
3.4.3	Influence of the specific heat ratio	75
3.4.4	Dense gas simulations	78

The present chapter aims at investigating the large-scale dynamics of compressible homogeneous isotropic turbulence in presence of dense gas effects. Section 3.1 provides some useful classical definitions largely used hereafter. Details of the numerical setup (initial and boundary conditions) adopted for the CHIT simulations are provided in section 3.2. The flow model is based on the compressible Euler equations, whose validity for large-scale dynamics is discussed in section 3.3. In addition, we also discuss the validity of the inviscid assumption by comparison with viscous results at various Reynolds numbers. A sensitivity study to the initial conditions, and specifically to the initial compressibility ratio and initial peak wavenumber, has been conducted in the case of a perfect gas and is presented in sections 3.4.1 and 3.4.2. Dense gases are characterized by values of the specific heat ratio closer to unity than diatomic gases like air or triatomic gases like carbon dioxide (see, e.g., [Harinck et al., 2009](#)). It is useful to recall that, for gases with γ close to one, the specific heat coefficients tend to infinity (this is easily seen, e.g., for calorically perfect gases); hence, isentropic transformations are also approximately isothermal. To the author’s knowledge, all of the results about CHIT available in the literature up to now have been obtained for air, modelled as a perfect gas with $\gamma = 1.4$. Since changing the specific heat ratio has an impact on the coupling of the kinematic and thermodynamic fields, we first perform a parametric investigation of the effect of γ on perfect-gas CHIT simulations. Specifically, we generate reference results for $\gamma = 1.0125$, that is a value representative of the PP11 gas of interest here; Results are discussed in section 3.4.3. In section 3.4.4, dense gas inviscid CHIT at various initial turbulent Mach numbers is investigated by using the VDW model, and the results are compared with those of a PFG characterized by the same heat ratio.

The simulations discussed in this chapter have been published in [Sciacovelli et al. \(2016a\)](#).

3.1 Definitions

In the following, we recall some useful relations for the analysis of compressible homogeneous isotropic turbulence. Since the mean velocity field is zero, we define the turbulent fluctuating velocity as $u' = u = \langle u_i^2/3 \rangle^{1/2}$, where the operator $\langle \bullet \rangle$ refers to a volume average over the computational domain at a fixed time instant and the index $i = 1, 2, 3$ represents the three Cartesian

coordinates. The root-mean-square (r.m.s.) values are computed as $(\bullet)_{\text{rms}} = \sqrt{\langle (\bullet)^2 - \langle \bullet \rangle^2 \rangle}$, where (\bullet) is a generic fluctuating quantity. The integral length scale L_I is defined as:

$$L_I = \frac{3\pi}{4} \frac{\int_0^\infty E(k)/k \, dk}{\int_0^\infty E(k) \, dk} \quad (3.1)$$

where $k = \|\mathbf{k}\|$ is the wavenumber and $E(k)$ is the spectrum of the turbulent velocity u_i , integrated over shells of radius k . The Taylor microscale λ_f is defined as in [Hinze \(1975\)](#)

$$\lambda_f = \frac{u'^2}{\left\langle \left(\frac{\partial u_1}{\partial x_1} \right)^2 \right\rangle}. \quad (3.2)$$

According to [Jiménez *et al.* \(1993\)](#), the Taylor microscale can be computed directly from integral quantities, by using the relation:

$$\lambda_f^2 = \frac{5K}{\Omega}, \quad (3.3)$$

where $K = \int_0^\infty E(k) \, dk$ is the integrated energy, and $\Omega = \int_0^\infty k^2 E(k) \, dk$ is the enstrophy. The turbulent Mach number M_t and the root-mean-square Mach number M_{rms} are defined as:

$$M_t = \frac{\sqrt{\langle u_i^2 \rangle}}{\langle c \rangle}, \quad M_{\text{rms}} = \langle M_{\text{loc}}^2 \rangle^{1/2} = \sqrt{\left\langle \frac{u_i^2}{c^2} \right\rangle}, \quad (3.4)$$

In the definition of M_{rms} in equation (3.4) it is assumed $\langle M_{\text{loc}} \rangle = 0$ since the mean flow is zero and only the fluctuating components of the kinetic energy are computed.

In the spectral space, the k -th harmonic of the turbulent velocity $\hat{\mathbf{u}}(k)$ can be properly decomposed in a solenoidal component, $\hat{\mathbf{u}}^S(k)$, and a dilatational component, $\hat{\mathbf{u}}^D(k)$. The latter is computed as $\hat{\mathbf{u}}^D = [\mathbf{k} \cdot \hat{\mathbf{u}}] \mathbf{k}/k^2$, whereas the former is $\hat{\mathbf{u}}^S = \hat{\mathbf{u}} - \hat{\mathbf{u}}^D$. Considering a discrete representation of the spectrum over N uniformly spaced grid points, the total and compressible kinetic energies K and K^D are computed as follows:

$$K = \frac{1}{2} \sum_{k=1}^{N/2} E(k) n_k, \quad K^D = \frac{1}{2} \sum_{k=1}^{N/2} E^D(k) n_k, \quad (3.5)$$

where n_k is the number of Fourier modes in the k -th bin, satisfying $n_k = \sum_{k-1/2 < \|\mathbf{k}\| \leq k+1/2} 1$. The spectra of the total kinetic energy and its dilatational component are computed as, respectively:

$$E(k) = \frac{1}{2} \sum_{k-1/2 < \|\mathbf{k}\| \leq k+1/2} \|\hat{\mathbf{u}}(k)\|^2 / n(k), \quad E^D(k) = \frac{1}{2} \sum_{k-1/2 < \|\mathbf{k}\| \leq k+1/2} \|\hat{\mathbf{u}}^D(k)\|^2 / n(k), \quad (3.6)$$

Finally, the compressibility ratio χ is defined as $\chi = K^D/K$.

The skewness and flatness factors of the resolved velocity gradients are defined as the third and fourth moment of the fluctuating velocity gradient, namely

$$S_n := \left\langle \left(\frac{\partial u}{\partial x} \right)^n \right\rangle / \left\langle \left(\frac{\partial u}{\partial x} \right)^2 \right\rangle^{n/2}, \quad (3.7)$$

with $n = 3$ and $n = 4$, respectively. These quantities are used in order to describe the characteristics of the flow and to quantify turbulence (since in compressible isotropic turbulence, the non-Gaussian

nature of the skewness velocity derivative determines the dissipation rate, as stated in [Mansour & Wray, 1994](#)). [Sreenivasan & Antonia \(1997\)](#) experimentally showed that the skewness value slightly increases with Re_λ , but it is approximately -0.5 for $10 < Re_\lambda < 800$.

3.2 Initial and boundary conditions

The CHIT decay problem is solved on a cubic computational domain with extension $[0, 2\pi]^3$. Periodic boundary conditions are imposed in the three Cartesian directions. The issue of the initial conditions for compressible isotropic turbulence has been addressed by various authors ([Blaisdell *et al.*, 1993](#); [Ristorcelli & Blaisdell, 1997](#); [Samtaney *et al.*, 2001](#)). In general, the shape of the initial three-dimensional spectrum and the root-mean-square level of each flow variable must be provided. Different spectra can be assigned to the solenoidal and dilatational components. The main difference between an incompressible and compressible initialization is the presence of an intrinsic velocity scale for the latter, which is related to the speed of sound. The initial r.m.s. velocity u_{rms} is defined by prescribing the turbulent Mach number ($u_{\text{rms}} = M_t \langle c \rangle$, where $\langle c \rangle$ is the prescribed average speed of sound). Temperature and pressure fluctuations are specified in accordance with the velocity fluctuations. Several simplifying hypotheses are usually made in the compressible case ([Blaisdell *et al.*, 1993](#)): usually, the same spectrum shape is imposed for all the fluctuating fields; furthermore, fluctuations of the thermodynamic quantities are neglected. A review of initialization methods for CHIT can be found in [Samtaney *et al.* \(2001\)](#), as well as an analysis of their influence on the evolution of turbulent quantities. The latter authors show that for turbulent Mach numbers up to 0.5 (the maximum value considered in their analysis), initial conditions have moderate influence on the turbulence decay. Incompressible-like initialization leads to a fast transient in which the dilatational velocity component grows and becomes coherent with the solenoidal one, while fluctuations of thermodynamic quantities develop. This transient leads to higher values of the r.m.s. of the velocity divergence. Nevertheless, for PFG, neglecting fluctuations of the thermodynamic quantities in the initial conditions has been found to lead to weaker compressibility effects on the turbulence decay ([Blaisdell *et al.*, 1993](#)).

For PFG cases, the initialization is similar to the one described in [Sarkar *et al.* \(1991\)](#) and [Pirozzoli & Grasso \(2004\)](#). In the case of dense gases that use a complex EoS, additional assumptions are required. Since the thermodynamic variables are non-linearly related, contrary to the perfect gas case it is not possible to assume a direct proportionality between density (or temperature) and dilatational velocity fluctuations. In all of the following PFG and Dense Gas (DG) simulations, we have imposed an initial velocity spectrum of the Passot-Pouquet type ([Passot & Pouquet, 1987](#)):

$$E(k) = Ak^4 \exp \left[-2 \left(\frac{k}{k_0} \right)^2 \right] \quad (3.8)$$

where k_0 is the initial peak wavenumber and A is a constant that depends on the initial amount of kinetic energy. For small values of k_0 , this distribution associates most of the energy to the largest scales and practically none to the smallest ones. As a consequence, the large-scale dynamics (which is of interest here) is enhanced, while the impact of the small scales (which are not meaningful in an inviscid simulation) is reduced.

To ensure fair comparisons between perfect and dense gas simulations, fluctuations of the thermodynamic quantities are set to zero, and the turbulent velocity field is assumed to be purely solenoidal in all of the following simulations. With this choice, turbulent scales set at the beginning of the simulation can be controlled accurately. The expression for the initial turbulent kinetic energy spectrum is used to compute analytically the initial turbulent kinetic energy K_0 , the initial

enstrophy Ω_0 , the initial integral length scale L_I and the initial large-eddy turnover time τ_{LE} :

$$K_0 = \frac{3A}{64}\sqrt{2\pi}k_0^5, \quad \Omega_0 = \frac{15A}{256}\sqrt{2\pi}k_0^7, \quad L_I = \frac{\sqrt{2\pi}}{k_0}, \quad \tau = \sqrt{\frac{32}{A}}(2\pi)^{1/4}k_0^{-7/2}. \quad (3.9)$$

3.3 Assessment of the numerical strategy

The numerical method used in this work is first assessed versus results available in the literature for inviscid CHIT of perfect gas. Results provided by the DNC9 scheme are compared to those obtained by Garnier *et al.* (1999), who studied the capability of various shock-capturing schemes, including Jameson's (Jameson *et al.*, 1981), TVD-MUSCL (Van Leer, 1979) and ENO (Shu & Osher, 1989; Shu, 1990; Liu *et al.*, 1994), to behave as implicit subgrid scale models for several schemes. For the sake of comparison, we also run computations with the classical lower-order scheme by Jameson available in our code. Computational grids made of 64^3 and 128^3 cells have been used, and all of the results are expressed in terms of the non-dimensional time of Garnier *et al.* (1999) based on a

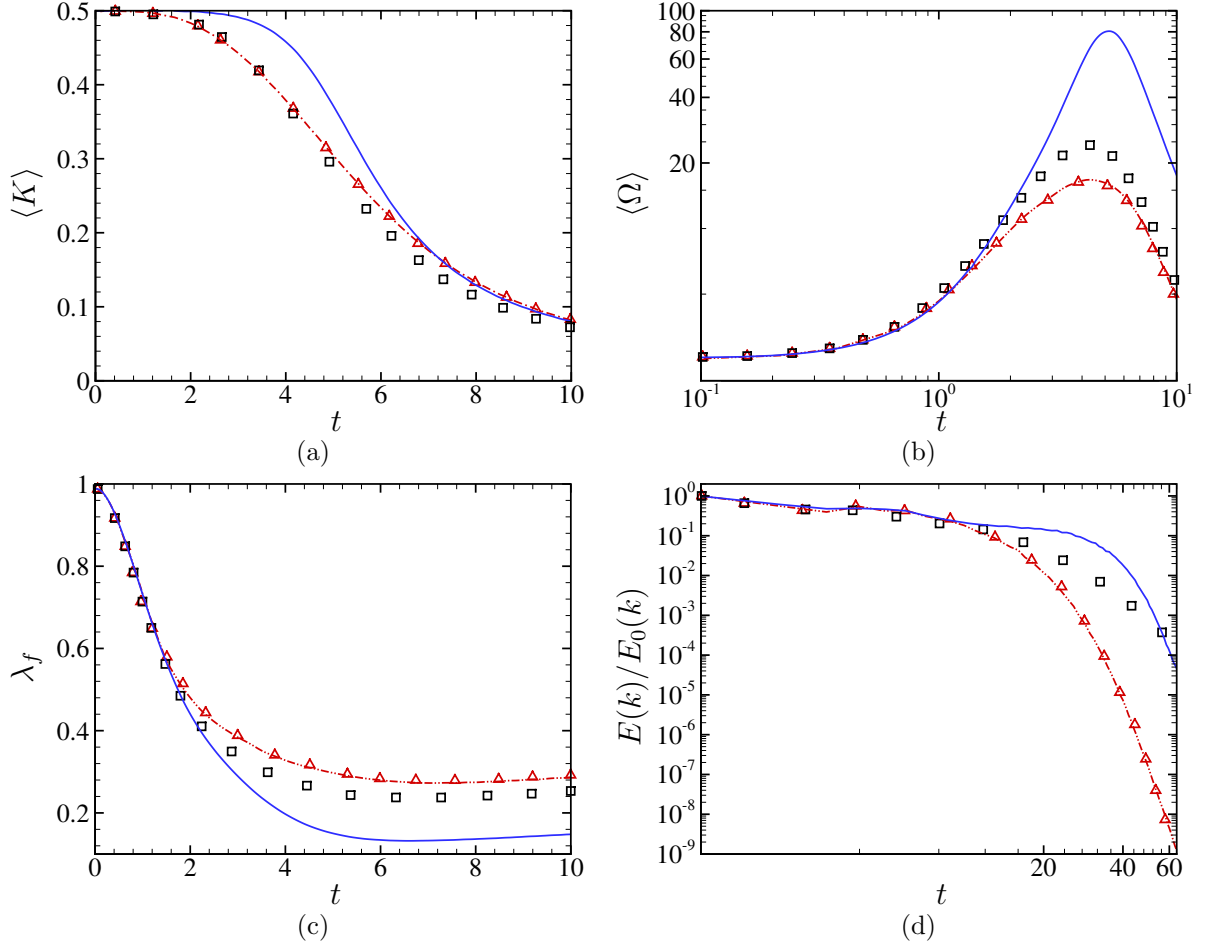


Figure 3.1. Comparison between the present results for CHIT decay at $M_{t_0} = 0.2$ and $\chi_0 = 0$ using the 9th-order scheme and Jameson's second-order scheme and those of Garnier *et al.* (1999) based on a 5th-order modified ENO scheme (MENO) and Jameson's schemes. Time histories of the turbulent kinetic energy (a), enstrophy (b), pseudo-Taylor microscale (c), and spectrum of the turbulent kinetic energy at $t = 10$ (d). \triangle : Garnier et al. - Jameson; \square : Garnier et al. - MENO; $-\cdot-\cdot-$: present - Jameson; $—$: present - DNC9.

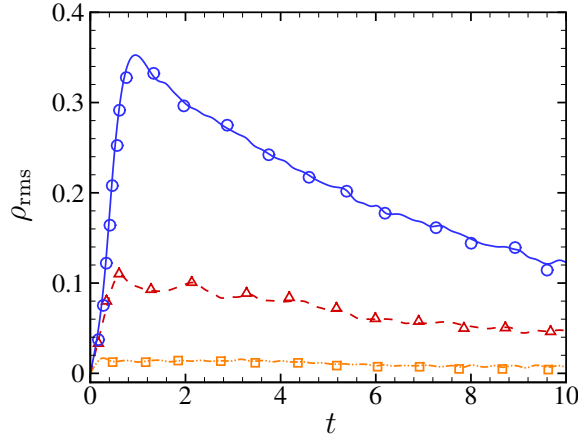


Figure 3.2. Comparison of the present results for a 9th-order accurate scheme with those provided by Garnier *et al.* (1999) using a 4th-order ENO scheme, for different choices of the initial conditions. Lines denote the present results, symbols results from the reference. —: $M_{t_0} = 0.2$, $\chi_0 = 0$; - - - : $M_{t_0} = 0.5$, $\chi_0 = 0$; —: $M_{t_0} = 1$, $\chi_0 = 0$.

unit length and the initial r.m.s. velocity.

Figure 3.1 shows results obtained for case 1 of Garnier *et al.* (1999), corresponding to $M_{t_0} = 0.2$ and $\chi_0 = 0$. For comparison, we show in figure 3.1 the time histories of kinetic energy, enstrophy, and pseudo-Taylor microscale λ_f (Porter *et al.*, 1994), as well as the kinetic energy spectrum at the non dimensional time $t = 10$. Note that the pseudo-Taylor microscale λ_f , defined in equation (3.3), should tend to zero in a purely inviscid simulation. Here, due to the numerical dissipation introduced by the scheme, it tends to a small but non-zero value. λ_f can be seen as a measure of the smallest scales resolved by a numerical method, and its limit value becomes smaller as the grid is refined or dissipation errors are reduced.

DNC9 scheme has very low phase and dissipation errors. Far from flow discontinuities, its leading truncation error term is of the form $k_{10}\Delta x^9 \frac{\partial^{10} w}{\partial x^{10}}$, i.e. it is consistent with a tenth-order viscosity. Such viscosity term acts differently according to the wavenumber. It dissipates scales characterized by reduced wavenumbers of about 0.35π or higher, i.e. wavelengths that are discretized with less than 6 mesh points, leaving larger scales essentially unaffected. As one would expect, the 9th-order scheme improves the results dramatically not only with respect to the low-order scheme (which exhibits a very dissipative behaviour), but also with respect to a 5th-order accurate modified ENO scheme (MENO). We observe that: 1) the kinetic energy is preserved for longer times (figure 3.1a); 2) the enstrophy peak is shifted to the right and the maximum value is more than five times greater than the one obtained with Jameson’s scheme and more than 2.5 times the one provided by the MENO scheme (figure 3.1b); 3) the pseudo Taylor microscale is reduced by about a factor 6 for times greater than 4 (where the solution is dominated by the smaller scales) with respect to the low-order scheme, and more than a factor 2 with respect to the 5th-order scheme (figure 3.1c); 4) the cut-off in the kinetic energy spectrum is also moved toward wavenumbers that are closer to the grid aliasing limit (figure 3.1d). Finally, figure 3.2 reports the time evolution of the r.m.s. density values at various initial turbulent Mach numbers. Comparisons with the results provided by Garnier *et al.* (1999) for a ENO scheme match to within plotting accuracy.

The sensitivity of the present numerical simulations to mesh resolution has been assessed for both a perfect gas ($\gamma = 1.4$) and a VDW gas, at $M_{t_0} = 0.8$. For that purpose, we have considered four grids with number of cells equal to 64^3 , 128^3 , 256^3 , and 512^3 . The time histories of λ_f , ρ_{rms} and of Ω normalized with the initial enstrophy, as well as the kinetic energy spectrum and the probability distribution function of the velocity divergence at $t = 2.5$ are reported in figure 3.3 for the PFG

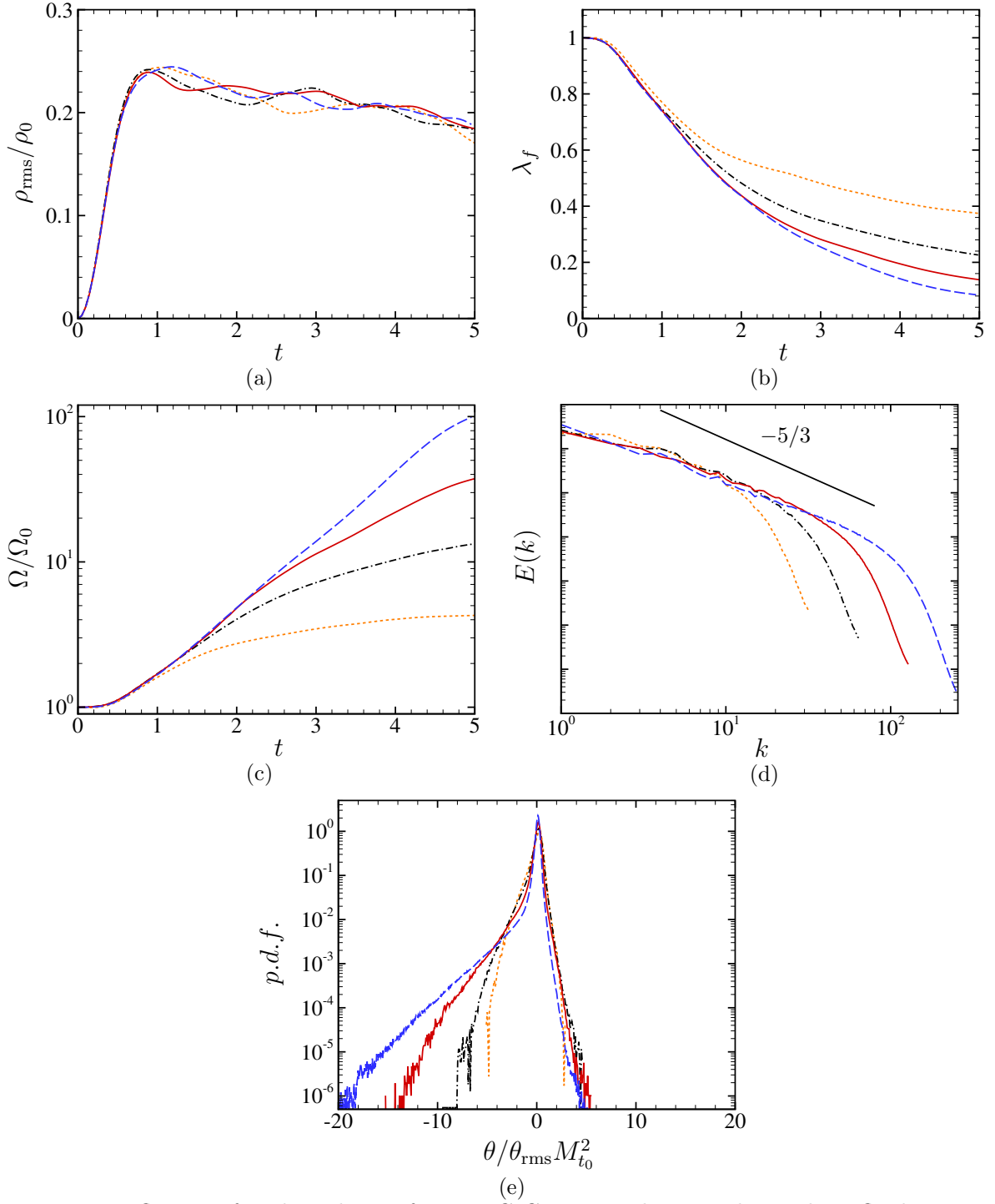


Figure 3.3. Influence of grid resolution for a PFG CHIT simulation. The working fluid is a perfect gas with $\gamma = 1.4$, and the initial turbulent Mach number is $M_{t_0} = 0.8$. Panels a-c show the time histories of the normalized r.m.s. density (a), the pseudo Taylor microscale (b) and the normalized enstrophy (c); panels d-e show the turbulent kinetic energy spectrum (d) and the p.d.f. of velocity divergence (e) at $t = 2.5$. \cdots : 64^3 ; $-\cdot-\cdot-$: 128^3 ; $—$: 256^3 ; $- - -$: 512^3 .

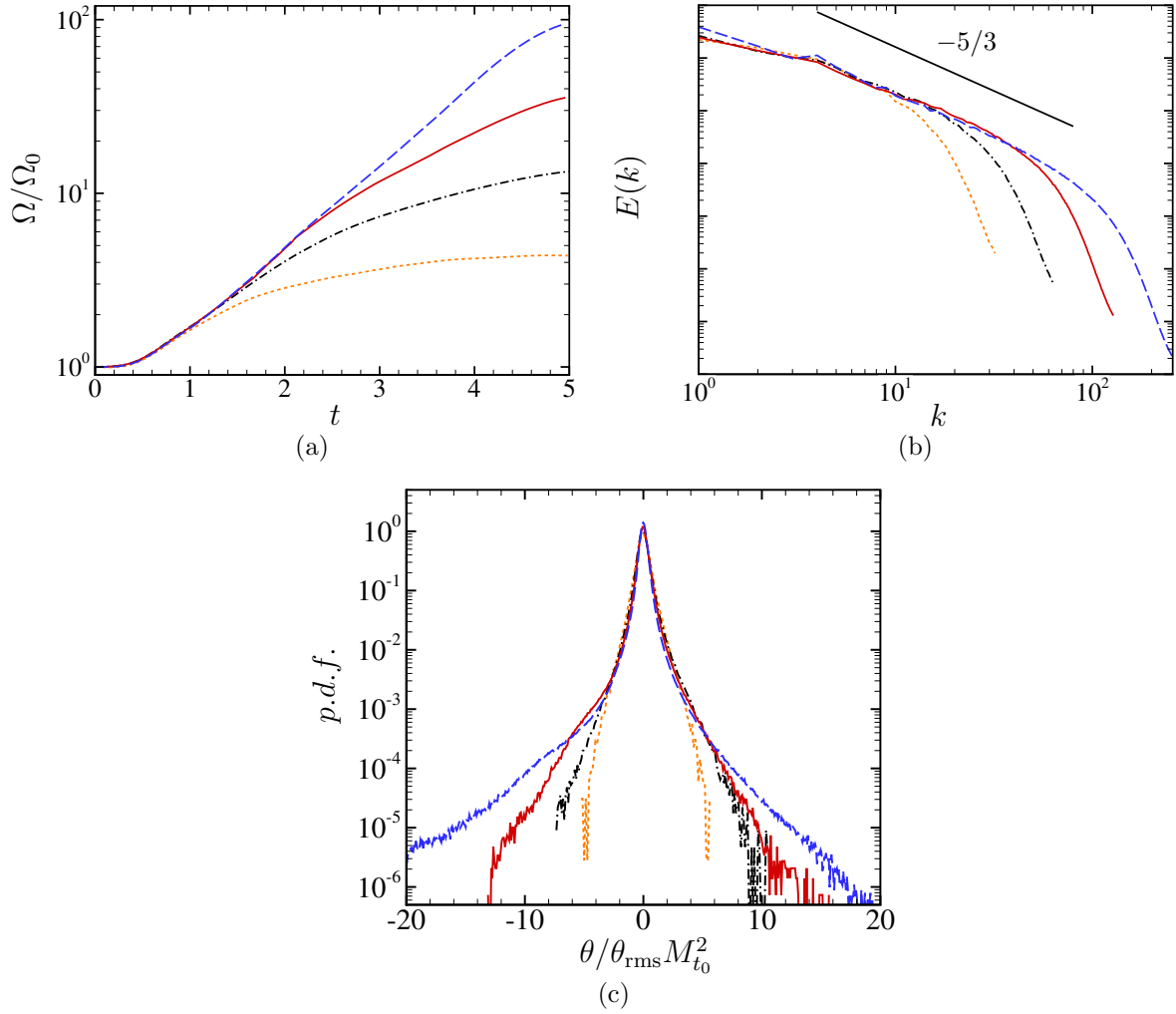


Figure 3.4. Influence of grid resolution for a DG CHIT simulation. Here, the working fluid is PP11, modelled as a polytropic VDW gas, and the initial turbulent Mach number is $M_{t_0}=0.8$. Panel a shows the time history of the normalized enstrophy; panels b-c show the turbulent kinetic energy spectrum (b) and the p.d.f. of velocity divergence (c) at $t = 2.5$. \cdots : 64^3 ; $---$: 128^3 ; $—$: 256^3 ; $- - -$: 512^3 .

case. The figure shows that ρ_{rms} is little affected by grid resolution and is well captured even on a 64^3 grid (panel a). The same is true for the average and r.m.s. of the other thermodynamic quantities. Differences measured between the two finest grids are found to be of the order of 1% or lower. Resolution has a stronger influence on the pseudo Taylor microscale (panel b), which is reduced by a factor of about 1.6 when halving the mesh size (Garnier *et al.*, 1999). We observe that the enstrophy should become unbounded within a finite time in a purely inviscid simulation and should exhibit a peak increasing with the Reynolds number in viscous simulations. In the present calculations, due to numerical dissipation, the enstrophy peaks at nondimensional time of the order of 5. Due to the creation of smaller scales, its amplitude tends to double when doubling the mesh (panel c). Note that the solutions on the two finest grids are superposed up to $t = 2$ and tend to depart from each other at later times. At time $t = 2$, a significant inertial range has not developed yet, and most of the energy is still contained in scales much larger than the grid size. At time $t = 2.5$ (considered for the analyses discussed later), a well-identified inertial range is observed already on the 128^3 grid (see panel d), and enstrophy values computed on the two finest

grids differ of about 5%. The inertial range extends approximately over more than a decade for a grid resolution of 256^3 , and a bit less than two decades for 512^3 (panel d). The exponential roll-off of the spectra at the end of the inertial range is due to the numerical viscosity cutoff, and moves toward higher wavenumbers as grid resolution increases. The observed cutoff wavenumber is rather close to the grid resolvability limit (four points per wavelength), in agreement with the spectral properties of the current numerical method.

In the aim of assessing the influence of the numerical cutoff on local turbulence properties, the p.d.f. of the velocity divergence $\theta/\theta_{\text{rms}}$ normalized with respect to $M_{t_0}^2$ at $t = 2.5$ is also reported (panel e). Grid resolution modifies mainly the tails of the distribution, which are however characterized by rather low probability values (less than 10^{-3}). This leads to some differences between the various grids in terms of integrated probabilities, like the volume fractions occupied by flow structures with given divergence levels. Nevertheless, the order of magnitude are well conserved, and the associated percentages are reliable at least to one significant digit or more, according to the considered divergence level. Similar trends are observed for different initial turbulent Mach numbers (not reported) and for VDW simulations (only results for the more sensitive quantities on the two finest grids are shown in figure 3.4). The p.d.f. exhibits a shape different than the one observed for perfect gas, independently of the grid. The physical mechanism leading to this different behaviour is discussed in the next section. The 256^3 grid leads to reasonably small numerical errors both on the mean and rms properties, as well as an adequate description of the inertial range over more than a decade at the non-dimensional time of interest ($t = 2.5$), and it has been selected for the parametric study discussed in later sections.

As pointed out in the introduction, due to the high-order dissipation of the scheme, the present Euler-based simulations can be considered as a form of implicit large eddy simulation of high Reynolds number CHIT. To further assess the numerical model, we have also carried out a series of Navier-Stokes-based simulations whereby the viscous fluxes are discretized by standard fourth-order central differences. Comparisons were first made for PFG CHIT at $M_{t_0} = 0.5$ and $Re_\lambda = 175, 1750$ and 17500 (Re_λ being based on the initial Taylor microscale); all simulations were carried out on the 256^3 grid (and setting $k_0 = 2$ and $\chi_0 = 0$). For the Euler-based simulation, the effective Reynolds number Re_λ^{eff} is estimated by using the numerical viscosity of the scheme. In particular, the numerical viscosity associated with the smallest wavenumbers is $\mathcal{O}(10^{-5})$ and $Re_\lambda^{\text{eff}} = \mathcal{O}(10^4)$, which is indeed of the same order of the highest Re_λ considered in the Navier-Stokes-based simulations. We observe that at $t = 0$, the smallest wavelength that can be resolved on the given grid, $k_{\text{max}}\eta$ (η being the Kolmogorov lengthscale), is equal to 4.8, 1.5, and 0.48, respectively for the three Re_λ . Hence, for the lowest Reynolds number case, all scales are well resolved up to the Kolmogorov one. The other viscous simulations do not resolve all of the scales, and represent instead implicit large eddy simulations, with the numerical dissipation acting as a subgrid model. Figure 3.5 compares the time histories of the Euler-based and Navier-Stokes-based results in terms of ρ_{rms} , c_{rms} , kinetic energy and θ_{rms} . The figure shows that, for the highest Reynolds number cases, the initial stages of the decay are well represented by inviscid simulations. At $t = 2.5$, the selected grid resolves accurately large and medium scales up to a cutoff wavenumber well within the inertial range for the high- Re_λ cases. This is clearly shown in figure 3.6 (panel a), where we compare the kinetic energy spectra. As the Reynolds number increases, the inertial range becomes larger and it extends up to a wavenumber k_v of about 10 for $Re_\lambda = 1750$ and about 20 for $Re_\lambda = 17500$ (for $Re_\lambda = 175$ there is no scale separation and the inertial range is virtually non existent). We observe that the inviscid model captures essentially the same energy spectrum as the viscous one at $Re_\lambda = 17500$, the effective Reynolds number being of the same order. The comparison of the p.d.f. of the velocity divergence (panel b) shows that the Euler-based and the Navier-Stokes-based results are almost superposed for all cases (except for the lowest Re_λ , for which the probability content of the tails is smaller; however, even in this unfavourable case the overall shape of the p.d.f. remains similar).

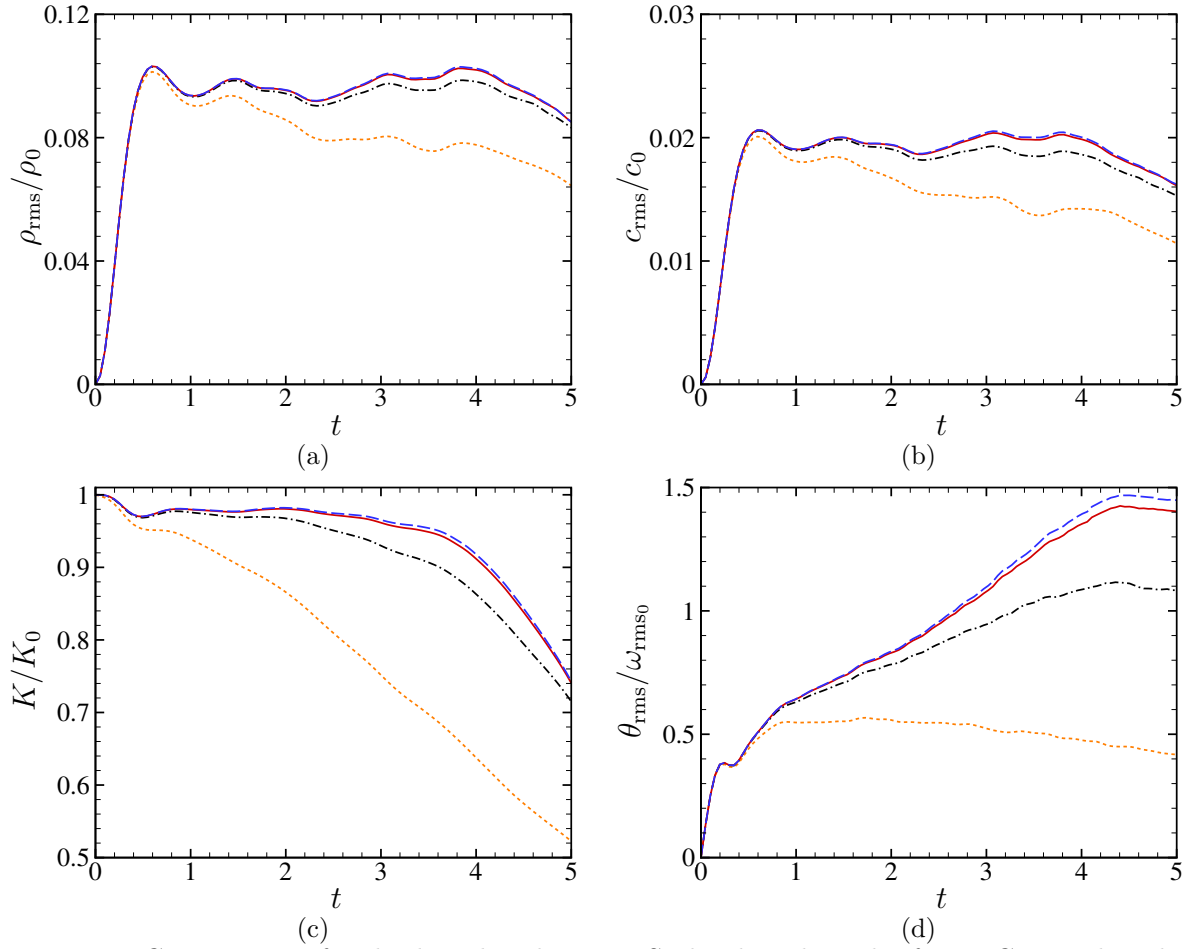


Figure 3.5. Comparison of Euler-based and Navier-Stokes-based results for PFG. Panels a-d show the time histories of the normalized r.m.s. density (a), the normalized r.m.s. sound speed (b), the turbulent kinetic energy (c) and the normalized r.m.s. velocity divergence (d) at various Reynolds numbers. \cdots : $Re_\lambda = 175$; $-\cdot-\cdot-$: $Re_\lambda = 1750$; $—$: $Re_\lambda = 17500$; $- - -$: Euler.

Finally, the influence of the artificial dissipation coefficients k_2 and k_{10} on the turbulence decay has been investigated considering a 256^3 grid and $M_{t_0} = 0.8$ and $\chi_0 = 0$. Four different parameter combinations were considered (see table 3.1). Sample results are shown in figure 3.7. The evolutions of kinetic energy (panel a) and r.m.s. of the thermodynamic properties are essentially insensitive to k_2 and k_{10} . Small changes in the enstrophy time history (panel b) are observed for t greater than ≈ 3 . At $t = 2.5$, the turbulent kinetic energy spectrum (panel c) is slightly dependent on k_{10} at high wavenumbers, whereas it is found to be largely insensitive to k_2 . Finally, the p.d.f. of the normalized velocity divergence at the same time (panel d) shows that the coefficients have only a small influence on the tails of the distribution. The following compressible computations were carried out using $k_2 = 2$ and $k_{10} = \frac{1}{420}$.

3.4 Results

3.4.1 Influence of the initial compressibility ratio

The influence of the initial compressibility ratio χ_0 on the turbulent kinetic energy decay is here discussed. We study the influence of χ_0 for CHIT at $M_{t_0} = 0.5$ and $k_0 = 2$ considering a perfect

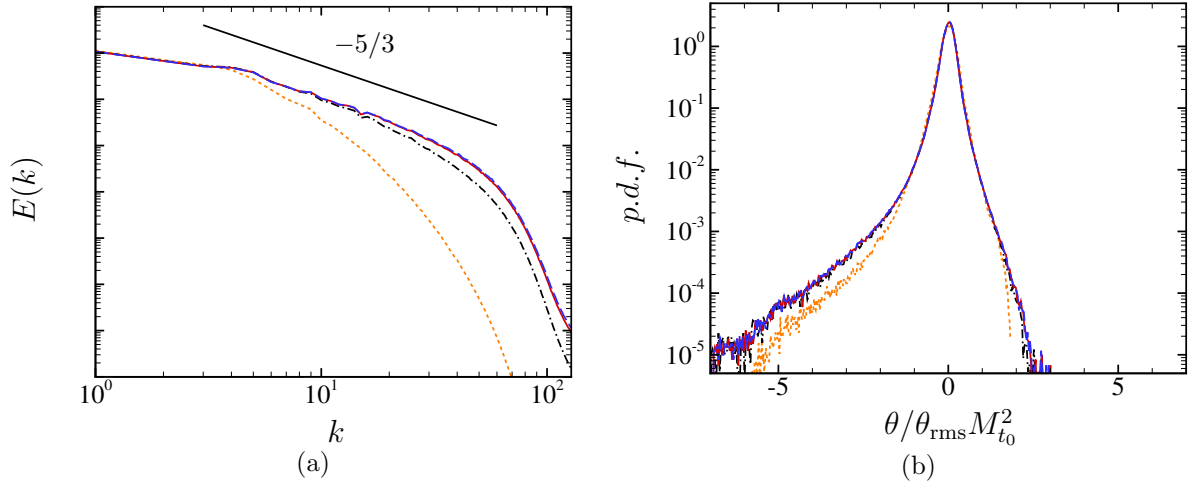


Figure 3.6. Comparison of Euler-based and Navier-Stokes-based results for PFG simulations. (a) Turbulent kinetic energy spectrum and (b) p.d.f. of the normalized velocity divergence evaluated at $t = 2.5$ at various Reynolds numbers. \cdots : $Re_\lambda = 175$; $-\cdots-$: $Re_\lambda = 1750$; $—$: $Re_\lambda = 17500$; $---$: Euler.

Table 3.1. Cases considered to study the influence of the artificial dissipation coefficients.

	k_2	k_{10}
case A	2	1/420
case B	3	1/630
case C	3	1/420
case D	4	1/420

gas with $\gamma = 1.4$. In particular, three values of χ_0 have been considered, namely 0, 0.1 and 0.2. In figure 3.8 we report the time evolution of ρ_{rms} , c_{rms} , and Ω/Ω_0 , as well as the p.d.f. of the local Mach number at $t = 2.5$. As discussed in [Blaisdell et al. \(1993\)](#), increasing the initial compressibility ratio leads to higher values of ρ_{rms} , c_{rms} (panels a and b) and velocity divergence. This leads to a slightly faster decay of the turbulent energy at the beginning of the simulation, due to the increased shock losses. The initial normalized enstrophy growth is therefore smaller with respect to the case $\chi_0 = 0$ (figure 3.8c). Nevertheless, at time 2.5, the p.d.f. of the local Mach number (figure 3.8d) is not significantly affected by χ_0 . In summary, even if the initial value of χ_0 has an influence on turbulence decay, the main effect of increasing χ_0 is to enhance compressibility effects, especially at the initial stages of the decay. Since our objective is to investigate how the compressible turbulence behaviour is modified by dense gases, we make the conservative choice of using $\chi_0 = 0$, since higher values of χ_0 tend to amplify the effects of interest.

3.4.2 Influence of the initial peak wavenumber

The influence of the initial peak wavenumber k_0 is now considered. Three values of k_0 are considered, namely 2, 4 and 8, for $M_{t_0} = 0.5$ and $\chi_0 = 0$. Figure 3.9 shows the time evolution of ρ_{rms} , θ_{rms} normalized by the initial r.m.s. of the vorticity, M_t , and the turbulent kinetic energy spectra at $t = 2.5$. The r.m.s. density is weakly affected by the peak wavenumber and increases slightly when using a smaller k_0 (panel a). The r.m.s. fluctuations of the velocity divergence also increase (panel b), due to the wider range of active scales. This leads to a different time evolution of the

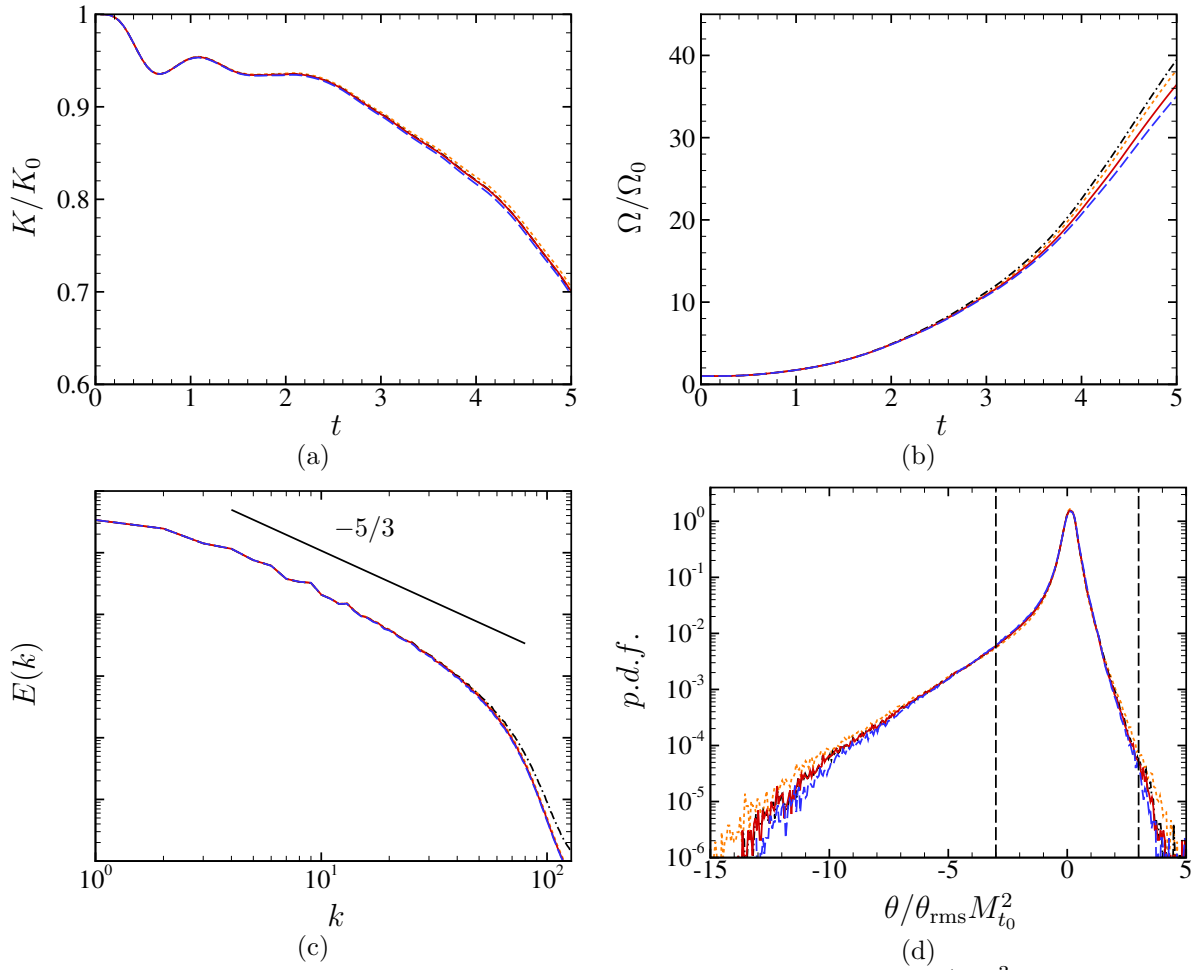


Figure 3.7. Influence of the artificial dissipation coefficients k_2 and k_{10} (256^3 grid, $M_{t_0} = 0.8$, perfect gas with $\gamma = 1.4$). Panels a-b show the time histories of the normalized turbulent kinetic energy (a), the normalized enstrophy (b). Panels c-d show the turbulent kinetic energy spectrum (c) and the p.d.f. of velocity divergence (d) at $t = 2.5$: case A; ----: case B; —: case C; -.-.-: case D.

turbulent Mach number (panel c), that exhibits a rather low decay rate during the first stages. At later times, the enhanced dilatational effects lead to higher losses and a quicker decay of turbulent kinetic energy (not reported for brevity). From the turbulent kinetic energy spectra (panel d) we observe that lower values of k_0 yield a wider inertial range. After $t = 5$, the decay is driven by the numerical dissipation and the turbulent kinetic energy exhibits a similar evolution for any choice of the initial peak wavenumber. In order to enhance the large scales motions that are of interest in this study, we have then used $k_0 = 2$ in all of the following simulations, thus concentrating about 99% of the initial energy at large scales (the ones that are well resolved on the grids used in the present study). As a consequence, the initial stages of the decay are practically not affected by numerical dissipation.

3.4.3 Influence of the specific heat ratio

We then run dense gas simulations using the VDW EoS with $\gamma = 1.0125$, and setting $k_0 = 2$ and $\chi_0 = 0$. In table 3.2 we report the different values of γ considered, as well as the values of the specific heat coefficients and fundamental derivative. Simulations were performed on the 256^3 grid

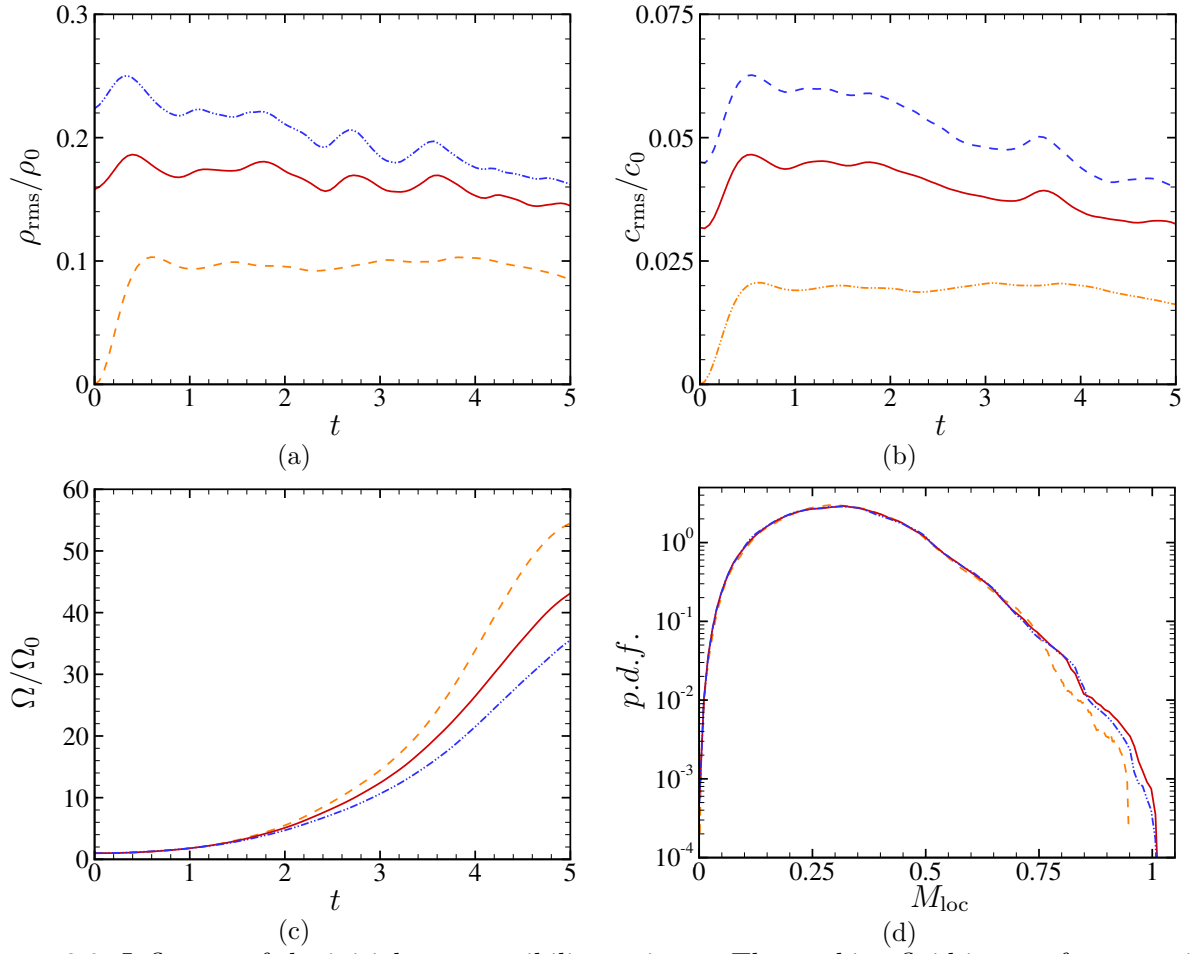


Figure 3.8. Influence of the initial compressibility ratio χ_0 . The working fluid is a perfect gas with $\gamma = 1.4$. Panels a-d show the time histories of the normalized r.m.s. density (a), normalized r.m.s. sound speed (b), time history of the normalized enstrophy (c), and p.d.f. of local Mach number at $t = 2.5$ (d). ---: $\chi_0 = 0$; —: $\chi_0 = 0.1$; - · - ·: $\chi_0 = 0.2$.

Table 3.2. PFG simulations: influence of the specific heat ratio. Values of the specific heat ratio (γ), specific heat coefficient at constant volume (c_v) and at constant pressure (c_p), and fundamental derivative of gas dynamics Γ .

Case	Gas	γ	c_v/R	c_p/R	Γ
G1	Monoatomic	1.6667	1.5	2.5	1.3335
G2	Diatomic	1.4	2.5	3.5	1.2
G3	Polyatomic, light gas (e.g., CO ₂)	1.289	3.46	4.46	1.1445
G4	Polyatomic, heavy gas (e.g., heavy fluorocarbon)	1.0125	80.0	81.0	1.00625

and assuming an initial turbulent Mach number $M_{t_0} = 0.8$.

Using dimensional analysis and momentum conservation, the pressure fluctuations can be related to the velocity fluctuations:

$$p_{\text{rms}} \sim \rho_0 u_{\text{rms}_0}^2 \sim \rho_0 M_{t_0}^2 c_0^2, \quad (3.10)$$

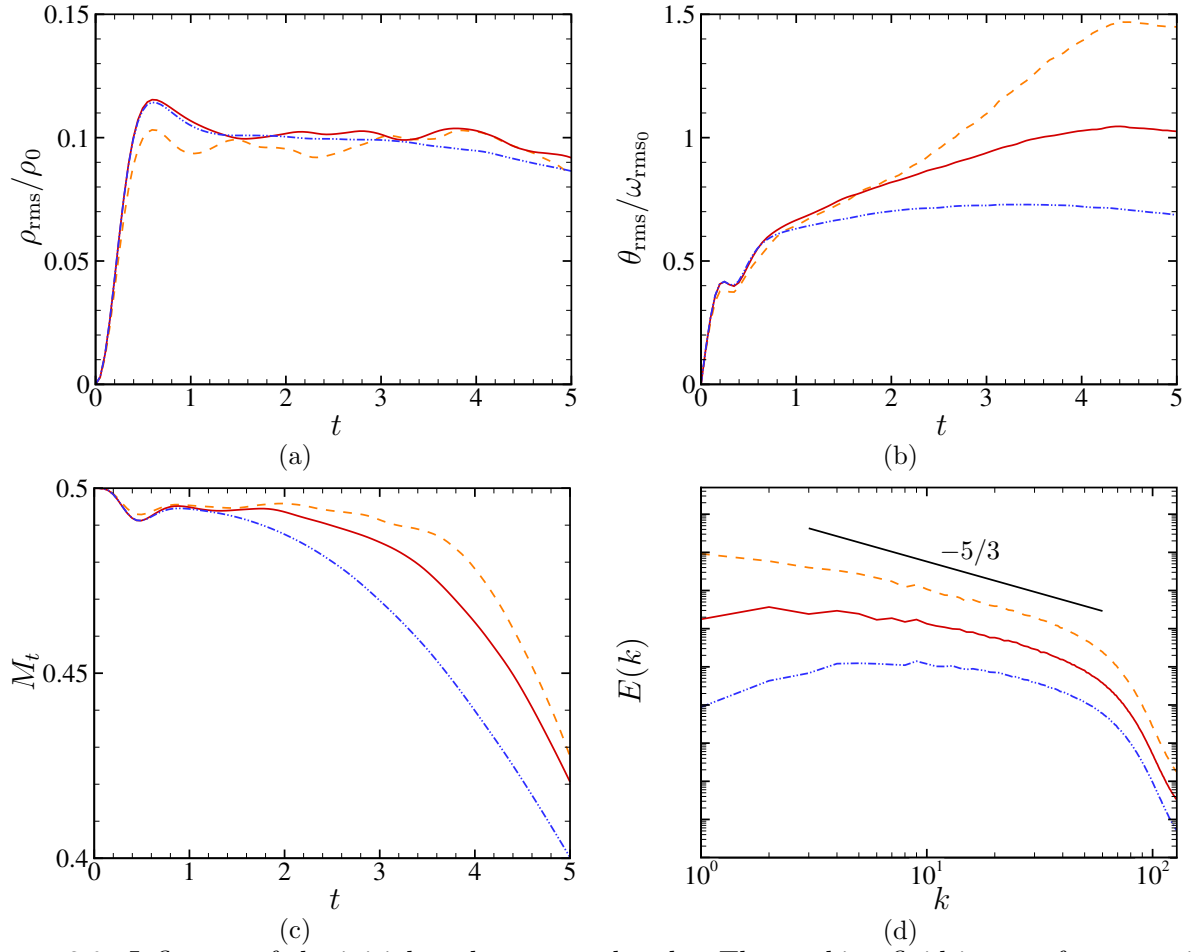


Figure 3.9. Influence of the initial peak wavenumber k_0 . The working fluid is a perfect gas with $\gamma = 1.4$. Panels a-d show the time histories of the normalized r.m.s. density (a), normalized r.m.s. velocity divergence (b), turbulent Mach number (c), and turbulent kinetic energy spectrum at $t = 2.5$ (d). ---: $k_0 = 2$; —: $k_0 = 4$; - · - ·: $k_0 = 8$.

hence:

$$\frac{p_{\text{rms}}}{p_0} \sim \gamma M_{t_0}^2. \quad (3.11)$$

On the other hand, the normalized density fluctuation is related to the normalized pressure fluctuations through the sound speed definition $\rho_{\text{rms}}/\rho_0 \sim p_{\text{rms}}/c_0^2$; hence using (3.11), one obtains

$$\frac{\rho_{\text{rms}}}{\rho_0} \sim M_{t_0}^2 \quad (3.12)$$

Recalling the definition of the fundamental derivative of gas dynamics in equation (1.1) and its expression with the PFG model, equation (1.2), one obtains:

$$\frac{c_{\text{rms}}}{c_0} \sim \frac{\rho_{\text{rms}}}{\rho_0} (\Gamma - 1) \sim \frac{\rho_{\text{rms}}}{\rho_0} \frac{\gamma - 1}{2} \sim \frac{\gamma - 1}{2} M_{t_0}^2 \quad (3.13)$$

The time evolution of the normalized root mean square of speed of sound, pressure and density at various γ are reported in figure 3.10, where p_{rms} and c_{rms} are rescaled according to equations (3.11) and (3.13). The results show that changing the specific heat ratio has a strong influence on c_{rms} , whose maximum value varies between 0.002 (for the low- γ case) and 0.84 (for the high- γ case).

Table 3.3. Volume fraction occupied by flow regions with different dilatation levels at time $t = 2.5$.

Case	$\theta/\theta_{\text{rms}}M_{t_0}^2$ (%)					
	$[-\infty, -2]$	$[-2, -1]$	$[-1, 0]$	$[0, 1]$	$[1, 2]$	$[2, +\infty]$
G1	1	5	38	53	3	0
G2	1	5	38	53	3	0
G3	1	5	38	53	3	0
G4	1	5	39	52	3	0

This is due to both direct and indirect effects. On the one hand, the speed of sound depends on $\sqrt{\gamma}$ for a perfect gas; on the other hand, lower values of γ correspond to higher values of the specific heats, and hence to smaller heating effects and lower values of the mean temperature. For the case of a polyatomic heavy gas (case G4 of table 3.2), characterized by high values of the specific heats, the mean sound speed remains roughly constant with time. The opposite behaviour is observed for monoatomic gases that are characterized by specific heats lower than air. Intermediate behaviours are observed for cases G2 and G3. The p_{rms} exhibits trends similar to c_{rms} , with higher fluctuations for case G4, which ρ_{rms} shows an opposite behavior, even though it is much less dependent on the value of γ .

The time evolution of M_t , K , ω_{rms} , and θ_{rms} , as well as the turbulent kinetic energy spectra and the p.d.f. of the local Mach number at $t = 2.5$ is reported in figure 3.11, at various γ . The figure shows that the vorticity fluctuations, the turbulent kinetic energy and its spectra are not affected by γ . The figure also shows that the probability of finding local Mach numbers greater than unity is greater for lighter gases.

To systematically quantify the effects of local compressibility, we classify the overall flow volume into six subregions, according to the local dilatation scaled by the initial turbulent Mach number, as done in Wang *et al.* (2012b) and Sciacovelli *et al.* (2016a):

$$\theta/\theta_{\text{rms}}M_{t_0}^2 \in \begin{cases} [-\infty, -2] & \text{Strong compressions} \\ [-2, -1] & \text{Moderate compressions} \\ [-1, 0] & \text{Weak compressions} \\ [0, 1] & \text{Weak expansions} \\ [1, 2] & \text{Moderate expansions} \\ [2, \infty] & \text{Strong expansions} \end{cases} \quad (3.14)$$

In table 3.3 we report the volume fractions conditioned on the local dilatation value. We observe that, independently of γ , weak expansions are more probable than compression ones (about 52% to 38%). On the contrary, moderate and strong compression regions are more likely to occur than expansion ones. However, overall weak compressions and expansions occupy more than 90% of the flow volume, and the probability of the occurrence of eddy shocklets (defined as regions for which $\theta/\theta_{\text{rms}}M_{t_0}^2 < -3$) exists, but it is rather small.

3.4.4 Dense gas simulations

This section presents a parametric study of the influence of dense gas effects on CHIT decay. We have considered the perfluoroperhydrophenanthrene that is assumed to obey the VDW EoS with $\gamma = 1.0125$. The results are compared to those of a perfect gas having the same specific heat ratio. Since the PFG and VDW models lead to different intrinsic scales (the sound speed being very different), it is not possible to set the same initial kinetic energy without changing

the thermodynamic conditions. Consequently, comparisons were performed by renormalizing the calculated quantities with respect to their initial values.

The initial thermodynamic state is reported in the $p - v$ plane (figure 3.12) for the VDW model; the initial thermodynamic conditions for both perfect and dense gas simulations are summarized

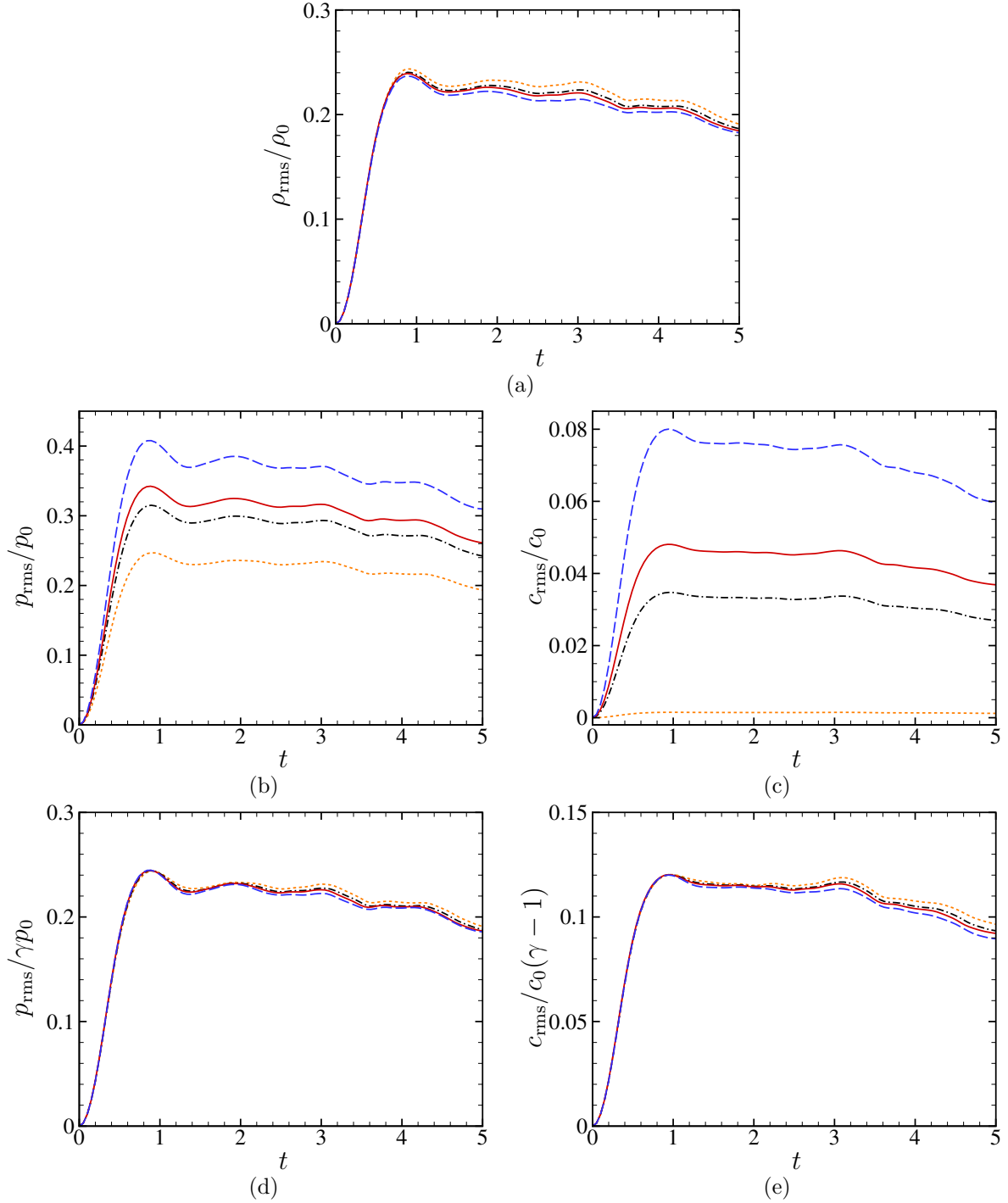


Figure 3.10. PFG simulations: influence of the specific heat ratio. Time evolution of the r.m.s. of the density (a), the pressure (b), the sound speed (c), and the rescaled values of p_{rms} (d) and c_{rms} (e) according to equations (3.13) and (3.11), respectively. \cdots : $\gamma = 1.0125$; $-\cdot-\cdot-$: $\gamma = 1.289$; $—$: $\gamma = 1.4$; $- - -$: $\gamma = 1.667$.

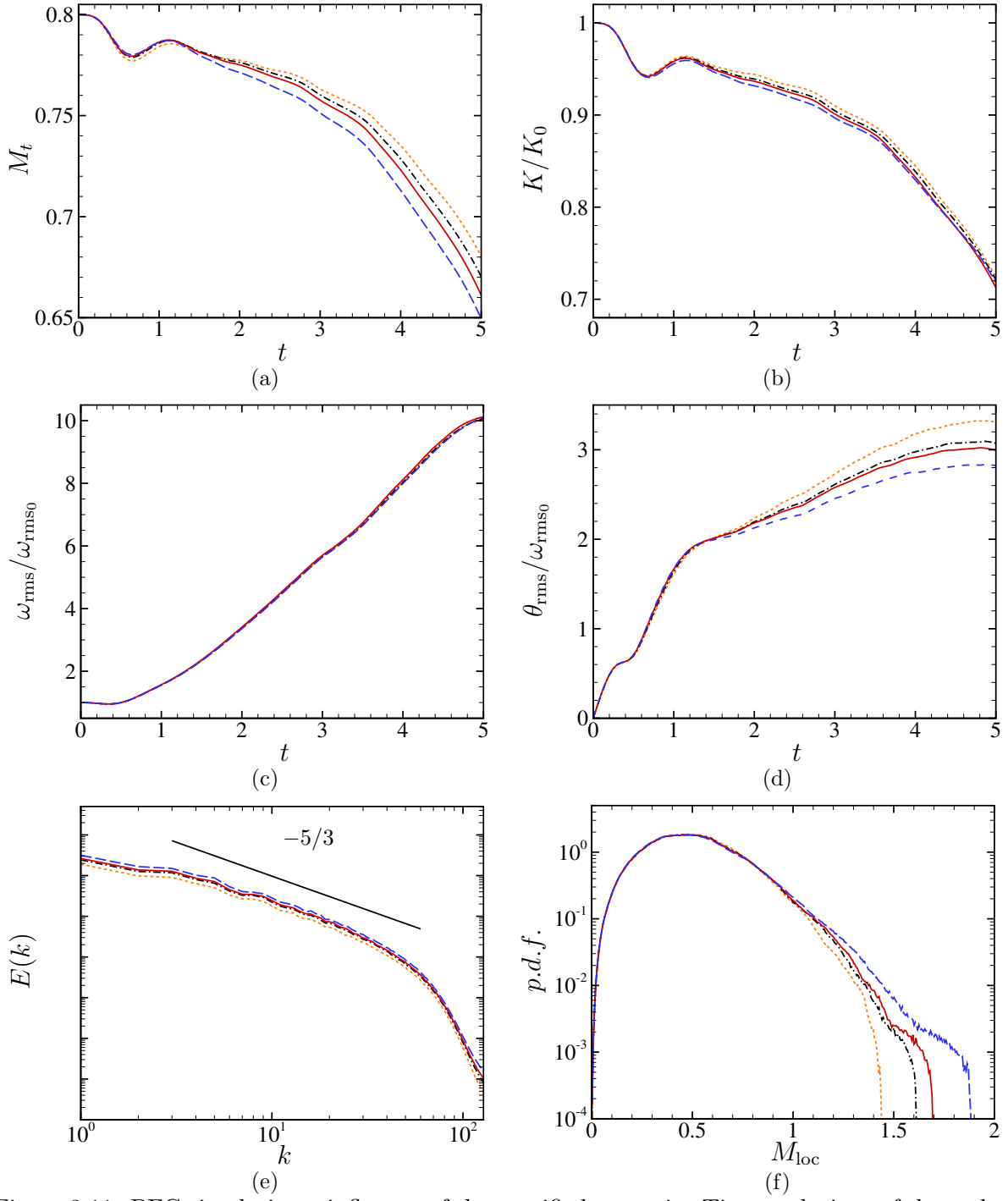


Figure 3.11. PFG simulations: influence of the specific heat ratio. Time evolutions of the turbulent Mach number (a), turbulent kinetic energy (b), normalized r.m.s. of the vorticity (c), normalized r.m.s. of the dilatation (d), kinetic energy spectrum (e) and p.d.f. of the local Mach number at $t = 2.5$ (f). \cdots : $\gamma = 1.0125$; $-\cdot-\cdot-$: $\gamma = 1.289$; $—$: $\gamma = 1.4$; $- - -$: $\gamma = 1.667$.

in table 3.4, where all variables are normalized with respect to their critical value. Figure 3.12 shows the location of the (uniform) initial thermodynamic state in the $p-v$ plane for the VDW model. The initial state is located close to the transition line and corresponds to a negative initial value of the fundamental derivative of gas dynamics. As a consequence, non classical gas dynamic

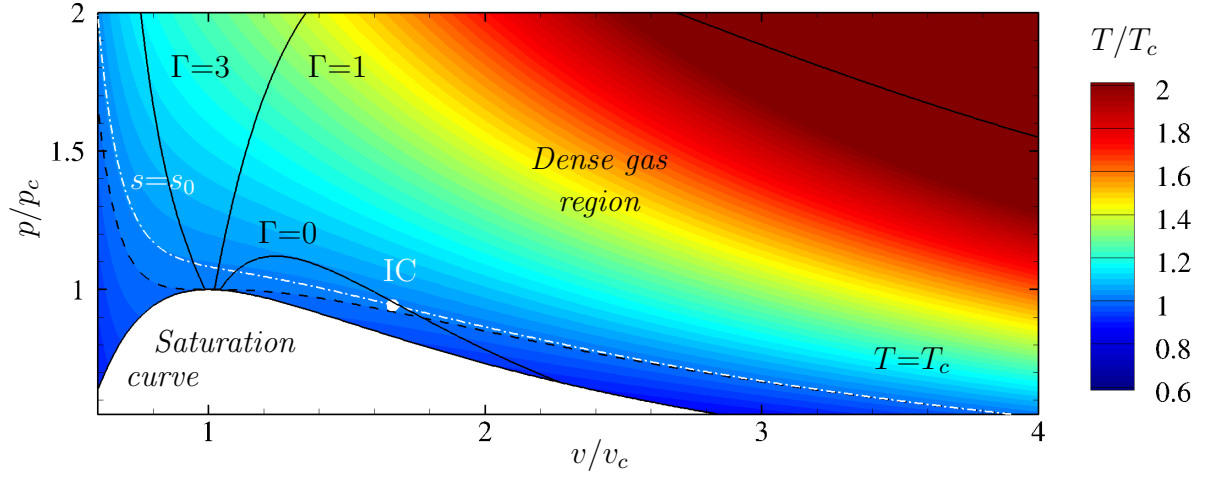


Figure 3.12. Representation in the $p-v$ plane of the initial thermodynamic conditions used for the dense gas simulations with the VDW model (isocontours of reduced temperature). I.C. represents the initial thermodynamic state; the dashed line $s = s_0$ is the isentropic curve containing the initial thermodynamic state; $T = T_c$ the critical isotherm; the curves $\Gamma = 0$ and $\Gamma = 1$ define the BZT and the dense-gas region, respectively.

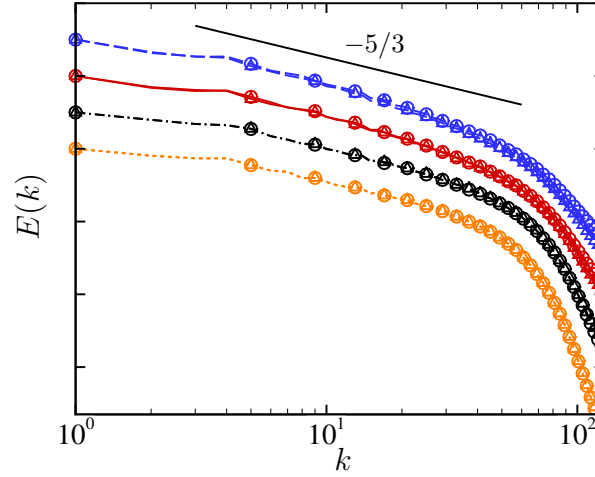


Figure 3.13. PFG and DG simulations. Kinetic energy spectra at $t = 2.5$ at various initial turbulent Mach numbers. $\cdots\cdots$: $M_{t_0} = 0.2$; $-\cdot-\cdot-$: $M_{t_0} = 0.5$; $—$: $M_{t_0} = 0.8$; $---$: $M_{t_0} = 1$. \circ : VDW; \triangle : PFG.

behaviours are likely to appear in supersonic flow regions. We have then carried out a parametric study by considering various initial turbulent Mach numbers ($M_{t_0} = 0.2, 0.5, 0.8$ and 1).

Table 3.4. Initial thermodynamic conditions used for the dense gas simulations using the PFG and VDW equations of state.

Case	ρ/ρ_c	T/T_c	p/p_c	$c/\sqrt{p_c/\rho_c}$	Γ
VDW	0.6	1.012	0.944	0.818	-0.04471
PFG	0.6	1.012	0.607	1.012	1.00625

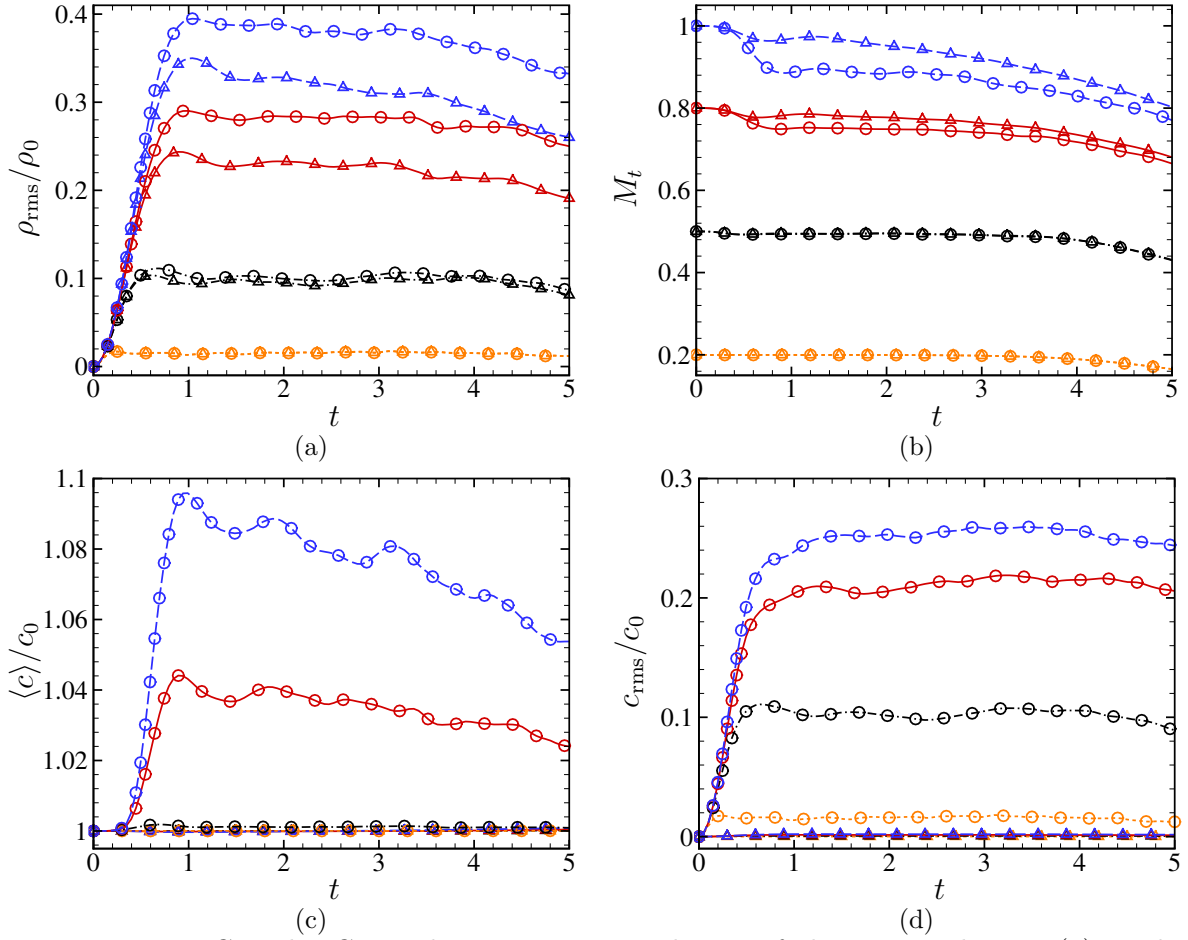


Figure 3.14. PFG and DG simulations. Time evolution of the r.m.s. density (a), turbulent Mach number (b), average speed of sound (c) and r.m.s. speed of sound (d).: $M_{t_0} = 0.2$; -.-.-: $M_{t_0} = 0.5$; —: $M_{t_0} = 0.8$; ---: $M_{t_0} = 1$. ○: VDW; △: PFG.

The computed kinetic energy spectra at $t = 2.5$, reported in figure 3.13, exhibit an inertial range for all values of the initial turbulent Mach number and the perfect and dense gas solutions do not show any difference. However, the thermodynamic variables as well as the turbulent Mach number are strongly affected by the dense gas effects as shown in figure 3.14, where the time histories of ρ_{rms} , M_t , $\langle c \rangle$, and c_{rms} (normalized by the respective initial values) are reported at various M_{t_0} . In particular, we observe that for the lower M_{t_0} cases ($M_{t_0} = 0.2, 0.5$) there are no significant differences between PFG and VDW solutions. For the PFG, the average and the r.m.s. speed of sound remain almost constant in time independently of M_{t_0} . In the VDW dense gas case these quantities increase strongly with M_{t_0} . As a consequence the mean and r.m.s. fundamental derivative of gas dynamics (which is directly related to sound speed variations) also exhibits a strong dependence on M_{t_0} (figure 3.15). This behavior is due to the fact that for VDW gases both c and Γ depend on temperature and density, which are changing. For the lowest values of M_{t_0} , fluctuations of the thermodynamic quantities are small and all the thermodynamic states remain close to the initial one.

This is confirmed by inspection of figure 3.16 that shows the representation of the thermodynamic states in the $p - v$ diagram at $t = 2.5$ for various M_{t_0} . The thermodynamic states are distributed along the isentropic line corresponding to $s = s_0$ (s_0 being the initial entropy). At $M_{t_0} = 0.2$ (panel a), the thermodynamic variables exhibit weak variations and $\langle \Gamma \rangle$ is rather constant in time.

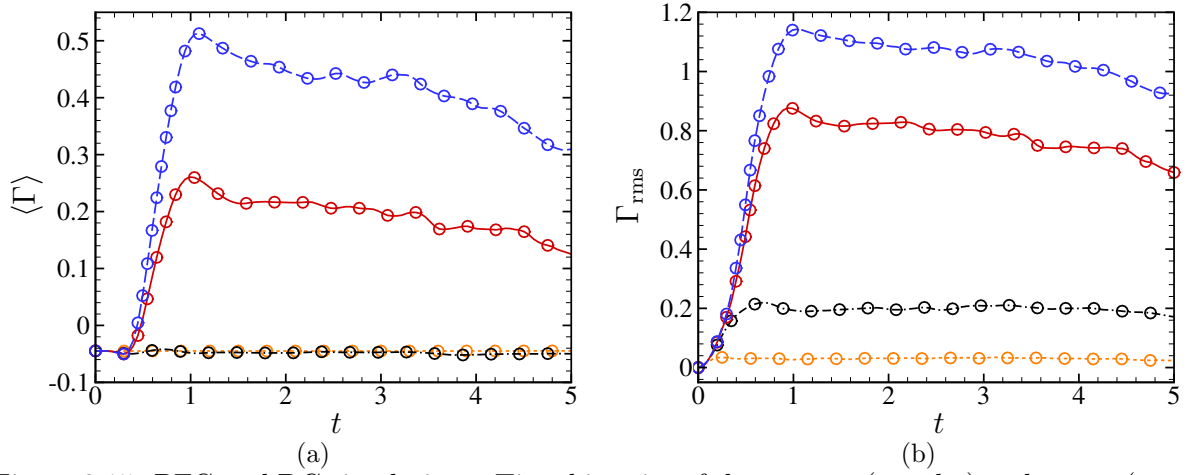


Figure 3.15. PFG and DG simulations. Time histories of the average (panel a) and r.m.s. (panel b) fundamental derivative of gas dynamics for the dense gas at various initial turbulent Mach numbers. \cdots : $M_{t_0} = 0.2$; $-\cdot-\cdot-$: $M_{t_0} = 0.5$; $—$: $M_{t_0} = 0.8$; $- - -$: $M_{t_0} = 1$. \circ : VDW; \triangle : PFG.

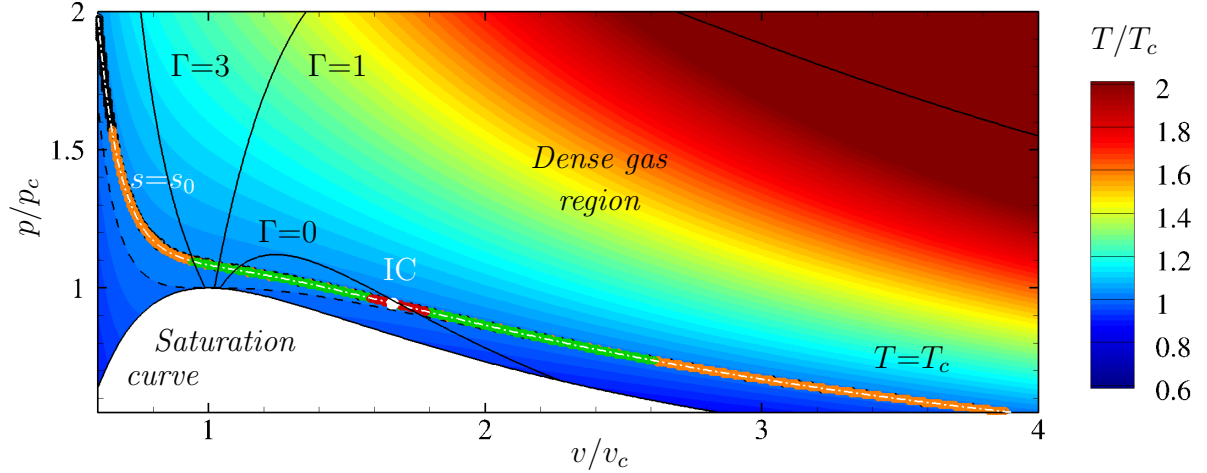


Figure 3.16. Representation in the $p - v$ diagram of the thermodynamic states at $t = 2.5$ for various initial turbulent Mach numbers. Each symbol represents the thermodynamic conditions computed at a given mesh points at various initial Mach numbers. The spread of thermodynamic states (approximately distributed along an isentropic curve) increases with the Mach number, due to compressibility effects. \bullet : $M_{t_0} = 0.2$; \bullet : $M_{t_0} = 0.5$; \bullet : $M_{t_0} = 0.8$; \bullet : $M_{t_0} = 1$.

As the initial turbulent Mach number increases, thermodynamic states attained by the flow lay along isentropic line, and the thermodynamic variables exhibit strong variations, thus explaining the strong dependence of $\langle \Gamma \rangle$ and Γ_{rms} observed in figure 3.15. The rapid growth of both quantities (attaining a maximum at about $1 \div 1.5$) is likely due to the appearance of strong local compression phenomena (namely, eddy shocklets). A close-up of the instantaneous iso-contours of Γ , taken along a mesh plane at $t = 2.5$, for a dense gas simulation with $M_{t_0} = 1$ is shown in figure 3.17. The figure shows that there exist regions of the plane where Γ varies abruptly from negative to positive values (from about -0.5 to values greater than 4). The representation in the $p - v$ plane of the thermodynamic states at the same time (figure 3.16) shows that indeed for the high turbulent Mach numbers, strong compressions drive the thermodynamic states far away from the initial one, up to supercritical pressures and temperatures. In the high pressure region, the second nonlinearity parameter (the rate of change of Γ with respect to density at constant entropy) is positive, and Γ

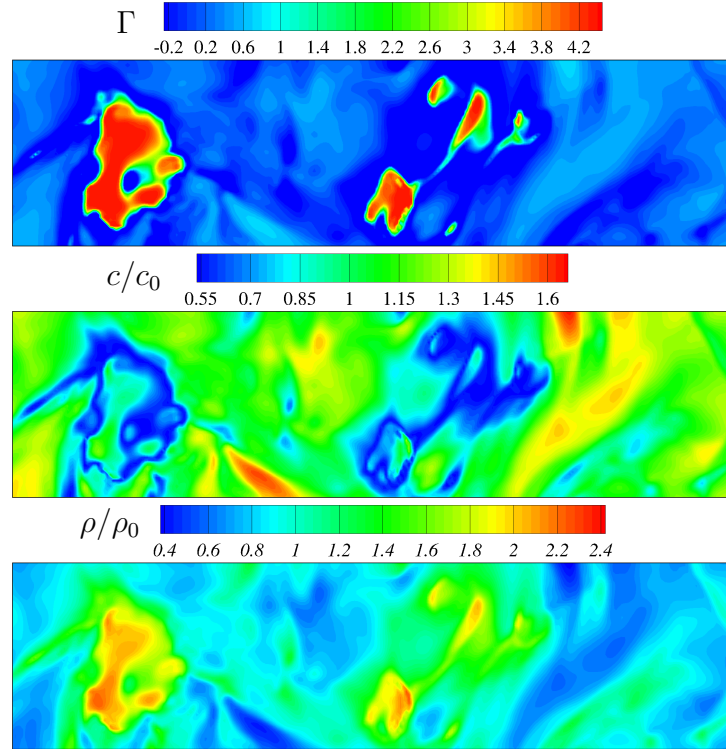


Figure 3.17. Instantaneous iso-contours ($t = 2.5$) of Γ (top), c/c_0 (middle), and ρ/ρ_0 (bottom) along a mesh plane for a dense-gas computation at $M_{t_0} = 1$. At high-Mach number dense gas computations, these thermodynamic properties exhibit significant large-scale fluctuations. Specifically, Γ can take both positive and negative values.

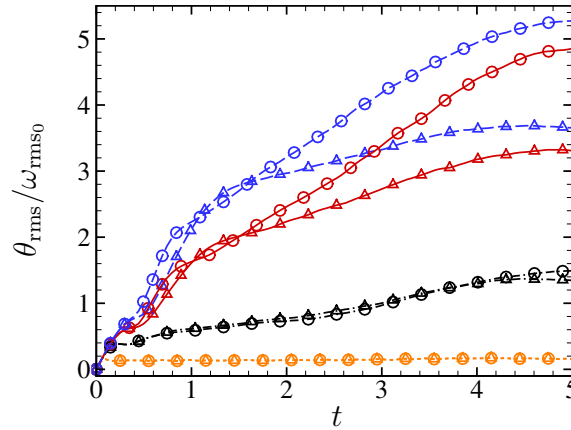


Figure 3.18. PFG and DG simulations. Time evolution of the r.m.s. divergence of the velocity field normalized with the initial vorticity at various initial turbulent Mach numbers.: $M_{t_0} = 0.2$; ----: $M_{t_0} = 0.5$; —: $M_{t_0} = 0.8$; - - - -: $M_{t_0} = 1$. ○: VDW; △: PFG.

increases rapidly with pressure, leading to the formation of spots characterised by very high values. As a consequence, the sound speed decreases abruptly, leading to large variations of the local Mach number.

To further analyse compressibility effects, figure 3.18 displays the time evolution of the r.m.s. velocity divergence normalized by the initial r.m.s. vorticity at various M_{t_0} . During the initial transient phase, the development of dilatational modes exhibits similar trends for both perfect and

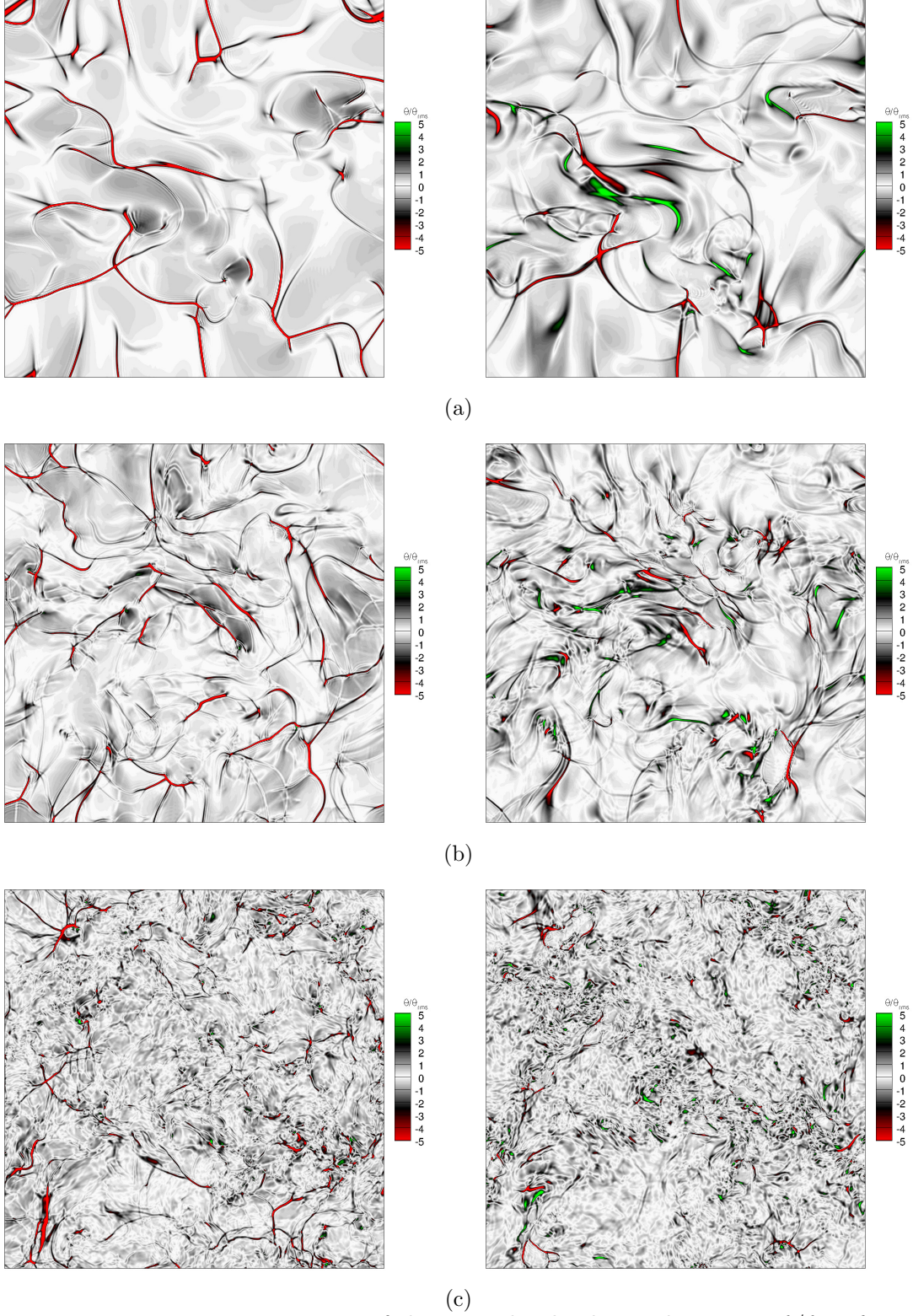


Figure 3.19. Instantaneous iso-contours of the normalized velocity divergence $\theta/\theta_{\text{rms}}$ for $M_{t_0} = 1$ at time $t = 1$ (a), $t = 3$ (b), and $t = 5$ (c). Results for the perfect gas case are represented on the left, dense gas on the right. Red regions correspond to strong compressions ($\theta/\theta_{\text{rms}} < -3$), green regions to strong expansions ($\theta/\theta_{\text{rms}} > 3$).

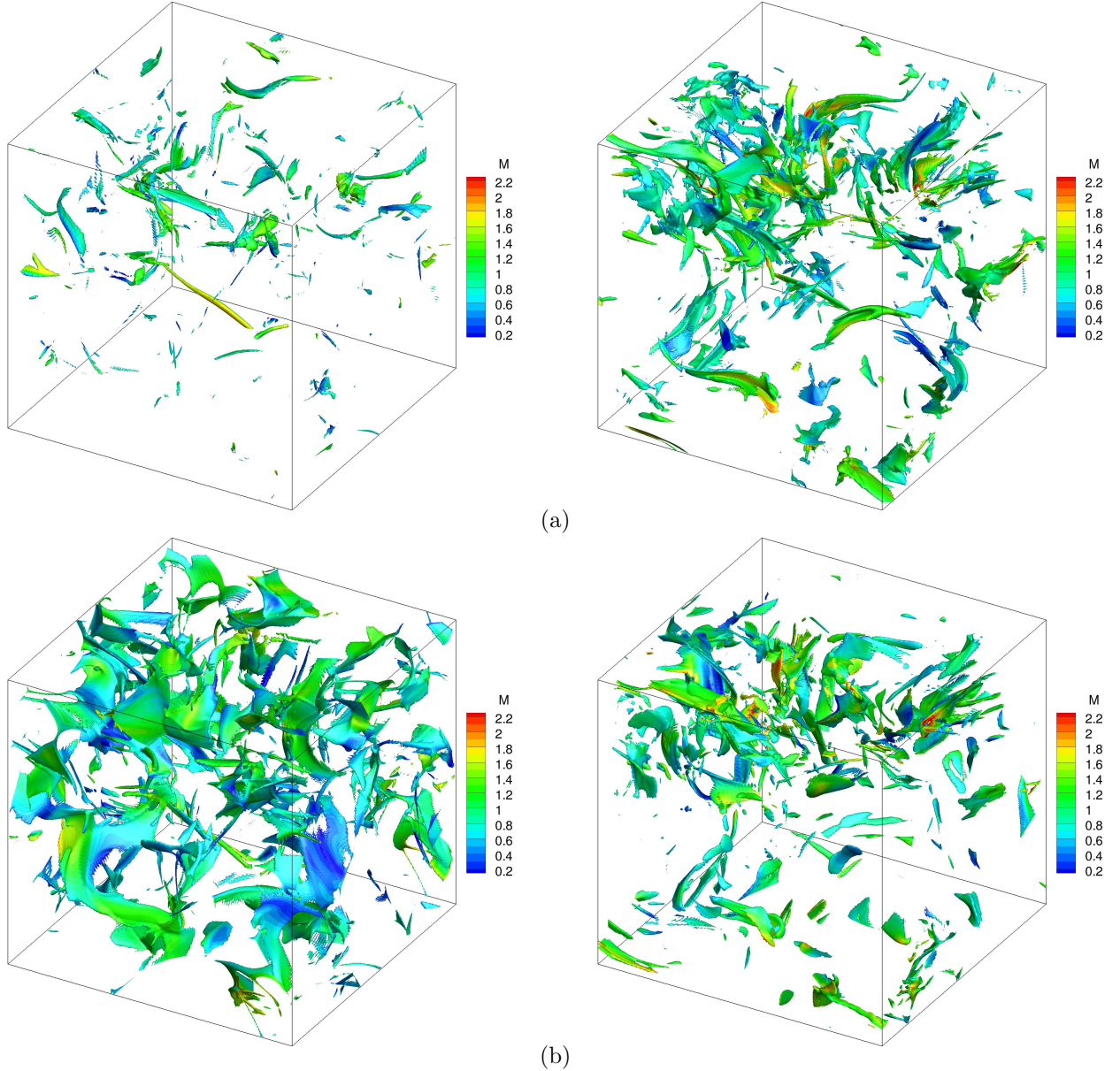


Figure 3.20. Snapshots at $t = 2.5$ of the isosurfaces $\theta/\theta_{\text{rms}} = 3$ (a) and of the iso-surfaces $\theta/\theta_{\text{rms}} = -3$ (b), coloured by the local Mach number, for perfect (left panel) and dense gas (right panel) simulations at $M_{t_0} = 1$.

dense gas. Afterwards, compressibility effects are enhanced for dense gas cases.

Regardless of the gas model in use, the observed dynamics is similar. The almost-incompressible initial distribution of large-scale eddies is modified at the beginning of the decay with the appearance of compressible modes, leading to the generation of eddy shocklets that start interacting at a later stage. As observed by [Passot & Pouquet \(1987\)](#), when shocklets collide they may either coalesce or “ignore” each other, pursuing their path with a slightly different velocity due to momentum exchange. Because of turbulence kinetic energy decay, the number and intensity of shocklets tend to decrease with time. Nevertheless, the nature of eddy shocklets for the perfect and dense gas is different. Figure 3.19 shows a snapshot of the ratio $\theta/\theta_{\text{rms}}$ on a slice of the domain at $t = 1, 3$ and 5 . Red regions correspond to values of $\theta/\theta_{\text{rms}} < -3$, which is considered as a threshold representative of strong compressions ([Samtaney *et al.*, 2001](#)); conversely, green regions correspond

Table 3.5. Volume fraction occupied by compression and expansion regions at time $t = 2.5$.

M_{t_0}	EoS	$\theta/\theta_{\text{rms}}M_{t_0}^2$ (%)					
		$[-\infty, -2]$	$[-2, -1]$	$[-1, 0]$	$[0, 1]$	$[1, 2]$	$[2, +\infty]$
0.2	PFG	0	0	50	50	0	0
	VDW	0	0	50	50	0	0
0.5	PFG	0	0	48	52	0	0
	VDW	0	0	51	49	0	0
0.8	PFG	1	5	39	52	3	0
	VDW	0.5	4	46	44	5	0.5
1.0	PFG	4	8	30	48	9	1
	VDW	3	9	38	38	9	3

Table 3.6. Volume fraction occupied by flow regions characterized by different Γ values, conditioned on dilatation levels (dense gas simulations at $M_{t_0} = 1$, $t = 2.5$). First row corresponds to regions characterized by $\Gamma < 0$ (thermodynamic states falling in the inversion zone); second row to regions with $0 < \Gamma < 1$ (dense gas region); third row to regions having $\Gamma > 1$. The last column provides the total volume fraction for each thermodynamic region.

$\langle \Gamma \theta/\theta_{\text{rms}} \rangle$	$\theta/\theta_{\text{rms}}M_{t_0}^2$ (%)						
	$[-\infty, -2]$	$[-2, -1]$	$[-1, 0]$	$[0, 1]$	$[1, 2]$	$[2, +\infty]$	$[-\infty, +\infty]$
$[-\infty, 0]$	1	4	16	14	4	1	40
$[0, 1]$	2	5	21	22	5	1	56
$[1, +\infty]$	0	1	1	2	1	0	4

to values of the relative divergence greater than 3, which identifies strong expansions. We observe that strong compression zones are somewhat more frequent and wider in perfect gas than in dense gas simulations. Conversely, strong expansion regions, which occupy a significant portion of the domain in the DG solution, are nearly absent in PFG.

The iso-surfaces $\theta/\theta_{\text{rms}} = 3$ and $\theta/\theta_{\text{rms}} = -3$ at $t = 2.5$ are reported in figure 3.20, both for PFG and DG. The figure shows that in the PFG case, strong compression regions correspond to sheet-like structures, while strong expansions have tubular shapes. On the contrary, the dense gas exhibits sheet-like and tubular structures, both in compression and in expansion regions.

Table 3.5 reports the volume fractions occupied by compression and expansion regions at $t = 2.5$, as defined in section 3.4.3. At the lowest M_{t_0} , only weak expansion and compression regions are present both for perfect and dense gas cases, with a balanced distribution. The percentage of moderate and strong compression and expansion regions increases as the initial turbulent Mach number increases. The volume distribution for the PFG case with $M_{t_0} = 1$ is similar to the one reported in Wang *et al.* (2012b). Strong compression regions become significant starting from $M_{t_0} = 0.8$. At $M_{t_0} = 1$, strong dilatation regions (including compressions and expansions) occupy about 5% of the total volume both for perfect and dense gases. However, in the latter case expansions and compressions are equally probable and the volume fraction shows a more symmetric statistical behavior (which is preserved for all M_{t_0} due to the nonclassical sound speed behaviour in zones with $\Gamma < 0$). For PFG the volume fraction distribution is symmetric only at the lowest M_{t_0} . At $M_{t_0} = 1$ strong expansion

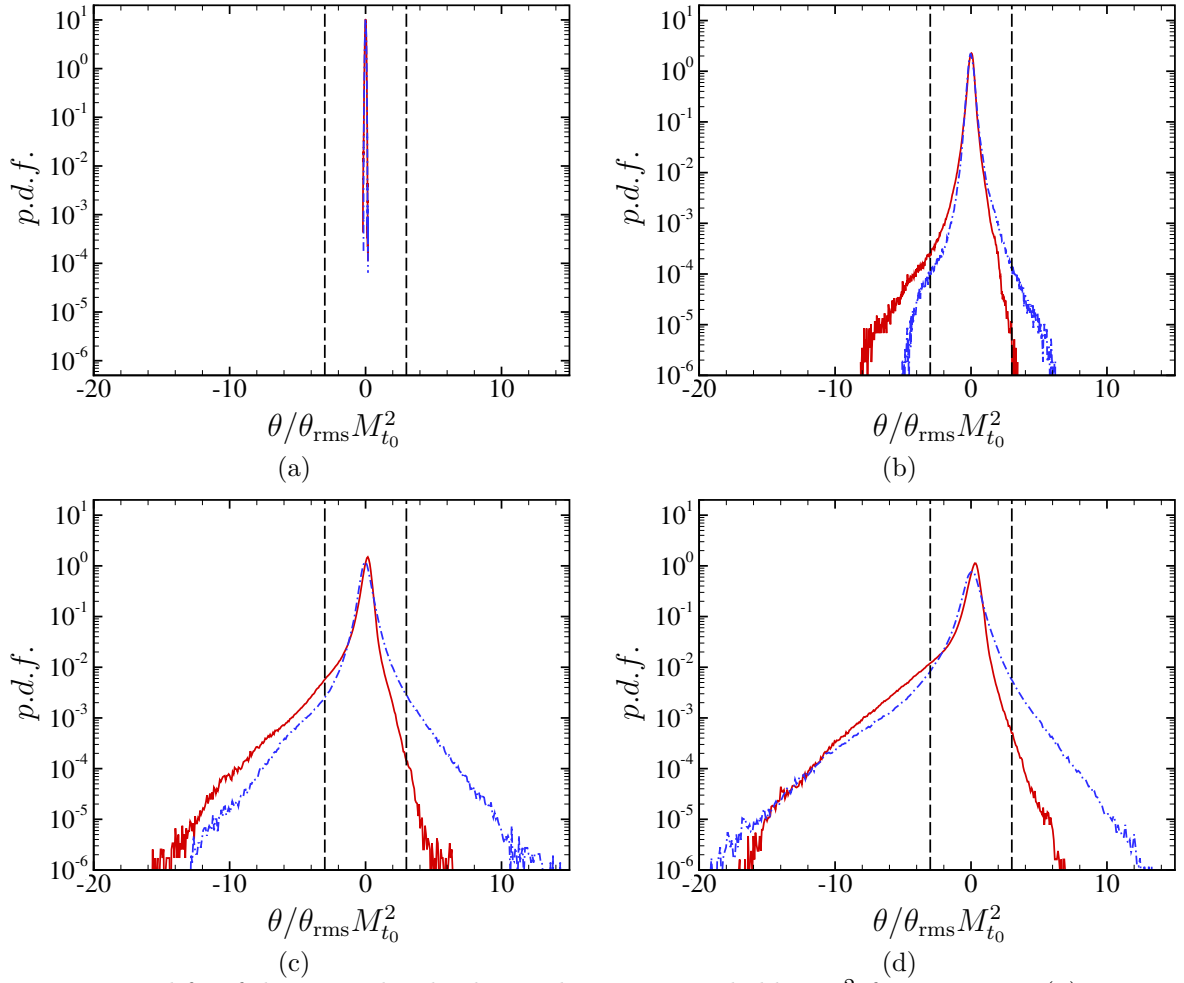


Figure 3.21. P.d.f.s of the normalized velocity divergence scaled by $M_{t_0}^2$ for $M_{t_0} = 0.2$ (a), $M_{t_0} = 0.5$ (b), $M_{t_0} = 0.8$ (c), and $M_{t_0} = 1$ (d) ($t = 2.5$). The vertical dashed lines indicate the values $\theta/\theta_{rms} = \pm 3$. —: PFG; - - -: VDW.

zones occupy a volume fraction which is about 400% less than strong compressions. In dense gases strong expansions occupy a volume fraction that is about 10% less than strong compressions at the same M_{t_0} . In the PFG case, moderate and weak expansion occupy 57% of the flow volume, while the weak and moderate compressions occupy 38%. However, in VDW case the volume occupied by weak and moderate compressions and expansions is approximately equal (about 47% each).

To further elucidate the influence of dense gas and compressibility, in figure 3.21 we report the p.d.f. of the normalized dilatation at various M_{t_0} ($t = 2.5$) both for PFG and VDW. The dashed vertical lines identify the regions of strong compression bounded by the area of negative (respectively, positive) values of θ/θ_{rms} to the left (respectively, to the right) of $\theta/\theta_{rms} = -3$ (respectively, $\theta/\theta_{rms} = 3$). In the case of the perfect gas, the p.d.f. of the dilatation is highly skewed, as already observed in weakly and moderately compressible turbulent flows at high M_{t_0} (and $\gamma = 1.4$) by Porter *et al.* (2002), Pirozzoli & Grasso (2004). In the dense gas case, strong expansion are enhanced, resulting in a more symmetric p.d.f. (i.e. strong compressions and strong expansions are equally probable). Table 3.6 shows the volume fractions occupied by flow regions having different Γ values conditioned on the dilatation for the dense-gas case at $M_{t_0} = 1$. We observe that 40% of the flow volume is characterized by thermodynamic states falling in the inversion zone (exhibiting $\Gamma < 0$), whereas only 4% is characterized by $\Gamma > 1$. Strong expansion regions characterized by a

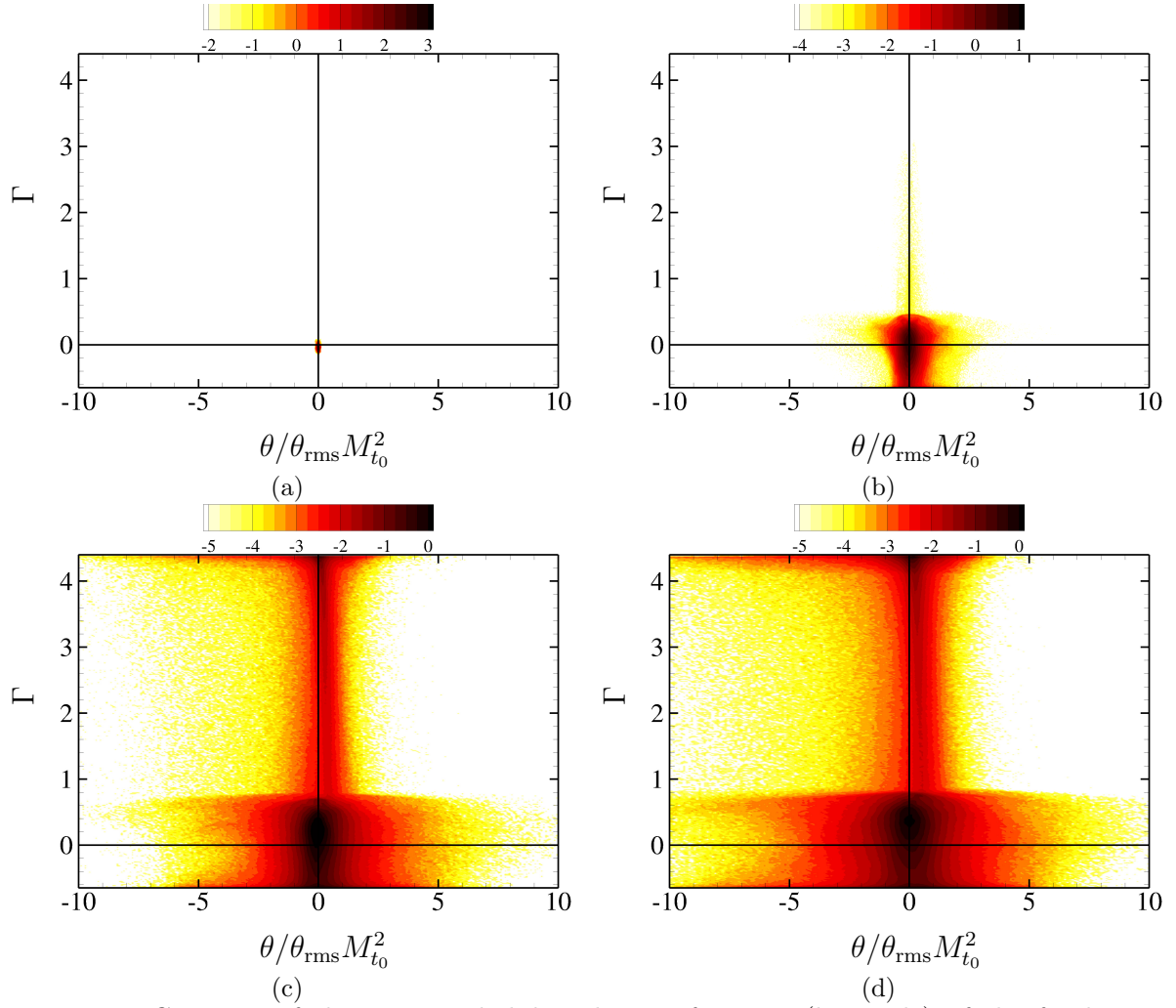


Figure 3.22. Contours of the joint probability density function (log scale) of the fundamental derivative of gas dynamics Γ with the scaled normalized local velocity divergence $\theta/\theta_{\text{rms}} M_{t_0}^2$ at the initial turbulent Mach numbers $M_{t_0} = 0.2$ (a), $M_{t_0} = 0.5$ (b), $M_{t_0} = 0.8$ (c), and $M_{t_0} = 1$ (d) .

negative Γ occupy a volume fraction of about 1%, which represents 50% of all Γ values, whereas strong expansion regions having $\Gamma > 1$ represent a negligible fraction. Strong compression regions having positive Γ occupy about 70% of the total volume. This suggests that in the dense gas the occurrence of both eddy shocklets and eddy "expansion shocklets" is admissible.

In figure 3.22 we report the joint p.d.f. of Γ with $\theta/\theta_{\text{rms}}$ at various initial turbulent Mach numbers at time $t = 2.5$. For $M_{t_0} = 0.2$, the weak dilatation levels cause the p.d.f.s to be concentrated in the neighbourhood of the initial condition ($\Gamma \approx -0.045$). At $M_{t_0} = 0.5$, the p.d.f. becomes broader, but most of the states are characterized by $\Gamma < 1$ and $\theta/\theta_{\text{rms}} \in [-1, 1]$. At higher M_{t_0} , due to strong dilatation effects, the thermodynamic states spread over a large range of thermodynamic conditions, and a secondary peak is obtained around $\Gamma \approx 4$ and small positive values of $\theta/\theta_{\text{rms}}$. When strong compressions occur, flow particles becomes increasingly difficult to compress as density grows. This results in a clustering of the thermodynamic states in the high-pressure region, close to the critical isotherm.

Figure 3.23 shows that, in the case of dense gas, the p.d.f. of the normalized local speed of sound $c/\langle c \rangle$ for the dense gas spans over a wider range than PFG, for a Dirac-like distribution is recovered (i.e. the speed of sound is nearly constant). This is true for the total p.d.f. (conditioned on all

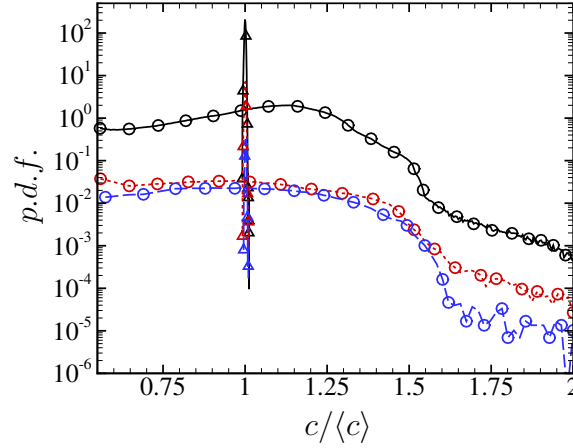


Figure 3.23. Probability density function of the normalized sound speed conditioned on $\theta/\theta_{\text{rms}}$ at $M_{t_0} = 1$: $[-\infty, -2]$; ----: $[2, \infty]$; —: $[-\infty, \infty]$; ○: VDW; △: PFG.

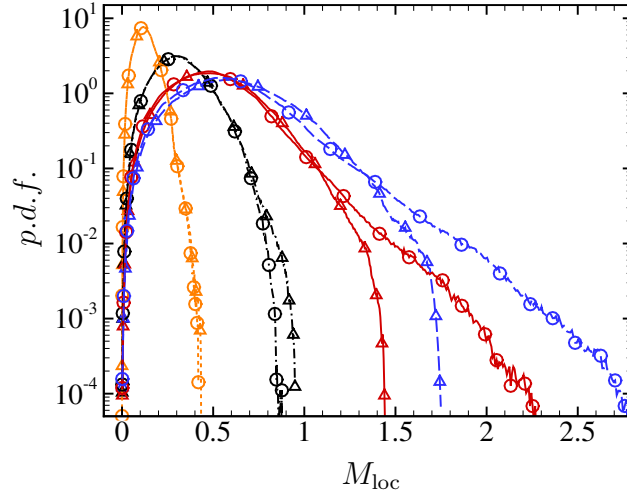


Figure 3.24. Probability density functions of the local Mach number at various initial turbulent Mach numbers ($t = 2.5$).: $M_{t_0} = 0.2$; ----: $M_{t_0} = 0.5$; —: $M_{t_0} = 0.8$; ----: $M_{t_0} = 1$. ○: VDW; △: PFG.

possible values of $\theta/\theta_{\text{rms}}$) and for p.d.f.s conditioned on either strong expansions either strong compressions.

The heavy right tail of the dense-gas p.d.f.s, for $c/\langle c \rangle > 1.5$, is due to high compression regions characterized by high Γ values, for which the sound speed increases considerably. In fact, the p.d.f. conditioned on strong compressions exhibits a heavy right tail as well, whereas the p.d.f. conditioned on strong expansions attributes lower probability to high values of the speed of sound. On the other hand, in compression regions low values of c are also very probable when $\Gamma < 0$, since in this case the sound speed initially decreases. This explains the higher probability associated with values of $c/\langle c \rangle$ below 0.7 in the case of strong compressions, with respect to strong expansions.

The peculiar behaviour of the speed of sound deeply modifies the p.d.f. of the local Mach number (figure 3.24). However, the probability of having high local Mach number is higher in dense gases. In figure 3.25 we report the p.d.f. of the local Mach number (panel a) and of the normalized vorticity $\omega/\omega_{\text{rms}}$ (panel b) conditioned on the strong compression and expansion regions at $M_{t_0} = 1$. The dense-gas and the perfect-gas case exhibit a bell-shaped form with an exponential right tail, as also found by Wang *et al.* (2012b) and Moisy & Jiménez (2004) for a perfect gas with $\gamma = 1.4$. Restricting

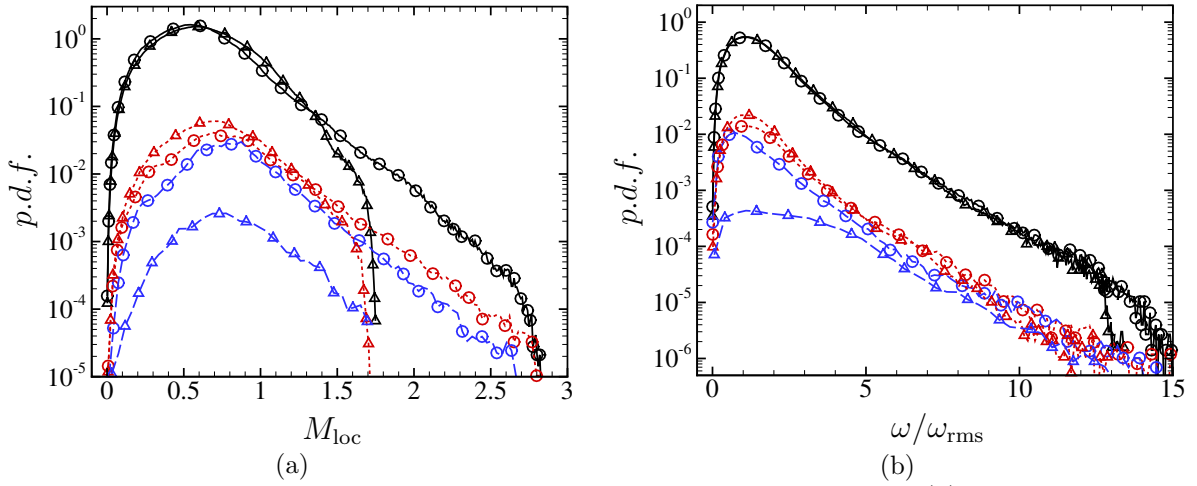


Figure 3.25. Total probability density function of the local Mach number (a) and the normalized local vorticity (b), and p.d.f. conditioned on strong compressions ($\theta/\theta_{\text{rms}} < -2$) and strong expansions ($\theta/\theta_{\text{rms}} > 2$) for $M_{t_0} = 1$ at time $t = 2.5$: $[-\infty, -2]$; ----: $[2, \infty]$; —: $[-\infty, \infty]$; ○: VDW; △: PFG.

our attention to the conditional p.d.f. we note that for dense gas, unlike the PFG, the p.d.f.s conditioned on strong dilatations and on strong compressions do not exhibit significant differences. In other terms, the probability of producing a given vorticity is similar in both regions. A possible explanation is that, on the one hand, extra vorticity may be generated in strong expansion regions through expansion eddy shocklets; on the other hand, shocklets of any kind are expected to be weaker in dense gases with Γ close to zero and specifically compression shocklets are weaker than in a PFG. For the PFG case, vorticity production in high compression regions is more likely than in high dilatation ones, as observed also by Wang *et al.* (2012b).

Chapter Summary

A numerical study of the influence of dense-gas effects on the large-scale dynamics of decaying homogeneous isotropic turbulence is carried out by using the Van der Waals gas model. The simulations are based on the inviscid conservation equations, solved by means of the DNC9 scheme with the shock-capturing strategy presented in section 2.2.

- Assessment of the numerical strategy:
 - Concerning grid resolutions, The 256^3 grid leads to reasonably small numerical errors both for mean and r.m.s. properties, as well as an adequate description of the inertial range. It has been retained as best compromise between accuracy and computational cost.
 - Different dissipation coefficients were tested. They do not alter essentially the thermodynamic quantities, but slightly modify the tails of the p.d.f.s of dilatation, the enstrophy value for $t > 3$ and the energy spectrum at high wavenumbers.
- Influence of the initial conditions.
 - Higher initial values for the compressibility ratio lead to higher fluctuations of thermodynamic quantities and velocity divergence; hence, the non-physical, yet conservative value of $\chi_0 = 0$ is chosen.
 - The initial peak wavenumber $k_0 = 2$ is retained since it concentrates energy in the biggest scales, enhancing large-scale motions and yielding a wider inertial range.
- Influence of the specific heat ratio γ in perfect gases:
 - Fluctuations of thermodynamic quantities are shown to scale according to dimensional analysis and momentum conservation.
 - Kinematic quantities exhibit a similar behaviour, although strong dilatation regions are slightly enhanced for low- γ fluids.
- Dense-gas simulations:
 - Significant influence for flows characterized by initial turbulent Mach numbers higher than 0.5.
 - Thermodynamic properties deeply affected and different behaviour in strong dilatation regions:
 - * For the perfect gas, strong compressions occupy a much larger volume fraction than strong expansions; vorticity is more likely to be created in strong compressions, and strong expansions are characterized by tubular eddy structures.
 - * For the dense gas, strong compressions and expansions are more balanced, as shown by the p.d.f.s of the normalized local dilatation, and vorticity is created with equal probability in both regions. Strong expansions, furthermore, are characterized by sheet-like structures, suggesting the possibility of the occurrence of eddy shocklets.

4 Small scale dynamics of dense-gas homogeneous isotropic turbulence

Contents

4.1 General statistics	93
4.1.1 Influence of the thermodynamic and transport property models	95
4.1.2 Influence of the fluid type	100
4.1.3 Mach number effects	100
4.2 Small-scale features	107
4.2.1 Local flow topology	107
4.2.2 Contribution of flow structures to dissipation	114
4.2.3 Enstrophy generation mechanisms	121

In the present chapter, we focus on the role of viscous effects involved in the small-scale dynamics of dense gas CHIT. On the one hand, we investigate how differences due to the complex thermodynamic behaviour affect the dynamics at smallest scales. On the other hand, we elucidate the role of the peculiar transport properties of dense gases. To this aim, we carry out DNS of the compressible Navier-Stokes equations at various initial turbulent Mach numbers and for two different choices of the initial thermodynamic state, corresponding to a small positive and a small negative value of the fundamental derivative Γ , and compared with DNS results for a perfect gas. The effect of the dense gas EoS and transport-property models adopted is quantified in section 4.1 by comparing results with those provided by the simple polytropic VDW EoS along with a power law model for the thermophysical properties. Afterwards, in order to evaluate the differences and similarities with the PFG case, we focus on highly compressible CHIT and in section 4.2 we analyze the statistical properties of the turbulent structures. The mechanisms of viscous dissipation of kinetic energy and enstrophy production are also investigated, with an emphasis on phenomena related to dilatational effects, which are more likely to be affected by the gas thermodynamic behaviour. The results reported in this chapter have been submitted to the Journal of Fluid Mechanics (Sciacovelli *et al.*, 2016b).

4.1 General statistics

Direct simulations of dense gas CHIT have been carried out at $Re_{\lambda_0} = 200$ and $k_0 = 2$, using a computational grid of 512^3 cells. In order to assess the influence of both thermodynamic and transport property models, we first focus on CHIT at $M_{t_0} = 1$, considering MAH and VDW models at the same reduced initial pressure and temperature (cases PP11-MAH-IC1 and PP11-VDW), as well as the perfect gas model assuming $\gamma = 1.0125$, a value which is representative of PP11 (referred to as PP11-PFG). The initial thermodynamic conditions used in each case are reported in table 4.1. At the selected initial conditions the thermodynamic state lies within the inversion zone for the VDW model, and immediately outside for MAH. Specifically, MAH-IC1 belongs to an isentrope that does not cross the inversion zone, yet it is characterized by an initial value of Γ close to zero. Hence, no BZT effects can appear since the entropy can only increase during the flow evolution.

Table 4.1. Summary of the thermodynamic models and initial thermodynamic conditions used in the study.

Case name	Model	T_0/T_c	p_0/p_c	ρ_0/ρ_c	Γ_0
Air	PFG	2.21	2.69×10^{-3}	3.85×10^{-3}	1.2
PP11-PFG	PFG	1.01	1.02	1.01	1.006
PP11-VDW	VDW	1.01	1.02	0.53	-0.674
PP11-MAH-IC1	MAH	1.01	1.02	0.62	0.125
PP11-MAH-IC2	MAH	1.001	0.98	0.62	-0.093

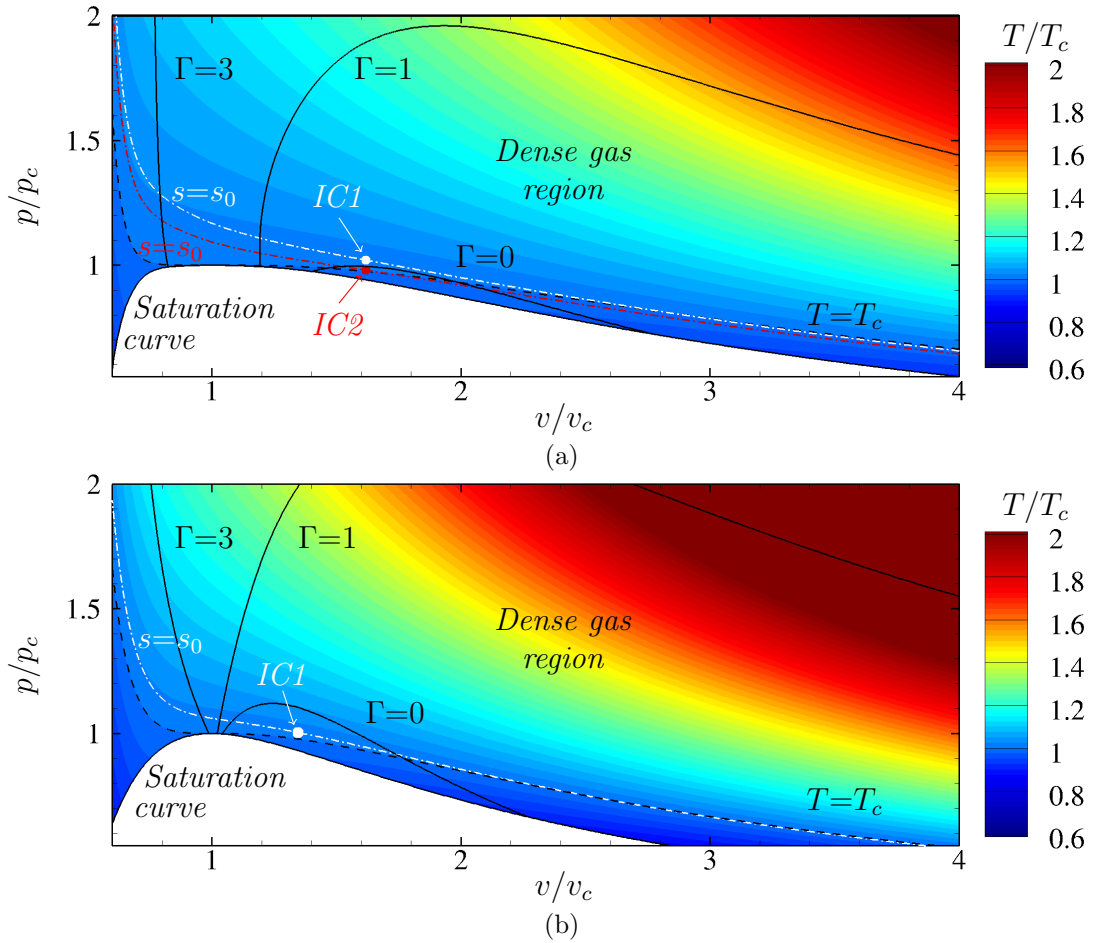


Figure 4.1. Isocontours of the reduced temperature in the Clapeyron diagram for PP11 using Martin-Hou (a), and Van der Waals (b) model. Three iso- Γ lines are also represented. The black dashed line denotes the critical isotherm. White circles are the initial thermodynamic conditions chosen for the MAH and VDW cases. The red circle in panel (a) denotes the PP11-MAH-IC2 initial condition. White and red dash-dotted lines are used to highlight the corresponding initial isentropes.

To further assess the role played by BZT effects when using a more realistic EoS, we have then also considered a different initial state that falls in the inversion zone (case PP11-MAH-IC2). The

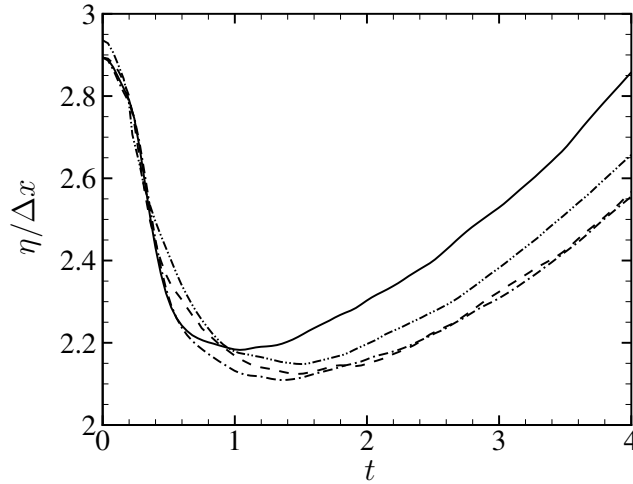


Figure 4.2. Grid resolution of the dense gas computations. Time history of the ratios of the Kolmogorov length scale to the mesh size, $\eta/\Delta x$. — air, - · - · - PP11-PFG, · · · · · PP11-VDW, - - - - - PP11-MAH-IC1.

initial thermodynamic states of the MAH and VDW cases are reported in the Clapeyron diagram (figure 4.1, panels a and b, respectively).

In figure 4.2 we report the time history of the ratio of the Kolmogorov length scale over the mesh size for the different thermodynamic models at $M_{t_0} = 1$ (value for which compressibility effects are strongest). The figure shows that η is discretized with more than 2 mesh points at all times and $k_{\max}\eta \geq 6.5 - 7$, thus confirming the adequacy of the selected grid.

DNS of PP11-MAH-IC1 are then carried out at various M_{t_0} , ranging from 0.2 to 1, and the dense gas effects are assessed by comparing the results with those of air behaving as a perfect gas.

4.1.1 Influence of the thermodynamic and transport property models

In figure 4.3, we report the time evolution of the turbulence kinetic energy (left figure) and the enstrophy (right) for the different cases of table 4.1. The thermodynamic model has a minor influence on the decay of these kinematic quantities. However, this is in general not true for the r.m.s. properties as figure 4.4 shows, where we report the time evolution of the r.m.s. of the pressure, temperature and speed of sound. The PP11-PFG solution exhibits higher pressure fluctuations compared to VDW and MAH results. On the other hand, temperature fluctuations are very small for all cases (including PFG), due to the high specific heat of the PP11 gas. The most significant differences are observed in the r.m.s. of the speed of sound. These are close to zero for case PP11-PFG, whereas they exhibit similar levels and trends both for PP11-VDW and PP11-MAH, and in general the decay rates are very similar, independently of the initial conditions. The times histories of the average (a) and the r.m.s. of the fundamental derivative of gas dynamics (b) are reported in figure 4.5. In the VDW case, due to the strong compressibility effects that lead to a considerable scattering of the thermodynamic states (as already observed in the previous chapter for inviscid CHIT), $\langle \Gamma \rangle$ changes rapidly from negative to positive values attaining a maximum over a time scale $t \approx 0.4$. Afterwards, it decays at a rate faster than MAH, and reaches negative values at the final simulation time $t = 4$. The MAH model exhibits a significant initial increase, reaching a maximum over approximately 0.4 initial eddy turnover time units. $\langle \Gamma \rangle$ then decays at a rate lower than in the VDW case, and remains positive even when starting from a negative initial value (IC2 initial conditions), due to the smaller inversion zone exhibited by the MAH model. The distribution of thermodynamic states in the Clapeyron diagram is reported in figure 4.6 both for VDW and

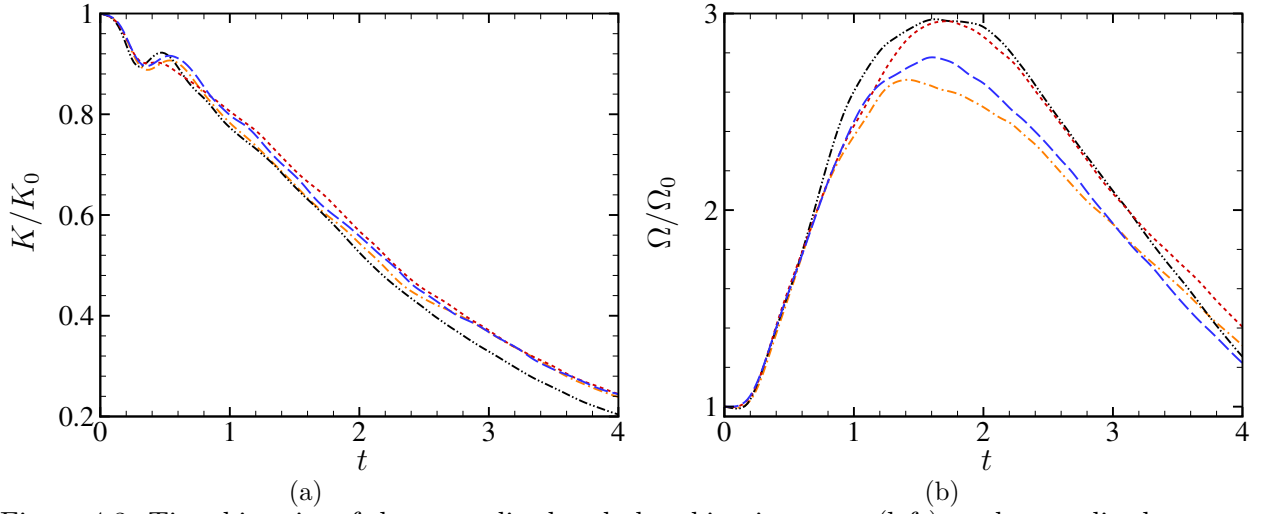


Figure 4.3. Time histories of the normalized turbulent kinetic energy (left), and normalized enstrophy (right) for various dense gas simulations at $M_{t_0} = 1$. \cdots : PP11-PFG; \cdots : PP11-VDW; \cdots : PP11-MAH-IC1; \cdots : PP11-MAH-IC2.

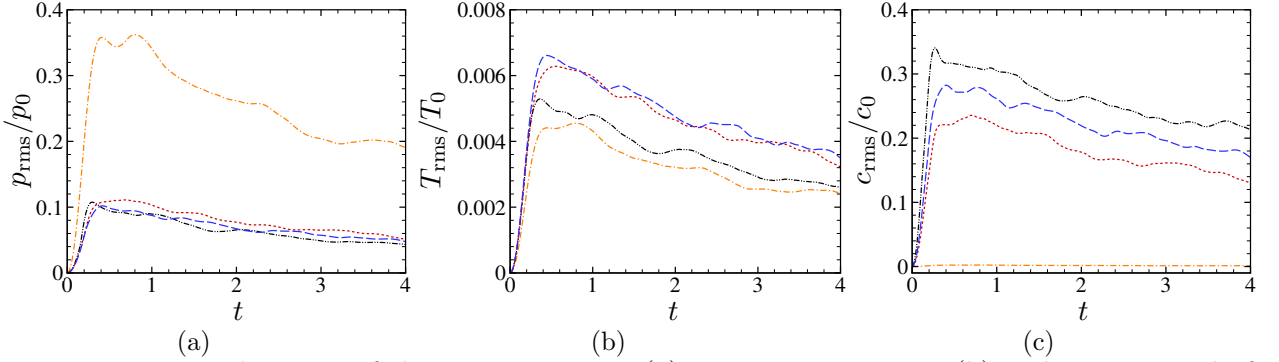


Figure 4.4. Time histories of the r.m.s. pressure (a), r.m.s. temperature (b) and r.m.s. speed of sound (c) for various dense gas simulations at $M_{t_0} = 1$. \cdots : PP11-PFG; \cdots : PP11-VDW; \cdots : PP11-MAH-IC1; \cdots : PP11-MAH-IC2.

MAH, along with iso-lines of Γ and iso-contours of the speed of sound. The figure confirms that the VDW model predicts much greater variations of Γ with p and v (figure 4.6b), which results in a considerable over-estimation of the r.m.s. of the same quantity with respect to MAH.

Other important quantities affecting the dynamics of dense gases are the viscosity and the local Eckert number. The results reported in figure 4.7 show that the viscosity behaviour is little dependent on the initial condition; however, it is drastically different depending on the model. The average Eckert number (figure 4.7b) exhibits a strong dependence on the type of gas (and on the selected thermodynamic model). For the dense gas case $\langle Ec \rangle$ is two orders of magnitude less than in air (not reported) and one order of magnitude less than in PP11-PFG. As a consequence, in the dense gas (and in particular for the MAH model) thermal and dynamic effects are loosely coupled. Similarly, the decrease of viscosity with time observed in the MAH cases may explain the flatter enstrophy peaks. The same figure also shows the influence of the thermodynamic model on the Eckert number. For PP11-PFG this is one order of magnitude smaller than in air (due to the much larger specific heat); in dense gas, it is further reduced by another order of magnitude, leading to a greater decoupling of thermal and dynamic effects.

The preceding considerations indicate that, despite quantitative differences in the prediction of the thermodynamic properties (and in particular Γ), all dense gas simulations based on either

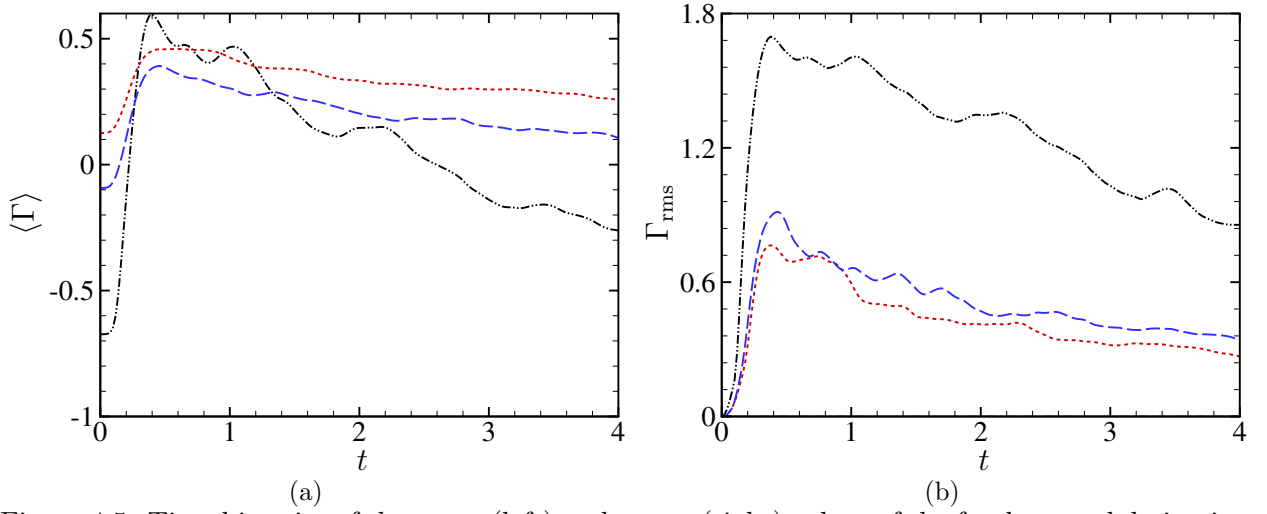


Figure 4.5. Time histories of the mean (left) and r.m.s. (right) values of the fundamental derivative of gas dynamics at $M_{t_0} = 1$. - · - · - : PP11-VDW; - - - : PP11-MAH-IC1; - - - : PP11-MAH-IC2.

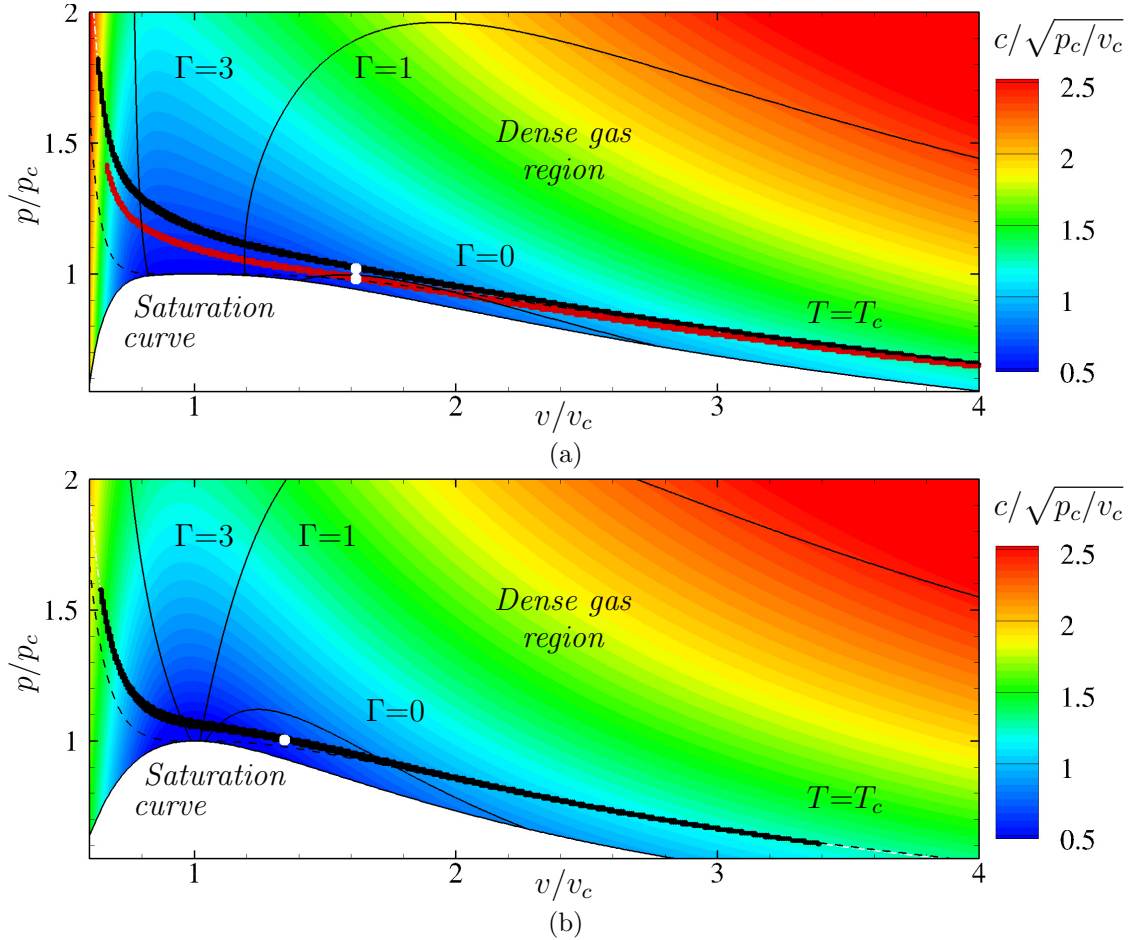


Figure 4.6. Distributions of thermodynamic states in the Clapeyron diagram, for PP11-MAH (a) and PP11-VDW (b) at $M_{t_0} = 1$ ($t = 2$). For PP11-MAH two initial thermodynamic conditions are considered, namely, IC1 (black symbols) and IC2 (red symbols).

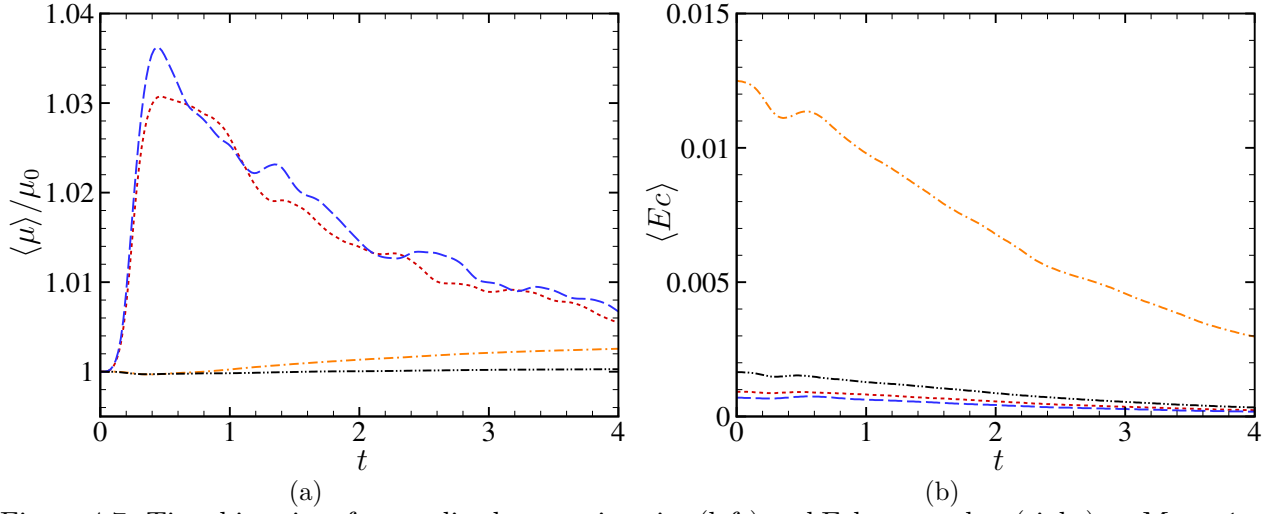


Figure 4.7. Time histories of normalized mean viscosity (left) and Eckert number (right) at $M_{t_0} = 1$. — · — ·: PP11-PFG; — · — · — ·: PP11-VDW; — — —: PP11-MAH-IC1; — — —: PP11-MAH-IC2.

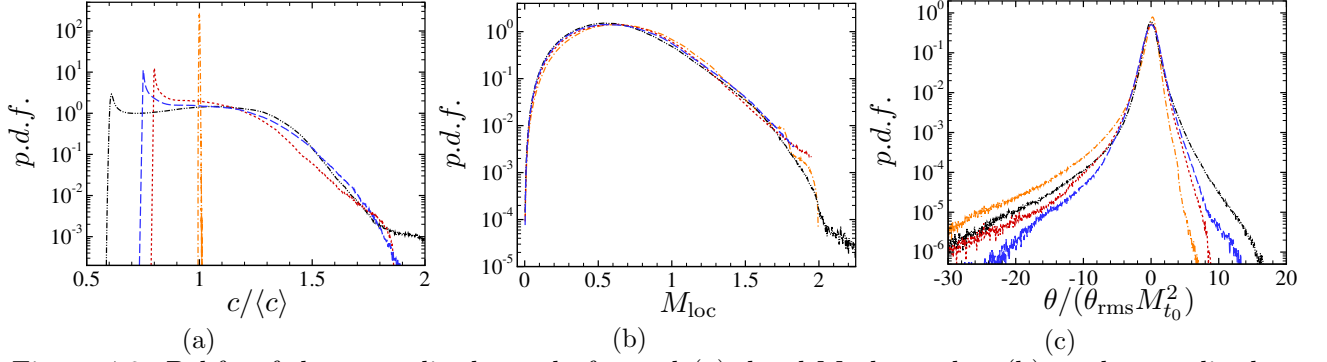


Figure 4.8. P.d.f.s of the normalized speed of sound (a), local Mach number (b), and normalized dilatation (c) for $M_{t_0} = 1$ ($t = 2$). — · — ·: PP11-PFG; — · — · — ·: PP11-VDW; — — —: PP11-MAH-IC1; — — —: PP11-MAH-IC2.

MAH or VDW provide similar qualitative behaviours of the general flow statistics. Specifically, the appearance of BZT effects plays only a minor role in the overall evolution of the general statistics. Similar conclusions are drawn for the initial thermodynamic state, provided the latter lies in the dense gas region.

The probability density function of the sound speed (a), local Mach number (b) and normalized dilatation (c) at $M_{t_0} = 1$ ($t = 2$), are reported in figure 4.8. For PFG, the speed of sound exhibits a Dirac-like p.d.f; on the contrary, a widespread, skewed p.d.f. is observed when a dense gas model is used. The p.d.f. is truncated on the left side (corresponding to the minimal value of the speed of sound in the supercritical vapour region), whereas it exhibits a long right tail (especially for BZT cases PP11-MAH-IC2 and PP11-VDW), representative of the sharp increase of the speed of sound in the vicinity of the critical isotherm. The p.d.f. of the local Mach number is also strongly affected by dense gas effects. Specifically, in the proximity of the inversion zone, due to lower values taken by the speed of sound for dense gases with $\Gamma \approx 0$, the maximum Mach number attained by the flow (in statistical sense) is higher than in PFG.

Finally, the p.d.f. of the dilatation, characterized by a heavy left tail in the PFG case (due to the occurrence of strong compression regions, namely shocklets) becomes more and more symmetric as dense gas effects are introduced, as already observed in figure 3.21 for inviscid CHIT. For case

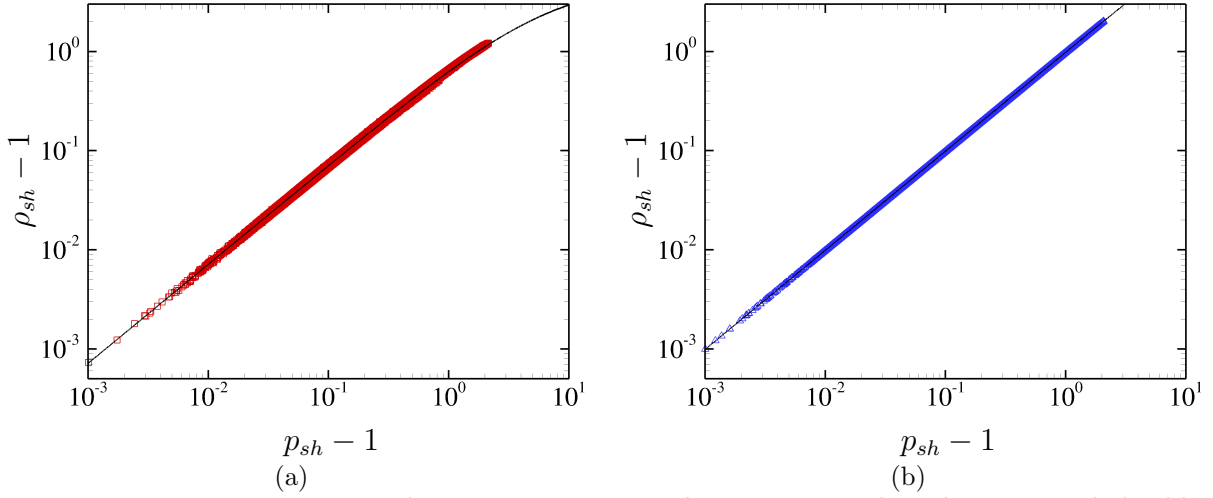


Figure 4.9. Pressure ratio p_{sh} vs density ratio ρ_{sh} in a direction normal to the extracted shocklets at $t = 2$ for Air (left panel) and PP11-PFG (right panel). The solid line denotes the ideal relation

PP11-MAH-IC1, the fundamental derivative is always positive and the reduction of the left tail is essentially due to the weakening of compression waves in the neighbourhood of $\Gamma = 0$ (see equation (1.3), compared to PFG for which $\Gamma = \mathcal{O}(1)$). For cases PP11-MAH-IC2 and PP11-VDW, the fundamental derivative takes negative values in some flow regions, which may lead to the formation of expansion shocklets in strong expansion regions, while inhibiting the formation of compression ones.

In order to detect the occurrence of eddy shocklets, [Samtaney *et al.* \(2001\)](#) developed an algorithm based on an edge-detection technique frequently used in image processing. The details of the algorithm and of its implementation are provided in appendix D. [Samtaney *et al.* \(2001\)](#) used the shocklet database to validate a simple model p.d.f. for the shocklet strength; afterwards, [Wang *et al.* \(2011\)](#) used the same algorithm to study the effect of shocklets on the velocity gradients and on the enstrophy generation in highly compressible isotropic turbulence. The algorithm uses the Rankine-Hugoniot relations to relate the states upstream and downstream the shocklet. For a perfect gas, the density ratio across the shock ρ_{sh} may be written as a function of the pressure ratio p_{sh} and the specific heat ratio γ , i.e.

$$\rho_{sh} = \frac{(\gamma + 1)p_{sh} + \gamma - 1}{(\gamma - 1)p_{sh} + \gamma + 1}. \quad (4.1)$$

Figure 4.9 shows the density jump against the corresponding pressure jump across shocks detected by the algorithm for air and PP11-PFG at $t = 2$. The solid line denotes the theoretical relation. Almost the totality of the points lie very close to the ideal curve, and their dispersion is much lower with respect to the case of [Samtaney *et al.* \(2001\)](#). This is mainly due to the higher turbulent Mach number and lower tolerance value for the penalty function. Nevertheless, the application of the algorithm for the detection of expansion shocklets in dense gases is not straightforward for several reasons. First, in dense gases it does not exist an equation of the type $\rho_{sh} = f(p_{sh})$ – being the specific heats not constant – and an iterative procedure must be used to find the theoretical downstream temperature (see, e.g. [Quartapelle *et al.* \(2003\)](#) for the nonpolytropic Van der Waals case). Furthermore, the algorithm is based on the Rankine-Hugoniot relations, which are derived from an inviscid framework, hence not taking into account the significant viscous effects that are present in the low- Re_λ configuration; the highest deviations from the ideal curve are indeed obtained for low pressure and density jumps. Being the shocklets in dense gases much weaker with respect to

perfect gases, the algorithm fails in identifying them. Moreover, the penalty function does not take into account shock curvatures and shock accelerations (the shock is supposed to be one-dimensional and steady), thus the error on the results of the algorithm increases with higher fluctuations due to the higher average shock speed. In order to assess whether a surface is a shocklet or not, an entropy condition should be imposed in addition to the Rankine-Hugoniot relations. For instance, if one consider the surfaces characterized by strong expansions and null density laplacian ($\nabla^2 \rho = 0$ and $\theta/\theta_{\text{rms}} > 3$), the algorithm find more than 2000 points for PFG cases, marking them as shocklets. Some modifications are therefore needed to apply the shock-detection algorithm in dense gases, representing an interesting perspective of this work.

4.1.2 Influence of the fluid type

Numerical simulations were performed also for other families of dense fluids. Specifically, we considered the siloxanes D5 and D6, and the refrigerants R134a and R245fa. The former are modelled by means of the Span-Wagner EoS for non-polar fluids, whereas for the latter the version for polar fluids is used. The thermodynamic properties of these fluids are listed in table 2.1, whereas the two equations of state are described in section 2.1.2. We set the same initial reduced temperature and pressure as for the PP11-MAH-IC1 case, i.e., $T/T_c = 1.01$ and $p/p_c = 1.02$, with $M_{t_0} = 1$, $k_0 = 2$ and $\chi_0 = 0$. Results are shown in figures 4.10-4.11. Globally, fluids of the same family exhibit a very similar behavior, the differences in their properties being small. This is especially the case for D5 and D6, whose slightly different behavior is due to the higher molecular weight of D6.

The decay of the kinetic energy and the kinetic energy spectrum are similar to the perfect gas case, independently on the fluid considered. The p.d.f. of the velocity divergence is highly skewed towards negative values; siloxanes exhibit a slightly lighter left tail and heavier right tail with respect to refrigerants and air. As shown before for PP11, this behavior is related to the value of the fundamental derivative Γ (shown in figure 4.11a), which is lower than unity for D5 and D6 throughout the decay. R.m.s. density values are of the same order of magnitude of refrigerants, whereas temperature fluctuations are lower due to the higher – on average – specific heats. Despite the lower T_{rms} values, c_{rms} is higher, highlighting the strong dependence of the speed of sound on density values, unlike the case of air.

4.1.3 Mach number effects

In this section we discuss the time evolution of the flow statistics at various M_{t_0} , focusing on the MAH model and condition IC1. The results are compared with those of a standard diatomic gas, namely air, modelled as a perfect gas with $\gamma = 1.4$.

Figure 4.12 reports the time evolution of K/K_0 (a) and Ω/Ω_0 (b), and the compensated energy spectra at a time at which the enstrophy approximately peaks (c), for various M_{t_0} (left panels, air; right panels, PP11-MAH). Perfect and dense gas exhibit similar qualitative behaviours. After an initial transient (that establishes to let the flow to adjust to the purely solenoidal initial conditions), the turbulent kinetic energy decays at a rate that is weakly affected by M_{t_0} , and at $t = 4$ approximately 75% of the turbulent kinetic energy is dissipated. The enstrophy evolution exhibits a peak in the range $t \approx 1.5 \div 2$ depending on the value of M_{t_0} (figure 4.12 b). Due to the increased dissipation, the normalized enstrophy peak decreases with the Mach number and tends to occur at earlier times. Figures 4.12 a and b also show that in the perfect gas case the decay of turbulence kinetic energy is slightly faster, and the enstrophy peak is slightly smaller than in the dense gas case for high M_{t_0} . The distribution of the computed energy spectra (figure 4.12 c) shows that, when scaled with Kolmogorov's length scale, all data collapse well up to $k_{\text{max}}\eta \approx 2$ independently of M_{t_0} .

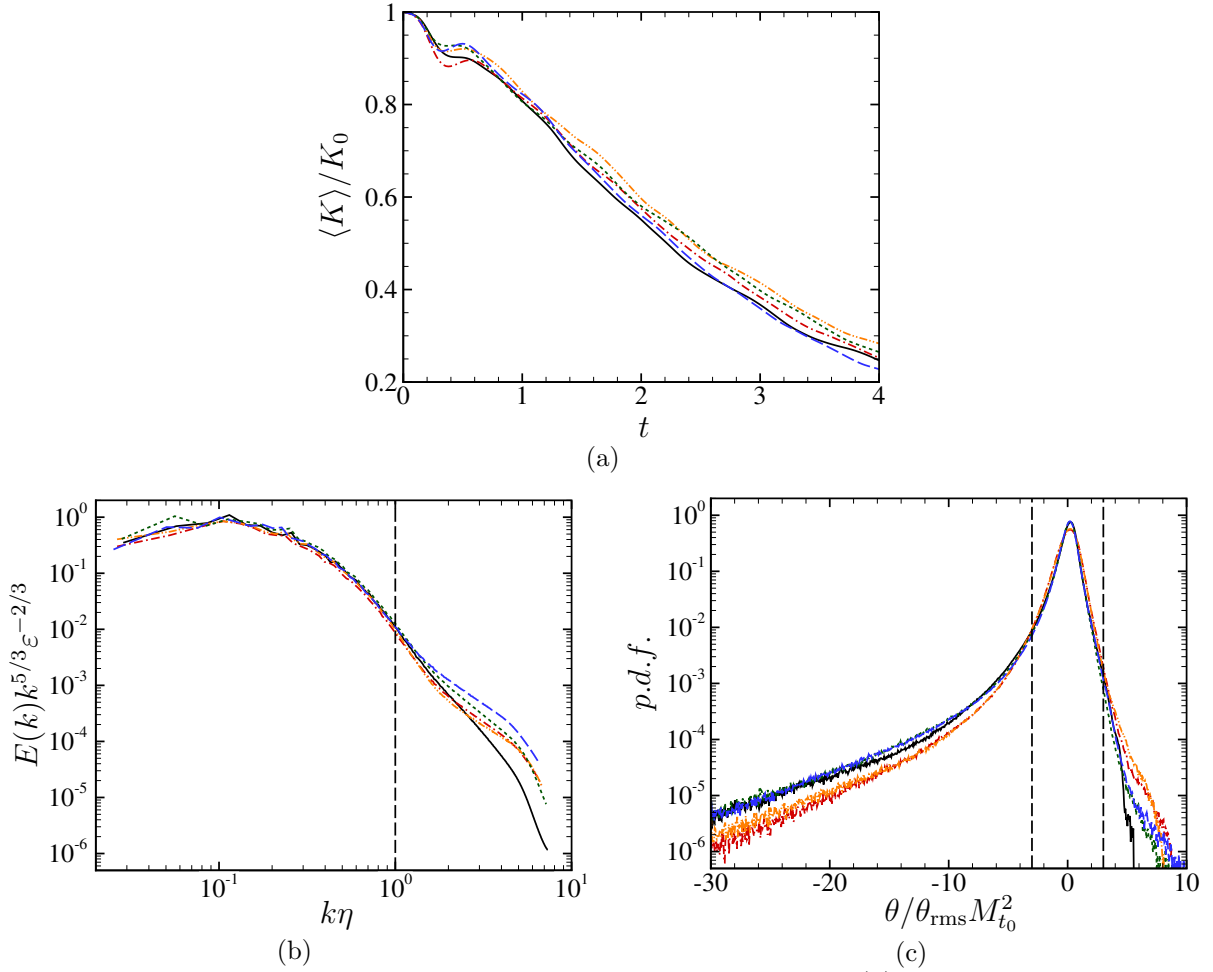


Figure 4.10. Time histories of the normalized turbulent kinetic energy (a), and premultiplied kinetic energy spectrum (b) and p.d.f. of the velocity divergence (c) at $t = 2$. —: Air; - - -: D5; . . . : D6; . . . : R134a; - - -: R245fa.

The p.d.f.s of the longitudinal velocity differences $\Delta u(\mathbf{r}) = \Delta u(\mathbf{r}) \cdot \mathbf{r} / \|\mathbf{r}\|$ have been computed at different separations, being \mathbf{r} the separation vector. Figure 4.13 shows the p.d.f. of $\Delta u(\mathbf{r})$ for air and PP11-MAH-IC1 at $M_{t_0} = 0.2$ (top panels) and 1 (bottom panels). At $M_{t_0} = 0.2$, the p.d.f.s exhibit stretched exponential tails at small spatial separations and approach Gaussian as the separation increases. Due to the low turbulent Mach number, these trends are very similar to those found in incompressible turbulence (Chen *et al.*, 1993). At $M_{t_0} = 1$, for both air and PP11 the shape of the p.d.f.s are highly skewed at small separations, due to the strong influence of the dilatational component of the velocity field (Wang *et al.*, 2012a).

Figure 4.14 reports the time histories of the r.m.s. of T , p and ρ . Temperature and pressure fluctuations in the dense gas are much smaller than in air. However, the dense gas solution significantly departs from the perfect gas one for $M_{t_0} \geq 0.5$. Finally, even if the time histories for the r.m.s. of the density are similar in both cases, the instantaneous ratio of maximum to minimum density is much smaller for the dense gas. At $M_{t_0} = 1$ the perfect gas density ratio is nearly 2.5 times greater than the dense gas. As the decay proceeds, compressibility effects decrease and the differences become smaller. This difference is likely to be due to the occurrence of compression shocklets that imply significant density variations, which are stronger in air than in the dense gas.

The observed differences between air and PP11 are tightly related to the fluid compressibility and

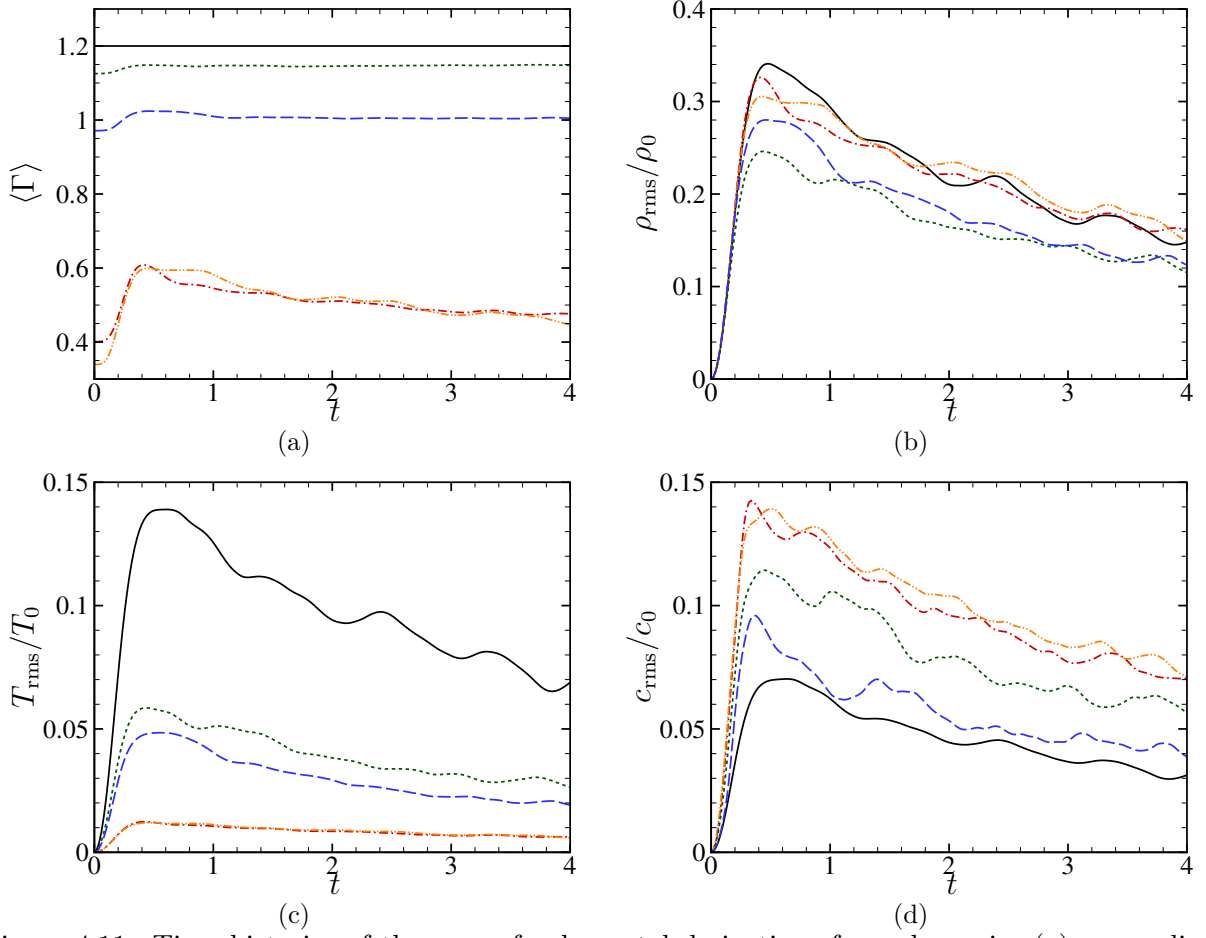


Figure 4.11. Time histories of the mean fundamental derivative of gas dynamics (a), normalized r.m.s. values of density (b), temperature (c) and speed of sound (d). —: Air; - · - ·: D5; · · · ·: D6; · · · ·: R134a; - - - -: R245fa.

are better understood by looking at the time evolution of the speed of sound, turbulent Mach number and dilatation (figure 4.15). At $M_{t_0} = 0.2$, compressibility effects are still weak in both cases and the two gases behave similarly. Departures from the standard behaviour start to become visible for $M_{t_0} = 0.5$ and increase significantly at higher Mach numbers. For air, $\langle c \rangle$ increases with the square root of the average temperature, while for the dense gas it strongly depends on density fluctuations, leading to a scattering of the flow thermodynamic states in the $p - v$ plane (see figure 4.16 where we report the thermodynamic states in the Clapeyron diagram at various M_{t_0}). In regions characterized by pressures higher than the initial one, the speed of sound is considerably higher than in low-pressure regions, resulting hence in an higher average sound speed than the initial one. At later times the scattering decreases due to turbulence decay, and $\langle c \rangle$ decreases accordingly. The r.m.s. of the dilatation has a peak (increasing with M_{t_0}) at $t \approx 0.6$ for the perfect gas case, whereas the dense gas exhibits a smoother behaviour and lower peak values. It is interesting to observe that the $\langle \Gamma \rangle$ remains below 1 throughout the decay (figure 4.17 a), while the Γ_{rms} (figure 4.17 b) is of the same order of $\langle \Gamma \rangle$ due to the considerable scattering in the thermodynamic space and to the strong increase experienced by the fundamental derivative in the high-pressure limit.

Regarding the time evolution of the viscosity, Eckert and Prandtl numbers we first observe that, both for PFG and DG gas, $\langle \mu \rangle$ varies as $\langle c \rangle$. Specifically $\langle \mu \rangle$ varies approximately as $\langle T \rangle^{0.7}$ in the

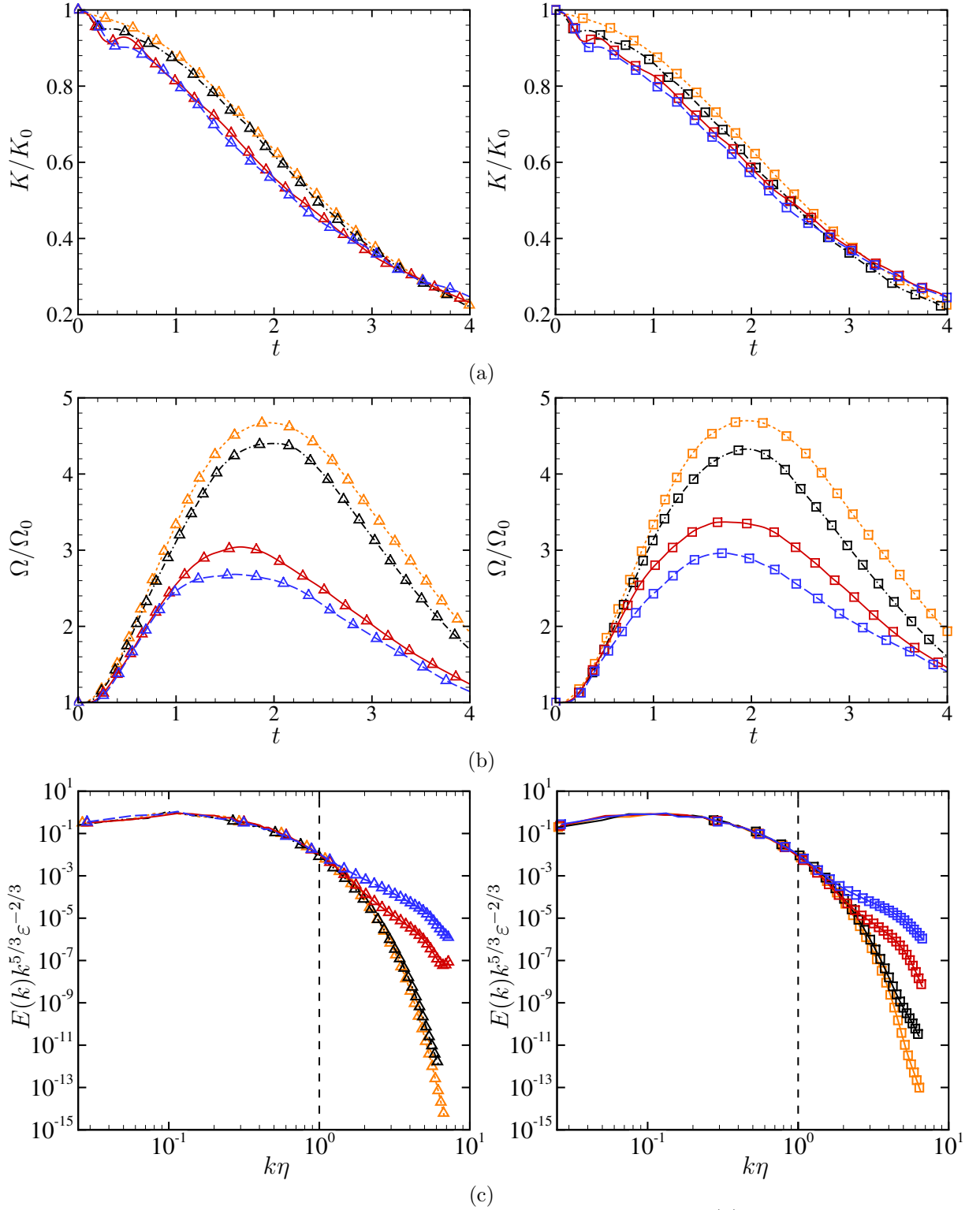


Figure 4.12. Time histories of the normalized turbulent kinetic energy (a), normalized enstrophy (b) and compensated turbulent kinetic energy spectra at $t = 2$ (c) for air (left panels) and PP11-MAH-IC1 (right panels) at various Mach numbers. ---: $M_{t_0} = 0.2$; -.-.-: $M_{t_0} = 0.5$; —: $M_{t_0} = 0.8$; ---: $M_{t_0} = 1.0$. Δ : Air; \square : PP11-MAH.

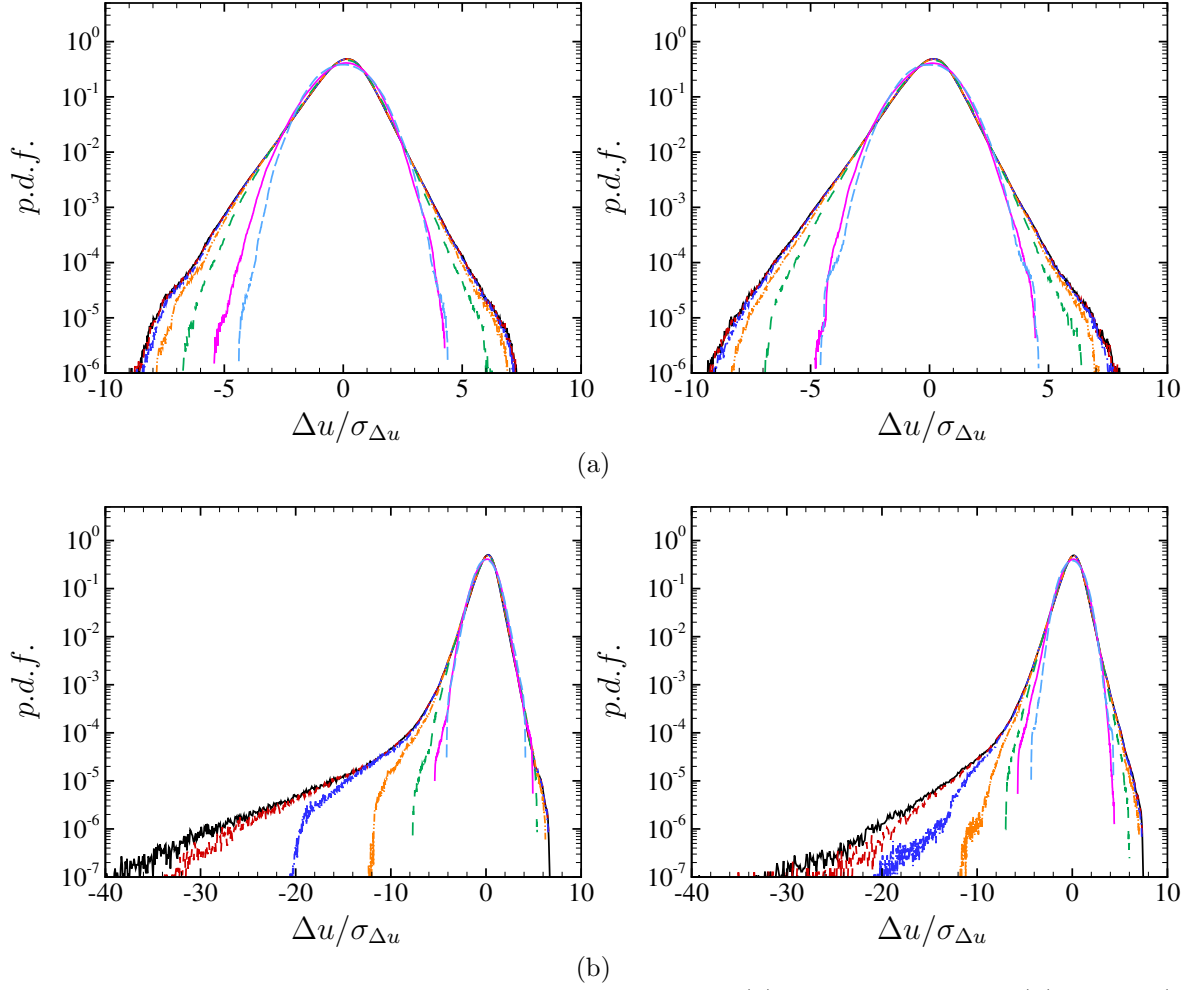


Figure 4.13. P.d.f.s of the velocity differences for $M_{t_0} = 0.2$ (a) and $M_{t_0} = 1$ (b) for air (left panels) and PP11-MAH-IC1 (right panels) at $t = 2$. —: $r = 1$; - - - : $r = 2$; - · - · : $r = 4$; · · · : $r = 8$; - - - - : $r = 16$; — : $r = 128$; - · - · - : $r = 256$.

perfect gas, while in the dense gas it is primarily driven by density variations (figure 4.18 a). As a result, viscosity grows with time in the perfect gas case and decreases (after the initial transient) for the dense gas. For air, the maximal value reached by the viscosity during the evolution is about 15% greater than the initial one (at the largest time considered in the simulations), whereas for the dense gas the peak of viscosity, reached at $t \approx 0.5$, is of the order of 3% only. The Eckert number (figure 4.18 b) is $\mathcal{O}(10^{-1})$ for PFG, whereas it is at least two orders of magnitude less for PP11, which implies that dynamical and thermal effects are loosely coupled at all M_{t_0} . Furthermore, $\langle Ec \rangle$ scales approximately with M_{t_0} both for air and PP11. It is interesting to observe that for the dense gas the Prandtl number (figure 4.18 c) varies in our case with M_{t_0} ranging approximately between 2.4 and 2.6 (whereas it is constant PFG), thus implying that energy transfer by viscous diffusion dominates with respect to heat conduction.

Figure 4.19 reports the time evolution of the skewness and flatness of the velocity gradients, computed as in equation (3.7). In both the perfect and dense gas case the considered higher-order statistics exhibit a minimum (maximum) at $t \approx 0.5$, which becomes lower (higher) as M_{t_0} is increased. Both quantities then evolve asymptotically toward the incompressible limit, the rate depending on M_{t_0} . We recall that the large magnitudes of the skewness and flatness observed for the highest Mach number cases are associated with the occurrence of strong compression re-

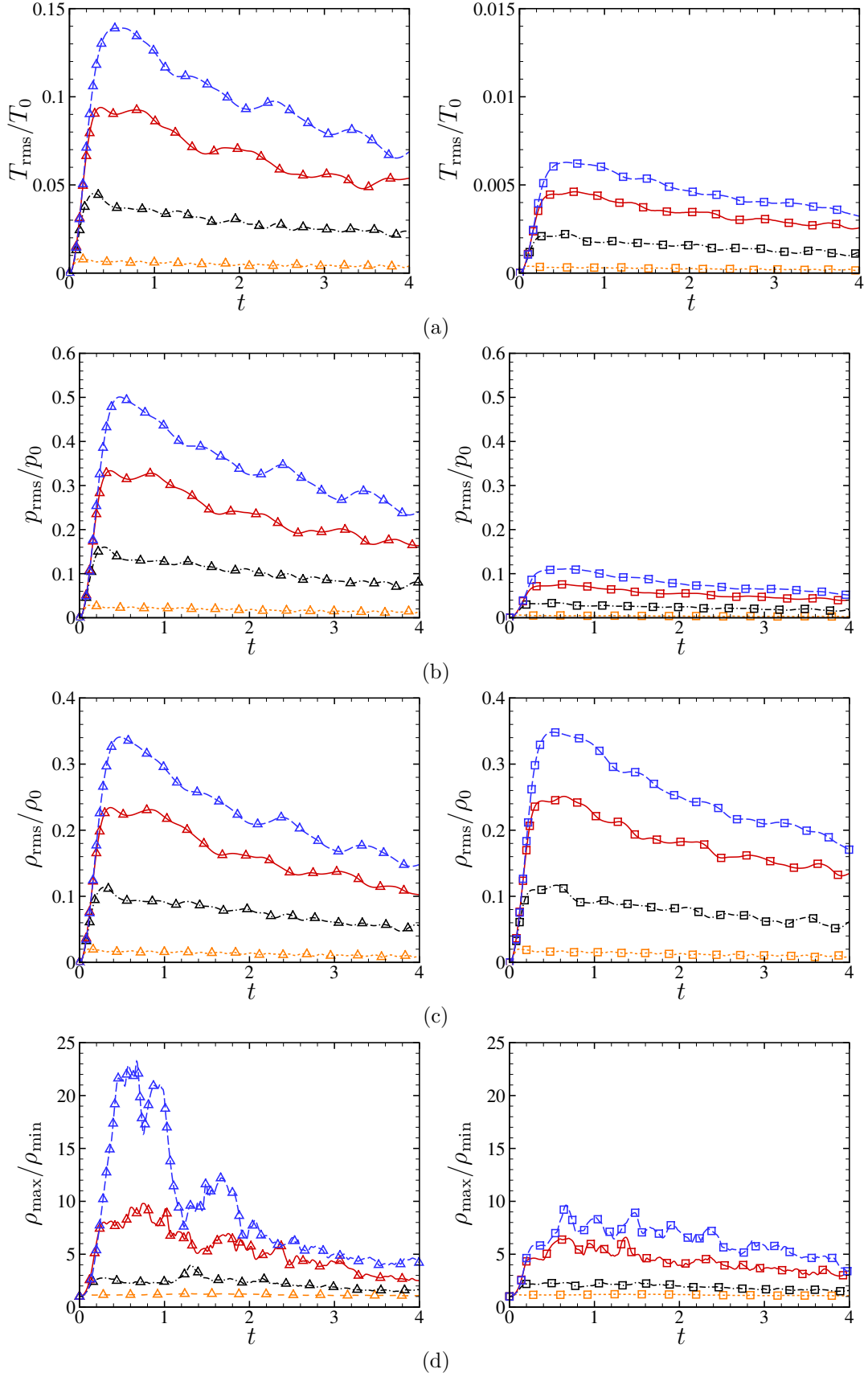


Figure 4.14. Time histories of the r.m.s. temperature (a), r.m.s. pressure (b), r.m.s. density (c), and maximum to minimum density ratio (d), for air (left panels) and PP11-MAH-IC1 (right panels) at various Mach numbers. ---: $M_{t_0} = 0.2$; -.-: $M_{t_0} = 0.5$; —: $M_{t_0} = 0.8$; ---: $M_{t_0} = 1$. \triangle : Air; \square : PP11-MAH.

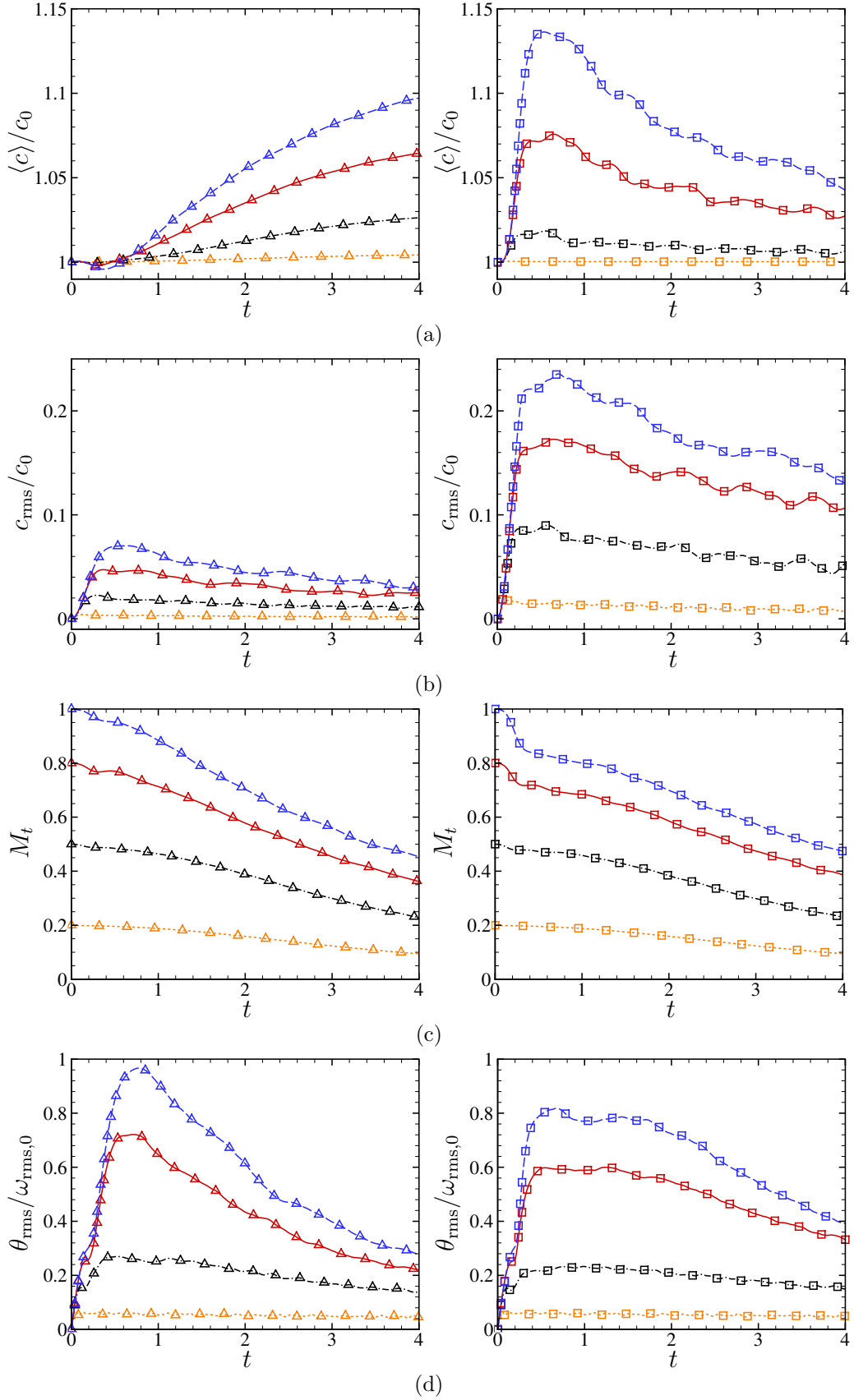


Figure 4.15. Time histories of normalized sound speed (a), r.m.s. sound speed (b), turbulent Mach number (c), and r.m.s. dilatation normalized with the initial r.m.s. vorticity (d), for air (left panels) and PP11-MAH-IC1 (right panels) at various Mach numbers. ---: $M_{t0} = 0.2$; ---: $M_{t0} = 0.5$; —: $M_{t0} = 0.8$; ---: $M_{t0} = 1.0$. \triangle : Air; \square : PP11-MAH.

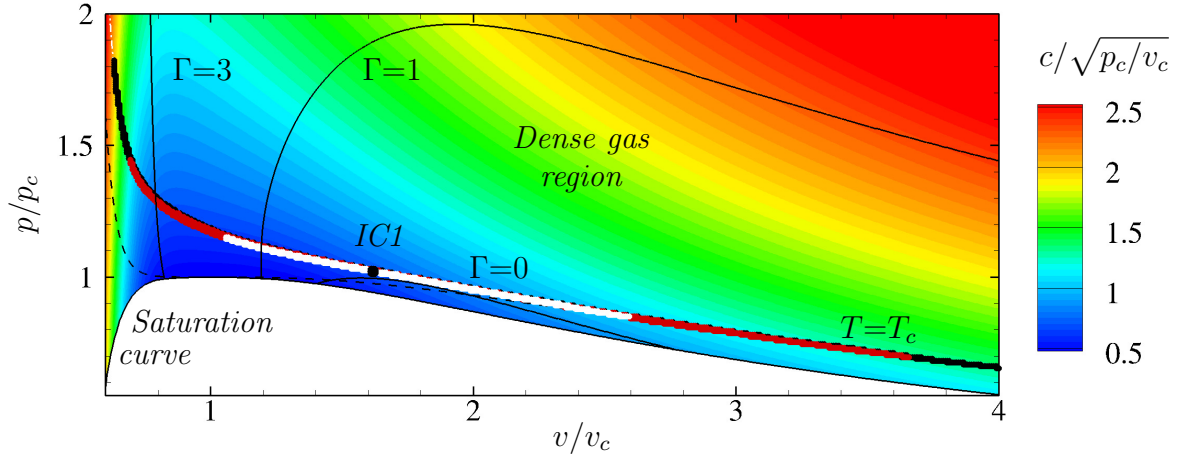


Figure 4.16. Distribution of the thermodynamic states in the Clapeyron diagram at $t = 2$ for PP11-MAH-IC1 at various M_{t_0} . White symbols: $M_{t_0} = 0.5$; red symbols: $M_{t_0} = 0.8$; black symbols: $M_{t_0} = 1$.

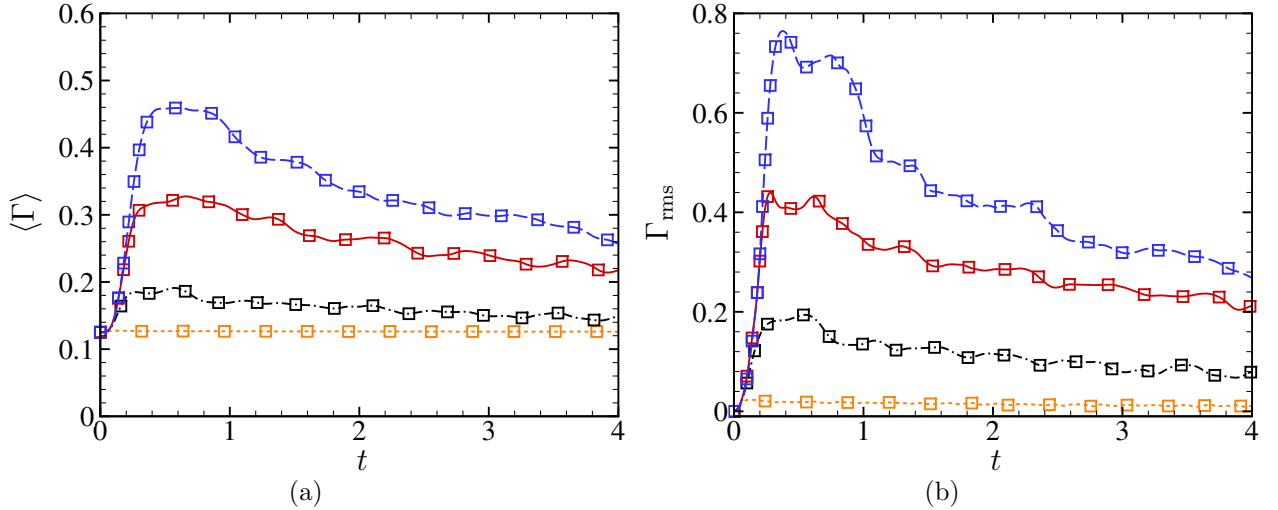


Figure 4.17. Time history of the average (a) and r.m.s. (b) fundamental derivative of gas dynamics at various M_{t_0} . ---: $M_{t_0} = 0.2$; -.-.-: $M_{t_0} = 0.5$; —: $M_{t_0} = 0.8$; - - -: $M_{t_0} = 1$. Δ : Air; \square : PP11-MAH.

gions, and specifically shocklets, as also pointed out by Wang *et al.* (2012b). We observe that the dense gas solution departs less from the incompressible behaviour and returns more quickly to the incompressible limit.

4.2 Small-scale features

4.2.1 Local flow topology

To elucidate the influence of dense gas effects on the statistical properties of turbulence structures, we consider the topological classification proposed by Perry & Chong (1987), Chong *et al.* (1990) and Kevlahan *et al.* (1992) in the framework of incompressible turbulence, and also employed by Pirozzoli & Grasso (2004) and Wang *et al.* (2012b) to analyse the small-scale behaviour of CHIT. As stated in section 2.1, the velocity gradient tensor A_{ij} may be broken up into a symmetric and an antisymmetric part, S_{ij} and W_{ij} respectively (equation (2.3)). Let P , Q and R be, respectively,

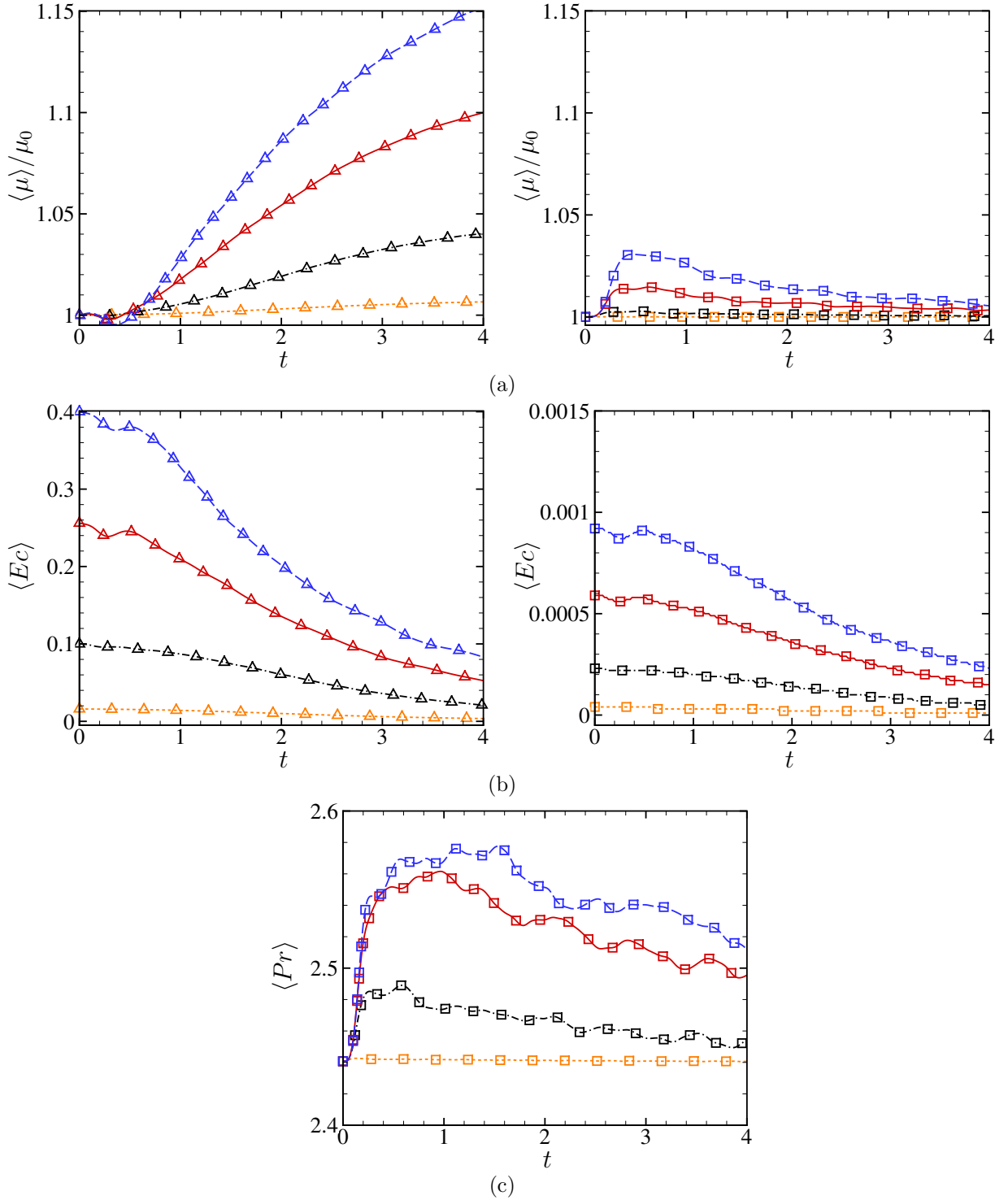


Figure 4.18. Time histories of the normalized average viscosity (a), Eckert number (b) for air (left panels) and PP11-MAH-IC1 (right panels) at various Mach numbers. The Prandtl number (c) is reported only for PP11, being constant and equal to 0.7 for air. ---: $M_{t_0} = 0.2$; -.-.-: $M_{t_0} = 0.5$; —: $M_{t_0} = 0.8$; ---: $M_{t_0} = 1$. \triangle : Air; \square : PP11-MAH.

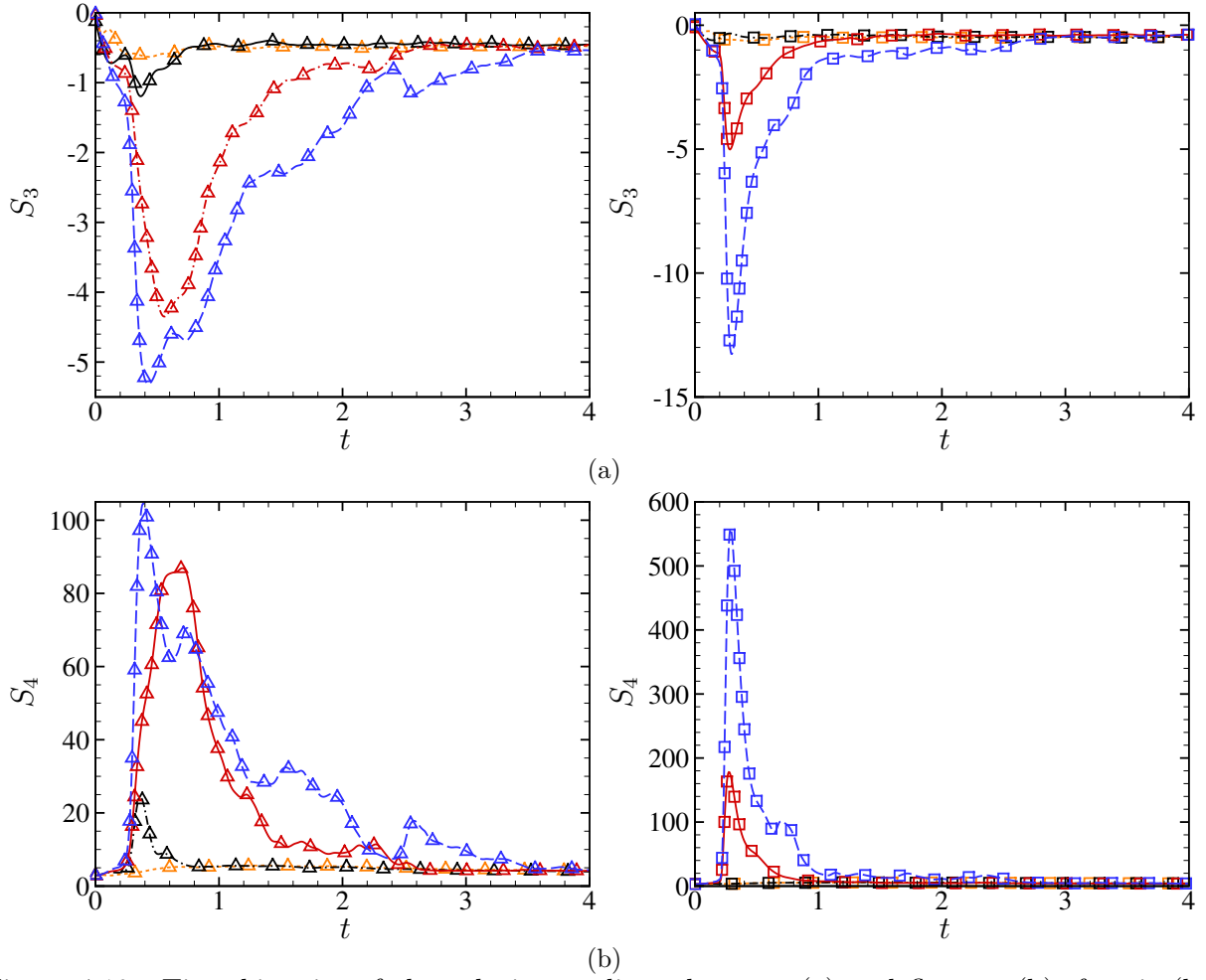


Figure 4.19. Time histories of the velocity gradient skewness (a) and flatness (b), for air (left panels) and PP11-MAH-IC1 (right panels) at various Mach numbers. ---: $M_{t_0} = 0.2$; -.-.-: $M_{t_0} = 0.5$; —: $M_{t_0} = 0.8$; ---: $M_{t_0} = 1$. \triangle : Air; \square : PP11-MAH.

the first, second and third invariant of A_{ij} , defined as

$$P = -\text{tr}[A_{ij}] = -S_{ii} = -(\lambda_1 + \lambda_2 + \lambda_3) \quad (4.2)$$

$$Q = \frac{1}{2}(P^2 - \text{tr}[A_{ij}^2]) = \frac{1}{2}(P^2 - S_{ij}S_{ij} + W_{ij}W_{ij}) = \lambda_1\lambda_2 + \lambda_1\lambda_3 + \lambda_2\lambda_3 \quad (4.3)$$

$$R = -\det[A_{ij}] = \frac{1}{3}(-P^3 + 3PQ - \text{tr}[A_{ij}^3]) = \frac{1}{3}(-P^3 + 3PQ - S_{ij}S_{jk}S_{ki} - 3W_{ij}W_{jk}S_{ki}) = -\lambda_1\lambda_2\lambda_3 \quad (4.4)$$

where λ_i are the three eigenvalues of A_{ij} . Similarly, the invariants of S_{ij} and W_{ij} are defined by their characteristic equations, and can be computed by setting $S_{ij} = 0$ for the invariants of W_{ij} and vice-versa for the invariants of S_{ij} .

The nature of turbulent structures is classified according to the sign of the discriminant of A_{ij} :

$$\Delta = \frac{27}{4}R^2 + (P^3 - \frac{9}{2}PQ)R + (Q^3 - \frac{1}{4}P^2Q^2) \quad (4.5)$$

When Δ is positive, the velocity gradient tensor has one real eigenvalue and two complex-conjugate

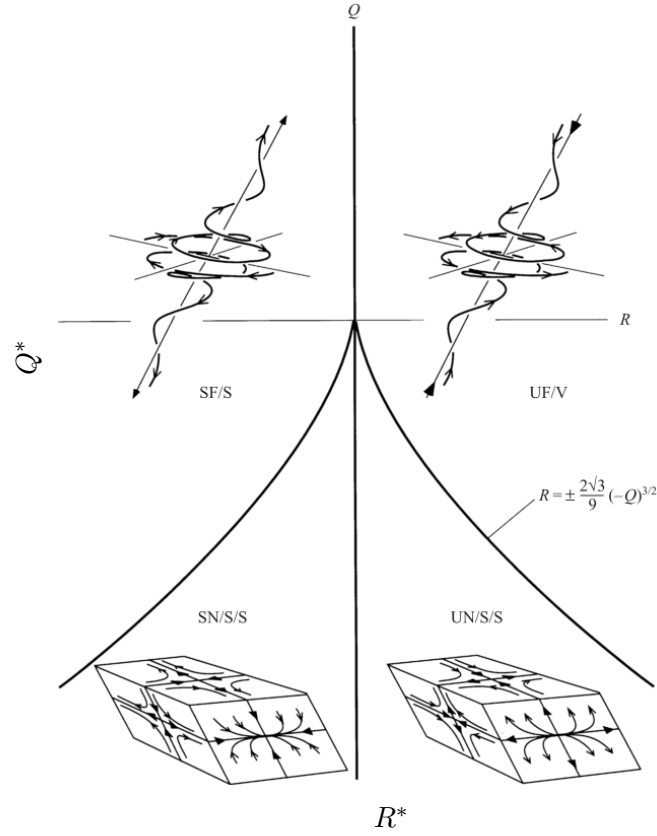


Figure 4.20. Local topologies for incompressible flows. Extracted from Ooi *et al.* (1999).

ones, and focal regions are present; on the contrary, when Δ is negative, the eigenvalues of A_{ij} are all real and turbulent regions are nonfocal. Moreover, in the case of incompressible turbulence ($P = 0$) flow regions are further classified according to the sign of R , as shown in figure 4.20, leading to the following families of configurations:

$$\begin{cases} \Delta > 0 & \begin{cases} R < 0 & \text{stable focus-stretching} \\ R > 0 & \text{unstable focus-compressing} \end{cases} \\ \Delta < 0 & \begin{cases} R < 0 & \text{stable node-saddle-saddle} \\ R > 0 & \text{unstable node-saddle-saddle} \end{cases} \end{cases} \quad (4.6)$$

In the case of compressible turbulence, according to the sign of P additional topologies can be identified, referred-to as stable-focus compressing, unstable focus-stretching, stable node-stable node-stable node, and unstable node-unstable node-unstable node regions (Chong *et al.*, 1990). In shock/turbulence interaction Kevlahan *et al.* (1992) have analyzed the evolution of turbulent structures in terms of the deviatoric part of the strain-rate tensor $S_{ij}^* = S_{ij} - \frac{1}{3}S_{kk}\delta_{ij}$ and the rotation-rate tensor W_{ij} , and have classified the flow into three regions, namely:

$$\begin{cases} W^2 < S^{*2}/2 & \text{convergence zones (essentially irrotational)} \\ S^{*2}/2 \leq W^2 \leq 2S^{*2} & \text{shear zones} \\ W^2 > 2S^{*2} & \text{eddy-dominated zones (highly rotational)} \end{cases} \quad (4.7)$$

Furthermore, turbulent structures behave as compressible or incompressible depending on the value

Table 4.2. Classification of turbulent regions in three-dimensional compressible flow according to Kevlahan *et al.* (1992).

	Incompressible $O \leq 0.05$	Compressed $O > 0.05$ $\theta < 0$	Expanding $O > 0.05$ $\theta > 0$
Eddy	EI	EC	EE
Convergence	CI	CC	CE
Shear	SI	SC	SE

of the parameter O :

$$O = \frac{\theta^2}{S^{*2} + W^2}; \quad \begin{cases} O \leq 0.05 & \text{incompressible structures} \\ O > 0.05 & \text{compressible structures} \end{cases} \quad (4.8)$$

All possible combinations of turbulent structures are summarized in table 4.2. Furthermore, as done in the inviscid case (section 3.4.3), we use the same classification to separate compressions and expansions into strong, moderate and weak dilatation regions, according to the local dilatation.

In the discussion that follows the statistical data are plotted at nondimensional time $t = 2$.

The distribution of the volume fractions $\langle V \rangle$ occupied by the different structures conditioned on the above-defined dilatation levels is presented in figure 4.21 as a function of M_{t_0} , for perfect and dense gas. Up to $M_{t_0} = 0.5$, moderate and strong dilatation regions are close to zero, and the flow volume is nearly symmetrically occupied by weak expansion and compression regions. At the higher M_{t_0} , due to the development of moderate and strong compression and the progressive reduction of weak expansion regions this symmetry is rapidly broken in the PFG cases. At $M_{t_0} = 1$, strong compressions occupy approximately 3.5% of the total volume for PFG, while they represent about 3% for PP11. The remaining 50% of the flow volume is mostly occupied by weak expansions for air, while strong expansions occupy only $\approx 0.5\%$ of the total volume (at $M_{t_0} = 1$), in agreement with results of Wang *et al.* (2012b). In dense gas, strong compressions tend to be inhibited and strong expansions enhanced, leading to a nearly symmetric repartition of the volume fractions, as already observed in inviscid CHIT of BZT Van der Waals gas (see section 3.4.4). At $M_{t_0} = 1$, weak dilatation regions occupy $\approx 40\%$ only, while moderate and strong expansion occupy, respectively, approximately 10% and 2% of the flow volume. The present results show that strong expansions are highly enhanced in the dense gas even when the operating conditions (IC1) do not allow BZT effects like expansion eddy shocklets. However, BZT effects contribute to further enhance expansions at the expense of compressions. Table 4.3 summarizes the percentage of focal and non focal structures conditioned on the different dilatation levels as a function of the initial turbulent Mach number. The results are quite insensitive to the type of gas up to $M_{t_0} = 0.5$, then the repartition changes more and more as compressibility effects increase. At $M_{t_0} = 1$, focal structures occupy 63% of the total volume for the PFG, whereas it is 58% for IC1 and even lower (57%) for IC2. The largest deviations are observed in moderate and strong expansion regions, which are much more populated by non focal structures in the dense gas than PFG.

For a variety of incompressible flows, including forced isotropic turbulence (Ooi *et al.*, 1999), plane mixing layers (Soria & Cantwell, 1994), channel flows (Blackburn *et al.*, 1996) and turbulent boundary layers (Chong *et al.*, 1998), an universal behavior has been observed when analyzing the flow topology in the $(Q - R)$ plane. Specifically, the joint p.d.f. (Q, R) is found to exhibits a tear drop shape. In order to analyze the influence of dense gas effects on the dynamics of CHIT, we follow the approach of Pirozzoli & Grasso (2004) developed for perfect gas flows. We have then

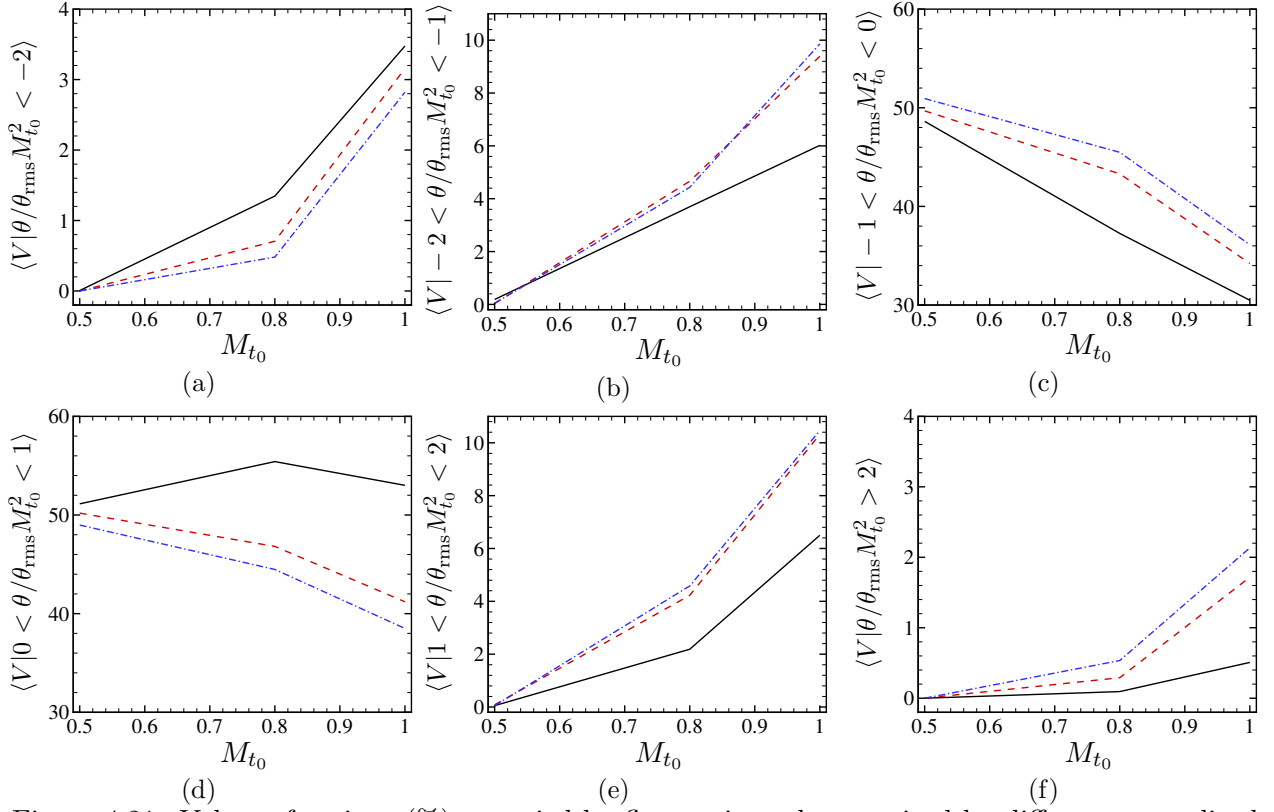


Figure 4.21. Volume fractions (%) occupied by flow regions characterized by different normalized dilatation intervals as a function of M_{t_0} ($t = 2$). —: Air; - - -: PP11-MAH-IC1; - · - · -: PP11-MAH-IC2. (a) Strong compressions; (b) moderate compressions; (c) weak compressions; (d) weak expansions; (e) moderate expansions; (f) strong expansions.

Table 4.3. Percentage of focal/non focal structures according to dilatation levels (at nondimensional time $t = 2$). PP11-IC1 and PP11-IC2 refer to MAH EoS.

M_{t_0}	$\theta/\theta_{rms}M_{t_0}^2$ (%)	$[-\infty, -2]$		$[-2, -1]$		$[-1, 0]$		$[0, 1]$		$[1, 2]$		$[2, +\infty]$	
		F.	N.F.	F.	N.F.	F.	N.F.	F.	N.F.	F.	N.F.	F.	N.F.
0.5	Air	0.0	0.0	0.1	0.1	30.6	18.0	31.7	19.5	0.0	0.0	0.0	0.0
	PP11-IC1	0.0	0.0	0.0	0.0	30.7	19.0	30.8	19.4	0.0	0.0	0.0	0.0
	PP11-IC2	0.0	0.0	0.0	0.0	31.2	19.8	29.3	19.6	0.0	0.0	0.0	0.0
0.8	Air	0.6	0.7	2.1	1.5	23.4	13.9	35.2	20.2	1.5	0.7	0.1	0.0
	PP11-IC1	0.3	0.4	2.3	2.4	26.6	16.7	28.4	18.4	2.2	2.0	0.1	0.2
	PP11-IC2	0.2	0.3	2.1	2.4	27.3	18.2	27.0	17.5	2.3	2.3	0.2	0.3
1.0	Air	1.5	1.9	3.3	2.7	18.7	11.8	34.5	18.5	4.4	2.1	0.3	0.2
	PP11-IC1	1.1	2.0	4.6	4.8	20.2	14.0	24.9	16.3	6.0	4.4	0.8	0.9
	PP11-IC2	1.0	1.9	4.7	5.2	21.5	14.7	23.0	15.5	5.5	4.9	0.9	1.3

formulated the problem in terms of the second and third invariants of the anisotropic part of the

velocity gradient tensor ($A_{ij}^* = A_{ij} - \theta\delta_{ij}/3$):

$$Q^* = -\frac{1}{2}(S_{ij}^*S_{ij}^* - W_{ij}W_{ij}) = Q - \frac{1}{3}P^2 \quad (4.9)$$

$$R^* = -\frac{1}{3}(S_{ij}^*S_{jk}^*S_{ki}^* + 3W_{ij}W_{jk}S_{ki}^*) = R - \frac{1}{3}PQ + \frac{2}{27}P^3 \quad (4.10)$$

where $P^* = 0$ and $\lambda_i^* = \lambda_i - \theta/3$ (note that, by construction, $\Sigma\lambda_i^* = 0$ and the discriminant reduces to $\Delta^* = 27/4R^{*2} + Q^{*3}$), and we have carried out a detailed analysis in the invariant plane, the objective being twofold: i) verify if the universal behaviour of the solenoidal component of the flow is recovered in dense gas flows, despite the peculiar transport properties of these gases; ii) investigate the influence of dense gas effects on the various flow structures.

In figure 4.22 we report the log of the total (left column) and conditioned joint p.d.f. of Q^* and R^* for air (panels a) and dense gas (MAH-IC1, panels b; MAH-IC2, panels c) for $M_{t_0} = 1$ (strong compressions, central column; strong expansions, right column). The joint p.d.f. is computed from the conditional averages of the data by dividing the (Q^*, R^*) plane into a number of equally sized partitions. For a good compromise between accuracy and statistical convergence each axis has been divided in $(2n)^{1/3}$ subdivisions, where $n = 512^3$ is the number of samples. As done in Chong *et al.* (1990) and Pirozzoli & Grasso (2004) the invariants are normalized by the average of the second invariant of the rotation-rate tensor ($\langle Q_W \rangle = \langle W_{ij}W_{ij}/2 \rangle$), which is a measure of the rotation energy. The thin solid line represents points where $\Delta^* = 0$ (so as to discriminate between focal and non focal regions). In the PFG and DG cases the joint p.d.f. (Q^*, R^*) exhibits a tear-drop shape as in the incompressible limit (Ooi *et al.*, 1999), with a statistical preference in the second and in the fourth quadrant, where points are aligned with the right branch of the zero-discriminant curve (Cantwell, 1993; Martín *et al.*, 1998; Pirozzoli & Grasso, 2004). It is interesting to observe that conditioning on strong compressions reveals an even stronger alignment with the right branch for all cases, as in Wang *et al.* (2012b). However, due to the weakening/suppression of compression structures, the tail of the tear-drop is slightly shorter in the dense gas cases, especially for the BZT condition IC2. The joint p.d.f.s conditioned on strong expansions exhibits more striking differences. For the dense gas case PP11-MAH-IC2 (whose initial thermodynamic state falls in the zone where Γ is negative) the p.d.f. tends to be skewed toward the left branch of the zero discriminant curve (in particular for probability levels of 10^{-3} , or higher), in contrast with PFG and PP11-MAH-IC1 that exhibit a more symmetric shape. The same result is obtained by conditioning the p.d.f.s on the type of local structures, namely, eddy, shear and convergence regions (as shown in figure 4.23). In dense gas, as in the case of air, eddies have focal character, shears have both focal and nonfocal topology, and convergence regions are essentially nonfocal and show a statistical preference for points to lie in the fourth quadrant, thus indicating that dense gas effects do not alter essentially the character of flow structures. However, the main differences are observed in convergence regions for PP11-MAH-IC2. This suggests that different flow structures may appear in the strong expansion regions of BZT flows. These structure have an influence on the dissipation and enstrophy generation, as discussed in the next sections. An interesting feature is that, for dense gas, expanding convergence regions (associated with strong expansion phenomena and, possibly, shocklets for the IC2 case) are almost as frequent as expanding shear zones, unlike the perfect gas for which shear regions dominate. This behaviour is likely to be related to the non-convex nature of the inviscid fluxes and to the degeneracy of the characteristic fields in the proximity of the inversion zone ($\Gamma \approx 0$), leading to the formation of steep expansion fronts, as discussed in greater detail in a later section.

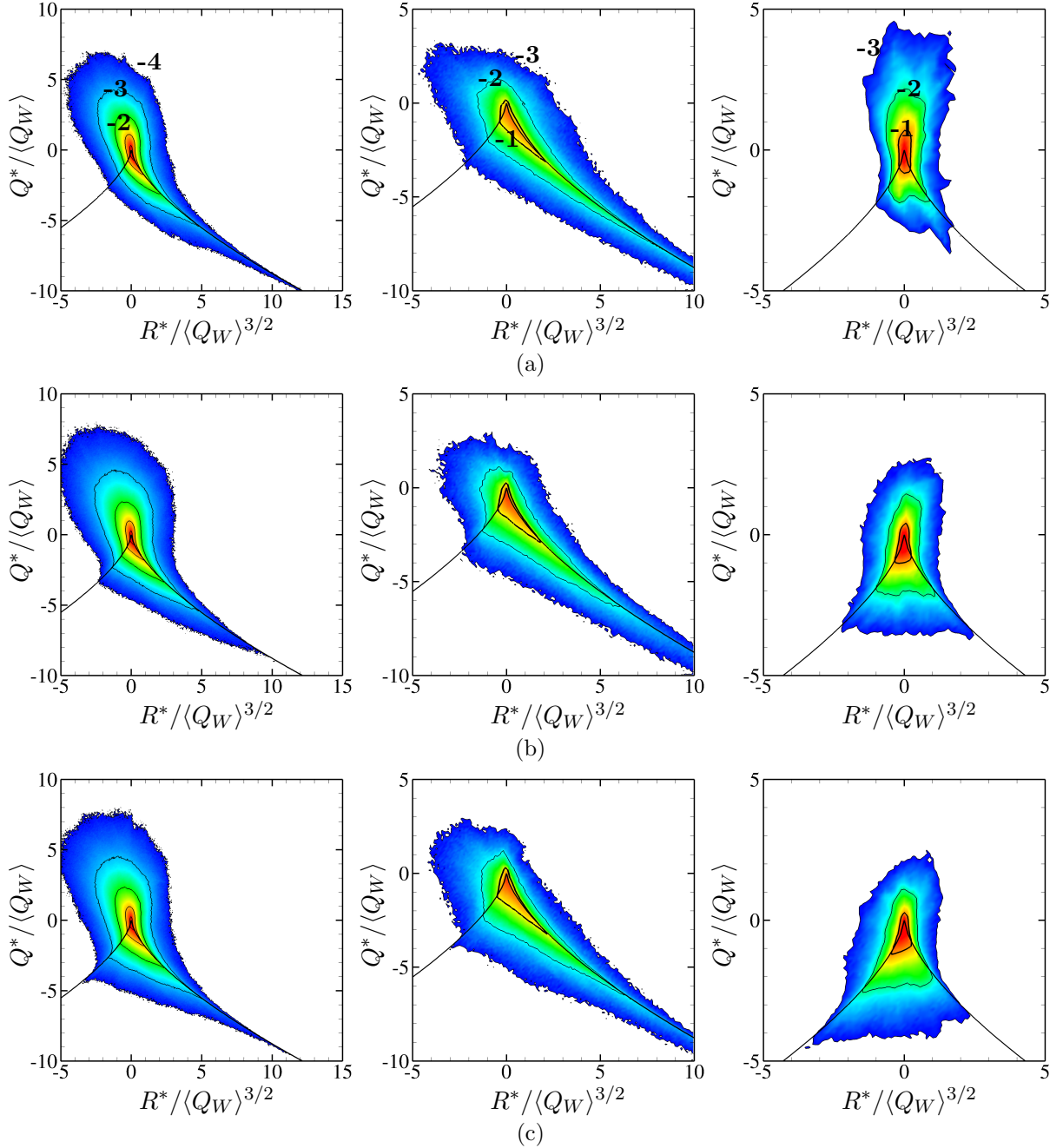


Figure 4.22. Iso-contours (-4 to 0, spacing equal to 1) of the \log_{10} of the joint p.d.f. of the scaled second and third invariants of the anisotropic part of the velocity gradient at $M_{t_0} = 1$ ($t = 2$) for air (panel a), PP11-MAH-IC1 (panel b) and PP11-MAH-IC2 (panel c). Left column: total joint p.d.f. Central column: p.d.f. conditioned on strong compressions (regions with $\theta/\theta_{\text{rms}} M_{t_0}^2 \in [-\infty, -2]$). Right column: p.d.f. conditioned on strong expansions (regions with $\theta/\theta_{\text{rms}} M_{t_0}^2 \in [2, \infty]$). The bold solid isoline denotes the iso-contour -3.

4.2.2 Contribution of flow structures to dissipation

To further elucidate the influence of dense gas on the role of focal and non focal structures, it is useful to consider the second invariants of the rotation-rate tensor ($Q_W = W_{ij}W_{ij}/2$) and of the anisotropic part of the strain-rate tensor ($Q_{S^*} = -S_{ij}^*S_{ij}^*/2$). We recall that for CHIT, under the

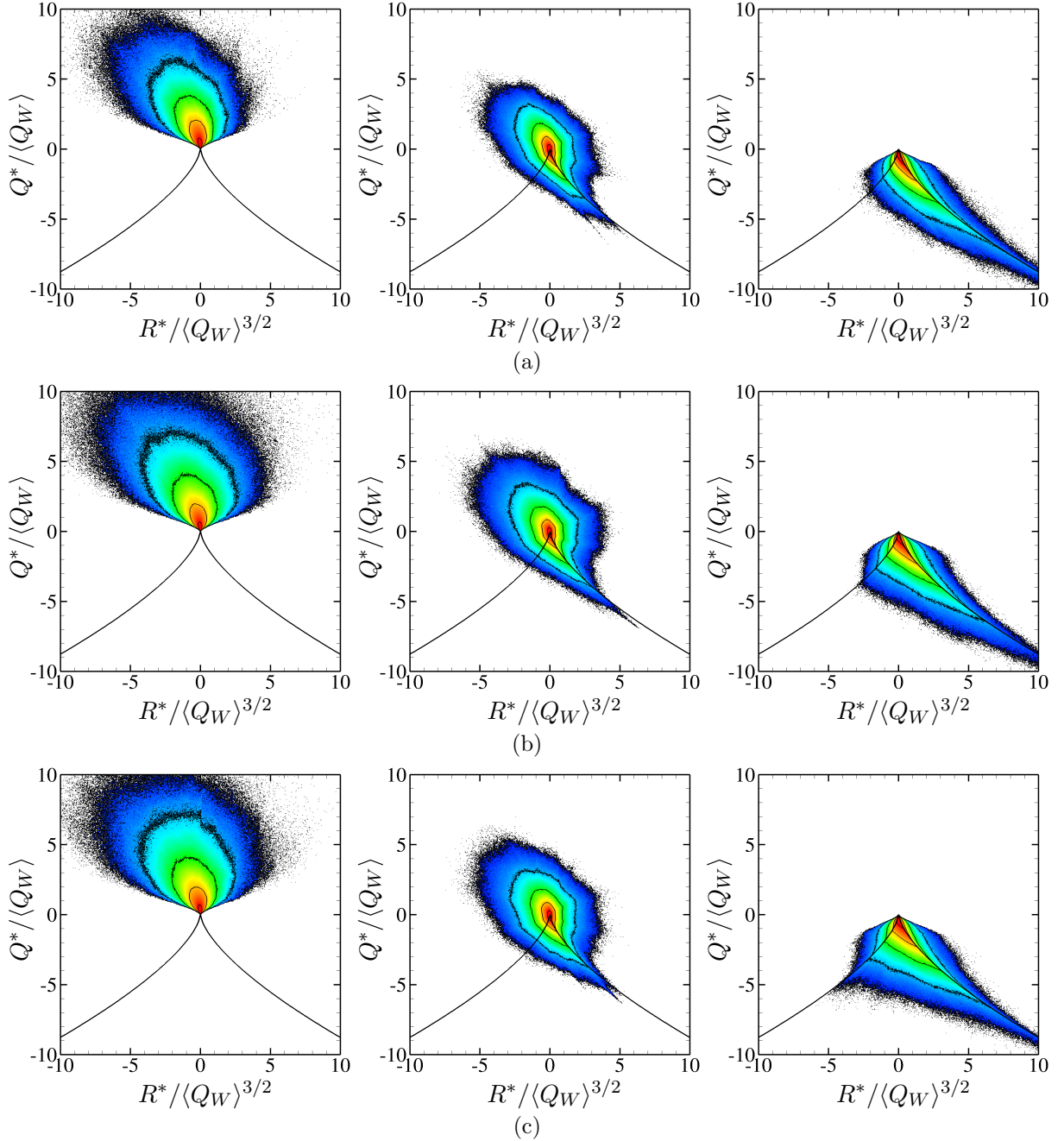


Figure 4.23. Iso-contours (-4 to 0, spacing equal to 1) of the \log_{10} of the joint p.d.f. of the scaled second and third invariants of the anisotropic part of the velocity gradient at $M_{t_0} = 1$ ($t = 2$) conditioned on the local type of structure for air (panel a), PP11-MAH-IC1 (panel b) and PP11-MAH-IC2 (panel c). Left column: eddy regions. Central column: shear regions. Right column: convergence regions.

assumption of weak variation of the viscosity coefficient (Sarkar *et al.*, 1991), one has

$$\varepsilon = -2\langle\mu\rangle\langle Q_{S^*}\rangle = 2\langle\mu\rangle\langle Q_W\rangle + \frac{2}{3}\langle\mu\rangle\langle P^2\rangle, \quad (4.11)$$

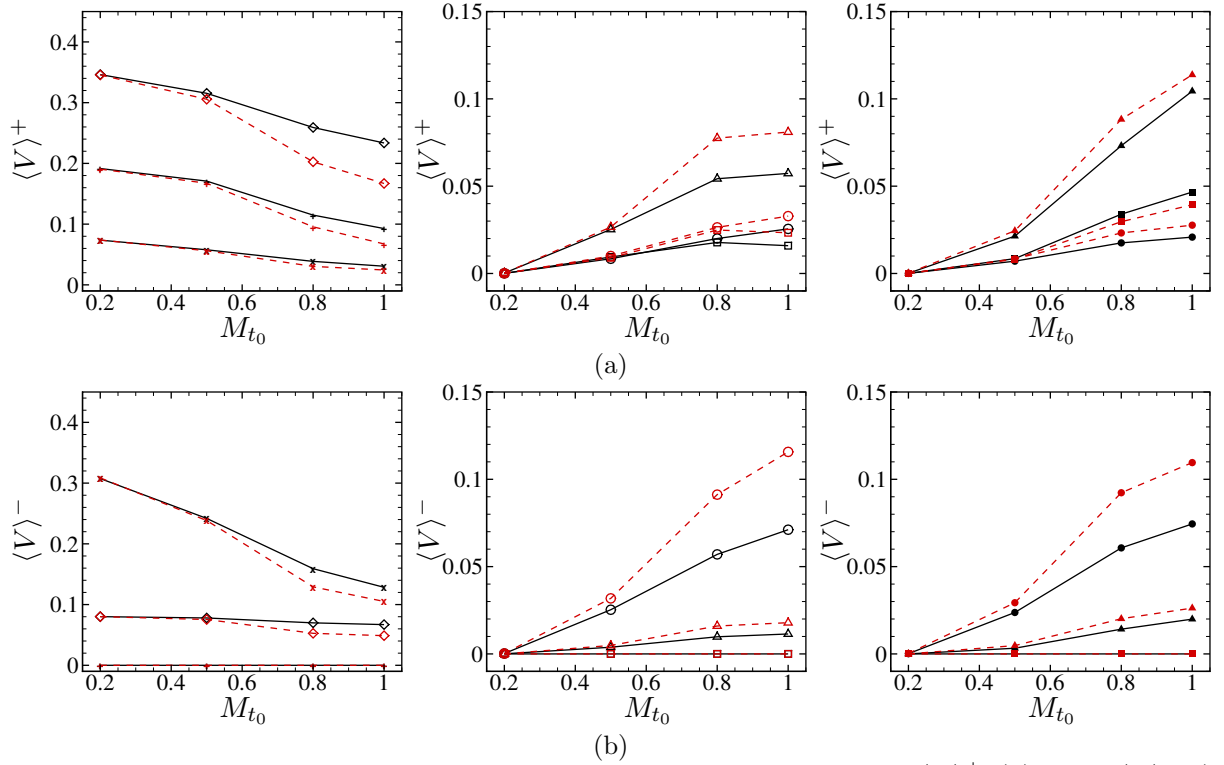


Figure 4.24. Fractional contribution of the various flow structures to $\langle V \rangle^+$ (a), and $\langle V \rangle^-$ (b) at various M_{t_0} ($t = 2$). Left column: incompressible structures; central column: compressed structures; right column: expanding structures. —: Air; - - - : PP11-MAH-IC1. +, EI; ×, CI; ◇, SI; □, EC; ○, CC; △, SC; ■, EE; ●, CE; ▲, SE.

where ε is the total dissipation, $2\langle\mu\rangle\langle Q_W\rangle$ and $\frac{2}{3}\langle\mu\rangle\langle P^2\rangle$ the solenoidal and dilatational components, respectively. Even though the analysis has been conducted at various M_{t_0} , in the following only the results corresponding to $M_{t_0} = 1$ are discussed.

The distribution of the volume fractions occupied by different structures is reported in figure 4.24 as a function of M_{t_0} (left column, incompressible structures; central column, compressed structures; right column, expanding structures) for air and PP11-IC1. In the following, we indicate with $\langle\cdot\rangle^+$ (respectively, $\langle\cdot\rangle^-$) a quantity associated to focal (respectively, non focal) structures. At low M_{t_0} we observe that, in the perfect gas case: i) structures of incompressible nature occupy a larger volume fraction than compressible ones; ii) shear-like structures are the most frequent and occupy $\approx 42\%$ of the flow volume; and iii) eddy and convergence zones represent $\approx 19\%$ and $\approx 38\%$ of the total flow volume, respectively. Up to $M_{t_0} = 0.5$, PP11 exhibits similar statistical volume fraction distributions. As the initial turbulent Mach number increases, the volume fraction occupied by incompressible structures is reduced significantly due to the development of compressible structures, whose volume fractions nearly triple when M_{t_0} is varied from 0.5 to 1. As compressibility effects become significant, the volume percentage associated to the different flow structures is most affected by the working fluid. Specifically, the volume fraction of compressible structures is 58% for PP11-IC1, whereas it is only 44% for air, and convergence and shear compressed regions are $\approx 30\%$ larger than in air. The choice of the initial conditions for the dense gas cases has a small influence on the computed volume fractions.

The fractional contributions of the different flow structures to the solenoidal, total and dilatational dissipation are shown, respectively, in figure 4.25, 4.26 and 4.27 (we only report case IC1, since the initial thermodynamic condition and, more generally, the thermodynamic model, has a negligible

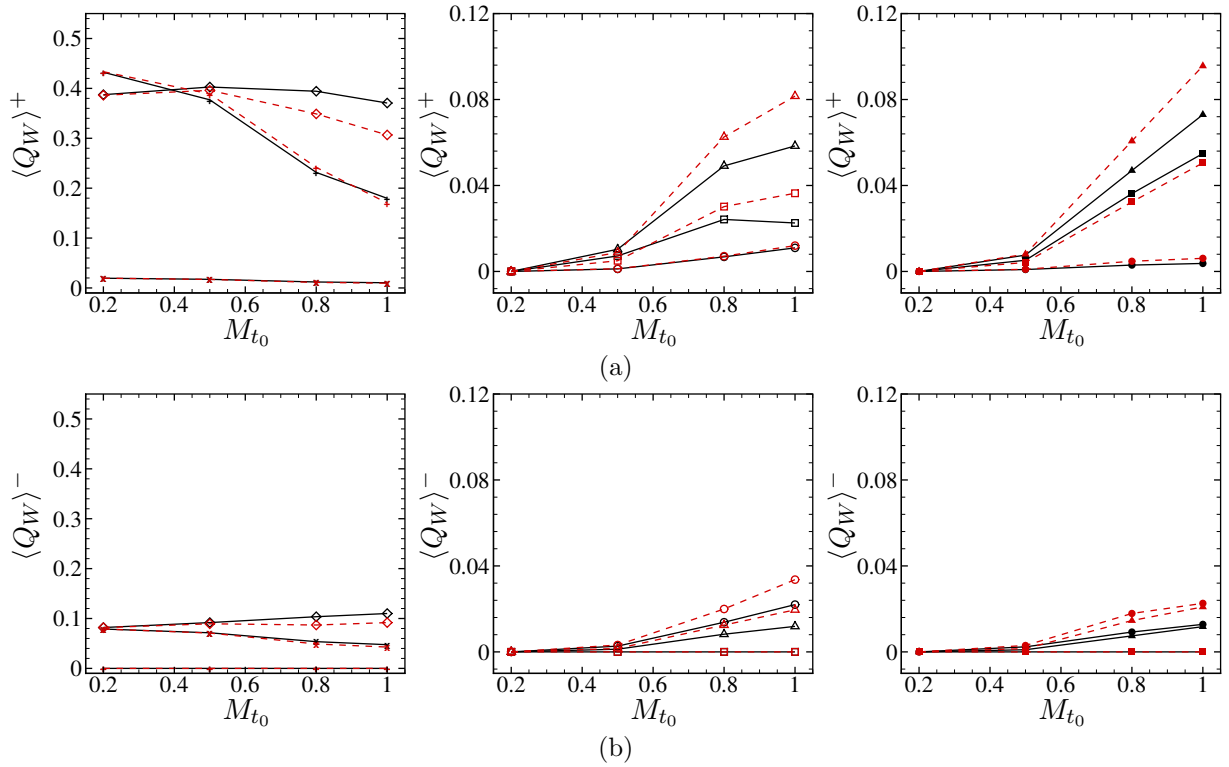


Figure 4.25. Fractional contribution of the various flow structures to the solenoidal dissipation $\langle Q_W \rangle^+$ (a) and $\langle Q_W \rangle^-$ (b), at various M_{t_0} ($t = 2$). Left column: incompressible structures; central column: compressed structures; right column: expanding structures. —: Air; - - -: PP11-MAH-IC1. +, EI; ×, CI; ◇, SI; □, EC; ○, CC; △, SC; ■, EE; ●, CE; ▲, SE.

influence on the solenoidal dissipation). For both perfect and dense gas cases, shear regions account approximately for 50% of the solenoidal dissipation (figure 4.25), albeit this percentage is slightly lower for PP11. The contribution of compressed and expanding structures to Q_W increases almost linearly with the turbulent Mach number, especially in focal regions. Nevertheless, even for the case $M_{t_0} = 1$ compressible regions contribute less than 20% of the total, the contribution being slightly higher for the dense gas. In all cases, the contribution of eddy-like regions is almost negligible.

At low M_{t_0} , both for perfect and dense gas, focal and non focal structures contribute to kinetic energy dissipation by the same amount, whereas at high M_{t_0} the contribution of nonfocal compressible convergence structures is significantly increased (figure 4.26). The increase is more significant in the dense gas case. In particular, the contribution of expanding non focal structures at $M_{t_0} = 1$ is about twice than the one found in the PFG.

The most interesting differences between the perfect and the dense gas concern the dilatational dissipation (figure 4.27). While the contribution of incompressible structures is almost the same both for PFG and DG, the contribution of compressible structures changes significantly. We observe in particular that, for the dense gas at high M_{t_0} , nonfocal expanding structures play a major role and contribute to the dilatational dissipation by an amount that is comparable to that of compressed focal structures ($\approx 20\%$ versus $\approx 30\%$). For condition IC2, for which the occurrence of expansion and compression shocklets is almost equally probable, this effect is even more accentuated (a comparison of the fractional contributions to $\langle Q_P \rangle^\pm$ for IC1 and IC2 is reported in figure 4.28). On the contrary, in the perfect gas compressed non focal structures (associated to the formation of eddy shocklets) contribute more significantly to dilatational dissipation than expanding ones. The amount of dilatational dissipation increases with the initial turbulent Mach number and, at

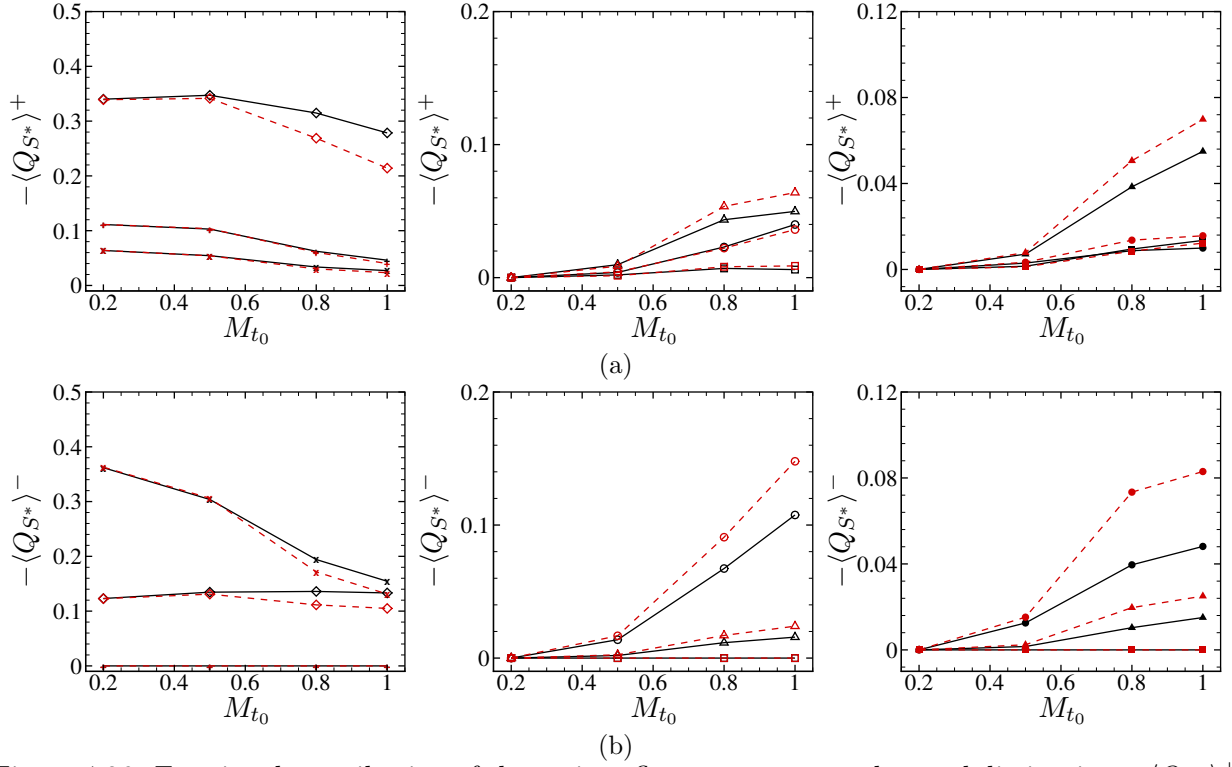


Figure 4.26. Fractional contribution of the various flow structures to the total dissipation $-\langle Q_{S^*} \rangle^+$ (a) and $-\langle Q_{S^*} \rangle^-$ (b) at various M_{t_0} ($t = 2$). Left column: incompressible structures; central column: compressed structures; right column: expanding structures. —: Air; ---: PP11-MAH-IC1. +, EI; ×, CI; ◇, SI; □, EC; ○, CC; △, SC; ■, EE; ●, CE; ▲, SE.

$M_{t_0} = 1$, it represents more than 50% of the total, whereas expanding ones contribute for less than 10% and the dependence on M_{t_0} is weak.

To further investigate the correlation between the various flow structures and the occurrence of strong compression/expansion phenomena, in figure 4.29 we report the volume fractions of the different flow structures conditioned with respect to strong compression ($\theta/\theta_{\text{rms}} M_{t_0}^2 < -2$) and strong dilatation zones ($\theta/\theta_{\text{rms}} M_{t_0}^2 > 2$). The former are populated by similar structures both in the perfect and dense gas, with convergence compressed zones representing more than 80% of the total volume and eddy zones being negligible. In the case of dense gas, convergence and shear zones represent, respectively, 75-80% (depending on the initial thermodynamic state) and 15-20% (eddy-like being negligible) of the volume occupied by expanding structures, whereas in air the different flow structures are nearly equally probable (45% shear, 30% convergence and 25% eddy-like).

Introducing the total flow volume having positive (negative) Δ^* greater (less) than the threshold value Δ_{th} , computed as

$$\mathcal{V}^\mp(\Delta_{th}) = \frac{\langle 1 | \Delta \lessgtr \mp \Delta_{th} \rangle}{\langle 1 \rangle} \quad (4.12)$$

we analyze the associated conditional cumulative averages of Q_{S^*} , Q_W and P^2 defined, respectively,

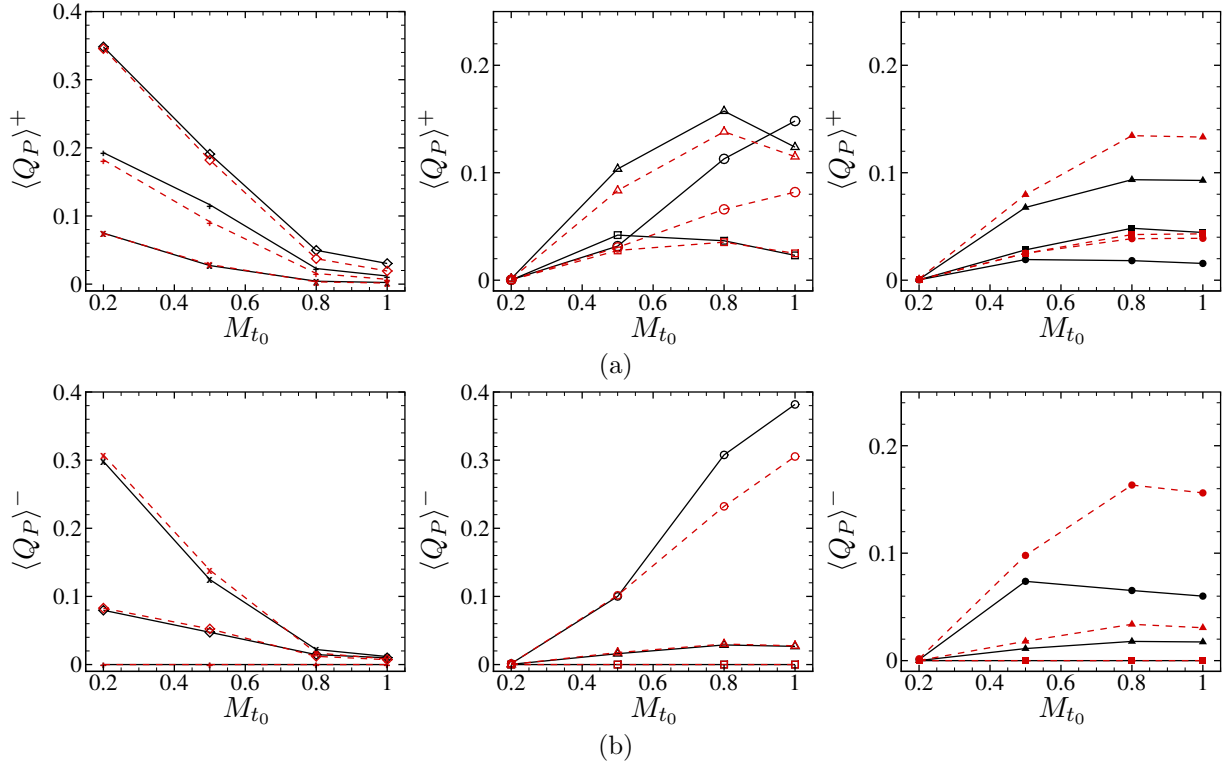


Figure 4.27. Fractional contribution of the various flow structures to the dilatational dissipation $\langle Q_P \rangle^+$ (a) and $\langle Q_P \rangle^-$ (b) at various M_{t_0} ($t = 2$). Left column: incompressible structures; central column: compressed structures; right column: expanding structures. —: Air; - - - : PP11-MAH-IC1. +, EI; ×, CI; ◇, SI; □, EC; ○, CC; △, SC; ■, EE; ●, CE; ▲, SE.

as:

$$\begin{aligned}
 Q_{S^*}^{\mp}(\Delta_{th}) &= \frac{\langle Q_{S^*} | \Delta^* \leq \mp \Delta_{th} \rangle}{\langle Q_{S^*} \rangle} \\
 Q_W^{\mp}(\Delta_{th}) &= \frac{\langle Q_W | \Delta^* \leq \mp \Delta_{th} \rangle}{\langle Q_W \rangle} \\
 Q_P^{\mp}(\Delta_{th}) &= \frac{\langle P^2 | \Delta^* \leq \mp \Delta_{th} \rangle}{\langle P^2 \rangle}
 \end{aligned} \tag{4.13}$$

where superscripts + and − indicate conditioning on focal and non focal structures, respectively. As already found by Pirozzoli & Grasso (2004), the dissipation (either total, solenoidal or dilatational) is approximately constant for $|\Delta/\langle Q_W \rangle^3| \leq 10^{-3}$ and structures are most active in the range $10^{-2} \leq |\Delta/\langle Q_W \rangle^3| \leq 10^3$ (see figure 4.30). We also observe that, contrary to the results reported in Pirozzoli & Grasso (2004), nonfocal, rather than focal structures, have a stronger influence on the dilatational dissipation, due to differences in Re_λ (simulations were carried out at $Re_\lambda = 50$ in Pirozzoli & Grasso (2004), while $Re_\lambda = 200$ in the current simulations).

The iso-surfaces of the strong compression regions $\theta/\theta_{rms} M_{t_0}^2 = -3$ (left panels) and of the strong expansion regions $\theta/\theta_{rms} M_{t_0}^2 = 3$ (right panels) are reported in figure 4.31 both for the air (a) and for the dense gas cases (b and c) at $M_{t_0} = 1$. For air, strong compression regions are populated by random sheet-like structures of convergence type topology over a wide range of scales, contrary to strong expansions that are characterized by sparse blob or tubular structures mainly of the eddy and shear type. The dense gas also exhibits compressed sheet-like shocklets and an increased volume percentage of expanding structures having tubular as well as sheet-like convergence topology. The

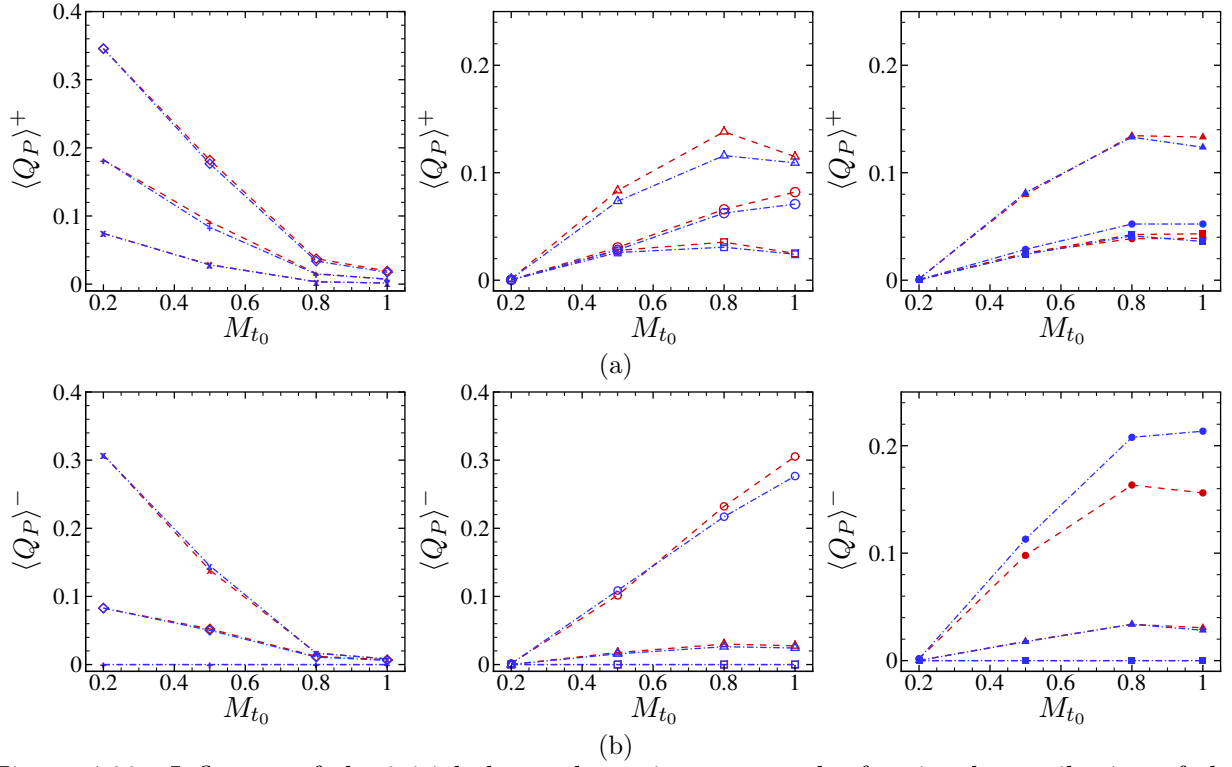


Figure 4.28. Influence of the initial thermodynamic state on the fractional contribution of the various flow structures to the dilatational dissipation $\langle Q_P \rangle^+$ (a) and $\langle Q_P \rangle^-$ (b) at various M_{t_0} ($t = 2$). Left column: incompressible structures; central column: compressed structures; right column: expanding structures. ---: PP11-MAH-IC1; -.-: PP11-MAH-IC2. +, EI; ×, CI; ◇, SI; □, EC; ○, CC; △, SC; ■, EE; ●, CE; ▲, SE.

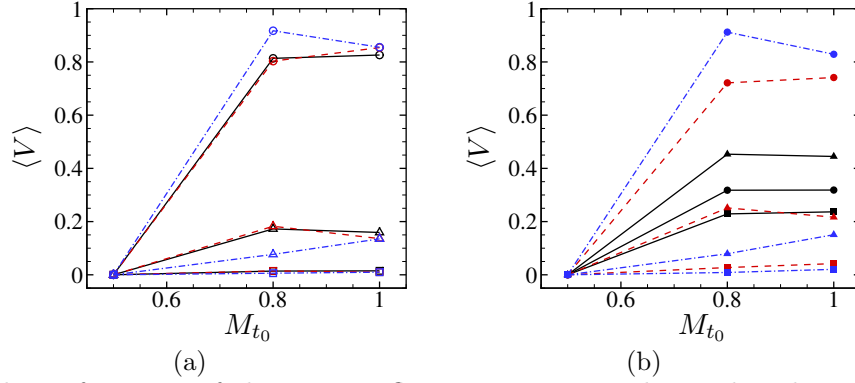


Figure 4.29. Volume fractions of the various flow structures conditioned with respect to strong compression regions (a) and strong expansion regions (b) at various M_{t_0} ($t = 2$). —: Air; ---: PP11-MAH-IC1; -.-: PP11-MAH-IC2. □, EC; ○, CC; △, SC; ■, EE; ●, CE; ▲, SE.

continuous convergence structures steepen in the case of IC2 (figure 4.31 c), leading to expansion shocklets that are admissible since the initial thermodynamic state falls in the inversion region.

In figure 4.32 we report the isosurfaces of $\log_{10}(|\Delta|/\langle Q_W \rangle^3) = 3$, conditioned on eddy-type structures (left panels) and convergence regions (right panels) for air (a), PP11-MAH-IC1 (b) and PP11-MAH-IC2 (c), coloured with the local dilatation $\theta/\theta_{\text{rms}}$. The figure shows that for eddy-type structures the dilatation levels are close to zero for each case, whereas the dynamically most active convergence regions are mainly sheet-like undergoing strong compressions and expansions, and the

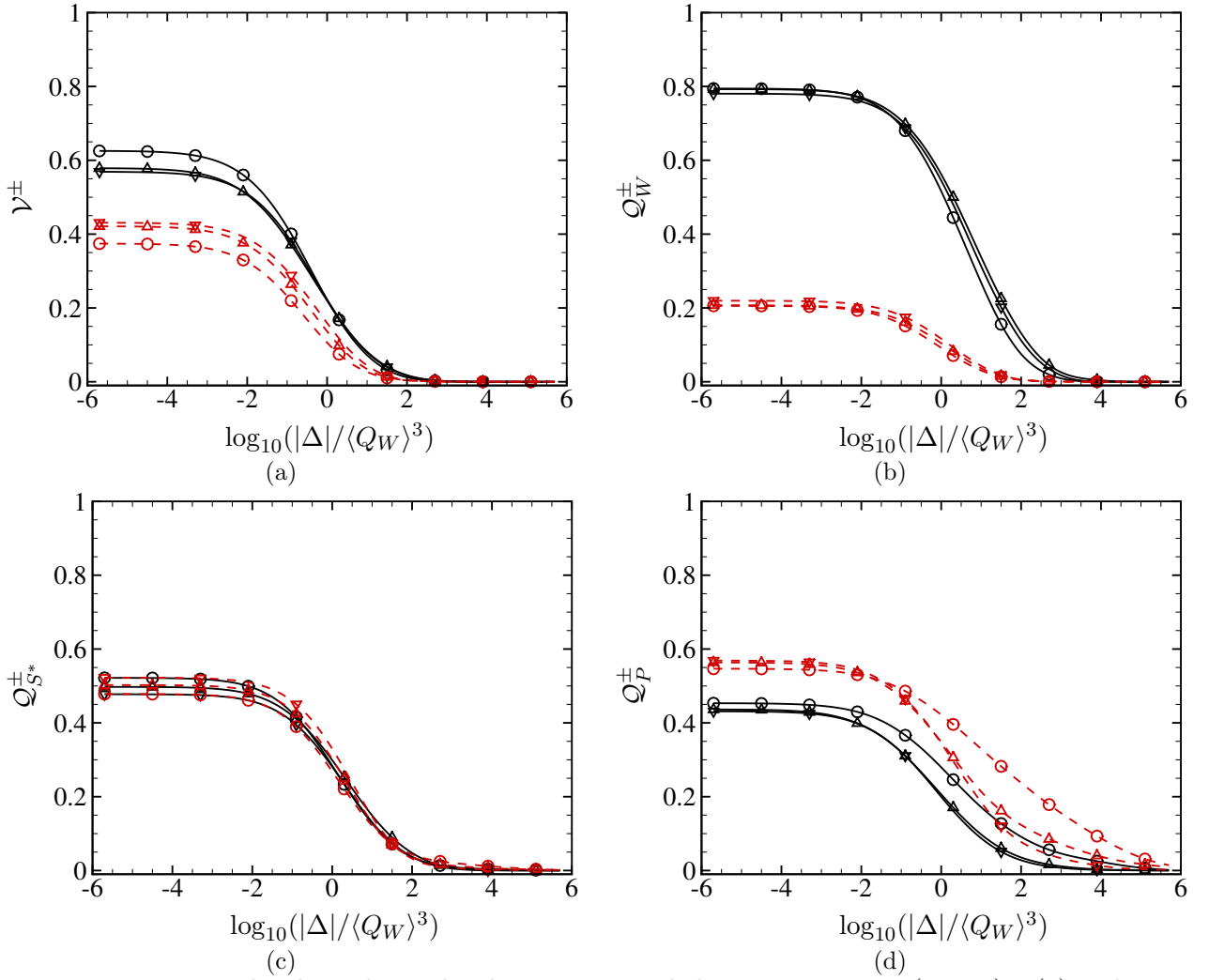


Figure 4.30. Normalized conditional volume-integrated data at $M_{t_0} = 1$ ($t = 2$). (a) Volume fraction \mathcal{V} ; (b) \mathcal{Q}_W ; (c) \mathcal{Q}_{S^*} ; (d) \mathcal{Q}_P . —, $\Delta > 0$; - - - , $\Delta < 0$; \circ : Air; \triangle PP11-MAH-IC1; ∇ : PP11-MAH-IC2.

latter are more and more significant in dense gas.

4.2.3 Enstrophy generation mechanisms

The works of Kida & Orszag (1989), Sarkar *et al.* (1991), Pirozzoli & Grasso (2004) and Wang *et al.* (2012b) show that the vortex stretching plays an essential role in compressible turbulence dynamics, namely in the mechanism of vorticity and enstrophy generation, highlighting in particular the role played by shocklets. Given the significant modification of flow structures and their contributions to mechanical energy dissipation in dense gas, we analyse in detail to which extent dense gas effects modify enstrophy generation. We recall that enstrophy is governed by the following transport equation (Erlebacher & Sarkar, 1993):

$$\frac{D}{Dt} \left(\frac{\omega^2}{2} \right) = \omega_i V_i^T + \omega_i \epsilon_{ijk} \frac{1}{\rho^2} \frac{\partial \rho}{\partial x_j} \frac{\partial p}{\partial x_k} + \omega_i \epsilon_{ijk} \frac{\partial}{\partial x_j} \left(\frac{1}{\rho} \frac{\partial \tau_{mk}}{\partial x_m} \right) \quad (4.14)$$

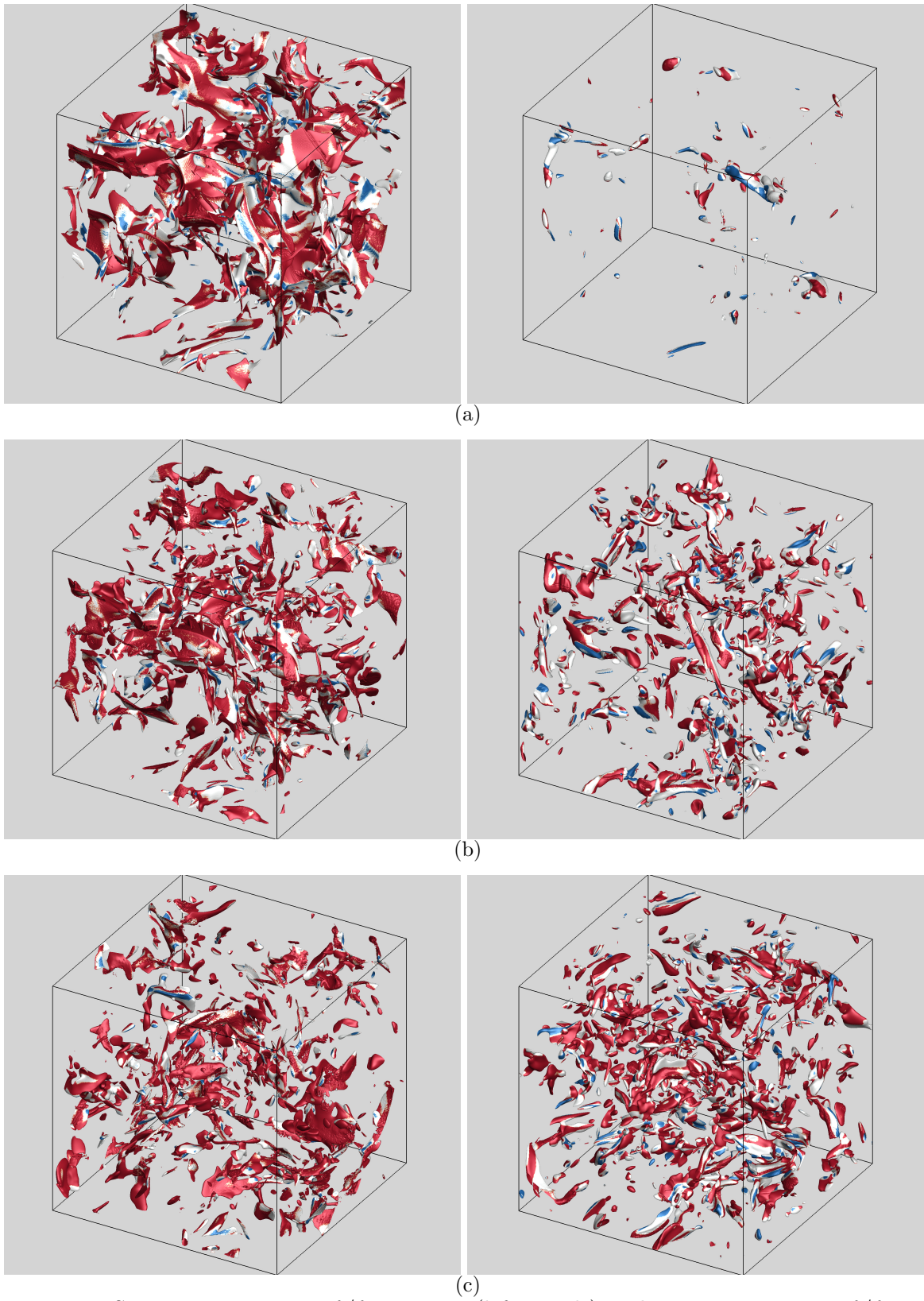


Figure 4.31. Strong compressions $\theta/\theta_{\text{rms}} = -3$ (left panels) and strong expansions $\theta/\theta_{\text{rms}} = 3$ (right panels) for air (a), PP11-MAH-IC1 (b) and PP11-MAH-IC2 (c) coloured with the local type of structure. Blue: eddy; white: shear; red: convergence.

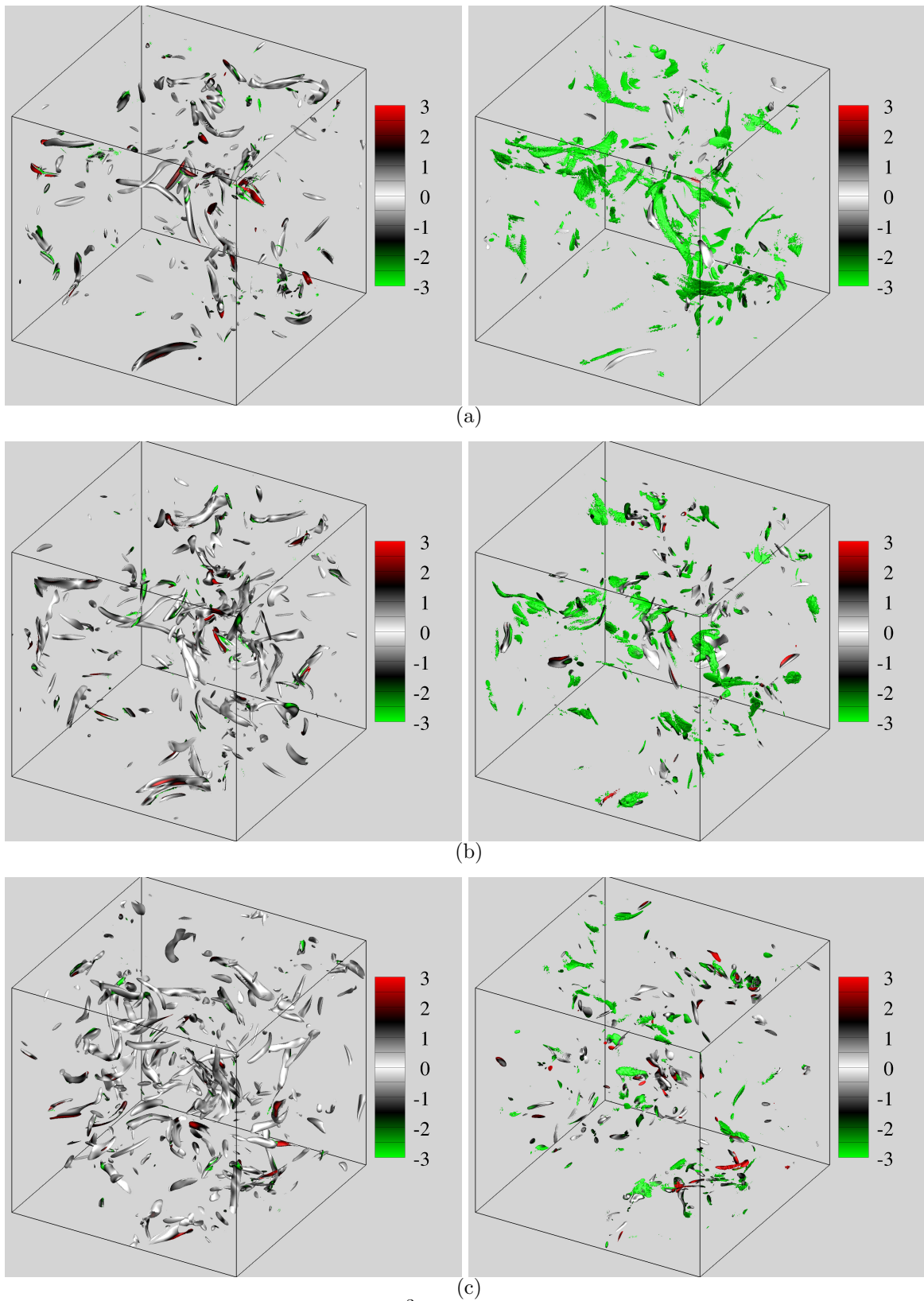


Figure 4.32. Iso-surfaces of $\log_{10}(|\Delta|/\langle Q_W \rangle^3) = 3$, conditioned on eddy-type structures (left panels) and convergence regions (right panels) for air (a), PP11-MAH-IC1 (b) and PP11-MAH-IC2 (c), coloured with the local dilatation $\theta/\theta_{\text{rms}}$.

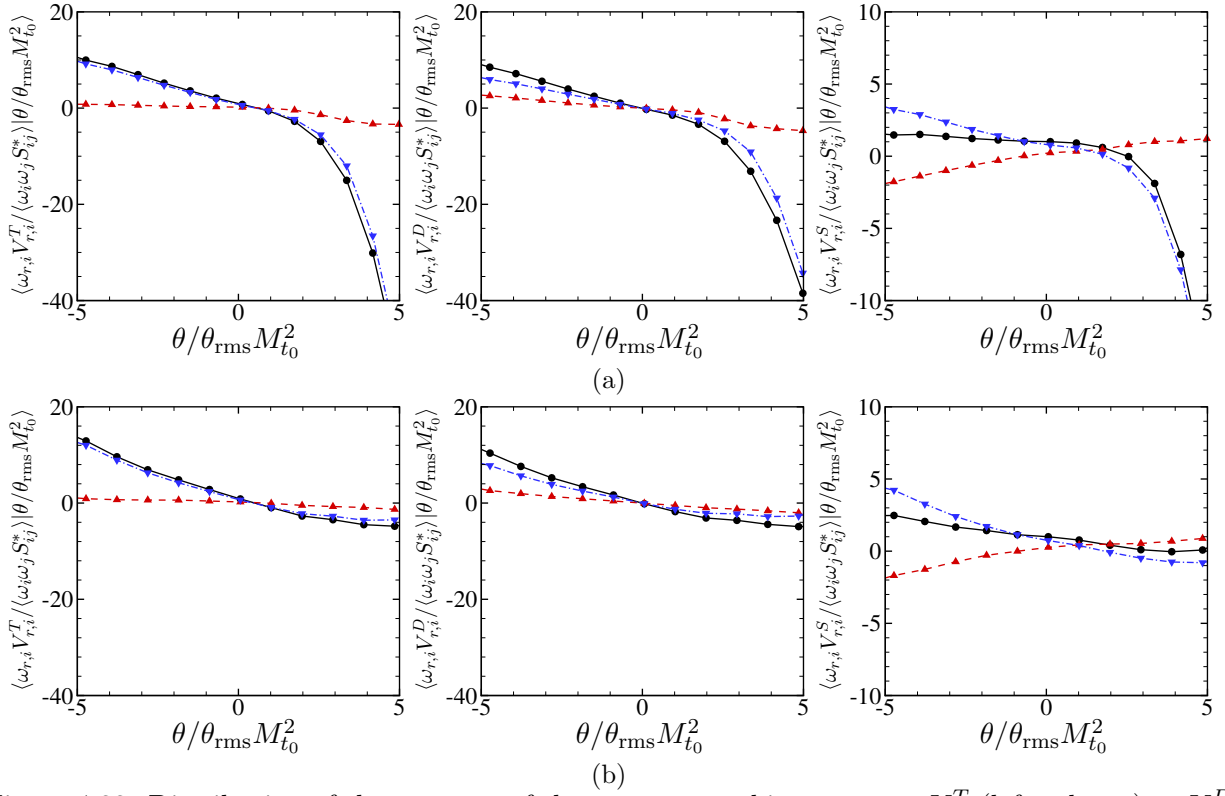


Figure 4.33. Distribution of the averages of the vortex stretching vector $\omega_i V_i^T$ (left column), $\omega_i V_i^D$ (central column), and $\omega_i V_i^S$ (right column) conditioned on the dilatation for air (a) and PP11-MAH-IC1 (b) at $M_{t_0} = 1$ ($t = 2$). In each figure the contributions to enstrophy generation in the direction parallel (---: $r = n$) and tangential (-.-.-: $r = t$) to the density gradient are also reported.

where $\omega^2/2 = \omega_i \omega_i/2$ is the enstrophy density, D/Dt is the material derivative, and the three terms on the right-hand side represent, respectively, enstrophy generation due to vortex stretching, the baroclinic term and the viscous diffusion. The vortex stretching vector V_i^T is the sum of two contributions due to the deviatoric strain rate ($V_i^S = \omega_j S_{ij}^*$) and to dilatation ($V_i^D = -\frac{2}{3}\theta\omega_i$).

Integration of equation (4.14) over the entire volume yields:

$$\frac{D\langle \omega^2/2 \rangle}{Dt} = \langle \omega_i V_i^S \rangle + \langle \omega_i V_i^D \rangle + \langle \omega_i \epsilon_{ijk} \frac{1}{\rho^2} \frac{\partial \rho}{\partial x_j} \frac{\partial p}{\partial x_k} \rangle + \langle \omega_i \epsilon_{ijk} \frac{\partial}{\partial x_j} \left(\frac{1}{\rho} \frac{\partial \tau_{mk}}{\partial x_m} \right) \rangle \quad (4.15)$$

Kida & Orszag (1989), Pirozzoli & Grasso (2004) and Wang *et al.* (2012b) showed that the baroclinic effects are negative and rather negligible, while the viscous dissipation acts as a sink.

We focus our analysis on the action of the strain rate $\langle \omega_i V_i^S \rangle$ and dilatation $\langle \omega_i V_i^D \rangle$ terms. To relate enstrophy generation with the occurrence of shocklets, as in Wang *et al.* (2012b), we project the vorticity and the vortex stretching vectors (both the one associated with the deviatoric strain rate and the dilatation rate) in the normal and tangential directions relative to the local density iso-surfaces, i.e. the direction aligned with the density gradient $\mathbf{n} = \text{grad}(\rho)/\|\text{grad}(\rho)\|$ and a direction \mathbf{t} orthogonal to \mathbf{n} .

In figure 4.33 we report the volume average of the rate of total enstrophy generation $\langle \omega_i V_i^T \rangle$ (left column), the rate of dilatational enstrophy generation $\langle \omega_i V_i^D \rangle$ (central column) and the deviatoric strain rate enstrophy generation $\langle \omega_i V_i^S \rangle$ (right column) conditioned on dilatation, both for air (panels a) and dense gas (panels b). The vorticity vector having a tendency to be orthogonal to

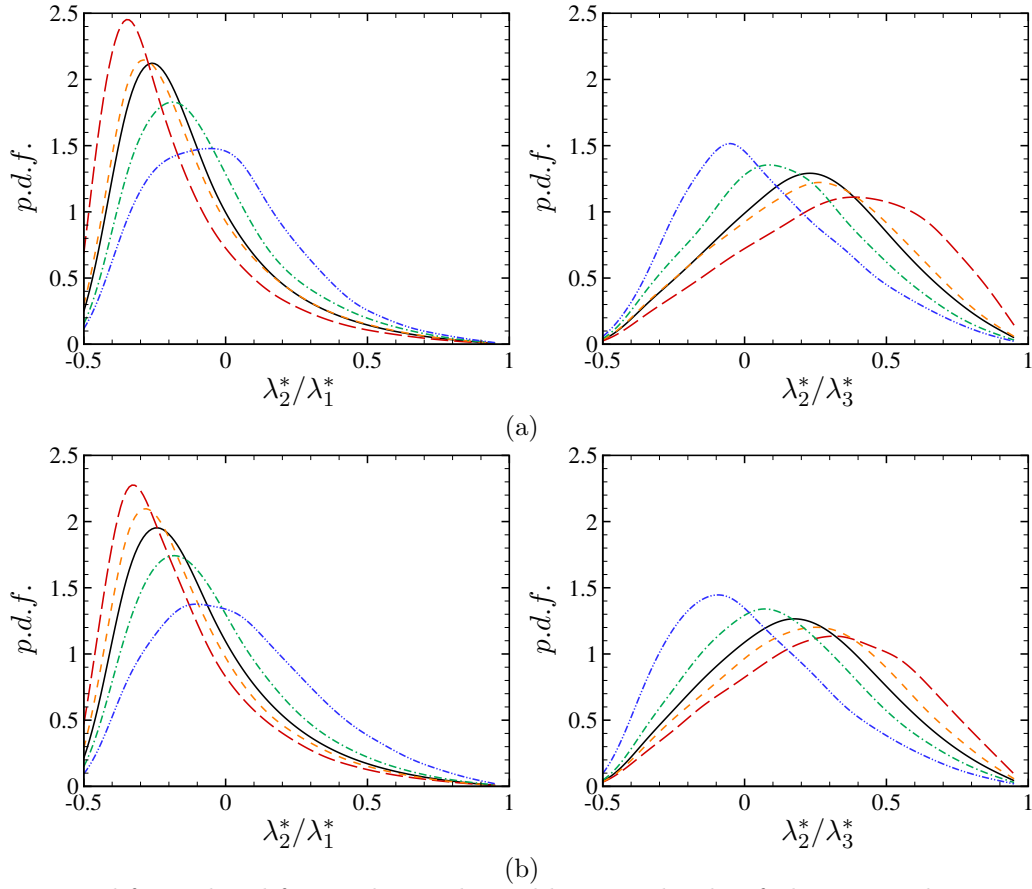


Figure 4.34. P.d.f. and p.d.f.s conditioned on dilatation levels of the eigenvalues ratios λ_2^*/λ_1^* (left) and λ_2^*/λ_3^* (right) of the deviatoric strain rate tensor at $M_{t_0} = 1$ ($t = 2$) for air (a) and PP11-MAH-IC1 (b). —: $[-\infty, +\infty]$; - - - : $[-\infty, -2]$; - - - : $[-2, -1]$; - - - : $[1, 2]$; - · - · - : $[2, \infty]$.

the density gradient, the main contribution to enstrophy generation is in the tangential direction. Enstrophy is produced due to vortex stretching across eddy shocklets (compressed structures). Expanding perfect gas structures destroy enstrophy and both $\langle \omega_i V_i^S \rangle$ and $\langle \omega_i V_i^D \rangle$ increase rapidly in magnitude with θ . On the contrary, dense gases have a tendency to strongly inhibit enstrophy destruction across moderate and strong expansions. Furthermore, dilatational enstrophy generation is of comparable order both in the directions normal and tangential to the expanding structures. The attenuation of enstrophy destruction in expansion regions is likely due to two competing mechanisms: expansion processes associated with thermodynamic states having $\Gamma = \mathcal{O}(1)$ that contribute to enstrophy destruction as in perfect gases, and (strong) expansions associated with thermodynamic states having Γ close to or less than zero that have a tendency to behave similar to compressions (thus producing enstrophy and counteracting its destruction).

To further elucidate into the enstrophy generation mechanism and its relation with the flow topology, we have also analyzed the contribution due to vortex stretching in the eigendirections of the deviatoric strain rate. We recall that in incompressible flows (Ashurst *et al.*, 1987; Cantwell, 1993), vorticity has a tendency to align with the eigendirection associated with the intermediate eigenvalue of the strain rate, which is found to be positive in the average (i.e. more often positive than negative). For compressible flows, we consider the deviatoric strain rate S_{ij}^* and project the vortex stretching vector in the eigendirections $\mathbf{\Lambda}_k$ associated with the eigenvalues λ_k^* of S_{ij}^* . The vortex

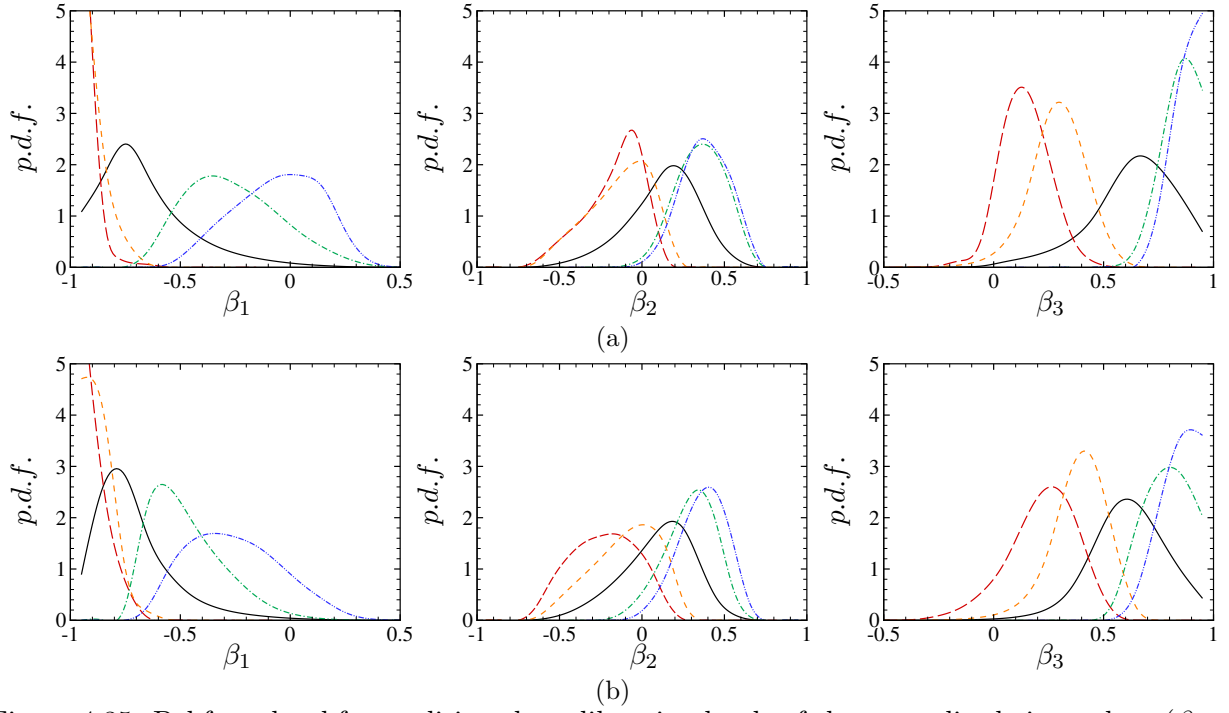


Figure 4.35. P.d.f. and p.d.f.s conditioned on dilatation levels of the normalized eigenvalues ($\beta_k = \lambda_k / \sqrt{\sum_i \lambda_i^2}$) of the strain rate tensor S_{ij} for air (a) and PP11-MAH-IC1 (b) ($M_{t_0} = 1$; $t = 2$).
 —: $[-\infty, +\infty]$; - - -: $[-\infty, -2]$; - - -: $[-2, -1]$; - - -: $[1, 2]$; - · - ·: $[2, \infty]$.

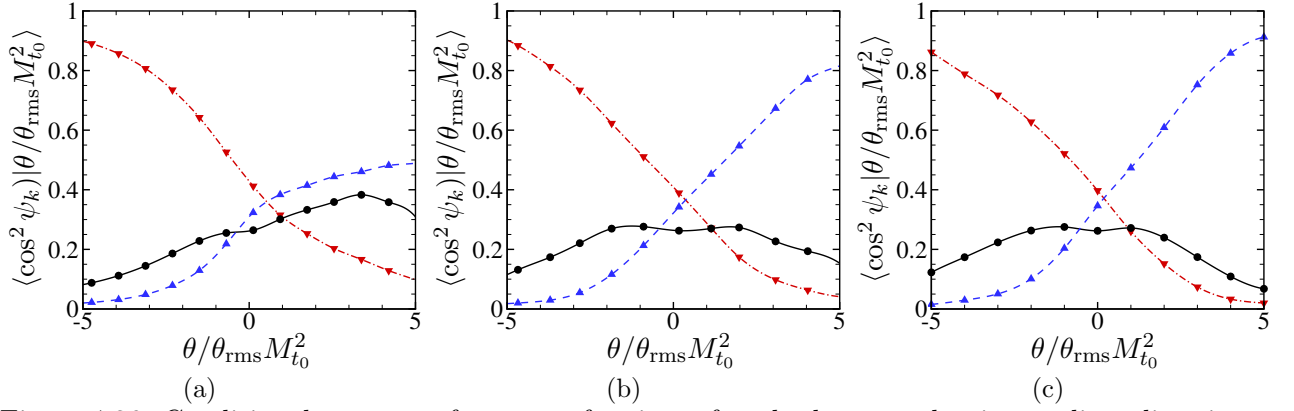


Figure 4.36. Conditional averages of squares of cosines of angles between density gradient direction \mathbf{n} and the strain rate eigenvectors $\mathbf{\Lambda}_k$ for air (a), PP11-MAH-IC1 (b) and PP11-MAH-IC2 (c) at $M_{t_0} = 1$ ($t = 2\tau$). - - ▽: $k = 1$; —●: $k = 2$; - - ▲: $k = 3$.

stretching term then reduces to:

$$\omega_i \omega_j S_{ij}^* = \omega^2 \sum_k \lambda_k^* \cos^2 \phi_k \quad (4.16)$$

where $\phi_k = \cos^{-1}(\boldsymbol{\omega} \cdot \mathbf{\Lambda}_k / \|\boldsymbol{\omega}\| \|\mathbf{\Lambda}_k\|)$ is the angle between the vorticity vector and the k -th eigendirection.

The p.d.f.s and the conditional p.d.f.s of the eigenvalue ratios $\lambda_2^* / \lambda_1^*$ and $\lambda_2^* / \lambda_3^*$ of the deviatoric strain rate are reported in figure 4.34 for air (left panels) and PP11-MAH-IC1 (right panels). The conditional p.d.f.s of the normalized eigenvalues of the strain rate tensor $\beta_k = \lambda_k / \sqrt{\sum_i \lambda_i^2}$ are

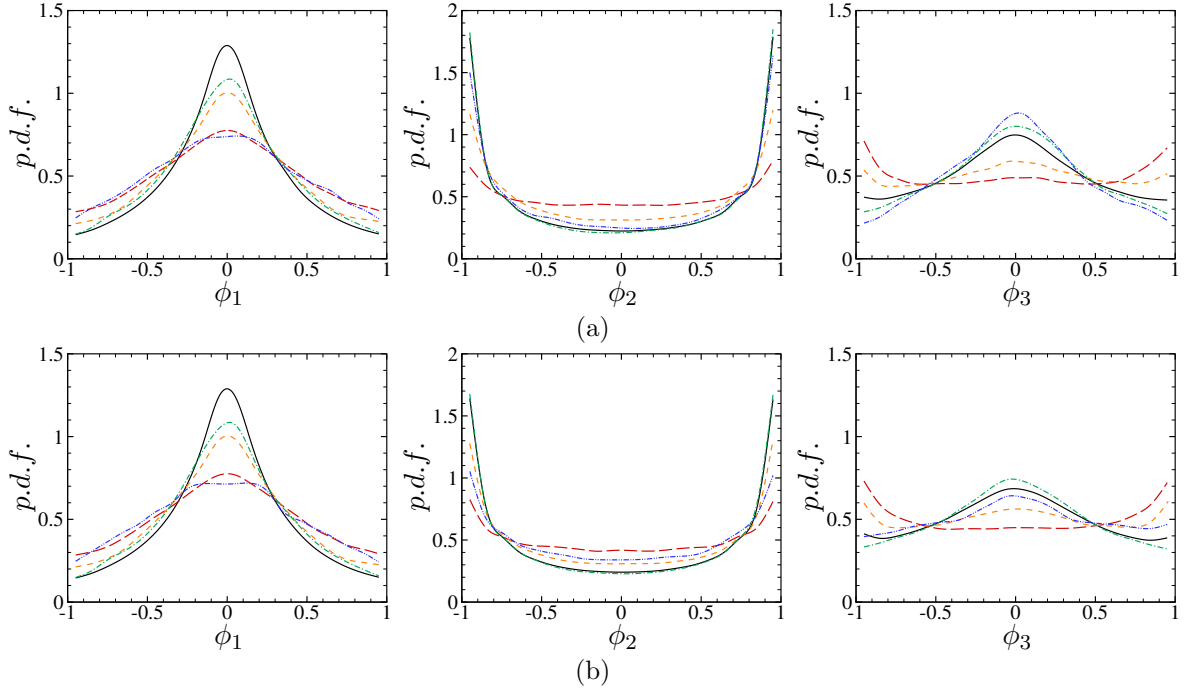


Figure 4.37. P.d.f.s and conditional p.d.f.s of the cosines of the angles between the vorticity ω and the strain rate eigenvectors Λ_k for air (a) and PP11-MAH-IC1 (b) at $M_{t_0} = 1$ ($t = 2$). —: $[-\infty, +\infty]$; - - - : $[-\infty, -2]$; - - - : $[-2, -1]$; - - - : $[-1, 0]$; - - - : $[0, 1]$; - - - : $[1, 2]$.

reported in figure 4.35. As found both in incompressible and compressible turbulence (Ashurst *et al.*, 1987; Erlebacher & Sarkar, 1993; Pirozzoli & Grasso, 2004; Lee *et al.*, 2009; Wang *et al.*, 2012b) the most probable values of λ_k^* are approximately in the ratio $[-4 : 1 : 3]$. As compression increases, the p.d.f. of β_1 peaks at lower values, β_2 and β_3 become much smaller than β_1 and the eigenvalues are approximately in the ratio $[-1 : 0 : 0]$. In strongly expanding regions the p.d.f. of β_3 peaks at approximately 1 and the eigenvalues are in the ratio $[0 : 0 : 1]$. Hence compression is dominant in the first eigendirection, while expansion is dominant in the third one.

Reported in figure 4.36 are the conditional averages of the squared cosines of the angles between the density gradient direction and the principal strain ones ($\psi_k = \cos^{-1}(\mathbf{n} \cdot \Lambda_k)$) for air (a), PP11-MAH-IC1 (b) and PP11-MAH-IC2 (c) at $M_{t_0} = 1$ ($t = 2$). In strong compressions, the eigendirection associated with the most negative eigenvalue of S_{ij} has a tendency to align with the density gradient (i.e. it tends to be perpendicular to shocklets) both for the perfect and the dense gas. In expansion regions, the first eigenvector is nearly orthogonal to the density gradient, while the third strain-rate eigendirection has a tendency to somewhat align with the density gradient. This tendency is strongly marked in dense gas, supporting the possibility of the occurrence of steep expansion fronts for condition IC1 and eventually expansion shocklets for IC2.

From equation (4.16) we observe that the amount of enstrophy production/destruction depends on the alignment between vorticity and the deviatoric strain rate eigendirections, and on the sign and magnitude of the associated eigenvalues. Reported in figure 4.37 are the p.d.f.s and the conditional p.d.f.s of the angles between vorticity and Λ_k s. As in Wang *et al.* (2012b), the vorticity is preferentially parallel or antiparallel to the intermediate eigenvector, and has a tendency to be orthogonal to the first eigendirection. The angle between vorticity and the eigendirection associated with the most positive eigenvector has a tendency to be more uniformly distributed as expansion strengthens (i.e. any angle between vorticity and Λ_3 is equally probable). This behaviour does not depend on the type of gas and is rather similar to that observed in incompressible flows (Erlebacher

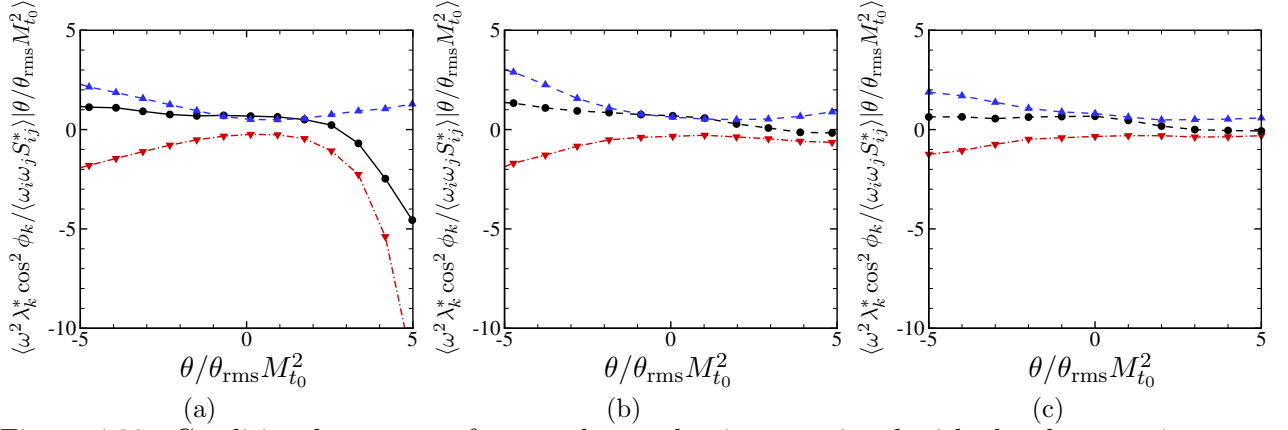


Figure 4.38. Conditional averages of enstrophy production associated with the three strain rate eigenvectors at $M_{t_0} = 1$ (at $t = 2$) for air (a), PP11-MAH-IC1 (b) and PP11-MAH-IC2 (c). $\text{---}\blacktriangledown\text{---}$: $k = 1$; $\text{---}\bullet\text{---}$: $k = 2$; $\text{---}\blacktriangle\text{---}$: $k = 3$.

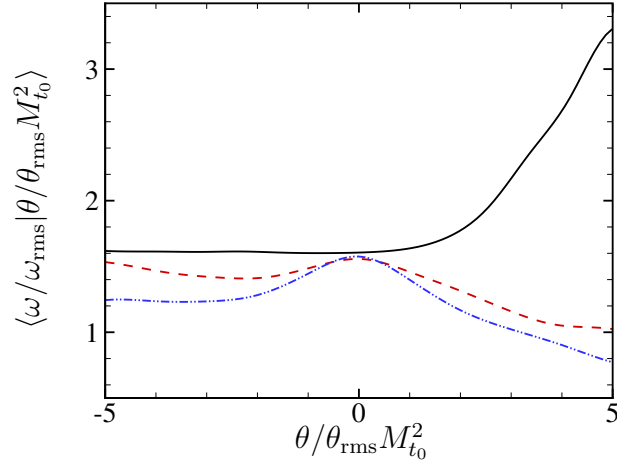


Figure 4.39. Conditional average of the normalized vorticity magnitude at $M_{t_0} = 1$ ($t = 2$). --- , Air; $\text{---}\text{---}$, PP11-MAH-IC1; $\text{---}\cdot\text{---}$, PP11-MAH-IC2.

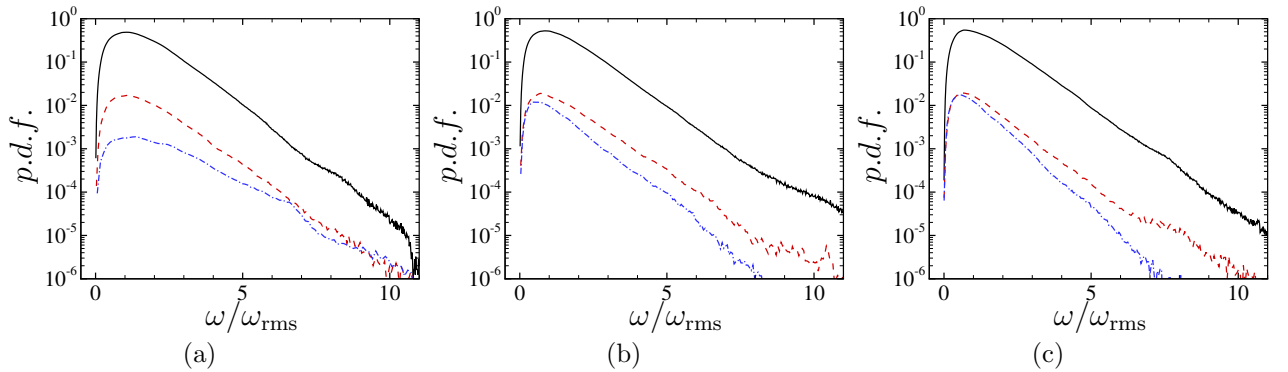


Figure 4.40. Total and conditional p.d.f. of the normalized vorticity magnitude. Air (a); PP11-MAH-IC1 (b); PP11-MAH-IC2 (c). --- , $[-\infty, +\infty]$; $\text{---}\text{---}$, $[-\infty, -2]$; $\text{---}\cdot\text{---}$, $[2, \infty]$.

& Sarkar, 1993).

The conditional averages of enstrophy production by vortex stretching in the principal strain rate directions is reported in figure 4.38 for air (a), PP11-MAH-IC1 (b) and PP11-MAH-IC2 (c). For

perfect gas, the main contributions to enstrophy production in strong compression are associated with the second and third eigenvectors, whereas in regions where the gas undergoes strong expansions the small positive contribution in the direction associated with the most positive eigenvalue (λ_3^*) is overwhelmed by the negative contributions in the other directions, as also found by Wang *et al.* (2012b). For dense gas, a similar behaviour is observed in compression regions. However, in expansion zones the large negative contributions in the Λ_1 and Λ_2 eigendirections are reduced by one order of magnitude, yielding striking differences with the perfect gas case. This can be interpreted by examining the vorticity distribution whose conditional average is reported in figure 4.39 as a function of dilatation for air (a), and PP11-IC1 (b) and IC2 (c). In general, dense gas effects reduce vorticity both in compression and expansion zones. In strong compressions, perfect and dense gases generate a comparable average vorticity. On the contrary, in strong expansions dense gas exhibits a stronger decrease in vorticity. The p.d.f. of vorticity magnitude conditioned on dilatation is reported in figure 4.40, which shows indeed that high vorticity magnitudes are somewhat less probable in dense gas (the effect being stronger for case PP11-IC2) than in perfect gas.

Chapter Summary

The statistical properties of dense gas CHIT decay are analyzed by means of DNS of PP11. Simulations were carried out at various initial turbulent Mach numbers and for two different choices of the initial thermodynamic state, corresponding to a small positive and a small negative value of the fundamental derivative Γ , and compared with DNS results for a perfect gas.

- Time evolution of general statistics:
 - The trends observed in the previous chapter for inviscid CHIT are confirmed, namely:
 - * Temperature variations are negligible due to the decoupling of dynamic and thermal effects
 - * The p.d.f.s of the local dilatation conserve a more symmetric shape than in perfect gas, especially for BZT initial conditions.
 - The fluid viscosity exhibits smaller average and r.m.s. variations than a perfect gas.
 - Thermodynamic statistics are slightly affected by the choice of the initial thermodynamic state, provided that the initial Γ value is close enough to zero.
 - Fluids of the same family exhibit similar evolutions for the thermodynamic quantities. Globally, the influence of the fluid type on kinematic features is small.
- The shocklet detection algorithm of [Samtaney *et al.* \(2001\)](#) has been implemented, but modifications are required in order to be able to capture expansion shocklets.
- Analysis of small scales dynamics and properties of turbulent structures:
 - The total joint p.d.f. (Q^*, R^*) is characterized by the same universal tear-drop shape found for incompressible and compressible perfect gas turbulence.
 - The joint p.d.f. conditioned on strong compression and expansion regions is modified due to the weakening of compressive structures and enhancement of expanding regions.
 - Strong expansions are found to be mostly populated by non-focal convergence structures, in contrast with the perfect gas that is dominated by eddy-like structures having focal topology.
 - Effects are enhanced for BZT initial thermodynamic conditions.
- Analysis of the role of different flow structures on viscous dissipation mechanism:
 - Enhanced contribution of non-focal expanding structures to dilatational dissipation.
 - The occurrence of steep expansion structures and, possibly, of expansion shocklets is confirmed by the preferential alignment of the density gradient with the third strain rate eigenvector. This effects deeply modifies the enstrophy generation in strong expansion regions, which mostly acts as a sink in perfect gases.
 - In dense gases, the presence of a much higher percentage of nonfocal convergence structures significantly decreases vorticity and counterbalances enstrophy destruction by means of the eddy-like ones.

5 Supersonic dense-gas turbulent channel flow

Contents

5.1 Numerical experiments of compressible channel flows	131
5.1.1 Setup and definitions	131
5.1.2 Validations	133
5.1.3 Description of the computed cases	133
5.2 Influence of dense-gas effects on flow properties	135
5.2.1 Global flow properties	135
5.2.2 Scalings and first-order statistics	140
5.2.3 Second-order statistics of the thermodynamic and transport properties	145
5.3 Influence of dense-gas effects on turbulence structure	148
5.3.1 Reynolds stresses and anisotropies	148
5.3.2 Turbulent kinetic energy budgets	154
5.3.3 Near-wall turbulent structures	156

In this chapter we investigate the influence of dense gas effects on compressible wall-bounded turbulence. Direct numerical simulations of supersonic turbulent channel flows are performed both for air and PP11 and a parametric study on the bulk Mach and Reynolds numbers is carried out. The analysis is performed by comparing with the flows for an ideal gas. The chapter is organised as follows. The setup of the test-case and some useful definitions are presented in section 5.1, along with validations with the classic literature references of [Kim *et al.* \(1987\)](#) and [Coleman *et al.* \(1995\)](#). In section 5.2, the effects of dense-gases on mean and fluctuating properties are analyzed. The profile of turbulence intensities, turbulent kinetic budgets and near-wall structures are investigated in section 5.3.

5.1 Numerical experiments of compressible channel flows

5.1.1 Setup and definitions

Numerical experiments are conducted for the plane channel flow configuration, i.e. the flow between two infinite parallel flat plates. This is reproduced by applying periodic conditions in the homogeneous streamwise (x) and spanwise (z) directions. Isothermal no-slip wall conditions are applied on the lower and upper walls. In order to counteract viscous friction and maintain a target bulk mass flow, the approach described in [Gerolymos *et al.* \(2010\)](#) and [Gerolymos & Vallet \(2014\)](#) is used to compute the forcing term. Specifically, at the end of each Runge-Kutta stage, the bulk density is explicitly constrained to maintain a fixed target value, whereas a source term f_{u_1} is injected in the streamwise momentum equation to enforce a constant massflow. The density correction is equivalent to including a source term in the continuity equation. Nevertheless, this term is very small and can be neglected ([Coleman *et al.*, 1995](#); [Huang *et al.*, 1995](#); [Lechner *et al.*, 2001](#); [Morinishi *et al.*, 2004](#); [Foysi *et al.*, 2004](#); [Wei & Pollard, 2011](#); [Gerolymos & Vallet, 2014](#)).

In the following, the subscripts $(\bullet)_B$, $(\bullet)_w$ and $(\bullet)_{cl}$ denote averaging over the whole computational domain, the walls and centreline, respectively; (\bullet) indicates Reynolds averaging over the homogeneous spatial directions and in time, whereas $(\bullet)'$ are Reynolds fluctuations; similarly, (\bullet) and $(\bullet)''$ denote Favre averaging and Favre fluctuations. In the following, we also use the centreline Reynolds and Mach numbers, respectively defined as $Re_{cl} = \bar{\rho}_{cl} \bar{u}_{cl} h / \bar{\mu}_{cl}$ and $M_{cl} = \bar{u}_{cl} / \bar{c}_{cl}$.

The DNS operating point is defined by a bulk Reynolds number Re_B and a bulk Mach number M_B , defined as:

$$Re_B = \frac{\rho_B \tilde{u}_B h}{\bar{\mu}_w}, \quad M_B = \frac{\tilde{u}_B}{\bar{c}_w}, \quad (5.1)$$

where ρ_B is the bulk density, h is the channel half-height, $\bar{\mu}_w$ is the dynamic viscosity and \bar{c}_w the sound speed at the walls. In the definition of the bulk reference numbers, wall values for viscosity and speed of sound are usually considered since this greatly simplifies the imposition of the reference conditions for isothermal walls. Indeed, for a perfect gas model, a fixed wall temperature implies $\bar{\mu}_w = \mu(T_w)$ and $\bar{c}_w = c(T_w) = \sqrt{\gamma R T_w}$. However, this is no longer true when using more complex thermodynamic models, since the speed of sound and the transport properties depend on both temperature and density values. In these cases, $\bar{\rho}_w$ is not known a priori and it is not possible to fix directly Re_B and M_B . To enforce the reference conditions, an iterative procedure has been followed: first, a preliminary calculation is run by choosing a reasonable value for the ratio $\bar{\rho}_w / \rho_B$. Once the solution is converged, the $\bar{\rho}_w$ obtained from the simulation is used to compute the updated values of $\bar{\mu}_w$ and \bar{c}_w , and the flow field is interpolated onto a new grid (adapted to the updated value of the Reynolds number). In order to achieve convergence to the desired state, about 3 to 4 iterative cycles are needed. In the following parametric study, higher- Re_B cases are initialized from lower- Re_B solutions by scaling the channel height and the forcing terms. Conversely, a change in the target bulk Mach number requires the preceding initialization procedure.

We recall the definition of the standard wall coordinates and friction Reynolds number

$$y^+ := \frac{\bar{\rho}_w u_\tau (y - y_w)}{\bar{\mu}_w}; \quad Re_\tau := \frac{\bar{\rho}_w u_\tau h}{\bar{\mu}_w} \quad (5.2)$$

where $u_\tau = \sqrt{\bar{\tau}_w / \bar{\rho}_w}$ is the friction velocity and $\bar{\tau}_w = (\mu \frac{\partial u}{\partial y})_w$ the shear stress at the wall. It is widely known that the Reynolds number based on the friction velocity does not correctly represent the effect of rapid wall-normal variations for density and viscosity profiles in presence of high compressibility effects. Huang *et al.* (1995) proposed an empirical semi-local scaling based on both wall and centreline quantities:

$$y^* := \frac{\bar{\rho}(y) u_\tau^* (y - y_w)}{\bar{\mu}(y)}; \quad Re_\tau^* := \frac{\bar{\rho}_{cl} \sqrt{\frac{\bar{\tau}_w}{\bar{\rho}_{cl}}} h}{\bar{\mu}_{cl}} = Re_\tau \sqrt{\frac{\bar{\rho}_{cl} \bar{\mu}_w}{\bar{\rho}_w \bar{\mu}_{cl}}} \quad (5.3)$$

with $u_\tau^* = \sqrt{\bar{\tau}_w / \bar{\rho}(y)}$ the semi-local friction velocity. This mixed scaling has proven to give quite satisfactory results in collapsing first- and second-order moments (Foysi *et al.*, 2004; Morinishi *et al.*, 2004; Modesti & Pirozzoli, 2016) obtained from a wide range of M_B and Re_B . Recently, Patel *et al.* (2015) and Trettel & Larsson (2016) have developed a mathematical framework giving a theoretical basis to the semi-local scaling. Even if this scaling was initially introduced in order to take into account the effects of compressibility, Patel *et al.* (2015) assessed its validity also for variable-property flows, since it inherently considers the evolution of transport properties and their relation with thermodynamic quantities.

5.1.2 Validations

In order to validate the code and the numerical strategy, two reference test-cases have been considered, namely the incompressible channel flow of [Kim *et al.* \(1987\)](#) and supersonic isothermal channel flow of [Coleman *et al.* \(1995\)](#). The parameters of the DNS are summarized in table 5.1. Note that a low subsonic Mach number, $M_B=0.3$, has been chosen for the comparison of our compressible solver with the incompressible case. Table 5.2 shows the main results of our simulations. Figure 5.1 shows the mean streamwise velocity profile in wall units, the profiles of r.m.s. velocity fluctuations and the evolution of the turbulent kinetic energy budgets (whose components are listed in subsection 5.3.2) compared to the data from [Kim *et al.* \(1987\)](#). Figure 5.2 shows similar comparison for the first- and second-order statistics for the supersonic case. A very good agreement with the reference results is obtained for both cases.

Table 5.1. Parameters used for the DNS of the selected test cases.

Case	Re_B	M_B	$L_x \times L_y \times L_z$	$N_x \times N_y \times N_z$
Subsonic (Kim <i>et al.</i>, 1987)	2795	0.3	$4\pi h \times 2h \times 2\pi h$	$192 \times 180 \times 160$
Supersonic (Coleman <i>et al.</i>, 1995)	3000	1.5	$8\pi h \times 2h \times 2\pi h$	$512 \times 256 \times 256$

Table 5.2. Results of the DNS computations of the selected test cases.

Case	Re_τ	Re_τ^*	Δx^+	Δz^+	Δy_w^+	Δy_{cl}^+	$-B_q$	$\bar{\rho}_w/\rho_B$	$\bar{\rho}_{cl}/\rho_B$	\bar{T}_{cl}/T_w
Subsonic	181	178	11.9	7.2	0.81	4.1	-0.002	1.01	0.99	1.01
Supersonic	219	147	10.7	5.4	0.78	3.2	-0.049	1.36	0.98	1.39

5.1.3 Description of the computed cases

Dense-gas effects are evaluated by means of a parametric study at three bulk Reynolds numbers (namely, $Re_B = 3000, 7000$ and 12000) and three bulk Mach numbers ($M_B = 1.5, 2.25$ and 3). For PP11 cases, the bulk density was imposed to be $\rho_B = 0.618\rho_c$, and the wall temperature was fixed to $T_w = 1.01T_c$. The density value ensures that the flow evolves in the dense-gas region, whereas the slightly supercritical wall temperature condition avoids the occurrence of a two-phase flow. It should be noted that for these conditions it is not possible to obtain negative values of the derivative of gas dynamics Γ , so no BZT phenomena are expected to occur.

In the following, we refer to each simulation with a unique tag of the form $XM\alpha R\beta$, where the first letter indicates the fluid (A for air and P for PP11), α refers to M_B ($\alpha = 1, 2, 3$ for $M_B = 1.5, 2.25, 3$, respectively) and β to Re_B ($\beta = 3, 7, 12$ for $Re_B = 3000, 7000, 12000$, respectively). For all the cases, the computational domain has dimensions $L_x \times L_y \times L_z = 8\pi h \times 2h \times 2\pi h$. The dimension in the streamwise direction is greater than the one used in the previous compressible channel DNSs ([Coleman *et al.*, 1995](#); [Lechner *et al.*, 2001](#); [Morinishi *et al.*, 2004](#); [Wei & Pollard, 2011](#)) in order to ensure uncorrelated inlet and outlet quantities for high- M_B cases. The computational grids are chosen in order to provide a good spatial resolution in all directions. Specifically, the chosen spatial resolutions, expressed in semi-local units, are in the ranges $\Delta x^* \in [10, 16]$, $\Delta y_w^* \in [0.5, 0.8]$, $\Delta z^* \in [4, 6]$, according to the considered flow conditions. The spatial resolution is also evaluated with respect to the wall-normal distribution of the Kolmogorov length-scale $\bar{\eta} = ((\bar{\mu}/\bar{\rho})^3 \bar{\rho}/\bar{\epsilon})^{1/4}$, where $\bar{\epsilon}$ is the turbulent kinetic energy dissipation. According to [Zonta *et al.* \(2012\)](#) and [Lee *et al.* \(2013\)](#), the resolution requirements are $\Delta x < 12\eta$, $\Delta y < 2\eta$ and $\Delta z < 6\eta$. However, higher

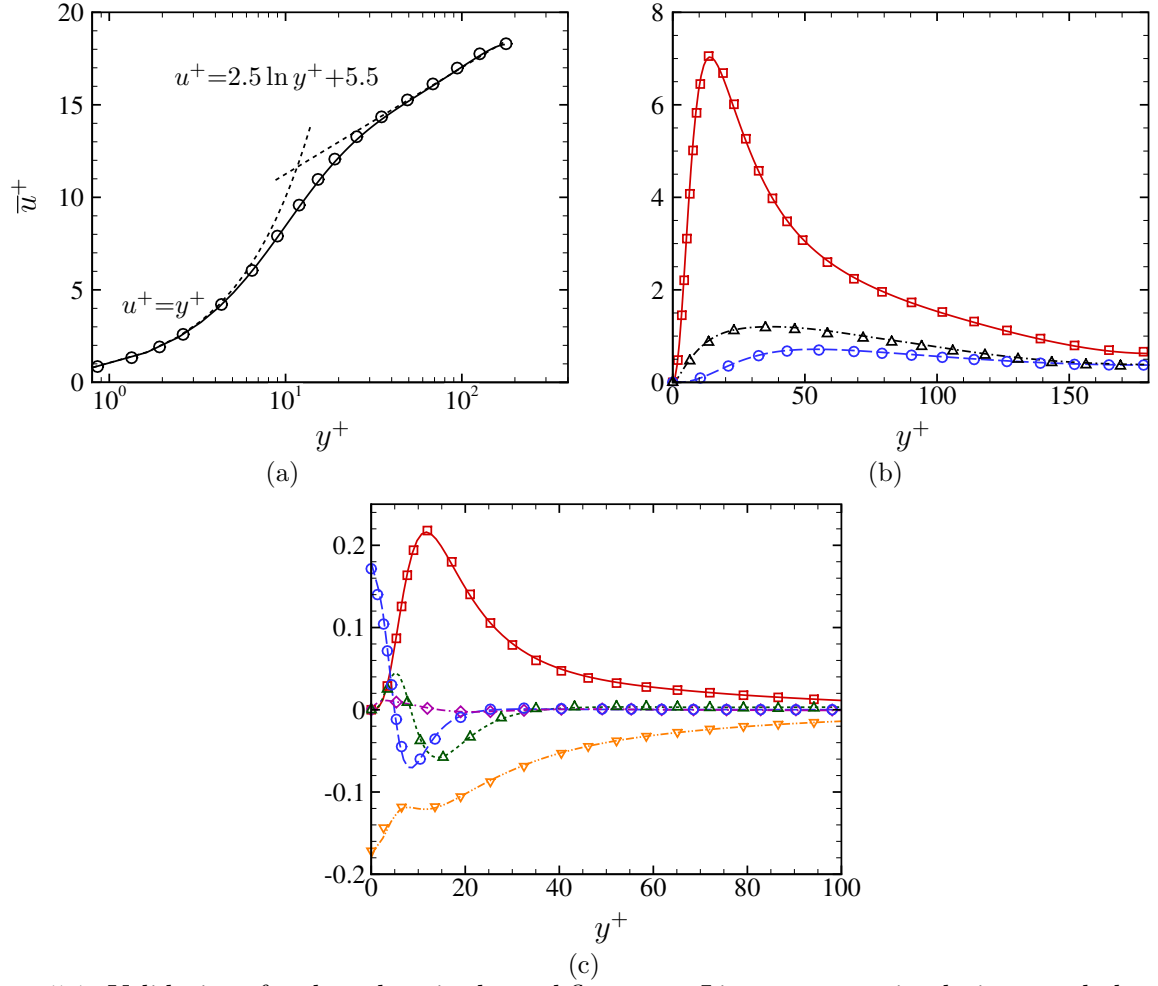


Figure 5.1. Validations for the subsonic channel flow case. Lines, present simulation; symbols, data from Kim *et al.* (1987). (a) Law of the wall; (b) r.m.s. velocity fluctuations; (c) turbulent kinetic energy budget. In (b), (—, \square) $\overline{u'u'^+}$; (---, \circ) $\overline{v'v'^+}$; (-.-.-, \triangle) $\overline{w'w'^+}$. In (c), (—, \square) production; (-.-.-, ∇) dissipation; (....., \triangle) turbulent diffusion; (---, \circ) viscous diffusion; (-.-.-, \diamond) turbulent pressure diffusion.

resolutions may be needed when complex terms involving high-order velocity gradient correlations are studied (Gerolymos & Vallet, 2014). In our simulations, the overall number of grid points varies between 3×10^6 and 1.2×10^9 .

Table 5.4 summarizes the conditions used for the parametric study. Wall-friction Reynolds numbers range from 218.7 to 1017 for air, and from 191.3 to 692.8 for PP11. The semi-local scaling drastically changes the predictions in terms of friction Reynolds number. For air, Re_τ^* goes from 88.7 to 324.7, the drop for each case being roughly proportional to M_B . For PP11, an opposite behaviour is observed: Re_τ^* is higher than Re_τ in each case, and the deviations increase with M_B . This is due to the different behaviour of the transport properties as it will be explained later. Thus, contrarily to air, the resolution requirements for PP11 are more severe in semi-local scaling than in the classical wall scaling. However, as reported in table 5.4, the chosen grids ensure a good resolution in each case. Once the Re_τ^* values is converged, statistics are collected each ten computational timesteps, with $\Delta t^+ \approx 0.02 \div 0.03$ in wall units for all the simulations, and during an observation time t_{OBS}^+ in the range $1000 \div 3000$.

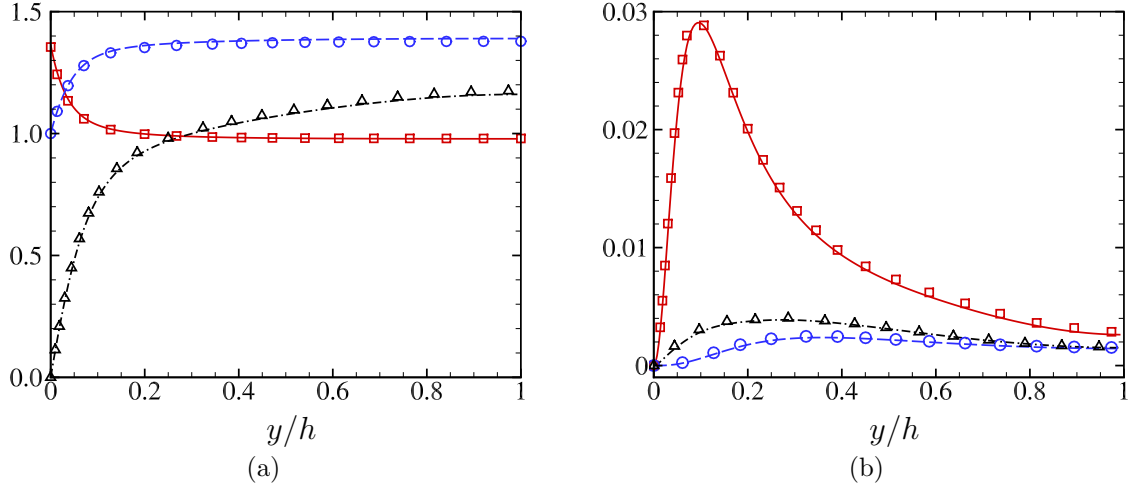


Figure 5.2. Validations for the supersonic channel flow case. Lines, present simulation; symbols, data from Coleman *et al.* (1995). (a) Profiles of mean quantities; (b) r.m.s. velocity fluctuations. In (a), (—, \square) $\bar{\rho}/\rho_B$; (---, \circ) \bar{T}/T_w ; (-·-·-, \triangle) \bar{u}/u_τ . In (b), (—, \square) $\overline{u'u'}/\tilde{u}_B^2$; (---, \circ) $\overline{v'v'}/\tilde{u}_B^2$; (-·-·-, \triangle) $\overline{w'w'}/\tilde{u}_B^2$.

5.2 Influence of dense-gas effects on flow properties

In this section we first present results for general flow properties and their dependency on the bulk parameters and fluid type. Then, we analyze cross-wise profiles of the first order statistics. For this purpose, we initially assess different wall scalings, and then focus more specifically on the variations of average thermodynamic properties across the channel, to highlight the peculiar behaviour of dense-gas flows compared with air flows. For the sake of clarity, we investigate the role of compressibility effects by focusing on cases characterised by $Re_B = 7000$ and various Mach numbers. The Reynolds number influence is also studied by considering sets of simulations M1R3 and M3R12. We complete the analysis by discussing dense-gas effects on second-order statistics of the thermodynamic and transport properties. Second-order moments of the velocity fields and, more generally, on turbulence structure are discussed in Section 4. For these sets of results, each case is uniquely identified with the line style defined in table 5.3, unless otherwise stated.

5.2.1 Global flow properties

Figure 5.3 reports M_B and $\bar{T}_{cl}^+ = \bar{T}_{cl}/T_w$ as functions of the average centreline Mach number \bar{M}_{cl} . Values obtained for air cases are in good agreement with reference DNSs in similar conditions (Foysi *et al.*, 2004; Wei & Pollard, 2011; Gerolymos & Vallet, 2014). For $M_B \geq 1.5$, \bar{M}_{cl} is systematically lower than M_B , since the walls are cooler than the channel core. Indeed for perfect gases, \bar{M}_{cl} increases non-linearly since \bar{T}_{cl} grows rapidly and $\bar{c} \propto \sqrt{\bar{T}}$. The average centreline temperature in figure 5.3b is approximately 1.4 times higher than the wall temperature for AM1R3 and more than 2.5 times higher for AM3R3 due to the significant increase of the viscous heating $\tau_{ij}S_{ij}$. The

Table 5.3. Line styles for some of the DNS cases considered.

M_B	1.5	1.5	2.25	3.0	3.0
Re_B	3000	7000	7000	7000	12000
	- - - - -	- - - - -	- - - - -	- - - - -	- - - - -

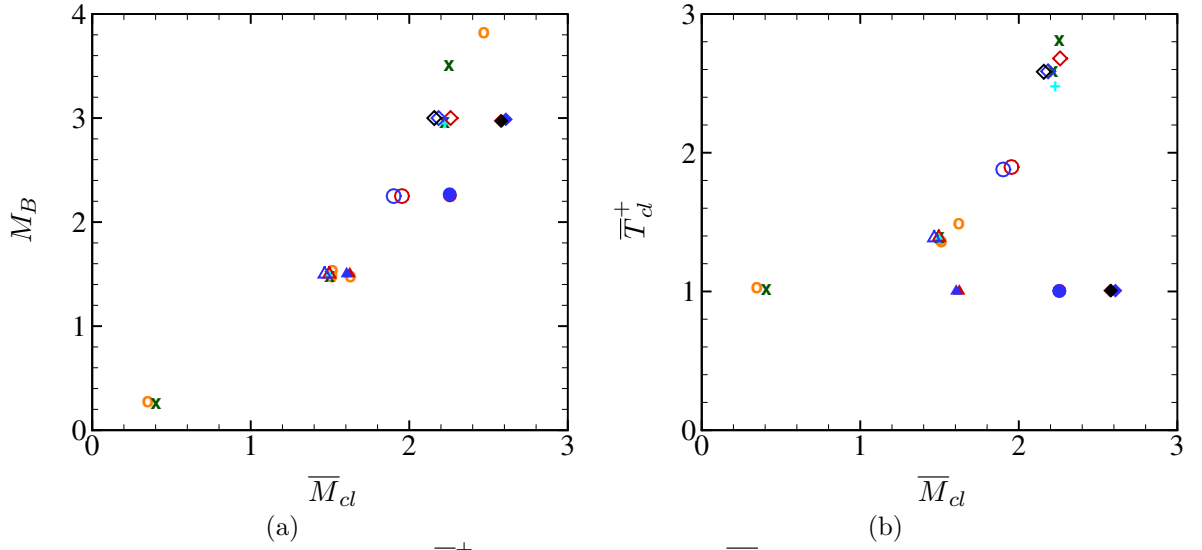


Figure 5.3. Evolutions of M_B (a) and \overline{T}_{cl}^+ (b) as a function of \overline{M}_{cl} for different cases. Open symbols: air; filled symbols: PP11. Symbol shapes: \blacktriangle : $M_B = 1.5$, \bullet : $M_B = 2.25$, \blacklozenge : $M_B = 3$. Symbol colours (online version): red, $Re_B = 3000$; blue, $Re_B = 7000$; black, $Re_B = 12000$. $+$ Coleman *et al.* (1995), \times Foysi *et al.* (2004), \circ Gerolymos & Vallet (2014).

dependence on the Reynolds number is weak on the considered range, with slightly lower values of \overline{T}_{cl}^+ for higher Re_B , which is more clearly appreciated for the highest Mach-number conditions. The centreline Mach number \overline{M}_{cl} tends to decrease as the bulk Reynolds is higher due to more flattened profile of the streamwise velocity. The variations are however relatively weak given the limited range of Reynolds numbers in the present study. The most important viscous effects are thus found for the highest M_B and the lowest Re_B . PP11 flows exhibit a rather different behaviour since the results are highly dependent on the specific heats of the fluid. By increasing the molecular complexity, the gas specific heat coefficients rise sharply and PP11 flows show an evolution closer to the incompressible flows.

Table 5.4. Numerical parameters and DNS results for air and PP11. N_x , N_y and N_z are the numbers of grid points in the streamwise, wall-normal and spanwise directions; Re_τ is the friction Reynolds number; Re_τ^* is the semi-local friction Reynolds number; Δx^+ , Δz^+ , Δy_w^+ and Δy_d^+ are the mesh sizes in wall units; Δx_{cl}^* , Δz_{cl}^* and Δy_{cl}^* are the mesh sizes in semi-local units; $(\Delta x/\eta)_{\max}$, $(\Delta z/\eta)_{\max}$, $(\Delta y_{\min}/\eta)_{\max}$ and $(\Delta y_{\max}/\eta)_{\max}$ are the spatial resolutions normalised by the Kolmogorov lengthscale, t_{OBS}^+ is the observation period in wall units; Δt^+ is the computational time step in wall units.

	Air												PP11					
	1.5	3000	1.5	7000	2.25	3000	2.25	7000	3	3000	3	7000	1.5	3000	2.25	7000	3	3000
Case	AM1R3	AM1R7	AM2R3	AM2R7	AM3R3	AM3R7	AM3R12	AM3R12	PM1R3	PM1R7	PM2R3	PM2R7	PM3R3	PM3R7	PM3R12	PM3R12	PM3R12	PM3R12
N_x	512	768	512	768	512	1024	1536	1536	512	768	512	768	512	768	512	768	1280	1280
N_y	256	384	256	384	256	512	768	768	256	384	256	384	256	384	256	384	768	768
N_z	256	512	256	512	384	768	1024	1024	256	512	256	512	256	512	256	512	1024	1024
Re_τ	218.7	466.5	248.6	538.6	290.8	627	1017	1017	191.3	401.6	193.9	404.6	205.1	425.1	205.1	425.1	692.8	692.8
Re_τ^*	147.1	314.8	115.0	252.0	88.7	199.7	324.7	324.7	196.4	412.1	205.8	428.0	245.3	492.1	245.3	492.1	800.2	800.2
Δx^+	10.7	15.3	12.2	17.6	14.3	15.4	16.6	16.6	9.4	13.1	9.5	13.2	10.1	13.9	10.1	13.9	13.6	13.6
Δz^+	5.4	5.7	6.1	6.6	4.8	5.1	6.2	6.2	4.7	4.9	4.8	5.0	5.0	5.2	5.0	5.2	4.2	4.2
Δy_w^+	0.78	0.79	0.79	0.78	0.77	0.77	0.81	0.81	0.76	0.64	0.77	0.72	0.66	0.68	0.66	0.68	0.69	0.69
Δy_{cl}^+	3.2	5.5	3.9	6.9	5.1	5.7	6.2	6.2	2.6	4.9	2.6	4.7	3.2	5.2	3.2	5.2	3.7	3.7
Δx_{cl}^*	7.2	10.3	5.7	8.3	4.4	4.9	5.3	5.3	9.7	13.5	10.1	14.0	12.1	16.1	12.1	16.1	15.7	15.7
Δz_{cl}^*	3.6	5.7	2.8	3.1	1.5	1.6	2.0	2.0	4.8	5.1	5.1	5.3	6.0	6.1	6.0	6.1	4.9	4.9
Δy_{cl}^*	2.2	5.5	1.8	3.3	1.5	1.8	2.0	2.0	2.7	5.0	2.8	5.0	3.9	6.0	3.9	6.0	4.3	4.3
$(\Delta x/\eta)_{\max}$	6.8	10.1	7.4	11.5	8.3	9.8	10.9	10.9	6.1	8.9	6.2	9.0	7.2	9.9	7.2	9.9	9.7	9.7
$(\Delta z/\eta)_{\max}$	3.4	3.8	3.7	4.3	2.8	3.3	4.1	4.1	3.1	3.3	3.1	3.4	3.6	3.7	3.6	3.7	3.1	3.1
$(\Delta y_{\min}/\eta)_{\max}$	0.5	0.5	0.5	0.5	0.5	0.5	0.5	0.5	0.5	0.4	0.5	0.5	0.4	0.5	0.4	0.5	0.5	0.5
$(\Delta y_{\max}/\eta)_{\max}$	0.6	0.9	0.6	0.8	0.5	0.5	0.5	0.5	0.8	1.1	0.7	1.1	1.0	1.3	1.0	1.3	0.8	0.8
t_{OBS}^+	2769	2307	3689	2279	3270	2076	1174	1174	3353	2891	2054	3534	2754	1406	2754	1406	674	674
$\Delta t^+ \times 10^2$	2.47	2.31	2.46	2.25	2.18	2.04	2.03	2.03	2.79	2.11	3.13	2.62	2.62	2.49	2.62	2.49	2.38	2.38

Table 5.5. DNS results for air and PP11 cases. $\overline{M}_{cl} = \overline{u_{cl}}/\overline{c_{cl}}$ is the centreline Mach number; $M_{\tau_w} = u_{\tau}/\overline{c_w}$ the friction Mach number; $Re_{cl} = \overline{\rho_d \tilde{u}_{cl} h}/\overline{\mu_{cl}}$ the centreline Reynolds number; $Re_{\theta_w} = \overline{\rho_w \tilde{u}_{cl} \theta}/\overline{\mu_w}$ the Reynolds number based on momentum thickness θ at wall conditions; $Re_{\theta_{cl}} = \overline{\rho_d \tilde{u}_{cl} \theta}/\overline{\mu_{cl}}$ the Reynolds number based on momentum thickness at centreline conditions; $Re_{Bb} = \rho_B \tilde{u}_B h/\mu_B$ the Reynolds number based at bulk conditions; $B_q = \overline{q_w}/(\overline{\rho_w} u_{\tau} \overline{h_w})$ the heat flux at the walls; $\overline{\rho_w}/\rho_B$ and $\overline{\rho_{cl}}/\rho_B$ the wall and centreline normalized density values; $\overline{T_{cl}}/\overline{T_w}$, $\overline{\mu_{cl}}/\overline{\mu_w}$ and $\overline{c_{cl}}/\overline{c_w}$ the centreline temperature, viscosity and speed of sound; $\overline{\Gamma_d}$ and $\overline{\Gamma_w}$ the centreline and wall values of the fundamental derivative of gas dynamics; $C_f = 2\overline{\tau_w}/(\rho_B u_B^2)$ the skin friction coefficient; $C_f^D = 0.073 Re_m^{-1/4}$ the skin friction coefficient based on Dean's correlation (Re_m is based on bulk quantities and channel height, i.e. $Re_m = 2Re_{Bb}$); $Nu_B = \overline{q_w} D_h/(\overline{\kappa_w}(T_B - T_w))$ the bulk Nusselt number; and $Pr_B = \mu_B * c_{p,B}/\kappa_B$ the bulk Prandtl number.

	Air										PP11									
	1.50		2.25		3.0		1.50		2.25		3.0		1.50		2.25		3.0		1.50	
M_B	3000	7000	3000	7000	3000	7000	3000	7000	3000	7000	3000	7000	3000	7000	3000	7000	3000	7000	3000	7000
Re_B	1.5	1.47	1.95	1.9	2.26	2.18	1.62	1.60	2.26	2.25	2.58	2.61	1.62	1.60	2.26	2.25	2.58	2.61	1.62	1.60
\overline{M}_{cl}	1.5	1.47	1.95	1.9	2.26	2.18	2.16	2.16	2.26	2.25	2.58	2.61	2.16	2.16	2.26	2.25	2.58	2.61	2.16	2.16
M_{τ_w}	0.08	0.07	0.1	0.09	0.12	0.11	0.1	0.1	0.13	0.12	0.16	0.15	0.09	0.08	0.13	0.12	0.16	0.15	0.09	0.08
Re_{cl}	2740	6319	2188	5071	1714	4035	6903	6903	3893	8866	4672	10256	3659	8423	3893	8866	4672	10256	3659	8423
Re_{θ_w}	418.6	968.5	248.6	538.6	887.5	1864	3143	3143	339.3	404.6	394.3	869.1	316.4	738.9	339.3	404.6	394.3	869.1	316.4	738.9
$Re_{\theta_{cl}}$	238.5	554.4	115.0	252.0	875.1	367.9	622.4	622.4	341.1	428.0	412.9	896.9	316.9	740.1	341.1	428.0	412.9	896.9	316.9	740.1
Re_{Bb}	2417	5627	1967	4582	1566	3690	6307	6307	3343	7728	4002	8944	3148	7346	3343	7728	4002	8944	3148	7346
$-B_q \times 10^3$	48.8	44.6	94.0	87.0	144	133	126	126	0.49	0.44	0.62	0.58	0.26	0.24	0.49	0.44	0.62	0.58	0.26	0.24
$\overline{\rho_w}/\rho_B$	1.36	1.37	1.82	1.84	2.49	2.49	2.51	2.51	1.11	1.11	1.29	1.25	1.05	1.05	1.11	1.11	1.29	1.25	1.05	1.05
$\overline{\rho_{cl}}/\rho_B$	0.98	0.99	0.95	0.97	0.92	0.96	0.97	0.97	1.00	1.00	0.99	0.99	1.00	1.00	1.00	1.00	0.99	0.99	1.00	1.00
$\overline{T_{cl}}/\overline{T_w}$	1.39	1.39	1.90	1.88	2.68	2.59	2.58	2.58	0.89	0.90	0.73	0.77	0.95	0.95	0.89	0.90	0.73	0.77	0.95	0.95
$\overline{\mu_{cl}}/\overline{\mu_w}$	1.26	1.26	1.57	1.56	1.99	1.95	1.94	1.94	1.16	1.14	1.36	1.32	1.07	1.07	1.16	1.14	1.36	1.32	1.07	1.07
$\overline{c_{cl}}/\overline{c_w}$	1.18	1.18	1.38	1.37	1.64	1.61	1.61	1.61	0.27	0.27	0.66	0.59	0.18	0.18	0.27	0.27	0.66	0.59	0.18	0.18
$\overline{\Gamma_{cl}}$	1.2	1.2	1.2	1.2	1.2	1.2	1.2	1.2	0.20	0.20	0.23	0.24	0.16	0.16	0.20	0.20	0.23	0.23	0.16	0.16
$\overline{\Gamma_w}$	1.2	1.2	1.2	1.2	1.2	1.2	1.2	1.2	0.20	0.20	0.23	0.24	0.16	0.16	0.20	0.20	0.23	0.23	0.16	0.16
$C_f \times 10^3$	7.60	6.39	7.14	6.26	6.85	6.13	5.52	5.52	7.52	6.12	7.33	5.98	7.76	6.29	7.52	6.12	7.33	5.98	7.76	6.29
$C_f^D \times 10^3$	8.73	7.07	9.15	7.43	9.64	7.83	6.86	6.86	8.07	6.54	7.71	6.31	8.19	6.63	8.07	6.54	7.71	6.31	8.19	6.63
Nu_B	82.5	159.	78.9	158.	76.5	156.	238.	238.	111.	225.	111.	212.	115.	226.	111.	225.	111.	212.	115.	226.
Pr_B	0.7	0.7	0.7	0.7	0.7	0.7	0.7	0.7	2.36	2.36	2.31	2.31	2.39	2.39	2.36	2.36	2.31	2.31	2.39	2.39

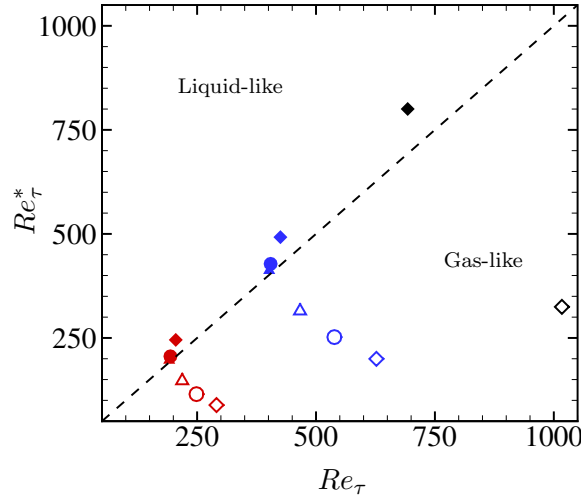


Figure 5.4. Evolution of Re_τ^* as a function of Re_τ for different cases. Same legend as figure 5.3.

Inspection of figure 5.3b shows that, for these cases, the centreline temperature is almost equal to the wall value for any choice of the Mach and Reynolds numbers. Considering an ideal model, one would obtain $\bar{c}_{cl} \approx \bar{c}_w$ and thus $\bar{M}_{cl} \approx M_B$. Nevertheless, the evolution of \bar{M}_{cl} changes significantly because in dense gases the speed of sound depends also on density, which decreases moving from the wall to the centreline. In turn \bar{c}_{cl} increases leading to lower values of \bar{M}_{cl} . Table 5.5 summarizes the main characteristic values of the simulations.

The relationship between Re_τ^* and Re_τ , depicted in figure 5.4, gives useful information about the differences between perfect and dense gases. We recall that, in the incompressible assumption, $Re_\tau^* = Re_\tau$ since density and viscosity are constant across the channel. Generally, for fluids exhibiting gas-like (resp. liquid-like) behaviour, one has $Re_\tau^* < Re_\tau$ (resp. $Re_\tau^* > Re_\tau$). Consequently, the semi-local friction Reynolds number reduces (resp. increases) the scaled turbulence intensity with respect to that predicted by the incompressible scaling. The greatest difference between the scalings are found for air: the semi-local scaling considerably modifies the friction by taking into account temperature variations. It is shown that for a given Re_B , higher bulk Mach numbers lead to lower Re_τ^* , whereas the opposite relation exists between M_B and Re_τ . For PP11 flows, $Re_\tau^* > Re_\tau$ due to the liquid-like behaviour of the transport properties of this fluid working in the dense gas region. Higher M_B lead to an increase in both Re_τ and Re_τ^* .

For practical applications, it is interesting to investigate the modifications of momentum and heat transfer coefficients when working with a dense gas. For that purpose, we consider the evolutions of the skin friction coefficient C_f and the bulk Nusselt number Nu_B , respectively defined as

$$C_f = \frac{\bar{\tau}_w}{\frac{1}{2}\rho_B u_B^2}; \quad Nu_B = \frac{\bar{q}_w D_h}{\bar{\kappa}_w (T_B - T_w)}, \quad (5.4)$$

which are depicted in figure 5.5. D_h denotes the hydraulic diameter, $D_h = 4h$ for a flat channel. The values predicted by the correlation of Dean (1978), i.e. $C_f^D = 0.073 Re_m^{-1/4}$, are denoted by the solid black line in figure 5.5a. The correlation has been established in the incompressible regime for $Re_m > 6000$, where Re_m is the Reynolds number based on bulk quantities and channel height, i.e. $Re_m = 2Re_{Bb} = \rho_B \bar{u}_B 2h / \mu_B$. For the dense-gas cases, the computed skin friction coefficients are slightly lower than the values predicted by Dean's correlation, but follow closely the trend with respect to the bulk Reynolds number. The deviations are greater for air flows with an underestimation more pronounced for higher Mach numbers. Some authors (Moneghan, 1953; Huang *et al.*, 1993) have proposed compressibility corrections, which work well for turbulent boundary layers

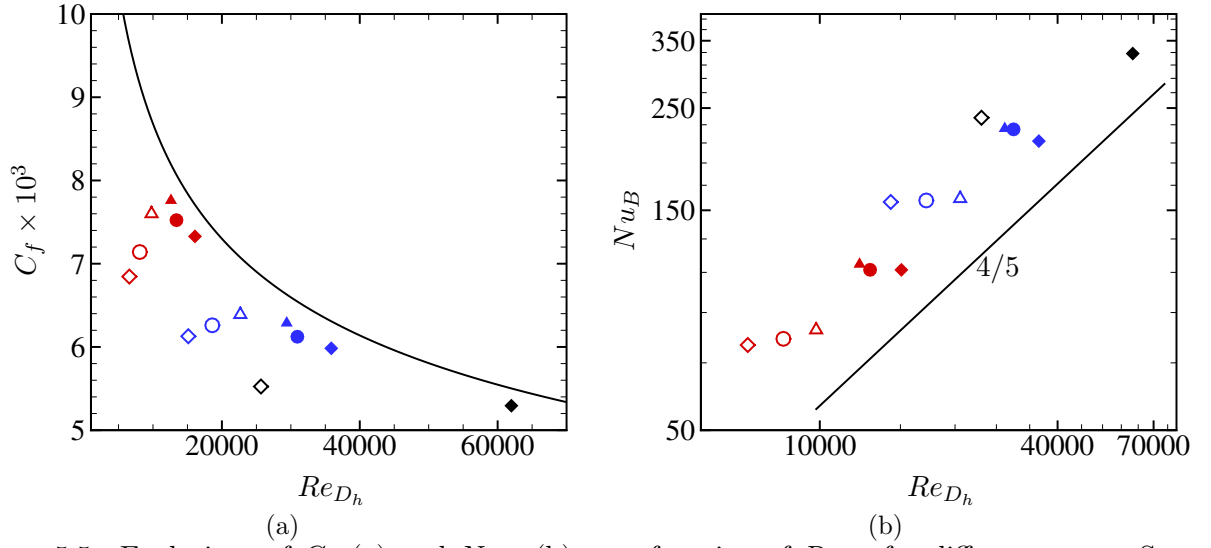


Figure 5.5. Evolutions of C_f (a) and Nu_B (b) as a function of Re_{D_h} for different cases. Same legend as figure 5.3.

over adiabatic walls. A similar extension for channel flows is not without ambiguities since the definition of the freestream values and of the dynamic pressure for normalisation is more arbitrary. It can however be concluded that Mach number effects in dense gas flows are less influential on the skin friction coefficient than in air flows, and Dean's formula yields a reasonable correlation.

In a similar manner, the Nusselt number is compared in figure 5.5b with a classical empirical correlation, commonly used to estimate heat transfer in hydraulic pipes (Incropera & DeWitt, 2007; Zonta, 2013). Specifically, we use the Sieder-Tate correlation, $Nu_B^{ST} = 0.027 Re_{D_h}^{4/5} Pr_B^{1/3} (\mu_B/\mu_w)^{0.14}$ (Sieder & Tate, 1936). Here, the Reynolds number at bulk conditions is based on the hydraulic diameter D_h , i.e. $Re_{D_h} = 2Re_m = 4Re_{Bb}$. This formula is an extension of the Dittus-Boelter/Colburn correlations including the viscosity dependence due to temperature change between the bulk average temperature and wall temperature. Figure 5.5b shows that the power law exponent of 0.8 capture well the Reynolds-number dependence for both fluids. The higher values obtained for dense-gas cases are explained by the Prandtl number dependence, which is constant and equal to 0.7 for air and varies between 2 and 4 for PP11. The enhanced heat capacities of dense gases reduces the heat conduction. A Mach-number effect can also be noticed, leading to lower Nusselt numbers when the Mach number increases. This compressibility effect, more visible for air flows, is not taken into account by the empirical correlation. The predicted values of C_f and Nu_B are reported in table 5.5. The heat flux towards the walls $B_q = \bar{q}_w/(\bar{\rho}_w u_\tau \bar{h}_w)$, with \bar{h}_w the specific enthalpy at the wall, is also given. Its order of magnitude is $\mathcal{O}(10^0 \div 10^1)$ for air and $\mathcal{O}(10^{-4})$ for PP11 flows. Hence, for dense gases, isothermal walls translate also into quasi-adiabatic conditions. Also given in table 5.5, the wall and centreline mean values of the fundamental derivative $\bar{\Gamma}_w$ and $\bar{\Gamma}_{cl}$ are globally lower than unity. Their increase with M_B is mainly associated with a higher dispersion of the instantaneous thermodynamic states.

5.2.2 Scalings and first-order statistics

Figure 5.6 displays the mean streamwise velocity profiles for air (top row) and PP11 flows (bottom row). It is known that the classical incompressible scaling (panels a and d) fails in collapsing the velocity profiles when compressibility effects are present. In particular, predictions get worse in presence of a substantial heat flux towards the walls. Several attempts have been made in the past in order to derive a transformation able to collapse the compressible velocity profiles into an

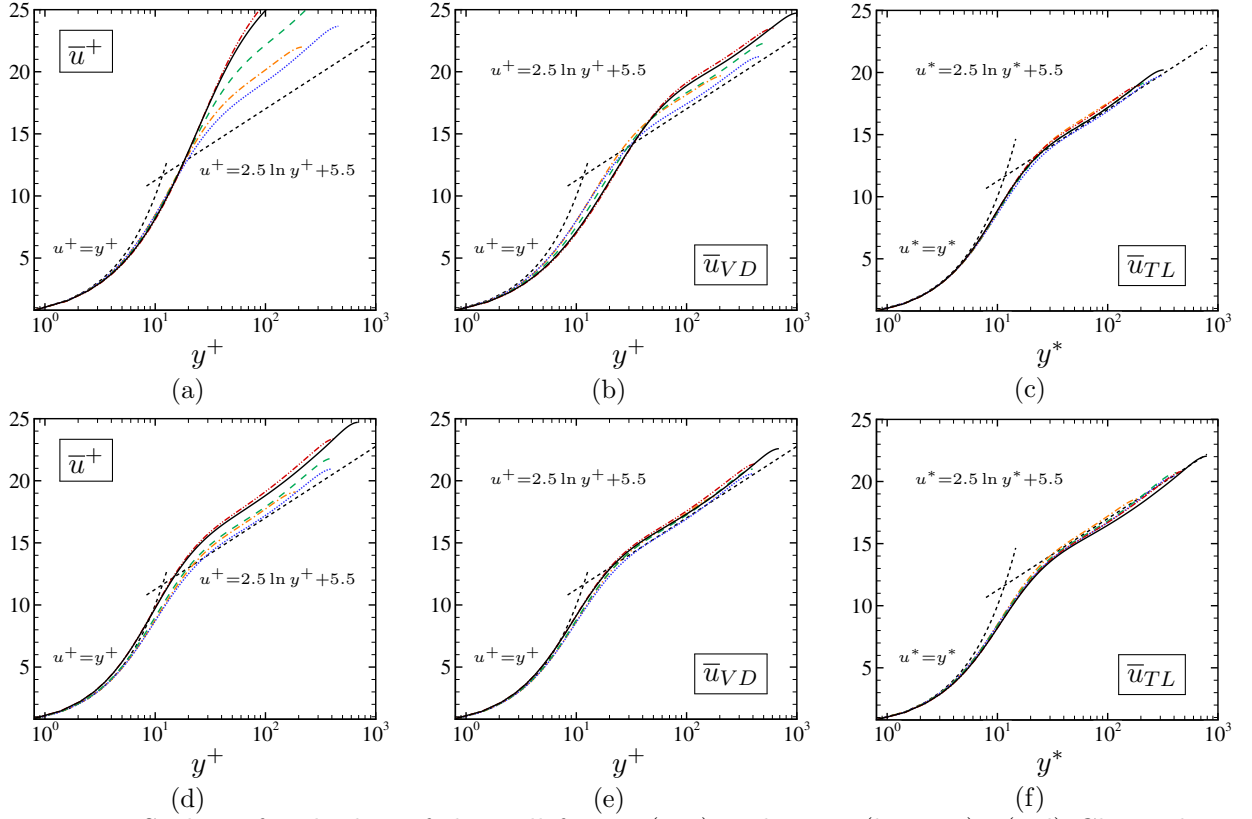


Figure 5.6. Scalings for the law of the wall for air (top) and PP11 (bottom). (a,d) Classical incompressible scaling u^+ ; (b,e) Van Driest transformation u_{VD} ; (c,f) Trettel-Larsson transformation u_{TL} in semi-local coordinates. Same legend as in table 5.3.

universal law of the wall for a wide range of Mach numbers. For non-hypersonic flows, [Van Driest \(1951\)](#) developed the transformation:

$$\bar{u}_{VD} = \int_0^{u^+} \sqrt{\frac{\bar{\rho}}{\bar{\rho}_w}} du^+, \quad (5.5)$$

which takes into account mean-density variations and translates the compressible profile into an equivalent "constant-density" profile keeping the same wall-normal coordinate y^+ . The Van Driest transformation provides a substantial improvement of the scaling (panels b and e), even if it departs from the log law as M_B increases. The size of the buffer layer increases rapidly for air since the beginning of the logarithmic zone moves towards higher y^+ values (from $y^+ \approx 20$ for AM1R7 to $y^+ \approx 70$ for AM3R12). On the other hand, for dense gases, the heat flux is greatly reduced and \bar{u}_{VD} -scaling provides quite satisfactory results. Indeed, this scaling was found to behave well for adiabatic walls ([Guarini et al., 2000](#); [Pirozzoli & Grasso, 2004](#)). Modifications for the value of the intercept of the log-law velocity profile, $u^+ = 1/\kappa \log y^+ + C$ were proposed by [Bradshaw \(1977\)](#), yielding empirical laws that relate C to the friction Mach number M_τ and to the heat flux B_q . [Modesti & Pirozzoli \(2016\)](#) have recently provided a thorough review of the main scalings available in the literature, and have shown that the transformation proposed by [Trettel & Larsson \(2016\)](#),

$$\bar{u}_{TL} = \int_0^{u^+} \sqrt{\frac{\bar{\rho}}{\bar{\rho}_w}} \left[1 + \frac{1}{2} \frac{1}{\bar{\rho}} \frac{d\bar{\rho}}{dy} y - \frac{1}{\bar{\mu}} \frac{d\bar{\mu}}{dy} y \right] du^+, \quad (5.6)$$

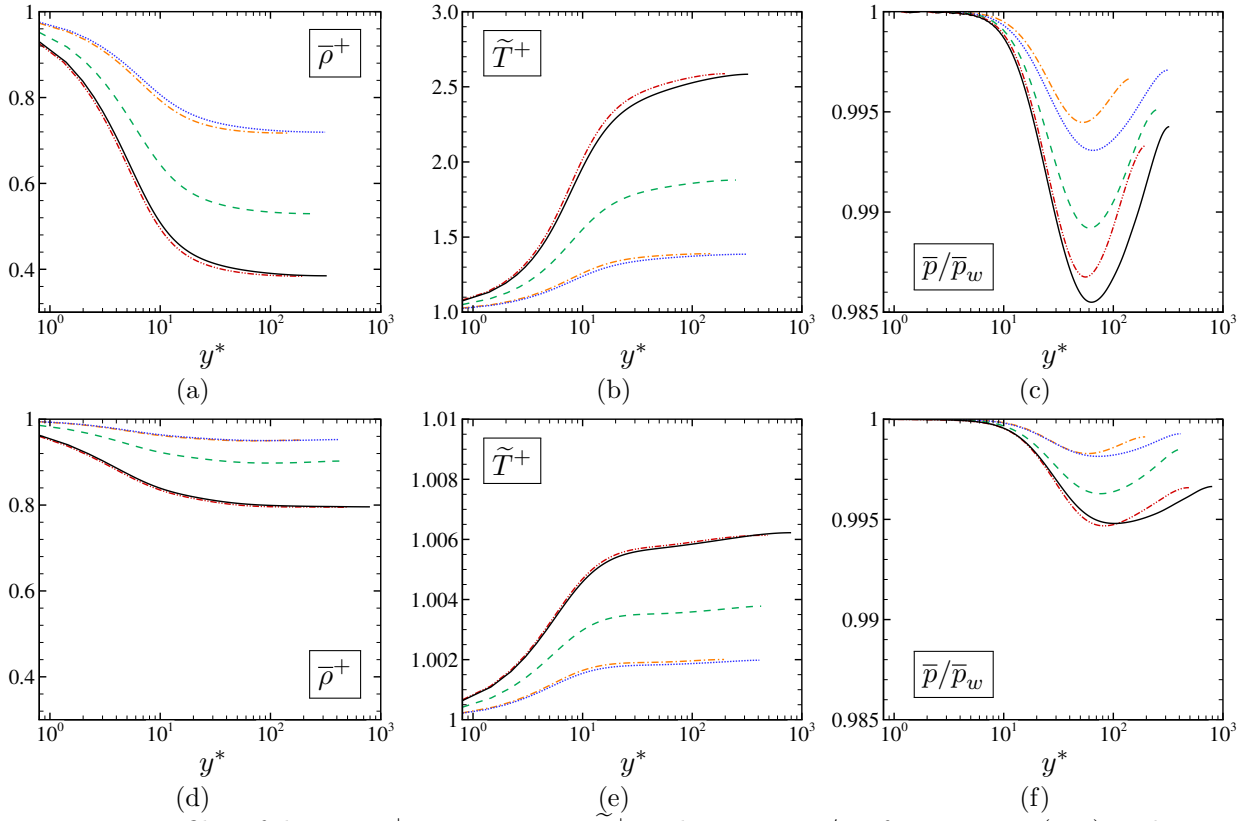


Figure 5.7. Profiles of density $\bar{\rho}^+$, temperature \tilde{T}^+ and pressure \bar{p}/\bar{p}_w for cases air (top) and PP11 (bottom). Same legend as in table 5.3.

accurately reproduces the mean velocity profile even for cases with high wall heat flux. Panels c and f confirm its validity even for dense gases. Note that, with this transformation, the wall-normal distance is normalised according to the semi-local scaling y^* , equation (5.3).

Figure 5.7 shows the density, temperature and pressure profiles normalised with wall quantities. The semi-local scaling y^* is retained from hereafter as the standard scaling for comparing perfect- and dense-gas cases. The rise of wall density values for increasing M_B is significant for air and less pronounced for PP11 flows. For instance, $\bar{\rho}/\rho_B = 2.51$ for AM3R12 and 1.25 for PM3R12 (see values in table 5.5). Mean density $\bar{\rho}^+$ decreases towards the centreline, with minimum values $\min_y\{\bar{\rho}_{cl}^+\} \approx 0.39$ for AM3R3 and ≈ 0.77 for PM3R3. An eventual influence on Re_τ^* is hidden by the strong dependence on \bar{M}_{cl} , noticeable for both $\bar{\rho}^+$ and \tilde{T}^+ . As prefigured by figure 5.3b, temperature profiles are quite different, with increases lower than 1% of the wall temperature for PP11 flows. Pressure is roughly constant across the channel. More precisely, it exhibits a constant value in the viscous sublayer and linear region, then it slightly decreases in the buffer layer reaching a minimum in the logarithmic zone, and afterwards increases in the outer region. For air, the relationship $\bar{p}/\bar{p}_w = \bar{\rho}^+ \tilde{T}^+ \lesssim 1$ (Gerolymos & Vallet, 2014) holds in each case. The minimum values for air flows are up to three times higher than for PP11 flows, with $\max_y\{(\bar{p} - \bar{p}_w)/\bar{p}_w\} \approx 1.5\%$ for AM3R12 and 0.5% for PM3R12. Although pressure is nearly constant, its mean value can be directly related to the turbulent fluctuations. In fact, by applying the Favre-averaging to the Navier–Stokes equations, one obtains for the mean equation in the y -direction (Huang *et al.*, 1995):

$$\frac{\partial \bar{\rho} \tilde{v}}{\partial y} + \frac{\partial \bar{p}}{\partial y} = \frac{\partial \bar{\tau}_{yy}}{\partial y} - \frac{\partial \bar{\rho} \tilde{v}'' v''}{\partial y} \quad (5.7)$$

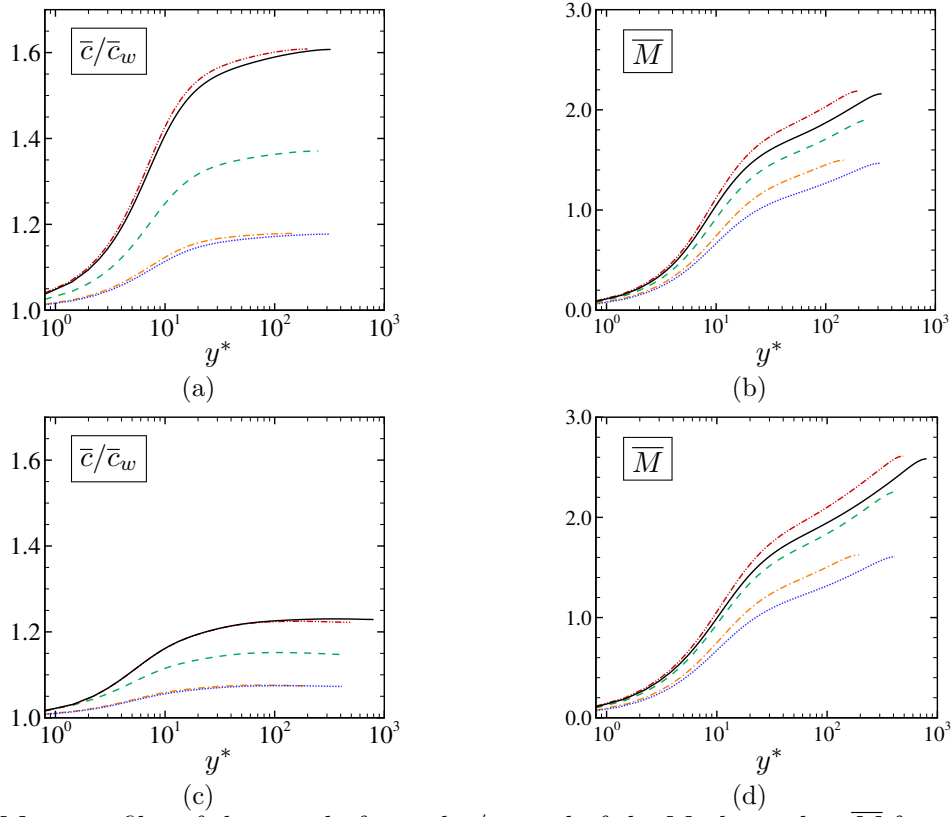


Figure 5.8. Mean profiles of the speed of sound \bar{c}/\bar{c}_w and of the Mach number \bar{M} for air (a,b) and PP11 (c,d) flows. Same legend as in table 5.3.

For incompressible flows, $\partial(\bar{p} + \overline{\rho v'v'})/\partial y = 0$, thus $\bar{p} = -\overline{\rho v'v'}$ up to an additive constant. For compressible flows, the first and the third terms are not equal to zero, yet they remain much lower than the other two. As a consequence, the minimum value of \bar{p} coincides with the maximum of the wall-normal Reynolds stresses, as it will be shown later.

Figure 5.8 shows the mean profiles of the speed of sound and Mach number across the channel. Sound-speed variations across the channel are related to temperature changes for air ($\bar{c}/\bar{c}_w = \sqrt{T^+}$), whereas they follow density variations for PP11. We notice that relative variations of the speed of sound are much smaller for PP11 (about 20% against 60% for air), leading to higher values of \bar{M} compared to air flows. Note however that, when comparing the Mach number profiles at the same y^* -location, similar values are found for both fluids (even if they are indeed slightly higher for PP11), proving the effectiveness of the semi-local scaling for comparing various variable property flows. For both fluids, a moderate dependence on the Re number is observed, with $\bar{M}(y^*)$ decreasing for higher Re_B . This is due to the fact that, for higher Re_B , momentum conservation tends to flatten the streamwise velocity profile in the outer layer in such a way that \bar{u}_{cl} decreases more quickly than the speed of decreases (heating effects being mitigated for higher Reynolds numbers). Note that using different definitions of the Mach number, namely \bar{u}/\bar{c} and \bar{u}/\bar{c} , leads to quite similar results, with differences below 1% for all cases.

The most striking differences between perfect and dense gas flow cases are highlighted in figure 5.9, presenting the profiles of viscosity, semi-local friction Reynolds number Re_τ^* and average Reynolds number \bar{Re} . For air flows, $\bar{\mu}/\bar{\mu}_w$ increases towards the centreline (gas-like behaviour), with a maximum deviation in AM3R3 for which $\max_y\{\bar{\mu}/\bar{\mu}_w\} \approx 2$. For PP11 flows, the ratio decreases (following approximately the $\bar{\rho}^+$ profile) up to $\min_y\{\bar{\mu}/\bar{\mu}_w\} \approx 0.75$ for PM3R3, which is a liquid-like behaviour. The viscosity behaviour largely influences the profiles of \bar{Re} , shown in figure 5.4, and

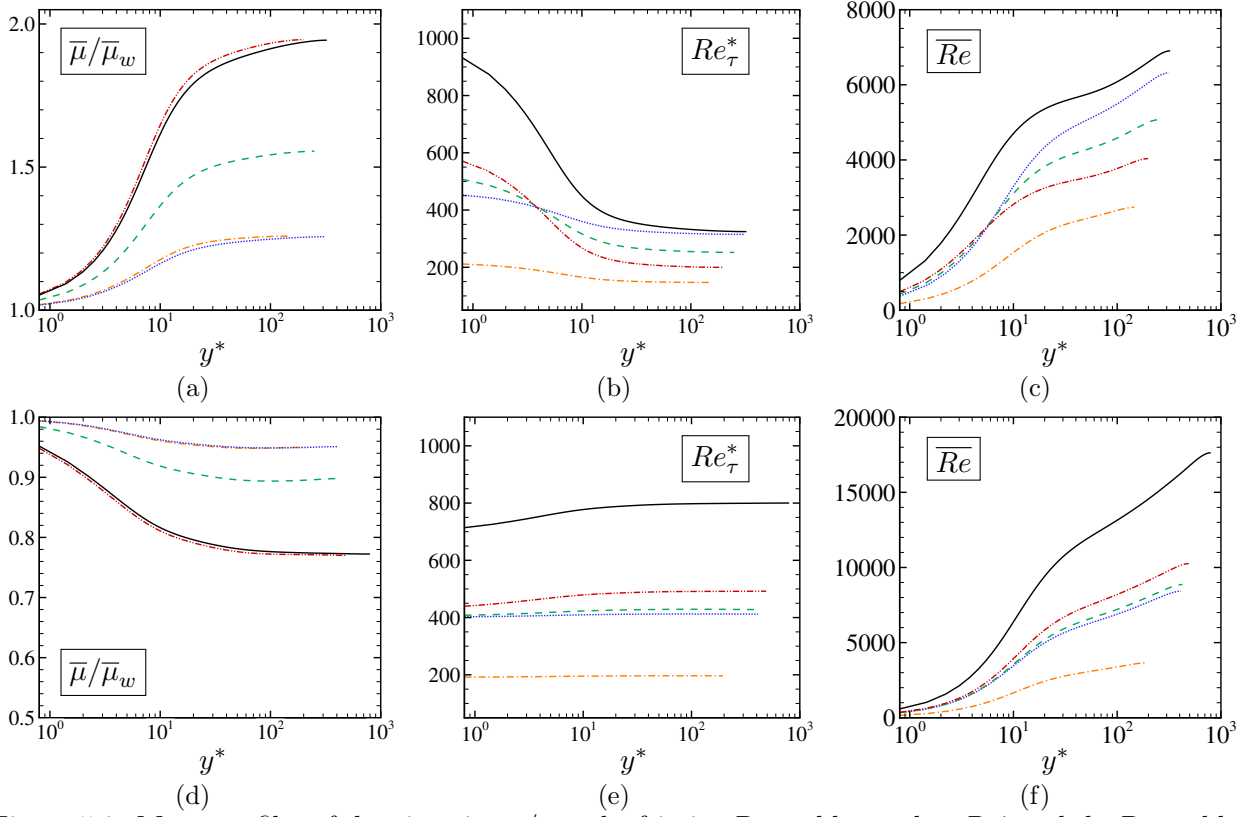


Figure 5.9. Mean profiles of the viscosity $\bar{\mu}/\bar{\mu}_w$, the friction Reynolds number Re_τ^* and the Reynolds number \overline{Re} for air (a,b,c) and PP11 (d,e,f) flows. Same legend as in table 5.3.

in particular the centreline values, that tends to be considerably larger for the dense gas flows. The evolution of Re_τ^* follows opposite behaviours for the two fluids, due to the aforementioned evolutions of transport properties. For air flows, it decreases rapidly up to the logarithmic layer and then more slowly in the outer region. For a given Re_B , a higher M_B leads to higher values of Re_τ^* near the wall, since μ_w is the same whereas ρ_w and $\partial u/\partial y|_w$ are increasing functions of the Mach number. At greater distance from the wall, Re_τ^* decreases even more quickly due to the strong temperature gradients in the wall-normal direction. Outside of the viscous sublayer, Re_τ^* is considerably lower than the near-wall one for the higher M_B cases, due to the combined effect of a rapid decrease of local density and an increase of local viscosity. Specifically, the centerline value may drop below the one obtained for lower Mach number cases, for which the fluid properties vary less. For PP11 flows, Re_τ^* exhibits an opposite behaviour, namely, it increases when moving from the wall to the centreline. The overall variations, of the order of 12% at most for high Mach number cases, are anyway much smaller than in the perfect gas (variations up to 60%). When increasing the wall distance, Re_τ^* slightly increases up to the buffer layer and remains roughly constant afterwards. Due to the increasing reduction of centerline viscosity for higher Mach number cases, the growth of Re_τ^* is enhanced when M_B becomes higher. The liquid-like viscosity behaviour clearly affects the profile of the local Reynolds number \overline{Re} (figure f) compared to the perfect gas (figure c). For instance, at the centreline, \overline{Re}_{cl} is about 2.5 times higher for PM3R12 than for AM3R12 results.

A direct consequence of the constant-Prandtl-number assumption in the ideal model is that $\bar{\kappa}/\bar{\kappa}_w = \bar{\mu}/\bar{\mu}_w$ for air. In PP11 simulations, variations of the thermal conductivity across the channel are smaller than the ones of viscosity ($\min_y\{\bar{\kappa}/\bar{\kappa}_w\} \approx 0.95$), nevertheless the ratio of the two transport properties remains roughly constant and $\bar{\mu}/\bar{\kappa} \approx 1.25$ throughout. Thus, the Prandtl number

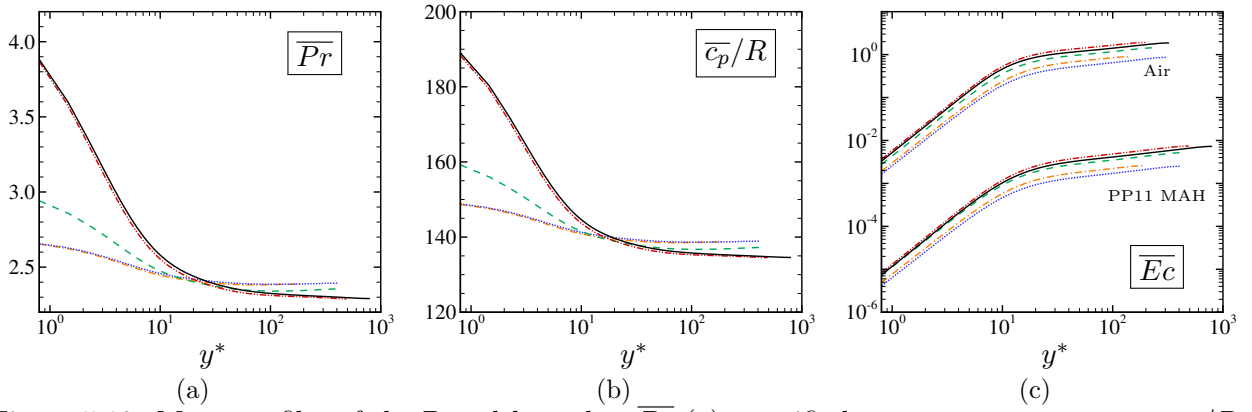


Figure 5.10. Mean profiles of the Prandtl number \overline{Pr} (a), specific heat at constant pressure $\overline{c_p}/R$ (b) for PP11, and Eckert number \overline{Ec} (c) for air and PP11. Same legend as in table 5.3.

profile (figure 5.10a) is essentially driven by the normalized specific heat at constant pressure $\overline{c_p}/R$ (figure 5.10b) which, in turn, follows a trend similar to the density profile (i.e. decreases with the wall distance). As pointed out in the above, the latter exhibit a strong dependency on M_B in the near-wall region, which is then fed back to \overline{Pr} . Specifically, the wall Prandtl number increases by about 50% when doubling the bulk Mach number and is almost insensitive to the Reynolds number. In the outer region, $\overline{Pr} \approx 2.3 - 2.4$ for all dense-gas cases. On the other hand, the high values of $\overline{c_p}/R$ for dense gases lead to very small values of the average Eckert number, $\overline{Ec} = \overline{u^2}/c_p \overline{T}$, a parameter that is representative of the degree of coupling between thermal and kinematic effects. We recall that for air flows, $\overline{c_p}/R = c_p/R = 3.5$, which is two order of magnitude lower than the mean values obtained with PP11. In figure 5.10c, \overline{Ec} exhibits a similar trend for both fluids, with two logarithmic zones connected near $y^* \approx 15$, but the curves are shifted by about two order of magnitude. In fact, the centreline values are of the order of $\mathcal{O}(1)$ for air and $\mathcal{O}(10^{-2})$ for PP11 cases.

5.2.3 Second-order statistics of the thermodynamic and transport properties

Root mean square values for the density, temperature and pressure are shown in figure 5.11. Gerolymos & Vallet (2014) have shown that for air flows $\mathcal{O}(\sqrt{T'^2}/\overline{T}) = \mathcal{O}(\sqrt{\rho'^2}/\overline{\rho}) = \mathcal{O}(\sqrt{p'^2}/\overline{p})$, regardless of the y^* location, Mach and Reynolds numbers. The same trend has been observed for both forced (Donzis & Jagannathan, 2013) and decaying (chapter 4 of this thesis) highly-compressible homogeneous turbulence. As discussed in Gerolymos & Vallet (2014) this behaviour is a direct consequence of the perfect-gas equation of state, and does not depend on the specific flow configuration under investigation. Indeed, the present relative r.m.s. distributions of thermodynamic quantities for air flows also verify this kind behaviour. After an initial growth in the linear region, $\sqrt{\rho'^2}/\overline{\rho}$ and $\sqrt{T'^2}/\overline{T}$ reach a peak in the buffer layer at $y^* \approx 10$ and then decay. The pressure fluctuations are rather nearly constant close to the walls, a slightly peak at the beginning of the logarithmic zone ($y^* \approx 40$) and finally decrease, reaching a minimum in the core region. For dense gases, the observed trends are very different. While the overall levels of density and pressure fluctuations remain of the same order of magnitude as for air cases, the relative temperature fluctuations are more than one order of magnitude lower. The fluctuating pressure distribution is much like the perfect-gas one, since it depends on the fluctuating velocity. Furthermore, ρ_{rms} decreased monotonically with the wall distance, the highest density fluctuations being observed close to the walls. The r.m.s. density levels decay at higher rates in the linear layer and in the outer region, and ex-

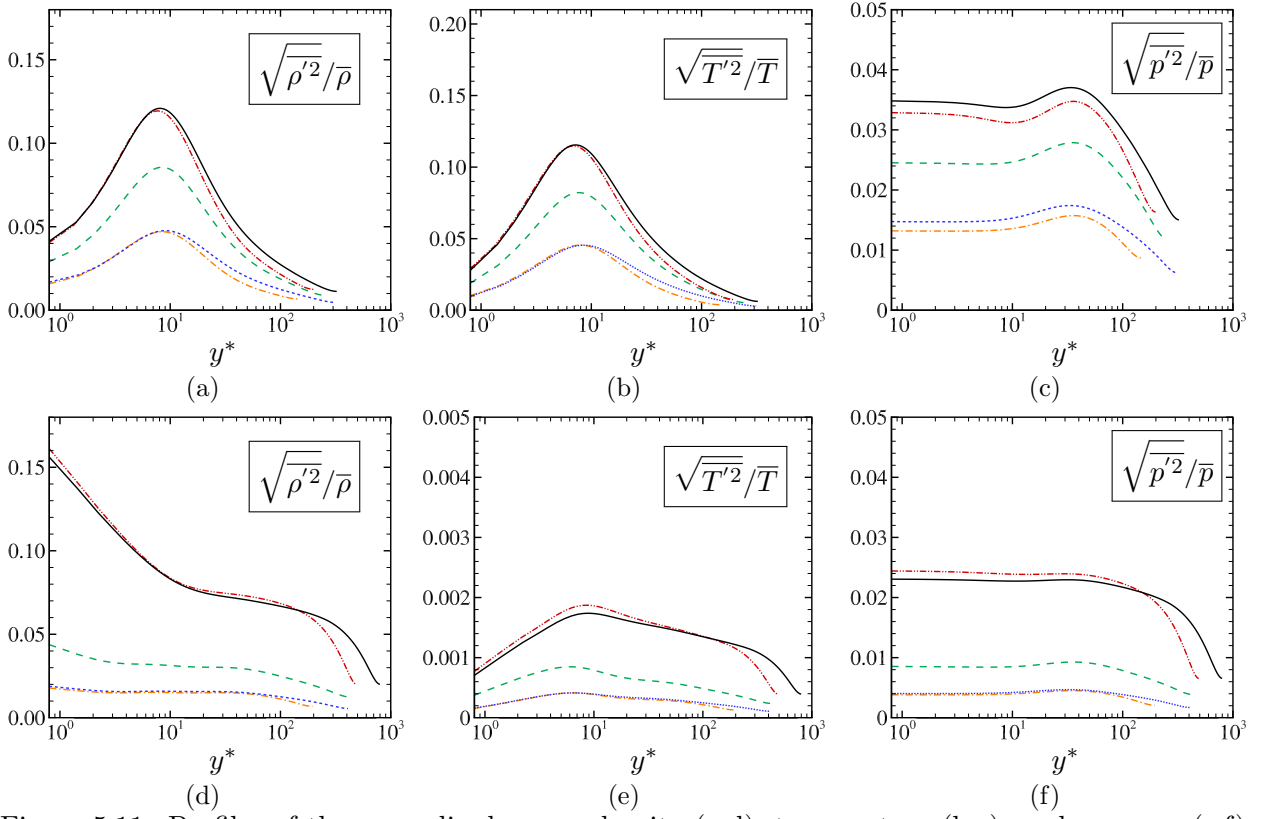


Figure 5.11. Profiles of the normalised r.m.s. density (a,d), temperature (b,e), and pressure (c,f) for air flows (top row) and PP11 flows (bottom row).

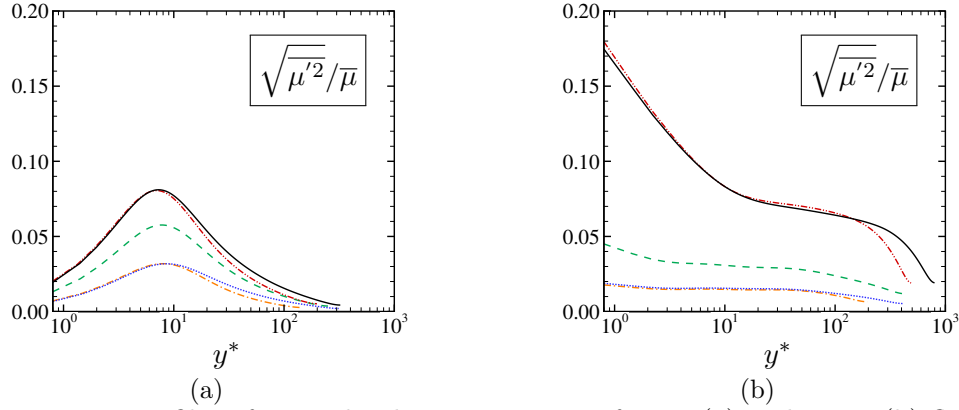


Figure 5.12. Profiles of normalised r.m.s. viscosity for air (a) and PP11 (b) flows.

hibit only weak variations in the logarithmic region. We have also seen that for PP11 the average density decreases with the wall-normal distance, and so thus the fluid compressibility (inverse of the speed of sound). The latter is $\mathcal{O}\left(\sqrt{\rho'^2}/\bar{\rho}\sqrt{p'^2}\right)$. Thus, relative density fluctuations decay due to the reduced compressibility and decaying r.m.s. pressure. The variance of viscosity is depicted in figure 5.12. As shown for the first-order moments, r.m.s. distributions of the transport properties inherit from the behaviour of the temperature fluctuations for air and of the density fluctuations for PP11 flows. Both viscosity and density fluctuations are sustained for PP11 (up to 18% of the mean value in the near wall region for the higher Mach number case). Yet, the hypothesis of Morkovin (1962) cannot be considered as invalid.

To further clarify the strong relations between density and pressure, correlation coefficients are

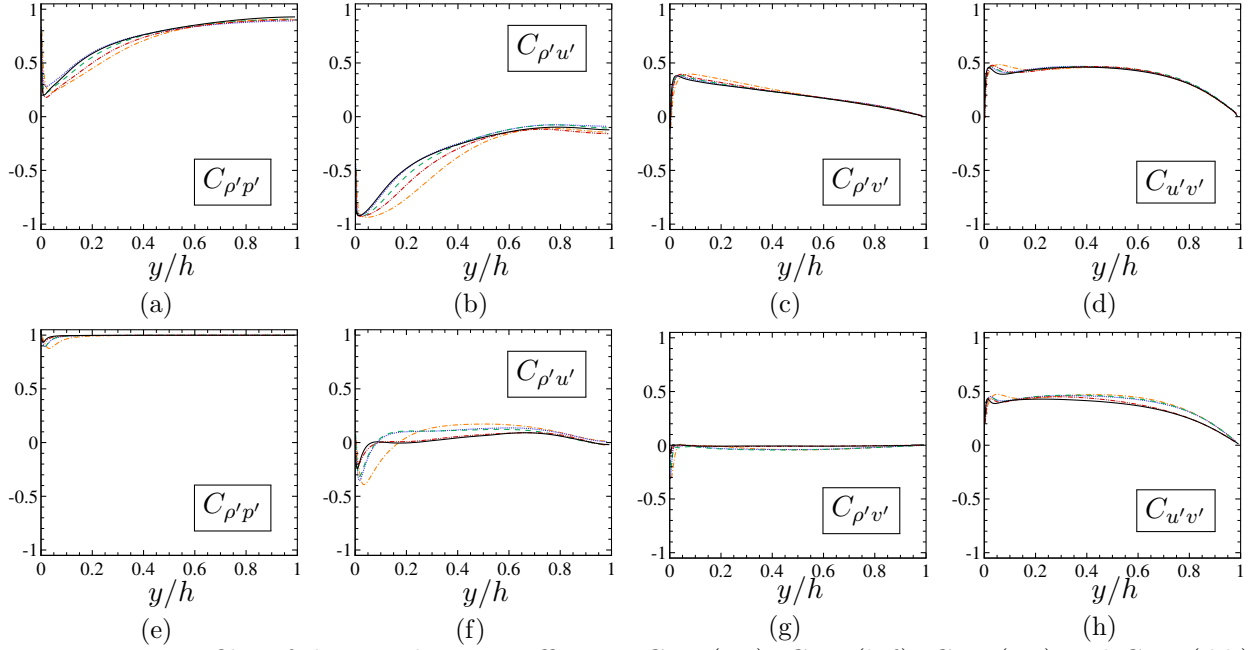


Figure 5.13. Profiles of the correlation coefficients $C_{\rho'p'}$ (a,e), $C_{\rho'u'}$ (b,f), $C_{\rho'v'}$ (c,g) and $C_{u'v'}$ (d,h) for air (top row) and PP11 (bottom row) flows.

calculated. Given two flow variables α and β , the correlation coefficient $c_{\alpha'\beta'}$ is defined as:

$$C_{\alpha'\beta'} = \frac{\overline{\alpha'\beta'}}{\sqrt{\overline{\alpha'^2}}\sqrt{\overline{\beta'^2}}} \quad (5.8)$$

Figure 5.13 shows the correlations $C_{\rho'p'}$, $C_{\rho'u'}$, $C_{\rho'v'}$ and $C_{u'v'}$ plotted with outer scaling. Due to the isothermal boundary conditions, the correlation coefficient $C_{\rho'p'}$ is equal to unity at the walls for both air and PP11. Afterwards, it decreases reaching a minimum at $y^* \approx 8$, approximately corresponding to the temperature variance peak, and then it increases again towards the centreline. For PP11 flows $C_{\rho'p'}$ approaches unity already at $y^* \approx 20$ and then remains constant. On the other hand, it raises slowly for air flows, with an asymptotic value close to 0.9. The correlation coefficients $C_{\rho'u'}$ and $C_{\rho'v'}$, which represent the transport of density fluctuations by the streamwise and wall-normal velocities, exhibit a totally different evolution depending on the fluid nature. Specifically, for air the streamwise correlation is negative and the spanwise is positive, whereas for PP11 both coefficients tend rapidly towards zero. Furthermore, $C_{\rho'u'}$ exhibits both a Mach and Reynolds dependence for air, whereas for PP11 it varies only with the Mach number. Lastly, the distributions $C_{u'v'}$ are similar even if a perfect collapse can be noticed for air, whereas a slight Mach dependence is observed for PP11.

Another way to interpret the peculiar behaviour of the thermodynamic quantities is to look at representations in Clapeyron's diagrams. Figure 5.14 shows distributions of the $p-v$ states in the computational box at one instant for PP11 flows. The different subfigures correspond successively to the influence of M_B , Re_B and the wall normal position. The different $p-v$ diagrams are coloured successively with values of the speed of sound, viscosity and Prandtl number in order to highlight the differences with respect to air. The $p-v$ states are recorded on slices parallel to the wall. The location is fixed at $y^* \approx 10$ where temperature fluctuations peak for figures 5.14 a and b. It is clear from figure 5.14a that the main effect of increasing M_B is a broadening of the region spanned by the $p-v$ states. For $M_B = 3$ cases, the states characterised by stronger compressions exit the dense

gas region and reach a supercritical zone where strong variations of the thermodynamic properties are observed. Higher values of M_B imply a greater dispersion in $\bar{\rho}_w$ values and in variances of the thermodynamic variables near the wall. Changing the Reynolds number Re_B for a given M_B in figure 5.14b reveals that the distributions of $p-v$ states are almost superimposed for the same y^* , providing an a-posteriori check of the validity of the semi-local scaling. Lastly, distributions for different y^* values are shown in figure 5.14c. The thermodynamic regions spanned by the $p-v$ states are reduced moving away from the wall. Even if most of the states are enclosed in the dense-gas region, none of the present simulations exhibit peculiar dense-gas effects, such as expansion shock waves. This can be explained by the fact that the turbulent Mach number, $M_t = \sqrt{u_i'^2}/\bar{c}$, does not reach sufficiently high values. For instance, figure 5.15 indicates that M_t approaches 0.4 for $M_B = 3$, whereas the simulations of decaying CHIT have shown that significant dense-gas effects can appear for M_t above 0.8. The distributions of M_t are similar as the simulations with air with slightly higher values for PP11 flows, showing that, notwithstanding liquid-like characteristics of dense gases, important compressibility is also present. The profiles of the fundamental derivative of gas dynamics $\bar{\Gamma}$, plotted in figure 5.15c, confirm that mean values are indeed lower than 1 for PP11 flows, with minimal values in the channel core. The flows thus evolve in the dense-gas region but with positive values of $\bar{\Gamma}$, so that BZT phenomena are not expected.

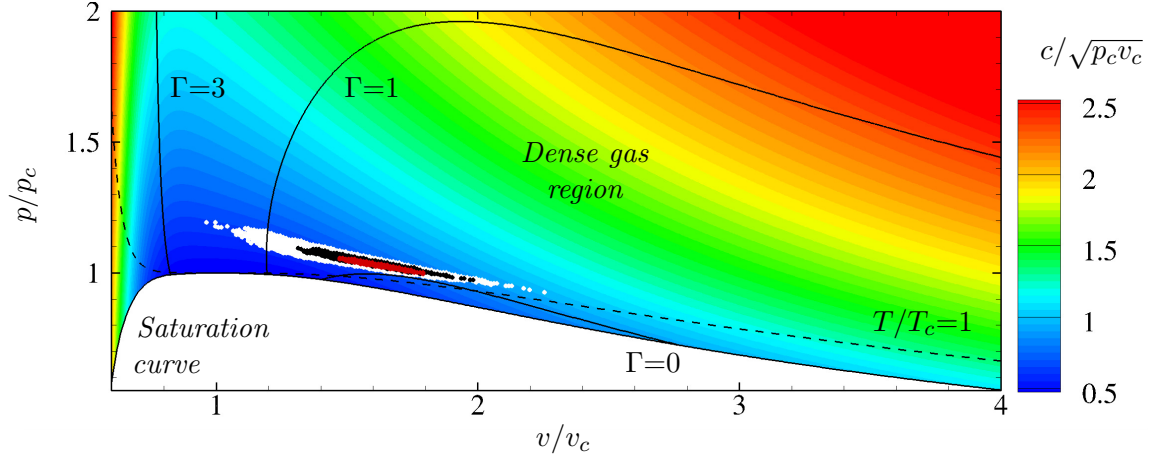
5.3 Influence of dense-gas effects on turbulence structure

5.3.1 Reynolds stresses and anisotropies

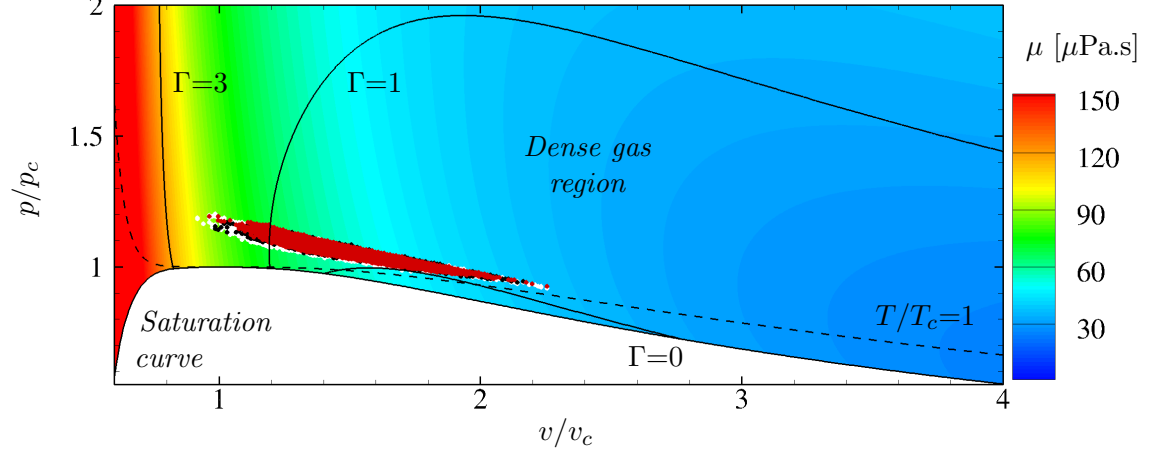
Figure 5.16 shows the Reynolds stresses $[\overline{\rho u_i'' u_j''}]^+ = \overline{\rho u_i'' u_j''}/\tau_w$ for the selected simulations. Patel *et al.* (2015) have shown that for variable-property turbulent channel flows, gas-like transport properties tend to lower the spanwise, wall-normal and shear Reynolds stresses with respect to the corresponding incompressible evolution, whereas the streamwise component increases. The opposite trend is expected when liquid-like properties are considered. In our cases the strong compressibility adds a complexity in the sense that higher M_B increase the velocity gradients near the wall –thus increasing the Reynolds stresses– but also dramatically affect viscosity distributions. For instance, the case AM1R7 ($Re_\tau^* \approx 315$) is characterised by a semi-local friction Reynolds number higher than case AM3R7 ($Re_\tau^* \approx 200$). For incompressible flows, all the Reynolds stresses would increase monotonically with Re_τ . However, since the temperature-dependent viscosity takes much higher values throughout the channel in the AM3R7 case, $\overline{\rho v'' v''}$, $\overline{\rho w'' w''}$ and $\overline{\rho u'' v''}$ are lower compared to AM1R7, whereas $\overline{\rho u'' u''}$ reaches higher levels. For PP11, a higher Mach number has the opposite effect on spanwise, wall-normal and shear stresses, coherently with a diminishing viscosity. For the streamwise stress, instead, the same behaviour is observed as in gas-like cases, mainly due to the more severe wall-normal velocity gradients counteracting viscosity variations. Indeed, Re_τ^* increases continuously from PM1R3 to PM3R12, as seen in figure 5.4.

Concerning the location of the peak values, for both air and PP11 flows they are roughly constant for the streamwise and spanwise components, namely around $y^* \in [10, 13]$ for $\overline{\rho u''^2}^+$, and $y^* \in [40, 50]$ for $\overline{\rho w''^2}^+$. On the other hand, a weak dependence on Re is observed for wall-normal and shear stresses. The slight shift towards higher y^* is more pronounced for PP11 flows since much higher Re_τ^* are achieved. The influence of Re is consistent with high-Reynolds-number incompressible simulations (Lee & Moser, 2015).

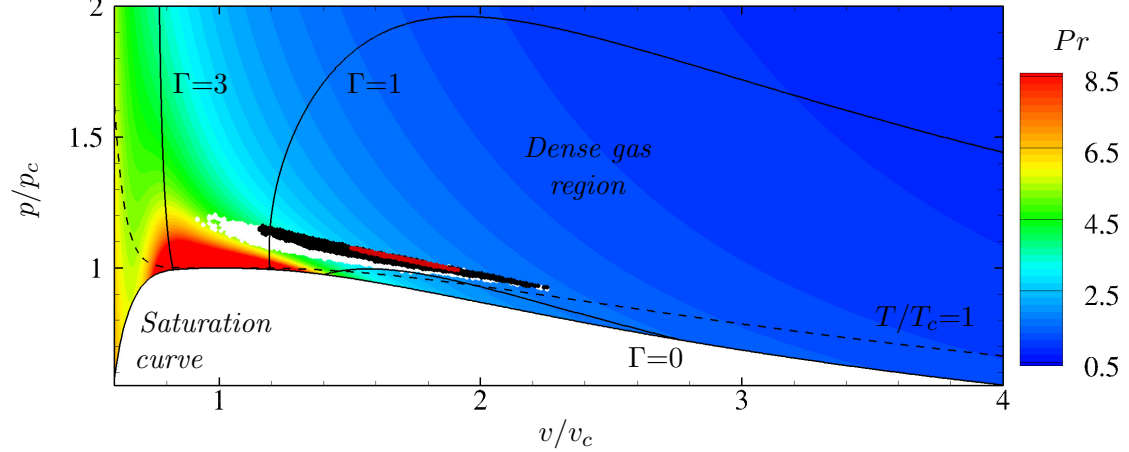
Despite the similar behaviour in the inner region, higher deviations are noticeable in the core region. A striking difference is found for the centreline evolution of the wall-normal stresses. Outer scaling y/h is used for the wall distance in figure 5.17 to stress this point. In air flows, all the computed stresses collapse logarithmically in the outer region, reaching approximately the same



(a) Influence of Mach number on the distribution of $p - v$ states for a slice at $y^* \approx 10$ and $Re_B = 3000$: \bullet $M_B = 1.5$; \bullet $M_B = 2.25$; \circ $M_B = 3$. The background colourmap shows isocontours of the speed of sound.



(b) Influence of Reynolds number on the distribution of $p - v$ states for a slice at $y^* \approx 10$ and $M_B = 3$: \bullet $Re_B = 3000$; \bullet $Re_B = 7000$; \circ $Re_B = 12000$. The background colourmap shows isocontours of the viscosity.



(c) Influence of y^* location on the distribution of $p - v$ states for $M_B = 3$ and $Re_B = 12000$: \bullet $y^* = 798$ (centreline); \bullet $y^* = 50$; \circ $y^* = 10$. The background colourmap shows isocontours of the Prandtl number. Figure 5.14. Distribution of $p - v$ states of an instantaneous flow field for PP11 in a Clapeyron diagram.

value at the centreline of the channel. On the contrary, wall-normal stresses $\overline{\rho v'' v''}^+$ for PP11 flows present different centreline values, notably for cases PM3R7 and PM3R12 at $M_B = 3$. The levels

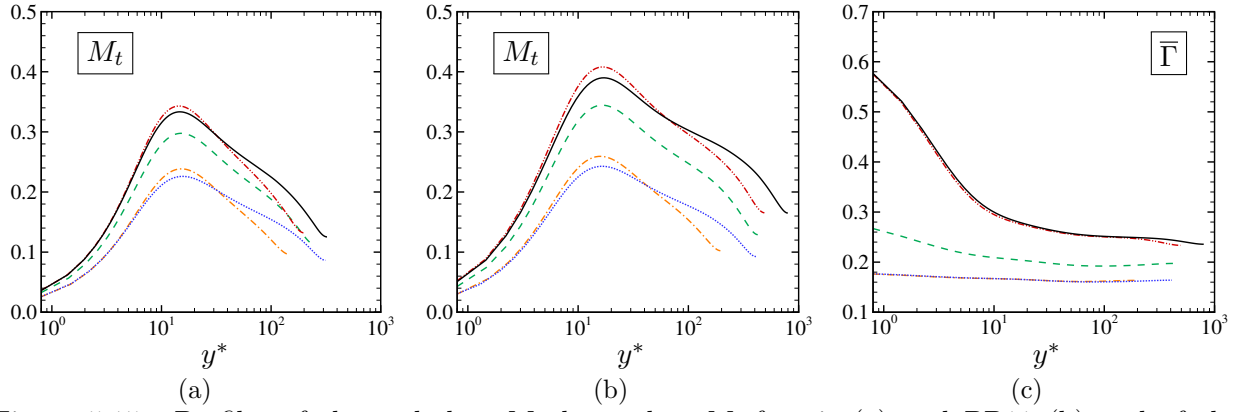


Figure 5.15. Profiles of the turbulent Mach number M_t for air (a) and PP11 (b) and of the fundamental derivative of gas dynamics $\bar{\Gamma}$ for PP11 (c). Same legend as in table 5.3.

of wall-normal fluctuations become then of the same level as those in the streamwise direction. A great change is thus expected in the anisotropies of the Reynolds stress tensor, which is defined as

$$a_{ij} = 2 \frac{\overline{\rho u_i'' u_j''}}{\overline{\rho u_k'' u_k''}} - \frac{2}{3} \delta_{ij} \quad (5.9)$$

The terms a_{ij} point out the role of compressibility and appear in the formulation of advanced turbulence models. Figure 5.18 shows the evolutions of the four non-zero elements of the anisotropy tensor. For air flows, it is shown that the behaviour of the diagonal elements of the anisotropy tensor is opposite to that of the Reynolds stresses. Specifically, anisotropy is reduced as the Reynolds number increases and is more marked for higher Mach numbers. Conversely, the cross component a_{12} increases for higher values of the shear stresses. The evolutions of the Reynolds anisotropies, as well as the turbulent kinetic energy budgets as shown later, are in accordance with the study of Sarkar (1995). This author has shown that, for homogeneous shear flows, compressibility has a “stabilizing” effect in the sense of a reduction of Reynolds-stress anisotropy, causing a reduction of the growth rate of the turbulent kinetic energy. For PP11 flows, the Mach number (hence, the thermodynamic conditions) has a much greater impact on the anisotropies than the Reynolds number. If the cross components are roughly similar to air cases, significant differences are found for the streamwise and wall-normal anisotropies at $M_B = 3$. These can be related to the different behaviour of $\overline{\rho v'' v''}$ after its peak value. In the channel core, the anisotropy components are close to zero.

To further assess the deviation of dense-gas behaviour from ideal one, we consider the non-dimensional shear rate Sk/ϵ (with $S = d\bar{u}/dy$) and the gradient Mach number $M_g = Sk^{3/2}/(\bar{c}\epsilon)$, plotted in figure 5.19. Sk/ϵ is a measure of the turbulence-to-mean-shear timescale ratio. It peaks in the buffer layer and attains approximately constant values in the logarithmic zone, where the flow is close to equilibrium ($Sk/\epsilon \approx 3$). For air flows, the peak values are higher with respect to PP11 flows. For instance, the maxima are $\max_y[Sk/\epsilon] \approx 22.8$ and 20 for AM3R7 and PM3R7 cases, respectively. The gradient Mach number, on the other hand, measures the importance of compressibility effects. For both fluids, a high dependency on both Re_B and M_B is observed. The magnitudes and locations of the peaks are similar in each case. The highest differences are observed for M3R12 cases, with a slightly higher M_g for PP11. Higher M_g is directly linked to important reductions of the turbulent shear stress and an increase of the diagonal components of Reynolds stress anisotropy tensor (Sarkar, 1995), as previously shown in figures 5.16 and 5.18.

Finally, important differences are found also by analysing the skin friction coefficient by means

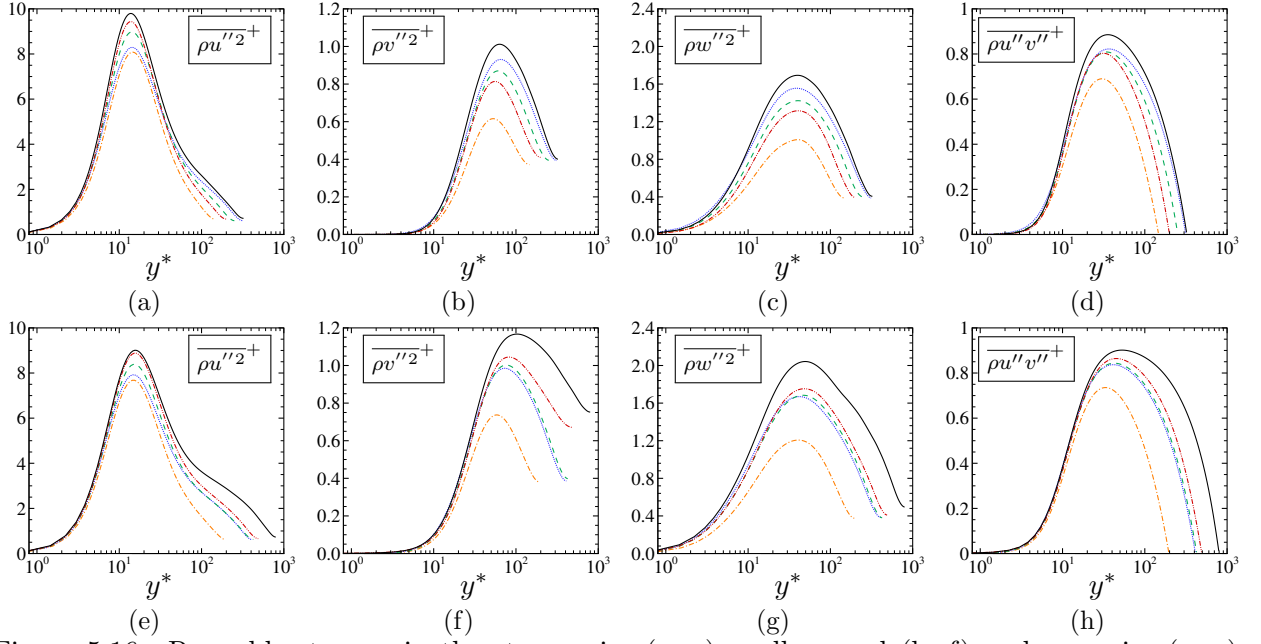


Figure 5.16. Reynolds stresses in the streamwise (a, e), wall-normal (b, f) and spanwise (c, g) directions and Reynolds shear stresses (d, h) for air (top row) and PP11 (bottom row) flows with semi-local scaling.

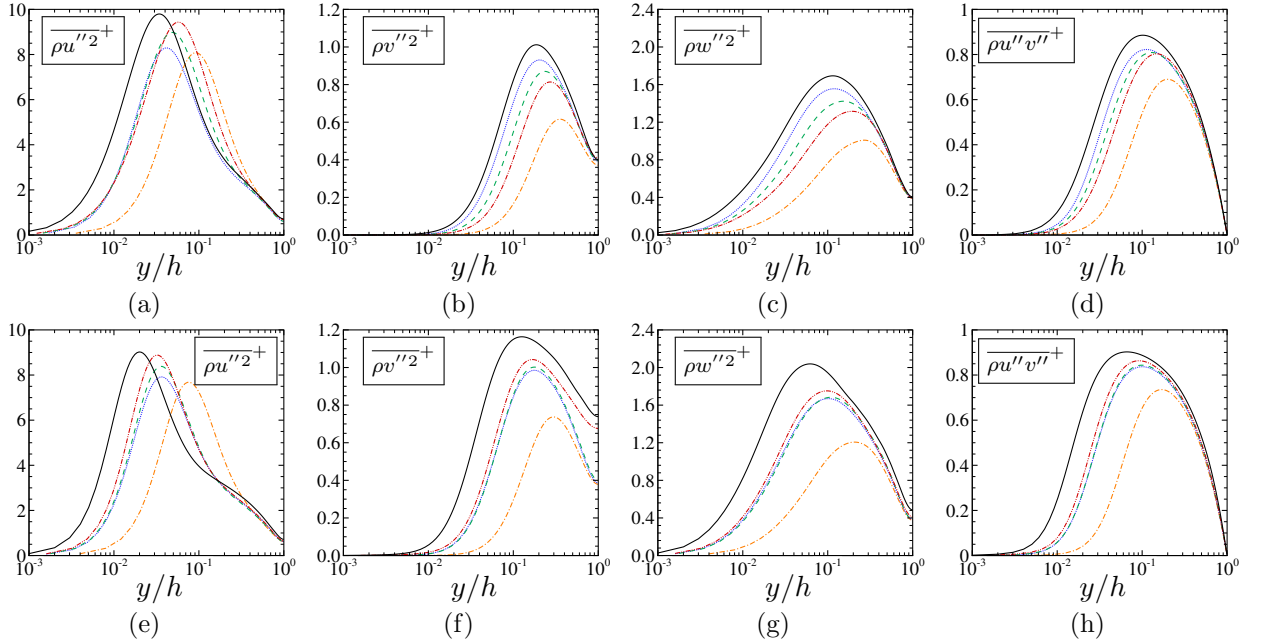


Figure 5.17. Reynolds stresses in the streamwise (a, e), wall-normal (b, f) and spanwise (c, g) directions and Reynolds shear stresses (d, h) for air (top row) and PP11 (bottom row) flows with outer scaling.

of the Fukagata–Iwamoto–Kasagi (FIK) identity. Starting from the incompressible expression of Fukagata *et al.* (2002), Gomez *et al.* (2009) derived an exact relationship for the analysis of the contribution of Reynolds stresses to the skin friction coefficient in compressible cases. The skin

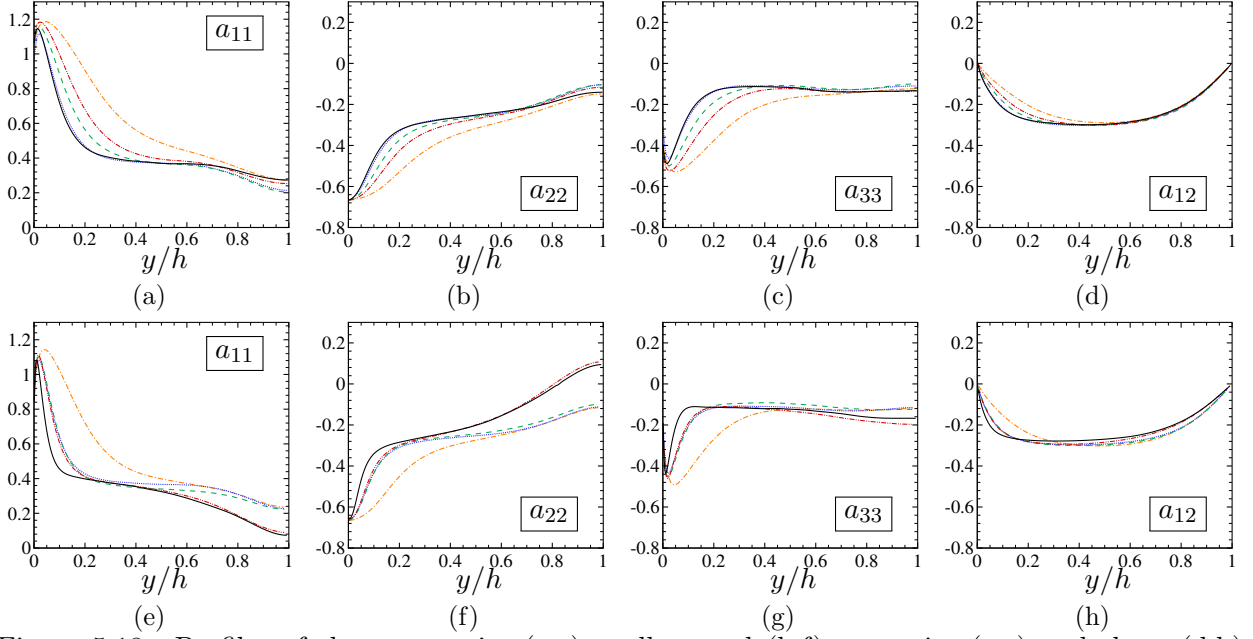


Figure 5.18. Profiles of the streamwise (a,e), wall-normal (b,f), spanwise (c,g) and shear (d,h) Reynolds stress anisotropies for air (top row) and PP11 (bottom row) flows.

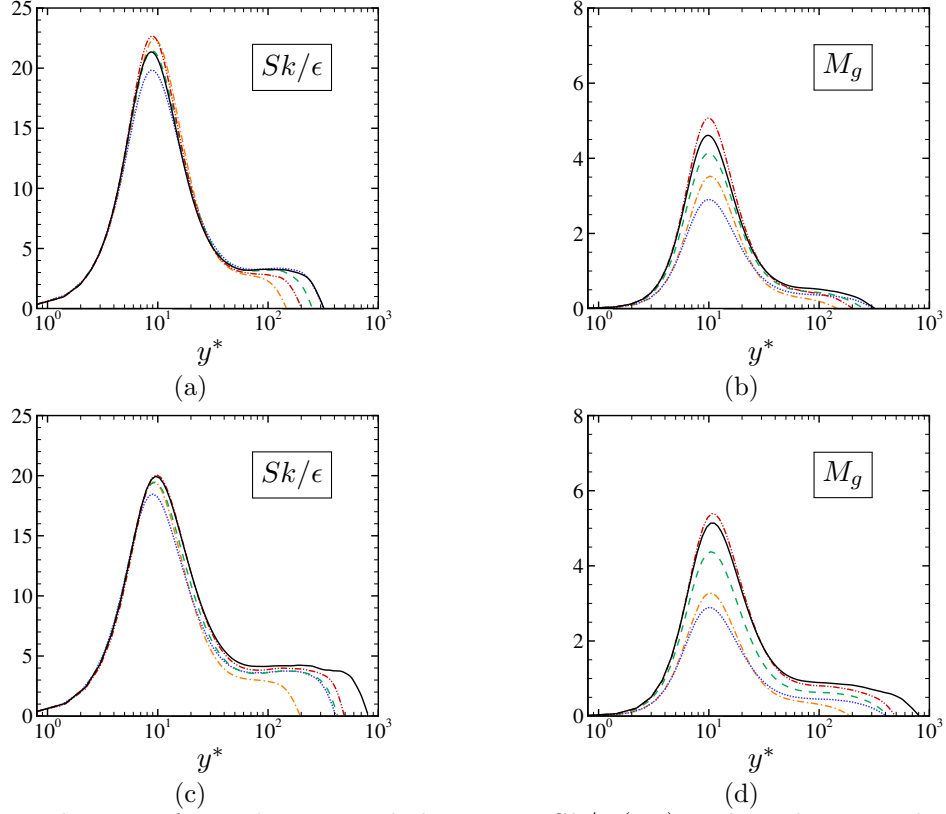


Figure 5.19. Evolutions of non-dimensional shear rate Sk/ϵ (a,c) and gradient Mach number M_g (b,d) profiles for air (top row) and PP11 (bottom row) flows.

friction coefficient may be break up into four contributions, namely:

$$\begin{aligned}
 C_f = & \underbrace{\frac{6}{Re_{Bb}}}_{C_L} + \underbrace{6 \int_0^1 (1-y) \overline{\rho(-u''v'')} dy}_{C_T} + \underbrace{\frac{6}{Re_{Bb}} \int_0^1 (1-y) \overline{\tilde{\mu} u'' v''} dy}_{C_C} + \\
 & \underbrace{\frac{6}{Re_{Bb}} \int_0^1 (1-y) \overline{\mu' \left(\frac{\partial u'}{\partial y} + \frac{\partial v'}{\partial x} \right) dy}}_{C_{CT}},
 \end{aligned} \tag{5.10}$$

Table 5.6. Contributions to the skin friction coefficient according to the compressible extension of the FIK identity of [Gomez *et al.* \(2009\)](#) for different cases.

Case	$C_f (\times 10^3)$	Error (%)	C_L (%)	C_T (%)	C_C (%)	C_{CT} (%)
AM1R7	6.41	0.3	13.28	84.63	2.04	0.05
AM2R7	6.37	1.8	13.26	82.19	4.45	0.11
AM3R7	6.36	3.8	13.15	79.08	7.60	0.17
PM1R7	6.24	-0.8	13.76	86.71	-0.48	0.02
PM2R7	6.15	0.4	14.05	87.00	-1.07	0.02
PM3R7	6.04	0.9	14.31	88.21	-2.55	0.02

being C_L the laminar contribution, C_T the turbulent contribution, C_C the compressible contribution (in which $\bar{\mu} = \bar{\mu} - 1$) and C_{CT} the compressible-turbulent interaction term. As observed by [Fukagata *et al.* \(2002\)](#), the turbulent term is proportional to the weighted average of Reynolds stresses, where the weight decreases linearly with the distance from the wall. This explains why the main contribution to the frictional drag is due to the turbulent structures close to the wall, rather than where the Reynolds stresses peak. The compressible term C_C is due to the mean viscosity variations and to the mean wall-normal velocity gradient, whereas C_{CT} represent the interaction between compressibility and turbulent effects, and usually it is rather small. Table 5.6 shows the C_f values obtained from equation (5.10) for different cases, as well as the relative error with respect to the values obtained from DNS and the relative weights of each contribution. In order to investigate the effect of compressibility, we consider the cases with $Re_B = 7000$ and different M_B , such that the laminar contribution C_L is approximately constant (*i.e.* $C_L \approx 13 - 14\%$). For air cases, the contribution due to the turbulent fluctuations C_T decreases for higher M_B , coherently with the decreasing of the Reynolds stress peak. The opposite is registered for PP11, for which the relative weight of C_T increases of about 1.5% due to the liquid-like behaviour. Moreover, the peculiar liquid-like behavior causes substantial changes in the compressible contribution C_C : namely, it becomes more important as the M_B increases for both fluids, but it is positive for air (being $\bar{\mu} > 0$) and negative for PP11 ($\bar{\mu} < 0$). This term, indeed, is related to variable-property effects rather than compressibility effects due to high-speed flows. Lastly, the compressible-turbulent interaction term, always quite small, contributes to the total skin friction coefficient for about 0.1% in air and one order of magnitude less (0.02%) in PP11.

5.3.2 Turbulent kinetic energy budgets

For fully developed, statistically stationary channel flow, the turbulent kinetic energy budget reads (Lechner *et al.*, 2001):

$$P_k + T_k + V_k + M_k + D_k + \varepsilon_k = 0 \quad (5.11)$$

with

$$P_k = -\overline{\rho u'' v''} \frac{d\tilde{u}}{dy} \quad (5.12)$$

$$T_k = -\frac{d}{dy} \frac{1}{2} (\overline{\rho u''^2 v''} + \overline{\rho v''^3} + \overline{\rho w''^2 v''}) \quad (5.13)$$

$$V_k = \frac{d}{dy} (\overline{u' \tau'_{xy}} + \overline{v' \tau'_{yy}} + \overline{w' \tau'_{yz}}) \quad (5.14)$$

$$M_k = \overline{u''} \left(-\frac{\partial \bar{p}}{\partial x} + \frac{d\overline{\tau'_{xy}}}{dy} \right) + \overline{v''} \left(-\frac{\partial \bar{p}}{\partial y} + \frac{d\overline{\tau'_{yy}}}{dy} \right) + \overline{w''} \frac{d\overline{\tau'_{yz}}}{dy} \quad (5.15)$$

$$D_k = \overline{p' \frac{\partial u'}{\partial x}} + \overline{p' \frac{\partial v'}{\partial y}} - \frac{d}{dy} \overline{v' p'} + \overline{p' \frac{\partial w'}{\partial z}} \quad (5.16)$$

$$\varepsilon_k = - \left(\overline{\tau'_{xj} \frac{\partial u'}{\partial x_j}} + \overline{\tau'_{yj} \frac{\partial v'}{\partial x_j}} + \overline{\tau'_{zj} \frac{\partial w'}{\partial x_j}} \right) \quad (5.17)$$

P_k is the turbulent production, T_k and V_k the turbulent and viscous transports, M_k the mass flux variation, D_k the velocity-pressure gradient tensor (composed of the sum of pressure-strain correlation and pressure-transport term) and ε_k the dissipation term. Figure 5.20 shows the turbulent kinetic energy budget for cases AM3R12 and PM3R12. Three different nondimensionalisations are tested, namely, a bulk scaling with $\tau_w u_B/h$ (Lechner *et al.*, 2001; Huang *et al.*, 1995), a wall scaling with $\bar{\rho}_w u_\tau^4/\bar{\nu}_w$ (Guarini *et al.*, 2000), and a semi-local scaling with $\tau_w^2/\bar{\mu}(y)$ (Foyi *et al.*, 2004). It is clear from the figure that the first two scalings are not able to take into account variable-property effects. The latter represents thus the most suitable scaling to compare perfect and dense gases. In semi-local scaling, the viscous and turbulent transports behave similarly, whereas the mass flux variation (which is zero for incompressible flows) is much smaller for PP11 case. In the core region, all the budget terms collapse.

A closer inspection of the turbulent production and dissipation for the selected simulations is provided in figure 5.21, which also shows their ratio, plotted both in linear and logarithmic semi-

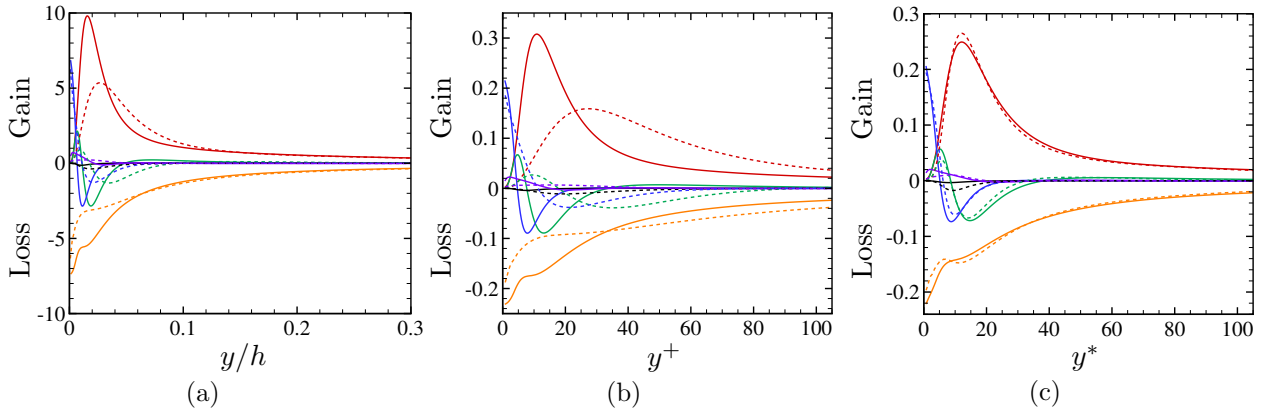


Figure 5.20. Comparisons of turbulent kinetic energy budgets for cases AM3R12 (dashed lines) and PM3R12 (solid lines) normalised by $\tau_w u_B/h$ (a), $\bar{\rho}_w u_\tau^4/\bar{\nu}_w$ (b) and $\tau_w^2/\bar{\mu}(y)$ (c). — P_k , — T_k , — V_k , — M_k , — D_k , — ε_k .

local coordinates. For both fluids, the production peak is located at $y^* \approx 11 - 12$ for all the considered bulk conditions. Lechner *et al.* (2001) and Sarkar (1995) showed that the main effect of compressibility is a reduction in the production and dissipation rate of the turbulent kinetic energy. Nevertheless, this effect can be associated to the strong variations of properties at high Mach numbers. The semi-local scaling $\tau_w^2/\bar{\mu}(y)$ is able to collapse, for instance, the budgets for cases M1R7, M2R7 and M3R7, for which substantial differences should be observed due to the doubling of the bulk Mach number. Globally, a common trend is observed for air and PP11 flows, where the peaks of production and dissipation terms slightly increase with Re_τ^* . The ratio of the production and dissipation rates $P_k/\varepsilon_k - 1$ exhibits a similar evolution for similar value of Re_τ^* (cases PM1R3 and AM3R7). The ratio peaks at the same y^* location as the production term. Furthermore, for cases with $Re_\tau^* > 200$, a second peak starts growing in the logarithmic region. For PP11 flows, the inner peak seems roughly unaffected, as found for high-Reynolds-number turbulent incompressible flows (Lee & Moser, 2015), whereas in air a slight decrease is observed with increasing Re_τ^* , as shown in the subfigure in logarithmic scale. Since the Re_τ^* values are low in air cases, the ratio always remains negative and no effective net turbulent production is observed in the outer layer.

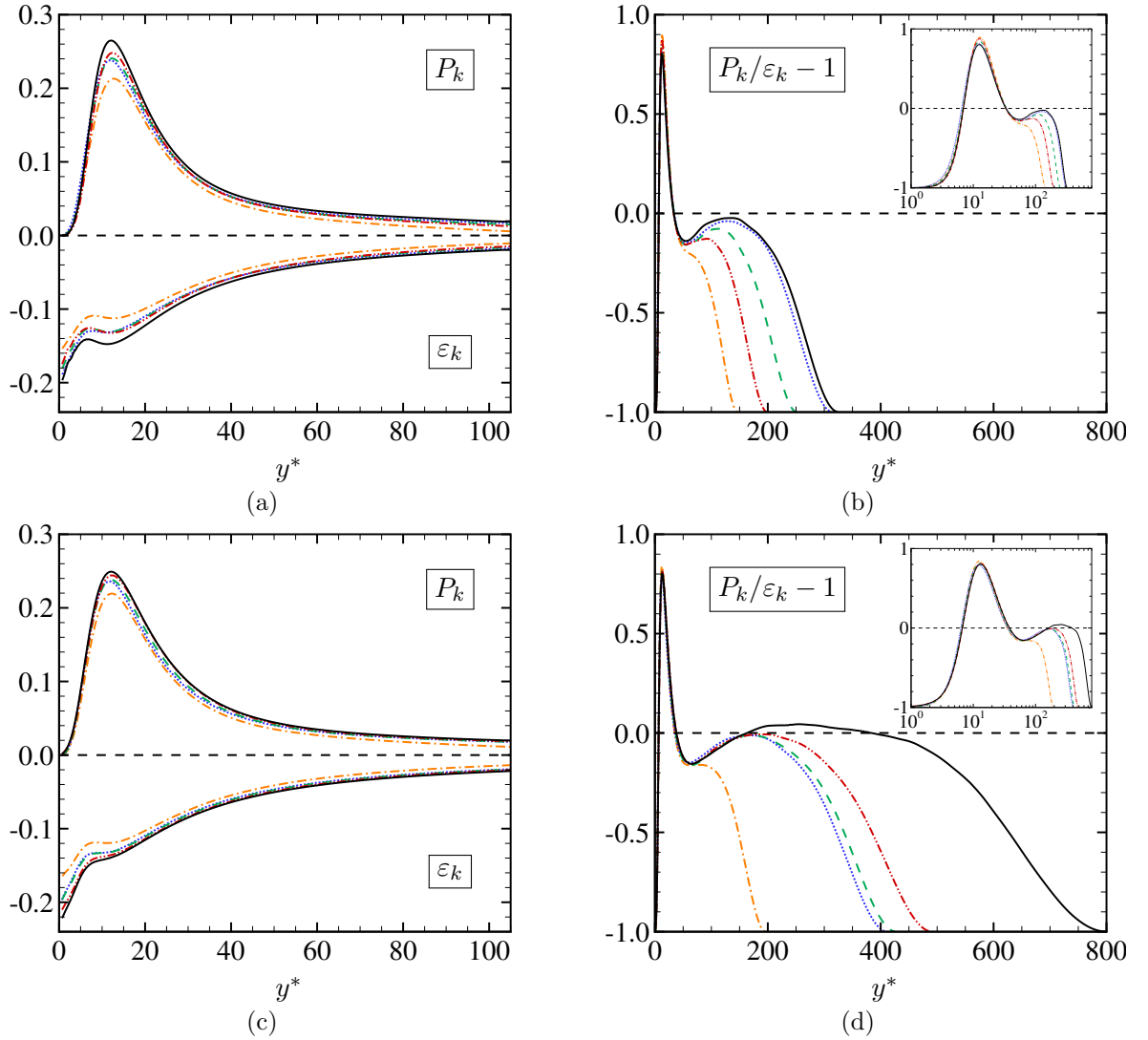


Figure 5.21. Profiles of the turbulent production P_k , the turbulent dissipation ε_k and the ratio of production to dissipation $P_k/\varepsilon_k - 1$ for air (top row) and PP11 (bottom row) flows.

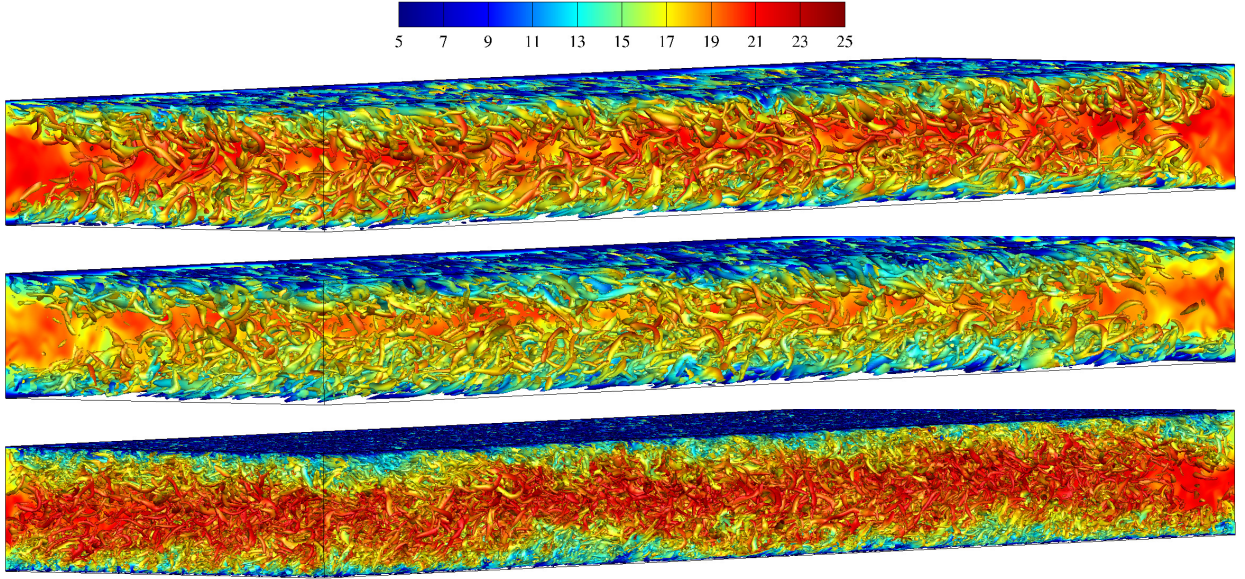


Figure 5.22. Isosurfaces of normalised Q -criterion $Q(h/u_B)^2 = 1$ coloured with normalised streamwise velocity $\sqrt{\rho}u/\sqrt{\tau_w}$. Top: AM3R7, centre: PM1R3, bottom: PM3R7.

For PP11, the case PM3R12 is the only one with a positive region, extending between $y^* \approx 180$ and $y^* \approx 400$.

5.3.3 Near-wall turbulent structures

The difference in near-wall turbulent structures is now analysed by means of instantaneous flow visualizations. Figure 5.22 shows the isosurfaces of the normalised Q -criterion coloured with the streamwise velocity for cases AM3R7, PM1R3, PM3R7. The Q -criterion is normalised with respect to the channel half-height h and the bulk velocity u_B in order to focus on differences in the outer region. A visual inspection of the instantaneous fields shows that similar structures are observed for iso- Re_τ^* cases, namely, AM3R7 and PM1R3 ($Re_\tau^* \approx 200$). For case PM3R7, smaller structures are visible due to the higher Re_τ^* , and the structures survive up to centreline, where a greater turbulent activity is observed.

Figures 5.23-5.25 show a slice of the instantaneous flow field at different values of y^* (namely, $y^* = 12, 50$ and centreline) coloured with levels of the normalised streamwise velocity fluctuations $\sqrt{\rho}u''/\sqrt{\tau_w}$ for cases AM3R7 and PM1R3 (hence for $Re_\tau^* \approx 200$). The local density value ρ is used for normalisation instead of $\bar{\rho}$, since it correlates better with the modulation of the streak magnitude (Patel *et al.*, 2015). In all cases, the computational box is scaled with respect to semi-local co-ordinates (x^*, z^*) . Differently from the classical wall scaling (x^+, z^+) that is the same for all heights, the semi-local scaling changes with the wall distance. The box size considered is 5000×1200 based on non-dimensional coordinates $x^* \times z^*$ for each case. For both fluids, the maps of the instantaneous streamwise velocity close to the wall exhibits the well-known organization in streaks (Coleman *et al.*, 1995; Chernyshenko & Baig, 2005; Gerolymos & Vallet, 2014). In past years, the role of compressibility on the modification of near-wall structures has been widely discussed. Initially, it was argued that its effect was to increase the streamwise correlation length, enhancing the coherence of near-wall streaks (Coleman *et al.*, 1995; Duan *et al.*, 2010; Lagha *et al.*, 2011). This statement was not confirmed when the semi-local scaling was taken into account (Morinishi *et al.*, 2004; Patel *et al.*, 2015). A rather universal behaviour was then observed. The latter conclusion holds in the present comparison between air and PP11 flows at the three heights shown in the figures. Figures 5.23 shows that near-wall layers are dominated by streaks with similar

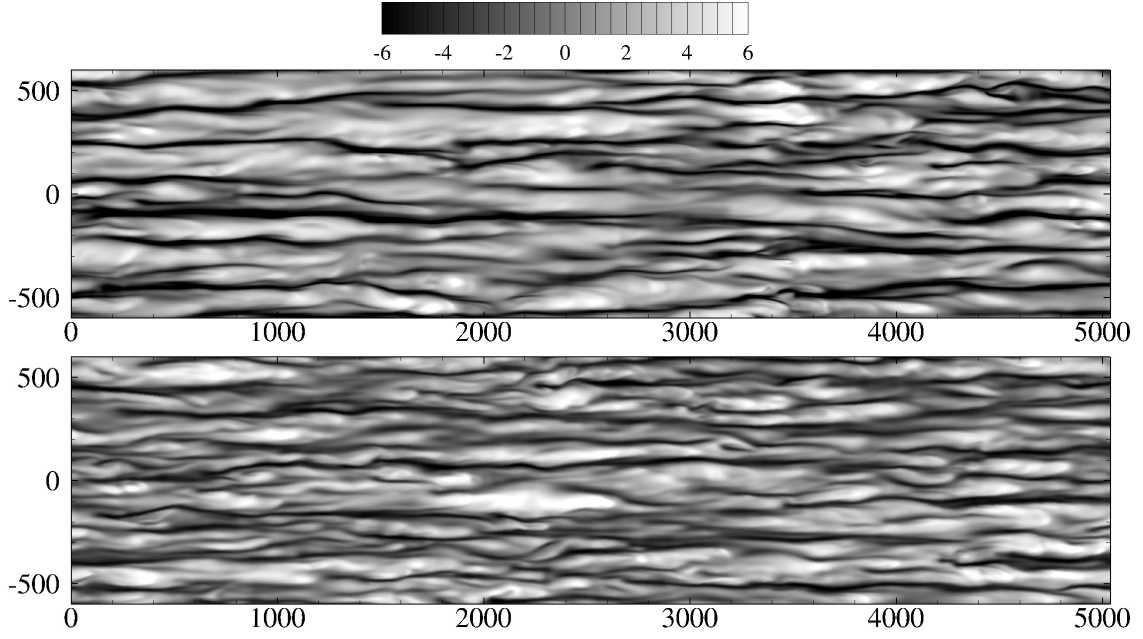


Figure 5.23. $\sqrt{\rho u''}/\sqrt{\tau_w}$ fluctuations at $y^* \approx 12$ for AM3R7 (top) and PM1R3 (bottom).

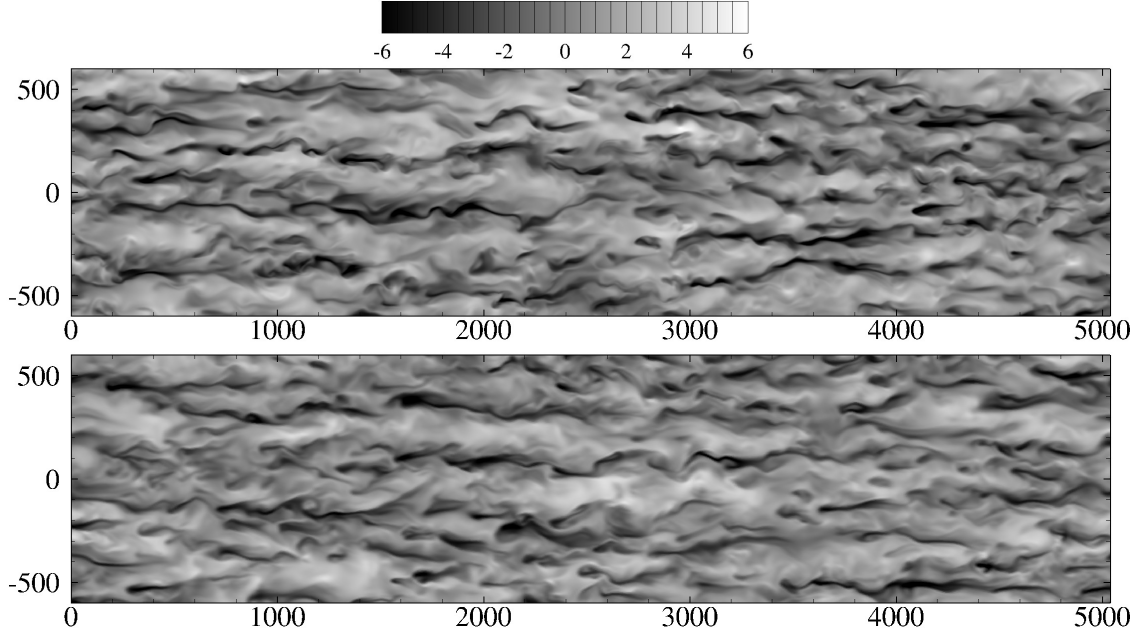


Figure 5.24. $\sqrt{\rho u''}/\sqrt{\tau_w}$ fluctuations at $y^* \approx 50$ for AM3R7 (top) and PM1R3 (bottom).

streamwise lengths and spanwise separations. At $y^* \approx 50$, in figure 5.24, the structures become less coherent and less energetic. At the centerline of the channel, as illustrated in figure 5.25, no prominent coherent structures can be found.

Differently from velocity fields which have a similar structural behaviour if represented with the semi-local scaling, the thermodynamic quantities are much more sensitive. Figures 5.26 and 5.27 show the instantaneous pressure p'^+ and density ρ'^+ fluctuations at $y^* \approx 12$. Pressure fluctuations are characterised in both cases by long-range interactions (Kim, 1989; Chang III *et al.*, 1999), even if the mean-square fluctuations mainly have local contributions (Kim, 1989). Higher deviations from the mean value are observed in air. Contrary to pressure, density fluctuations behave differently between air and PP11 flows. For air, very elongated scales in the streamwise direction

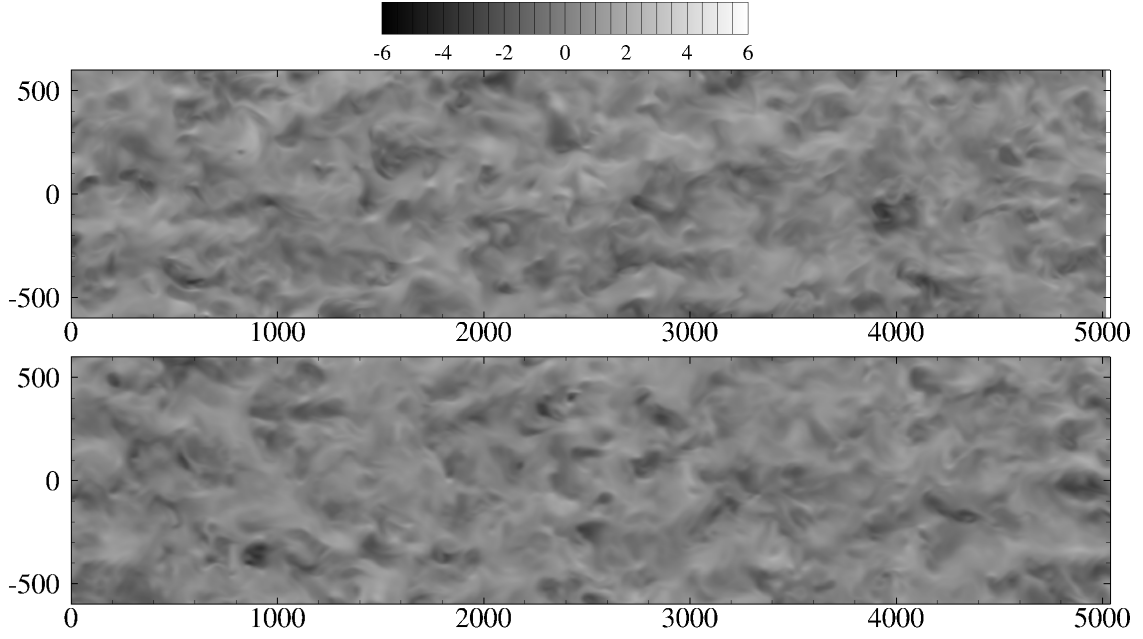


Figure 5.25. $\sqrt{\rho}u''/\sqrt{\tau_w}$ fluctuations at $y^* \approx 200$ for AM3R7 (top) and PM1R3 (bottom).

Table 5.7. Values of y^* and λ^* for the peak values of the spectra shown in figure 5.28

	$k_x E_{\rho uu}/\tau_w$		$k_z E_{\rho uu}/\tau_w$		$k_z E_{\rho vv}/\tau_w$	
	air	PP11	air	PP11	air	PP11
y^*	13.9	14.1	13.5	13.2	48.8	55.2
λ^*	1180	1220	115	114	116	116

are preferentially observed and follow approximately velocity fluctuations. In fact, the correlation $C_{\rho',u'}$ is close to -1 in the buffer layer. Consequently, negative (positive) density fluctuations are associated with positive (negative) velocity fluctuations. Low-speed streaks are thus characterised by higher-density fluid and vice versa. The behaviour for PP11 flows is rather different, as inferred from the correlation coefficients $C_{\rho',u'}$ and $C_{\rho',p'}$ in figure 5.13. $C_{\rho',u'}$ being much smaller in the buffer layer, the density modulation for low and high-speed streaks is less marked. Instead, the pressure signature is visible on the instantaneous density since $C_{\rho',p'} \approx 1$ across the whole channel height.

Figure 5.28 show the premultiplied kinetic energy spectra $k_x E_{\rho uu}/\tau_w$, $k_z E_{\rho uu}/\tau_w$ and $k_z E_{\rho vv}/\tau_w$ for cases AM3R7 and PM1R3 on the whole channel height as a function of semi-local streamwise k_x^* and spanwise k_z^* wavenumbers. The semi-local scaling provides an approximate collapse over a wide range of wavenumbers, improving substantially the classical inner scaling. The strongest modifications are obtained for air flows, in which the high gradients of variable properties near the wall alter the effective scaled wavenumbers up to the buffer layer. This corresponds to elongated (shortened) structures for gas-like (liquid-like) transport properties with respect to the incompressible regime (Coleman *et al.*, 1995; Duan *et al.*, 2010). The locations y^* and the wavelengths λ^* corresponding to the peak values are reported in table 5.7. Similar values with respect to those typically obtained in incompressible turbulence are found (i.e., for the streamwise velocity, $\lambda_x^+ \approx 1000$ and $\lambda_z^+ \approx 100$) for both fluids.

Near-wall turbulent structures can be also analysed by means of the quadrant analysis (Wallace, 2016). This representation allows a detailed study of the physical mechanisms producing the Reynolds shear stresses and, in a related way, underlying the turbulent kinetic energy production.

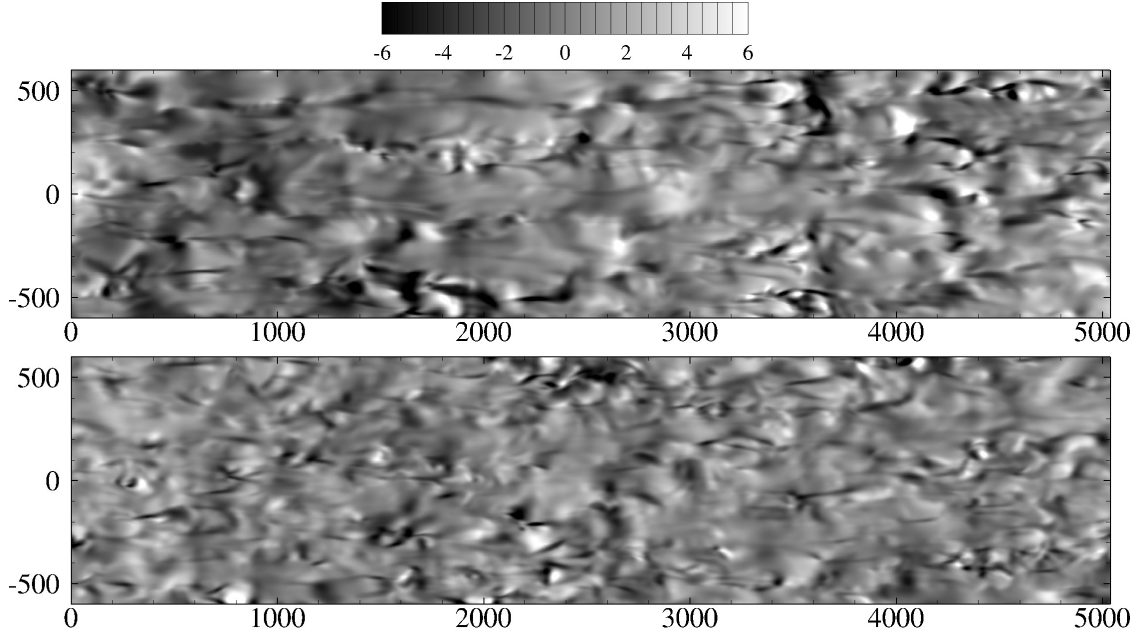


Figure 5.26. Pressure fluctuations p'^+ at $y^* \approx 12$ for AM3R7 (top) and PM1R3 (bottom).

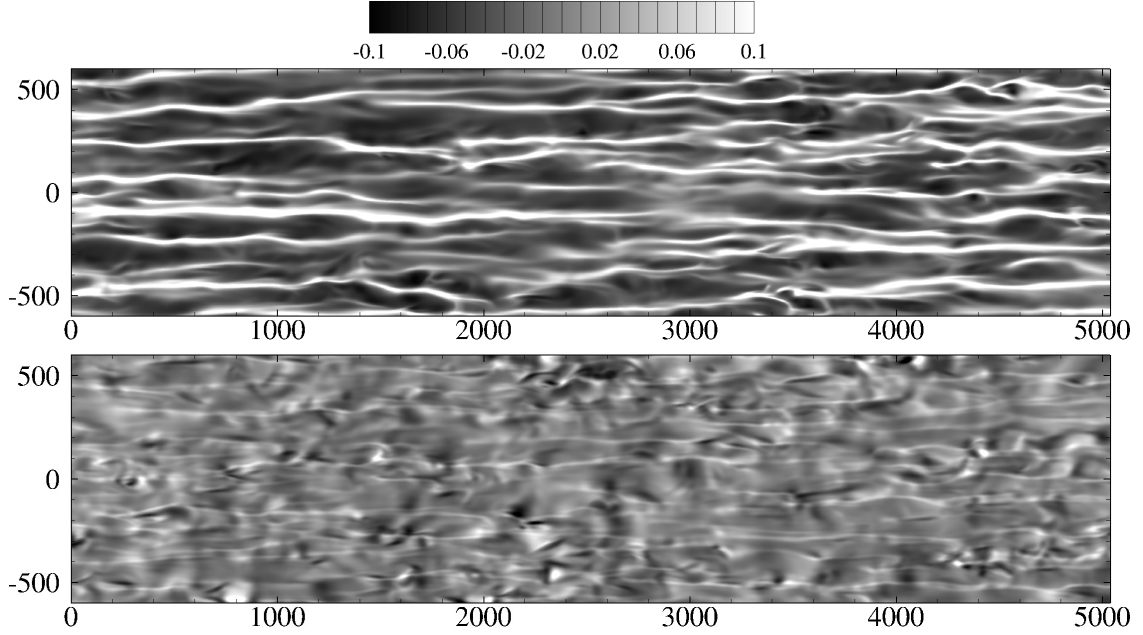


Figure 5.27. Density fluctuations ρ'^+ at $y^* \approx 12$ for AM3R7 (top) and PM1R3 (bottom).

The (u, v) plane is divided into four quadrants: Q1 $(+u'', +v'')$, Q2 $(-u'', +v'')$, Q3 $(-u'', -v'')$, Q4 $(+u'', -v'')$. Figure 5.29 shows the joint probability functions of $\sqrt{\rho}u''/\sqrt{\tau_w}$ and $\sqrt{\rho}v''/\sqrt{\tau_w}$ for air and PP11 flows at different y^* values. Near the walls the p.d.f.s appear stretched in the streamwise direction and flatter in the spanwise direction, with a preferential orientation in the Q2 and Q4 quadrants, corresponding respectively to ejections ($u'' < 0, v'' > 0$) and sweeps ($u'' > 0, v'' < 0$). Moving towards the centreline, the p.d.f.s tend to become more isotropic. The most important differences between air and PP11 are found in the buffer layer. Namely, strong ejections events are less likely to occur with the dense gas. Distributions in the logarithmic zone and in the core region, instead, exhibit similar values. The exact contribution of the different quadrants can be obtained by plotting the isocontours of the probability-weighted Reynolds shear stresses

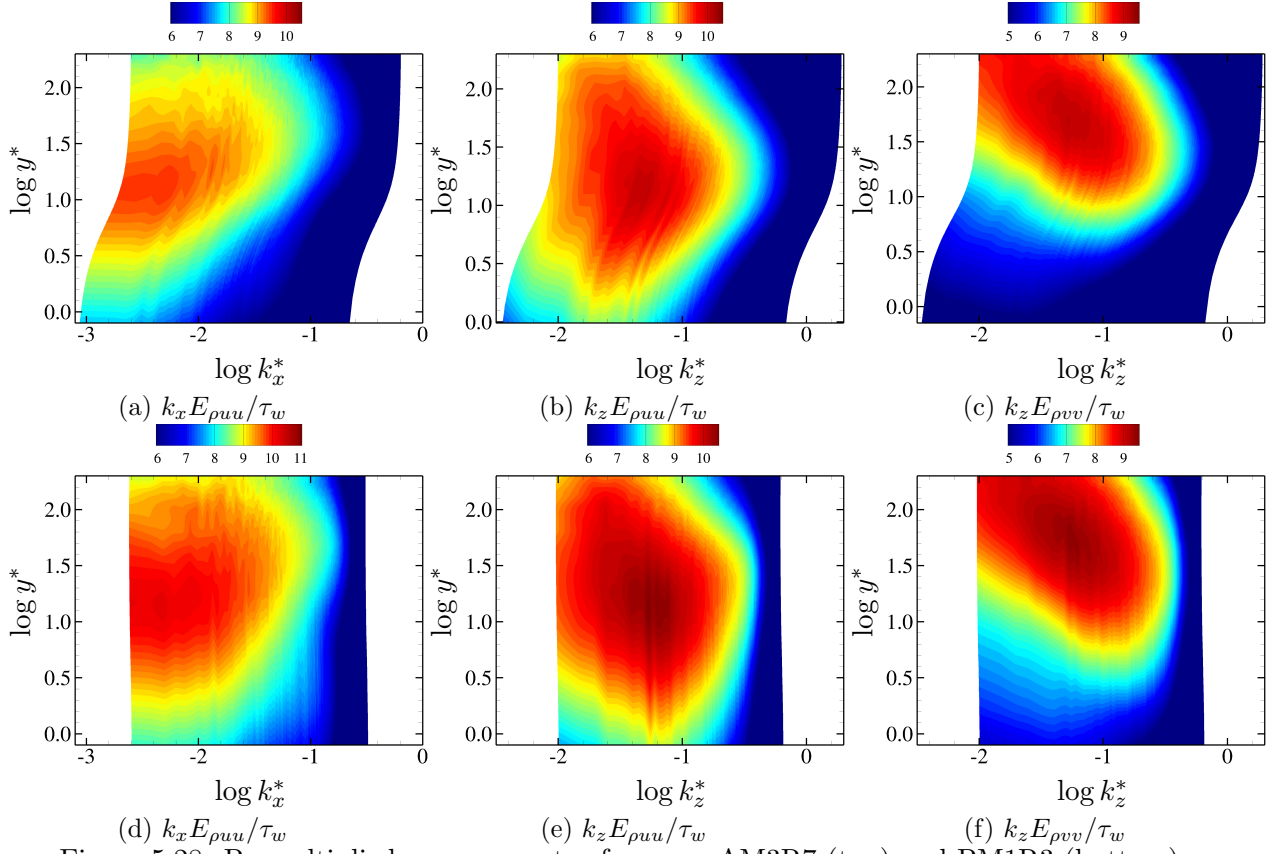
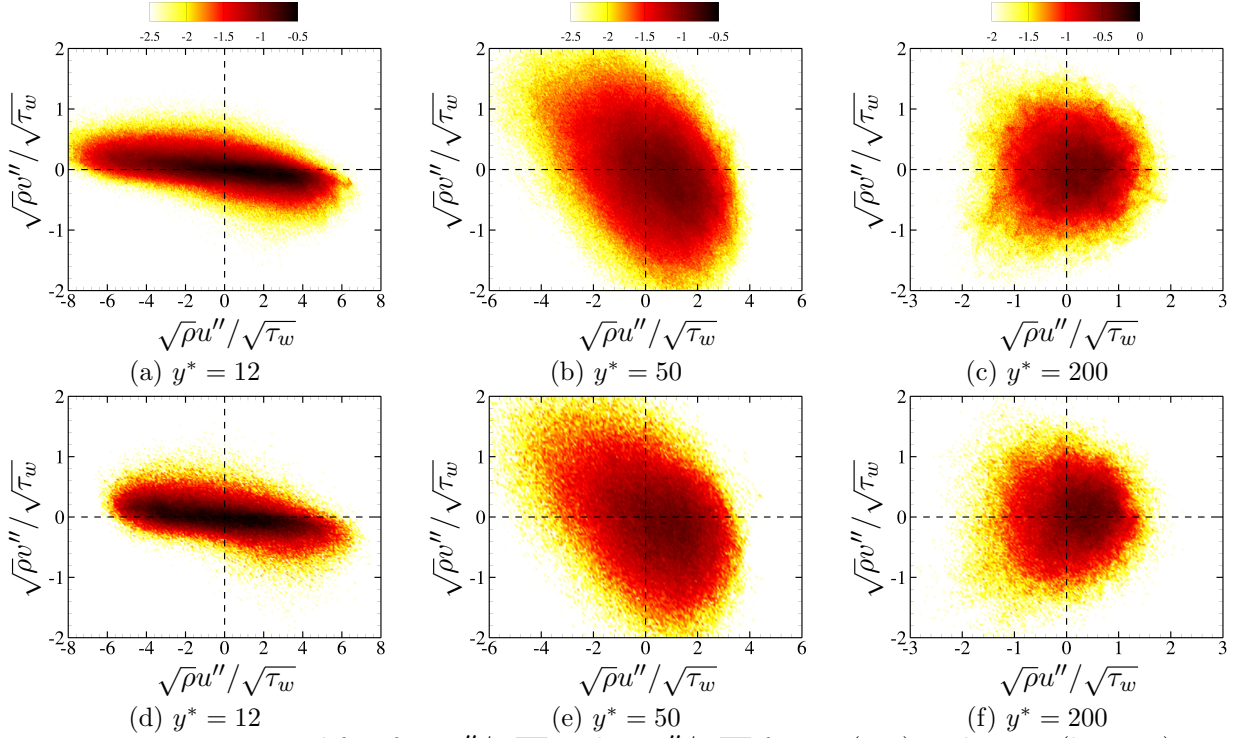


Figure 5.28. Premultiplied energy spectra for cases AM3R7 (top) and PM1R3 (bottom).

Figure 5.29. Joint p.d.f.s of $\sqrt{\rho} u'' / \sqrt{\tau_w}$ and $\sqrt{\rho} v'' / \sqrt{\tau_w}$ for air (top) and PP11 (bottom).

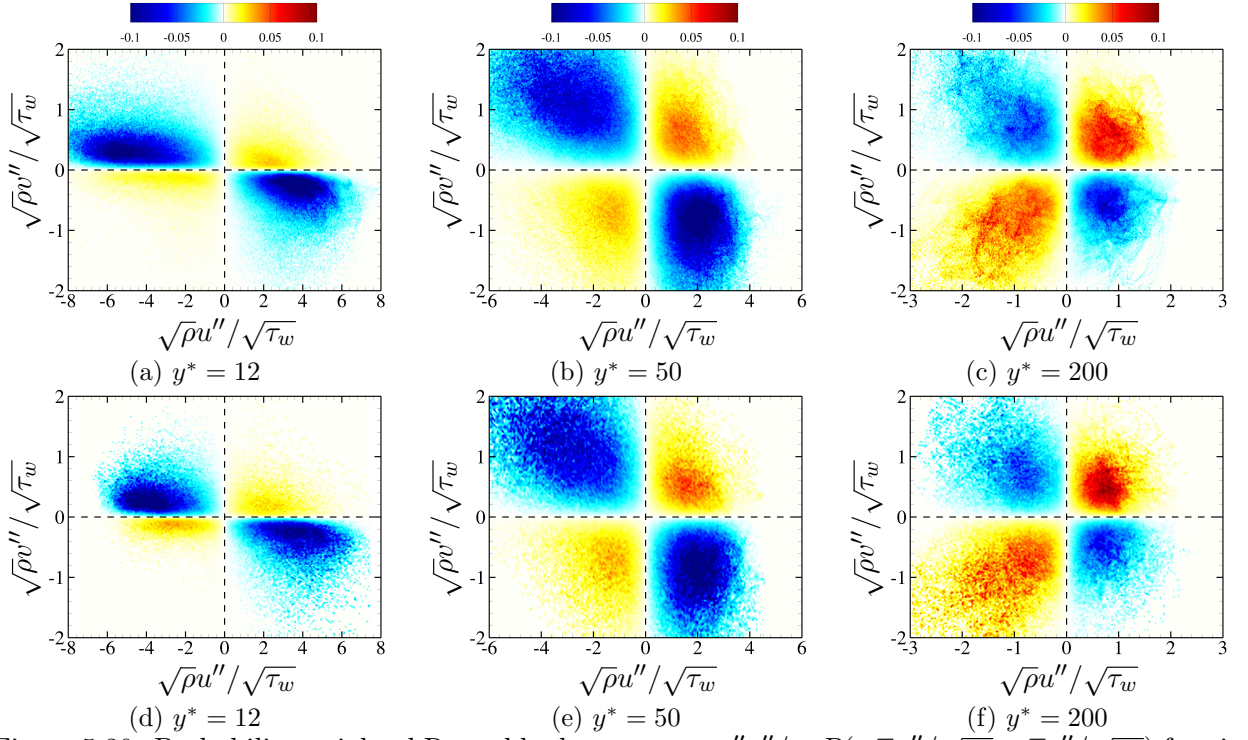


Figure 5.30. Probability weighted Reynolds shear stress $\rho u'' v'' / \tau_w P(\sqrt{\rho} u'' / \sqrt{\tau_w}, \sqrt{\rho} v'' / \sqrt{\tau_w})$ for air (top) and PP11 (bottom).

$\rho u'' v'' / \tau_w P(\sqrt{\rho} u'' / \sqrt{\tau_w}, \sqrt{\rho} v'' / \sqrt{\tau_w})$, depicted in figure 5.30. The contribution of ejections events to shear stresses appear lower for PP11 flows with respect to air flows. This is consistent with recent findings of Patel *et al.* (2015). Gas-like (liquid-like) transport properties tend to stabilise (weaken) the low-speed streaks, which lift less (more) intensely away from the wall.

Chapter Summary

Direct numerical simulations of supersonic turbulent channel flows of perfect and dense gases have been performed for different values of bulk Reynolds and Mach numbers.

- Mach numbers remain below the limit where strong compressibility effects are visible.
- The temperature being almost constant for dense gases, isothermal wall conditions are close to adiabatic conditions.
 - The Van Driest transformation already provides a good collapse for PP11 flows, the heat transfer at the walls being weak.
- Peculiar behavior of transport properties, the viscosity and thermal conductivity decreasing with density across the channel:
 - Dense gases behave similarly to incompressible flows with liquid-like transport properties
 - The semi-local scaling introduced by [Huang *et al.* \(1995\)](#), and later formalised by [Patel *et al.* \(2015\)](#), is well adapted to take into account variable properties. This is shown by the comparisons of Reynolds stresses, the instantaneous views of the velocity fields, the kinetic energy budgets and streamwise and spanwise pre-multiplied spectra.
 - Morkovin's hypothesis is well respected.
- Different profiles for r.m.s. of thermodynamic properties w.r.t. air cases
- Density fluctuations follow pressure ones in PP11 flows, their correlation being close to unity across the whole channel.
- The extension of the FIK identity for compressible flows ([Gomez *et al.*, 2009](#)) has been used to analyse the different skin friction values:
 - The compressible term has opposed sign, due to the liquid-like viscosity, and it is smaller than air, viscosity variations being higher in the latter case
 - The compressible-turbulent interaction term is one order of magnitude lower in PP11

6 Conclusions and Perspectives

Turbulent flows of dense gases represent a research field of great importance for a wide range of applications in the field of process engineering and energy conversion cycles. In this thesis, a numerical study of the influence of dense-gas effects on turbulent flows has been carried out. It is usual to identify dense gases as fluids that exhibit values of Γ lower than one in their vapour phase. In such conditions, the speed of sound tends to decrease in isentropic compressions and increase in expansions, contrary to the behaviour of lighter, "classical" gases, like air or steam. The reversed variations of the speed of sound deeply modify the behaviour of dense gas flows in the transonic and supersonic regime compared to more standard fluids. The most striking differences are obtained for BZT fluids, which exhibit an inversion zone leading to the appearance of non classical phenomena such as expansion shocks. A heavy fluorocarbon fluid, namely the PP11, has been systematically considered in the study since it presents a wide inversion region in which BZT non-classical phenomena can occur. Its thermodynamic behaviour is well represented with the Martin–Hou thermal equation of state, whereas the transport properties are modelled by means of the Chung–Lee laws, that take into account correction terms for the evolution of viscosity and thermal conductivity in the dense-gas region.

In order to have a preliminary idea of the differences between dense- and perfect gases, the large-scale dynamics of decaying homogeneous isotropic turbulence are investigated by using the simpler Van der Waals gas model. The simulations are based on the inviscid conservation equations, solved by means of the 9th-order accurate numerical method, validated beforehand against inviscid CHIT results available in the literature for perfect diatomic gases. Inviscid simulations rely on the numerical viscosity of the scheme to dissipate energy at the finest scales, while leaving the larger scales mostly unaffected. First, we have carried out a preliminary parametric study of the influence of the specific heat ratio γ for perfect-gas CHIT simulations. At high turbulent Mach numbers ($M_{t_0} \geq 0.8$), the flow thermodynamic properties are found to be highly dependent on γ . The root mean square of the pressure and sound speed scale respectively with γ and $(\gamma - 1)/2$, while the root mean square of density is weakly affected by γ . These findings have been shown on theoretical grounds using dimensional analysis and momentum conservation. On the contrary, kinematic properties like the kinetic energy and the vorticity are almost insensitive to γ . The influence of the specific heat ratio on local velocity divergence levels is also found to be weak. Afterwards, dense gas results are systematically compared with those obtained for a perfect gas. Once again, at high M_{t_0} the thermodynamic model has a significant influence on the time evolutions of the average and r.m.s. of the thermodynamic properties, whereas the influence on kinematic properties is smaller. However, the flow dilatational behaviour is deeply different. For a dense gas, the r.m.s. values of the thermodynamic properties show higher amplitudes than for a PFG. The simulations show that the most affected quantity is the speed of sound. In the PFG case, sound speed is nearly constant with time, independently of the initial turbulent Mach number, whereas for the dense gas it varies over a range of values that increases with M_{t_0} . Accordingly, the fundamental derivative of gas dynamics varies abruptly from negative to positive values. The peculiar behaviour of the speed of sound for a dense gas has a strong influence on the local Mach number and flow dilatation levels. The most significant differences between the perfect and the dense gas case are found for the repartition of dilatation levels. For PFG, strong compression regions occupy a much larger volume fraction than strong expansion regions. As a consequence, the probability distribution of the velocity divergence is

highly skewed toward negative values, even for values of γ typical of dense gases. For the dense gas, the volume fraction occupied by strong compression and expansion regions is much more balanced: strong compression regions are reduced by 30% and strong expansion regions are increased by 80% with respect to the perfect gas, and strong expansions and compressions are found to be equally probable. More than a half of the strong expansion regions are characterized by negative values of Γ , suggesting the possibility that expansion shocklets may occur in the dense gas. The presence of expansion shocklets is also suggested by the fact that, for the dense gas, strong expansion regions exhibit a sheet-like structure, rather than the tubular structure observed in the PFG case. In strong compression regions, both the dense and the perfect gas exhibit sheet-like structures, characteristic of eddy shocklets. Furthermore, for PFG the probability of producing a given vorticity is greater in strong compression regions, where compression shocklets possibly occur. For the dense gas, the production of vorticity in strong compression and expansions is equally probable. This is due to the vorticity generated across expansion eddy shocklets forming in strong expansion regions, and to the fact that shocklets of any kind are expected to be weaker in dense gases with Γ close to zero.

Afterwards, we focused our attention on the dynamics of small scales by means of direct numerical simulations of homogeneous isotropic turbulence. Simulations were carried out at various initial turbulent Mach numbers and for two different choices of the initial thermodynamic state, corresponding to a small positive and a small negative value of the fundamental derivative Γ , and compared with DNS results for a perfect gas. The influence of dense gas effects on the time evolution of general statistics was first investigated, confirming the ones obtained in inviscid simulations with the VDW EoS. In dense gas, turbulence temperature variations are negligible due to the decoupling of dynamic and thermal effects for fluids characterized by large specific heat coefficients. This leads, on the one hand, to weaker pressure fluctuations (with respect to a perfect gas like air), and large variations of the speed of sound that strongly depend on the density fluctuations; on the other hand, the fluid viscosity exhibits smaller average and r.m.s. variations than a perfect gas. The present results also confirm that, for high M_{t_0} , the p.d.f. of the local dilatation conserves a more symmetric shape than in perfect gas, especially for BZT initial conditions. Moreover, dense gas effects are found to be largely insensitive to the equation of state in use. Furthermore, the general statistics are little affected by the choice of the initial thermodynamic state, provided that the initial (positive or negative) Γ value is close enough to zero.

In the second part of the study we investigated how dense gas effects modify the small scale dynamics and the properties of turbulent structures. For that purpose we carried out an analysis in the invariant plane of the deviatoric strain rate tensor. The analysis showed that the total joint p.d.f. (Q^*, R^*) is characterized by the same universal tear-drop shape found for incompressible and compressible perfect gas turbulence. The joint p.d.f. conditioned on strong compression and expansion regions are somewhat modified due, on the one hand, to the weakening of compressive structures and, on the other hand, by the enhancement of expanding regions. Furthermore, strong expansions are found to be mostly populated by non-focal convergence structures, in contrast with the perfect gas that is dominated by eddy-like structures having focal topology. These effects are stronger for initial thermodynamic conditions allowing the occurrence of BZT effects, for which the formation of convergence compressed structures, like compression shocklets, is strongly reduced, while continuous convergence expanding structures tend to steepen into expansion shocklets. The analysis of the role of the different flow structures on viscous dissipation mechanisms shows the enhanced contribution of non-focal expanding structures (of the same order of that of compressed focal structures) to the dilatational dissipation. The occurrence of steep expansion structures and, possibly, of expansion shocklets is confirmed by the preferential alignment of the density gradient with the third strain rate eigenvector. This effects deeply modifies the enstrophy generation in strong expansion regions, which mostly act as a sink in perfect gases. In dense gases, the presence of a much higher percentage of nonfocal convergence structures significantly decreases vorticity and

counterbalances enstrophy destruction by means of the eddy-like ones.

Lastly, near-wall turbulence dynamics of dense gases is studied by means of direct numerical simulations of supersonic turbulent channel flows. A parametric study at three bulk Reynolds numbers and three bulk Mach numbers is performed and results are compared to the corresponding air cases. The analysis of mean and fluctuating thermodynamic and transport properties reveals the peculiar behaviour of wall-bounded dense-gas flows. In channel flows with isothermal walls, viscous heating lead to high centreline temperature, which amounts to consider cooled walls. An important difference with ideal gas is that, due to the high heat capacities of dense gases, the heat flux across the walls is dramatically reduced and the temperature variations are very limited. That means that the isothermal wall condition is close to an adiabatic condition, and a weak coupling of the dynamic and thermal boundary layers is noticed. Consequently, the classical Van Driest transformation for the longitudinal velocity profiles already provides a good collapse for PP11 flows.

A striking point is that dense gas transport properties are functions of both temperature and density. The former being approximately constant, viscosity and thermal conductivity follow essentially the density profile, decreasing across the channel. This make the evolution of wall-bounded dense-gas flows intermediate between the compressible regime for an ideal gas at supersonic speeds and the well-documented incompressible regime with liquid-like transport properties. Compressibility effects are related to the nonstandard variations of its sound speed, as in CHIT cases. The distributions of the turbulent Mach number are similar to those observed for a perfect gas but with slightly higher levels. Note that the maximum values obtained with the considered range of bulk Mach numbers remain below the limit where strong dense-gas effects are visible. Moreover, BZT phenomena are not observed since γ remain positive in the whole channel. As already shown in previous studies for both supersonic channel flows or low-speed variable-property channel flows, the semi-local scaling introduced by [Huang *et al.* \(1995\)](#), and later formalised by [Patel *et al.* \(2015\)](#), is well adapted to compare results from existing surveys and with the well-documented incompressible limit. The comparison of second-order statistics and instantaneous views of the velocity fields gives a strong support for the validity of semi-local scaling with dense-gas flows, and confirms the validity of the Morkovin's hypothesis even for dense gases. This conclusions is also reinforced by the fact that the order of magnitude of density and pressure fluctuations is roughly similar as air flows, whereas temperature fluctuations are strongly reduced. The structure of turbulence is thus not deeply altered in dense-gas supersonic channel flows. The main effect of variable properties can be taken into account by using the semi-local scaling, and comparing results with a constant semi-local friction Reynolds number. The streamwise and spanwise non-dimensional lengths of the near-wall structures, quantified using pre-multiplied spectra, are found to be universal and comparable to values for incompressible flows when semi-local coordinates are used. Same considerations hold concerning the generation of Reynolds stresses, analyzed by means of the joint p.d.f.s of streamwise and wall-normal velocity fluctuations. Some particular features are nonetheless observed with PP11 flows, notably for the highest value of the Mach number, $M_B=3$. Specifically, a different y -profile for the density fluctuations is observed, with $\sqrt{\rho'^2}$ decreasing monotonically with the wall distance due to the reduced compressibility. Furthermore, density fluctuations are highly dependent on pressure ones across the whole channel, as shown by the correlation coefficient and the flow visualizations in the buffer layer.

6.1 Future work

The analysis contained in this thesis represents a first step for a deeper understanding of dense gas turbulent flows. Further studies could be envisaged; for instance, concerning the configurations:

- Compressible homogeneous isotropic turbulence is a perfect framework for detailed analysis on the structure of turbulence. Simulations of forced CHIT could provide useful insights on the difference between perfect and dense-gas turbulent flows. The study performed in chapters 3 and 4 could be performed at higher turbulent Mach number, without concerning about the influence of initial conditions. Forced computations also allow to study higher-order moments and obtain cleaner data with respect to decaying CHIT due to the higher number of samples available (e.g., in strong dilatation regions). Furthermore, the study on isotropic turbulence could be enhanced by performing Helmholtz decompositions of the turbulent flow in order to study in detail the dense-gas dilatational velocity field. It would be also useful to adapt the shock-detection algorithm of Samtaney *et al.* (2001) to identify accurately expansion shocklets and isolate their contribution to modification of turbulent features.
- Concerning wall-bounded flows, due to the lower turbulent Mach numbers involved in such a configuration, less “exotic” phenomena should occur. Nevertheless, it would be interesting to investigate the development of a turbulent boundary layer of a dense gas over a flat-plate and, later, the shock - boundary layer interaction, particularly in the case of an impinging expansion shock waves.
- Clearly, one should remember that the main interest in studying dense gas turbulent flows concerns energy-production applications. Performing high-fidelity numerical simulations of dense gas flows in turbomachinery configurations would provide valuable information both from a practical and theoretical point of view. To this purpose, LES simulations of ORC turbines have been planned for the next future.

Then, further analysis are required concerning the thermodynamics of dense gases. This study has indeed focused on the behavior of PP11; but there are several dense fluids, commonly used for engineering applications, for which more accurate equations for the thermodynamic variables and the transport properties exist, and whose behaviour in the aforementioned turbulent configurations is not known. Parametric studies represent a good way to assess whether their behaviour could be considered as universal, or dependent on the chosen thermodynamic conditions.

Lastly, the numerical simulations performed for this thesis allowed the creation of a reliable database for perfect and dense gases that could be used, for instance, to perform a-priori analysis for RANS and LES closure models. This would allow to assess the validity of the application of classical closure models, or eventually provide a basis for the calibration of improved models tailored for dense gas applications.

6.2 Acknowledgement

The authors acknowledge the PhD fellowship from Pres HESAM, the financial support from “Université Franco-Italienne” (Programme Vinci) and the HPC resources of IDRIS under the allocation x2016a7332 by GENCI (Grand Equipement National de Calcul Intensif).

Appendices

A Basic thermodynamics relations

In order to develop analytical relations between thermodynamics variables, one needs to start from the two fundamental laws of thermodynamics and the definitions of the thermodynamic potentials, namely, the internal energy e , enthalpy h , Helmholtz free energy a and Gibbs free energy g . For instance, for e and h one has:

$$de = Tds - pdv \quad \text{and} \quad dh = Tds + vdp \quad (\text{A.1})$$

By means of simple manipulations and exploiting the Schwarz' theorem, it is possible to obtain the so-called Maxwell relations, i.e., a set of equations relating the derivatives of the thermodynamic properties. The four most common relations are shown in table A.1.

When complex equations of state are considered, usually the thermal equation is given, i.e., $p = p(T, v)$. The caloric equation is related to the thermal EoS by means of the compatibility relation, that will be derived in the following. First, the reciprocity relations are computed by deriving the potentials:

$$\left. \frac{\partial e}{\partial v} \right|_T = T \left. \frac{\partial s}{\partial v} \right|_T - p \left. \frac{\partial v}{\partial v} \right|_T = T \left. \frac{\partial p}{\partial T} \right|_v - p \quad (\text{A.2})$$

$$\left. \frac{\partial h}{\partial p} \right|_T = T \left. \frac{\partial s}{\partial p} \right|_T + v \left. \frac{\partial p}{\partial p} \right|_T = -T \left. \frac{\partial v}{\partial T} \right|_p + v \quad (\text{A.3})$$

$$\left. \frac{\partial e}{\partial T} \right|_v = T \left. \frac{\partial s}{\partial T} \right|_v - p \left. \frac{\partial v}{\partial T} \right|_v = T \left. \frac{\partial s}{\partial T} \right|_v \quad (\text{A.4})$$

$$\left. \frac{\partial h}{\partial T} \right|_p = T \left. \frac{\partial s}{\partial T} \right|_p + v \left. \frac{\partial p}{\partial T} \right|_p = T \left. \frac{\partial s}{\partial T} \right|_p \quad (\text{A.5})$$

Then, from the definitions of the specific heats at constant volume c_v and constant pressure c_p , one

Table A.1. Derivation of Maxwell relations from the fundamental laws of thermodynamics.

Fundamental potential	Variables to relate	Single derivative	Mixed derivative	Maxwell relation
$de = Tds - pdv$	s, v	$\left. \frac{\partial e}{\partial s} \right _v = T, \left. \frac{\partial e}{\partial v} \right _s = -p$	$\frac{\partial^2 e}{\partial s \partial v}$	$\left. \frac{\partial T}{\partial v} \right _s = - \left. \frac{\partial p}{\partial s} \right _v$
$dh = Tds + vdp$	s, p	$\left. \frac{\partial h}{\partial s} \right _p = T, \left. \frac{\partial h}{\partial p} \right _s = v$	$\frac{\partial^2 h}{\partial s \partial p}$	$\left. \frac{\partial T}{\partial p} \right _s = \left. \frac{\partial v}{\partial s} \right _p$
$da = -sdT - pdv$	T, v	$\left. \frac{\partial a}{\partial T} \right _v = -s, \left. \frac{\partial a}{\partial v} \right _T = -p$	$-\frac{\partial^2 a}{\partial T \partial v}$	$\left. \frac{\partial s}{\partial v} \right _T = \left. \frac{\partial p}{\partial T} \right _v$
$dg = -sdT + vdp$	T, p	$\left. \frac{\partial g}{\partial T} \right _p = -s, \left. \frac{\partial g}{\partial p} \right _T = v$	$-\frac{\partial^2 g}{\partial T \partial p}$	$-\left. \frac{\partial s}{\partial p} \right _T = \left. \frac{\partial v}{\partial T} \right _p$

obtains:

$$c_v := \left. \frac{\partial e}{\partial T} \right|_v = T \left. \frac{\partial s}{\partial T} \right|_v \quad \text{and} \quad c_p := \left. \frac{\partial h}{\partial T} \right|_p = T \left. \frac{\partial s}{\partial T} \right|_p. \quad (\text{A.6})$$

In general, however, heat capacity data are available only at ideal gas conditions. Hence, we need to relate the real heat capacity at any given temperature to the ideal gas heat capacity. We need to compute $\left. \frac{\partial c_v}{\partial v} \right|_T$ and then integrate from the volume of an ideal gas to the volume of the real gas v . Thus, using equation (A.2):

$$\begin{aligned} \left. \frac{\partial c_v}{\partial v} \right|_T &= \left[\left. \frac{\partial}{\partial v} \frac{\partial e}{\partial T} \right|_v \right]_T = \left[\left. \frac{\partial}{\partial T} \frac{\partial e}{\partial v} \right|_T \right]_v = \\ &= \left[\frac{\partial}{\partial T} \left[T \left. \frac{\partial p}{\partial T} \right|_v - p \right] \right]_v = \left. \frac{\partial p}{\partial T} \right|_v + T \left. \frac{\partial^2 p}{\partial T^2} \right|_v - \left. \frac{\partial p}{\partial T} \right|_v = T \left. \frac{\partial^2 p}{\partial T^2} \right|_v, \end{aligned}$$

and integrating:

$$\int_{id}^{real} dc_v = \int_{v_{id}}^{v_{real}} T \left. \frac{\partial^2 p}{\partial T^2} \right|_v dv \implies c_v^{real} = c_v^{id} + \int_{v_{id}}^{v_{real}} T \left. \frac{\partial^2 p}{\partial T^2} \right|_v dv \quad (\text{A.7})$$

Finally, since:

$$de = Tds - pdv = c_v dT + T \left. \frac{\partial p}{\partial T} \right|_v dv - pdv = c_v dT + \left(T \left. \frac{\partial p}{\partial T} \right|_v - p \right) dv, \quad (\text{A.8})$$

substituting equation (A.7) in (A.8), the compatibility relation is obtained:

$$de = \left(c_v^{id} + \int_{v_{id}}^{v_{real}} T \left. \frac{\partial^2 p}{\partial T^2} \right|_v dv \right) dT + \left(T \left. \frac{\partial p}{\partial T} \right|_v - p \right) dv. \quad (\text{A.9})$$

In the same way, one can derive the same relation for the enthalpy:

$$dh = \left(c_p^{id} - \int_{p_{id}}^{p_{real}} T \left. \frac{\partial^2 v}{\partial T^2} \right|_p dp \right) dT + \left(-T \left. \frac{\partial v}{\partial T} \right|_p + v \right) dp. \quad (\text{A.10})$$

B Computation of saturation curves

Generally, the thermal equations of state are conceived to work in the vapour phase of a fluid and are not able to predict a phase change. Nevertheless, these can be used to compute the saturation curve for certain thermodynamic properties.

A necessary condition for thermodynamic stability reasons is that the pressure does not increase with the specific volume, i.e.,

$$\left. \frac{\partial p}{\partial v} \right|_T \leq 0, \quad (\text{B.1})$$

which is always fulfilled for perfect gas equation of state. For more complex EoS, instead, it is not generally the case. An example is given in figure B.1a, in which we show the predictions of several isotherms computed by the Van Der Waals EoS and drawn in the Clapeyron plane. The colours blue, black and red denote respectively subcritical, critical and supercritical values for the temperature. Hence:

- For $T > T_c$, the function $p = f(v)$ is strictly monotonically decreasing, whereas for $T = T_c$, an inflection point appears at the critical point. Hence, the condition expressed in equation (B.1) is fulfilled for $T \geq T_c$.
- For $T < T_c$, the condition is generally not satisfied, and a correction must be applied, which is usually referred-to as the Maxwell reconstruction (Clerk-Maxwell, 1875).

The failing of the thermodynamic stability condition for subcritical temperatures implies the occurrence of a phase change and a jump from an equilibrium state characterized by a local entropy maximum (or a local energy minimum) to another. For first-order transitions, these two states have different values for entropy, volume and free Helmholtz energy, but are characterized by the

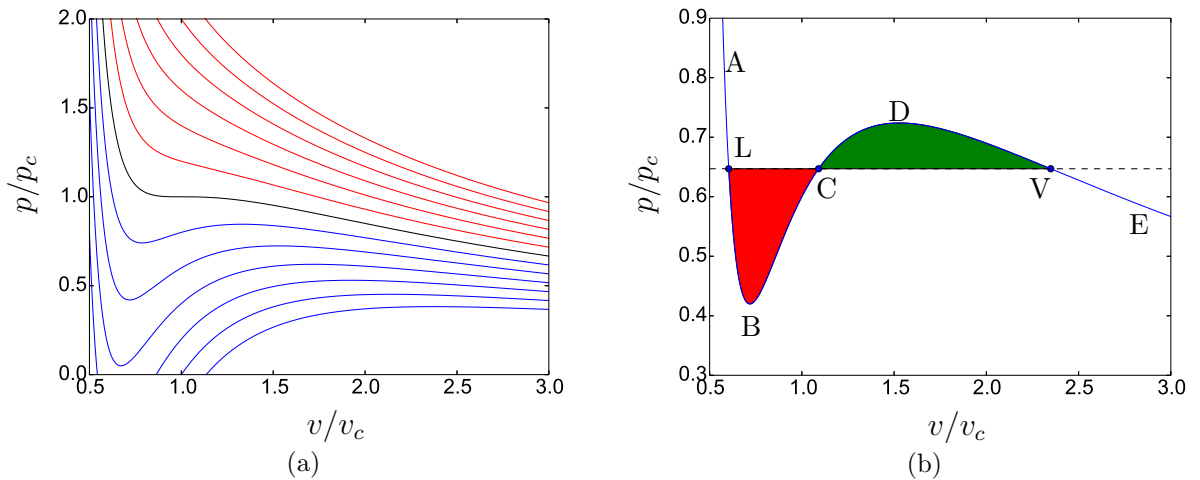


Figure B.1. Panel a: isotherms computed by means of the VDW EoS. Colours blue, black and red denotes respectively subcritical, critical and supercritical isotherms. Panel b: example of Maxwell reconstruction algorithm for the isotherm $\bar{T} = 0.9T_c$.

same values of pressure and Gibbs potential, i.e.:

$$\begin{cases} g(\bar{T}, v_L) = g(\bar{T}, v_V) \\ p(\bar{T}, v_L) = p(\bar{T}, v_V) \end{cases} \quad (\text{B.2})$$

where $(\bullet)_L$ and $(\bullet)_V$ denotes the saturated liquid and vapour values, respectively. This property can be used to correct the unstable branch of the isotherms and obtain, for a given isotherm $\bar{T} < T_c$, the corresponding values for v_L and v_V .

From the definition of the Gibbs potential $dg = -sdT + vdp$, integrating along the hypothetical isotherm ($dT = 0$) and considering system (B.2), one has:

$$g(\bar{T}, v_V) - g(\bar{T}, v_L) = \int_{p_L}^{p_V} v(p) dp = 0. \quad (\text{B.3})$$

A geometrical interpretation is shown in figure B.1b: since $p_L = p_V$, condition (B.3) implies that the areas included between the functions $p = f(\bar{T}, v)$ and $p = p_L = p_V$ (coloured in red and green in figure) must be equal, i.e. $A_{LBC} = A_{CDV}$. Hence, the nominal (non-monotonic) isotherm T_{ABCDE} is truncated by this equal-area construction to give the physical isotherm T_{ALVE} . Hence, provided the thermal EoS, it is possible to compute directly the saturated liquid and vapour curve by joining all the points (v_L, p_L) and (v_V, p_V) , respectively obtained for different values of the subcritical isotherm. No information about the caloric component is required.

The algorithm used in our code uses Newton–Raphson procedures to compute the inflection points of the subcritical isotherms. In the following, we denote with $f = p(T, v)$ the thermal EoS and with a prime its derivatives with respect to specific volume (at constant temperature). Specifically, we first compute the analytical functions f' , f'' and f''' for each EoS. Then, making reference to figure B.1b, for each isotherm (starting from $\bar{T} = 0.99T_c$) we proceed as follows:

1. In order to find point B and D , we compute the point H in which the isotherm change concavity for the first time, i.e. the smallest root of f'' for which $f''(v_H) = 0$;
2. The values of the local maximum and minimum v_B and v_D , are searched by solving the equation $f'(v) = 0$. Among the roots X of the solution, the one for which $v_X < v_H$ gives $X \equiv B$, whereas $v_X > v_H$ gives $X \equiv D$;
3. Starting from C' such that $v_{C'} = v_D - \epsilon$ (being ϵ a small positive value):
 - a) Search for the points L' and V' such that $f(L') = f(D') = f(C')$;
 - b) Compute the areas $A_{L'BC'}$ and $A_{C'DV'}$ analytically as

$$A_{L'BC'} = p_{C'}(v_{C'} - v_{L'}) - \int_{v_{L'}}^{v_{C'}} f(v) dv; \quad A_{C'DV'} = \int_{v_{C'}}^{v_{V'}} f(v) dv - p_{C'}(v_{V'} - v_{C'}); \quad (\text{B.4})$$

- c) if $A_{L'BC'} \equiv A_{C'DV'}$, then $L' \equiv L$ and $V' \equiv V$ are points belonging to the saturation curve. The algorithm restart for the following isotherm. Instead, if the areas are not equal, we compute C'' such that $v_{C''} = v_{C'} - \epsilon$ and the algorithm restarts from 3(a).

This algorithm has been used to compute the saturation curves for the fluids and the equations of state presented in section 2.1.

C Jacobian matrix for dense gases

The explicit form for the Jacobian Matrix for perfect gases reads

$$\mathbf{A}_1 = \frac{\partial \mathbf{U}}{\partial \mathbf{F}_1} = \begin{bmatrix} 0 & 1 & 0 & 0 & 0 \\ \frac{\gamma-1}{2}q^2 - u^2 & (3-\gamma)u & (1-\gamma)v & (1-\gamma)w & \gamma-1 \\ -uv & v & u & 0 & 0 \\ -uw & w & 0 & u & 0 \\ \left(\frac{\gamma-1}{2}q^2 - H\right)u & H + (1-\gamma)u^2 & (1-\gamma)uv & (1-\gamma)uw & \gamma u \end{bmatrix} \quad (\text{C.1})$$

$$\mathbf{A}_2 = \frac{\partial \mathbf{U}}{\partial \mathbf{F}_2} = \begin{bmatrix} 0 & 0 & 1 & 0 & 0 \\ -uv & v & u & 0 & 0 \\ \frac{\gamma-1}{2}q^2 - v^2 & (1-\gamma)u & (3-\gamma)v & (1-\gamma)w & \gamma-1 \\ -vw & 0 & w & v & 0 \\ \left(\frac{\gamma-1}{2}q^2 - H\right)v & (1-\gamma)uv & H + (1-\gamma)v^2 & (1-\gamma)vw & \gamma v \end{bmatrix} \quad (\text{C.2})$$

$$\mathbf{A}_3 = \frac{\partial \mathbf{U}}{\partial \mathbf{F}_3} = \begin{bmatrix} 0 & 0 & 0 & 1 & 0 \\ -uw & w & 0 & u & 0 \\ -vw & 0 & w & v & 0 \\ \frac{\gamma-1}{2}q^2 - w^2 & (1-\gamma)u & (1-\gamma)v & (3-\gamma)w & \gamma-1 \\ \left(\frac{\gamma-1}{2}q^2 - H\right)w & (1-\gamma)uw & (1-\gamma)vw & H + (1-\gamma)w^2 & \gamma w \end{bmatrix} \quad (\text{C.3})$$

where \mathbf{U} is the conservative variable vector and \mathbf{F}_i is the convective flux in the i -th direction. The matrix can be generalised to dense gases by taking the pressure as a function of the internal energy e . In particular, we have that for the speed of sound:

$$c^2 = \left. \frac{\partial p(\rho, e)}{\partial \rho} \right|_s = \left. \frac{\partial p}{\partial \rho} \right|_e \left. \frac{\partial \rho}{\partial \rho} \right|_s + \left. \frac{\partial p}{\partial e} \right|_\rho \left. \frac{\partial e}{\partial \rho} \right|_s = p_\rho + p_e e_\rho \quad (\text{C.4})$$

Since the fundamental potential is $Tds = de - \frac{p}{\rho^2}d\rho$, along an isentrope ($ds = 0$) one has $e_\rho = \frac{p}{\rho^2}$ and thus:

$$c^2 = p_\rho + \frac{pp_e}{\rho^2} \implies p_\rho = c^2 - \frac{pp_e}{\rho^2} \quad (\text{C.5})$$

Hence, the Jacobian in dense gases read:

$$\mathbf{A}_1 = \frac{\partial \mathbf{U}}{\partial \mathbf{F}_1} = \begin{bmatrix} 0 & 1 & 0 & 0 & 0 \\ c^2 - \frac{p_e}{\rho}(H^2 - q^2) - u^2 & (2 - \frac{p_e}{\rho})u & -\frac{p_e}{\rho}v & -\frac{p_e}{\rho}w & \frac{p_e}{\rho} \\ -uv & v & u & 0 & 0 \\ -uw & w & 0 & u & 0 \\ \left(c^2 - H - \frac{p_e}{\rho}(H - q^2)\right)u & H - \frac{p_e}{\rho}u^2 & -\frac{p_e}{\rho}uv & -\frac{p_e}{\rho}uw & \left(\frac{p_e}{\rho} + 1\right)u \end{bmatrix}$$

$$\begin{aligned}
\mathbf{A}_1 = \frac{\partial \mathbf{U}}{\partial \mathbf{F}_1} &= \begin{bmatrix} 0 & 0 & 1 & 0 & 0 \\ -uv & v & u & 0 & 0 \\ c^2 - \frac{p_e}{\rho}(H^2 - q^2) - v^2 & -\frac{p_e}{\rho}u & (2 - \frac{p_e}{\rho})v & -\frac{p_e}{\rho}w & \frac{p_e}{\rho} \\ -uw & 0 & w & v & 0 \\ \left(c^2 - H - \frac{p_e}{\rho}(H - q^2)\right)v & -\frac{p_e}{\rho}uv & H - \frac{p_e}{\rho}v^2 & -\frac{p_e}{\rho}vw & \left(\frac{p_e}{\rho} + 1\right)v \end{bmatrix} \\
\mathbf{A}_1 = \frac{\partial \mathbf{U}}{\partial \mathbf{F}_1} &= \begin{bmatrix} 0 & 9 & 0 & 1 & 0 \\ -uw & w & 0 & u & 0 \\ -vw & 0 & w & v & 0 \\ c^2 - \frac{p_e}{\rho}(H^2 - q^2) - w^2 & -\frac{p_e}{\rho}u & -\frac{p_e}{\rho}v & (2 - \frac{p_e}{\rho})w & \frac{p_e}{\rho} \\ \left(c^2 - H - \frac{p_e}{\rho}(H - q^2)\right)w & -\frac{p_e}{\rho}uw & -\frac{p_e}{\rho}vw & H - \frac{p_e}{\rho}w^2 & \left(\frac{p_e}{\rho} + 1\right)w \end{bmatrix}
\end{aligned}$$

One should note that for perfect gases $c^2 = \frac{\gamma p}{\rho}$ and $p_e = (\gamma - 1)\rho$, hence the perfect-gas formulation is recovered.

D Shock-detection algorithm

In this section we describe the algorithm developed by [Samtaney *et al.* \(2001\)](#) to detect a shocklet in a three-dimensional turbulent field.

The shocklets are mathematically defined as a set of disjoint surfaces $\mathcal{S} = \{S_l\}$ such that if $\mathbf{x}_k \in S_l$ then $\mathbf{x}_k \notin S_{\tilde{l}}$ ($\tilde{l} \neq l$), being \mathbf{x}_k the spatial coordinates of the k -th point in the domain. For a viscous shock in one dimension, the shock can be arbitrarily located where the density profile exhibits an inflection point. Hence, by extension, the set of shocklets is:

$$S = \{S_l | \nabla^2 \rho(\mathbf{x}) = 0, -\theta > 3\theta_{\text{rms}}\}. \quad (\text{D.1})$$

In the following, we summarize the main steps of the algorithm:

1. The Laplacian of density $\nabla^2 \rho(x, y, z)$ and the velocity divergence $\theta(i, j, k)$ is computed at each mesh node. The data is then divided into $(N - 1)^3$ uniform cubes, whose bounds are $[x_{i,j,k}, x_{i+1,j,k}] \times [y_{i,j,k}, y_{i,j+1,k}] \times [z_{i,j,k}, z_{i,j,k+1}]$ (with $i = 1, \dots, N - 1$, $j = 1, \dots, N - 1$, $k = 1, \dots, N - 1$).
2. A marching cube algorithm is used in order to generate the isosurface $\nabla^2 \rho(\mathbf{x}) = 0$; this algorithm is used only for cubes in which at least one vertex satisfies the condition $\theta/\theta_{\text{rms}} < -3$. The points of intersection between the surface and the edges of the cubes are computed by linear interpolation of the values at the vertices. These points are tessellate with triangles to obtain a piecewise triangular surface in each cube. The global triangle list obtained in such a way is denoted as

$$\Delta = \{\Delta_k | \Delta_k = \{\mathbf{x}_{k,1}, \mathbf{x}_{k,2}, \mathbf{x}_{k,3}\}\} \quad (\text{D.2})$$

3. A recursive surface growing algorithm is used to isolate each shocklet S_l (composed of a set of triangles sharing at least one vertex) from Δ .
4. $\forall S_l, \forall \Delta_k \in S_l$, we compute the unit normals $\hat{\mathbf{n}}$ and, by trilinear interpolation, the pressure and density at the following points:

$$\mathbf{x}_{k,\pm l} = \bar{\mathbf{x}}_k \pm (l - 1)\delta\hat{\mathbf{n}}, \quad l = 1, 2, \dots, L \quad (\text{D.3})$$

where $\hat{\mathbf{n}}$ is the centroid of triangle Δ_k , $\delta = 0.5\delta x$ and $L = 4$ (as in [Samtaney *et al.*, 2001](#)).

5. Compute the pressure and density ratio

$$p_{sh,l} = \frac{p(\mathbf{x}_{k,l})}{p(\mathbf{x}_{k,-l})} \quad \rho_{sh,l} = \frac{\rho(\mathbf{x}_{k,l})}{\rho(\mathbf{x}_{k,-l})}. \quad (\text{D.4})$$

If $(p_{sh,l} - 1)(\rho_{sh,l} - 1) < 0$, skip triangle Δ_k and move onto the next triangle. Moreover, if $p_{sh,l} < 1$, invert the ratios, i.e., $p_{sh,l} = 1/p_{sh,l}$ and $\rho_{sh,l} = 1/\rho_{sh,l}$.

6. Verify if the pressure and density jump verify the Rankine-Hugoniot (R-H) relation across the shock, i.e.,

$$\rho_{sh,l} = \frac{(\gamma + 1)p_{sh,l} + \gamma - 1}{(\gamma - 1)p_{sh,l} + \gamma + 1} \quad (\text{D.5})$$

However, equation (D.5) derives from an inviscid framework, hence it is not accurately satisfied in low-Reynolds configurations. Thus, we compute the following penalty function:

$$C_{s,l} = \frac{1}{\rho_{sh,l} - 1} \left| \rho_{sh,l} - \frac{(\gamma + 1)p_{sh,l} + \gamma - 1}{(\gamma - 1)p_{sh,l} + \gamma + 1} \right| \quad (\text{D.6})$$

If $C_{s,l} < 0.1$, then the triangle Δ_k is assumed to be a shocklet.

7. Repeat the same procedure $\forall l = 1, 2, ..L$ and choose the pressure and the density ratio using the index l where the penalty function is a minimum.

For dense gases, it is not possible to explicit equation (D.6), hence we use the relation

$$C_{s,l} = \left| 2(h_2 - h_1) - (p_2 - p_1) \left(\frac{1}{\rho_1} + \frac{1}{\rho_2} \right) \right| \quad (\text{D.7})$$

where $(\cdot)_1$ and $(\cdot)_2$ denotes the upstream and downstream states, respectively.

Bibliography

- ANDERS, J.B., ANDERSON, W.K. & MURTHY, A.V. 1999 Transonic similarity theory applied to a supercritical airfoil in heavy gas. *Journal of aircraft* **36** (6), 957–964.
- ANDERSON, W.K. 1991 Numerical study on using sulfur hexafluoride as a wind tunnel test gas. *AIAA journal* **29** (12), 2179–2180.
- ANGELINO, G. & COLONNA, P. 1998 Multicomponent working fluids for organic rankine cycles (orcs). *Energy* **23** (6), 449–463.
- ANGELINO, G. & INVERNIZZI, C. 1996 Potential performance of real gas stirling cycle heat pumps. *International journal of refrigeration* **19** (6), 390–399.
- ANGELINO, G. & INVERNIZZI, C. 2000 Real gas effects in stirling engines. In *Energy Conversion Engineering Conference and Exhibit, 2000.(IECEC) 35th Intersociety*, , vol. 1, pp. 69–75. IEEE.
- ARGROW, B.M. 1996 Computational analysis of dense gas shock tube flow. *Shock Waves* **6** (4), 241–248.
- ASHURST, W.M., KERSTEIN, A.R., KERR, R.M. & GIBSON, C.H. 1987 Alignment of vorticity and scalar gradient with strain rate in simulated Navier–Stokes turbulence. *Physics of Fluids (1958-1988)* **30** (8), 2343–2353.
- AUBARD, G., VOLPIANI, P.S., GLOERFELT, X. & ROBINET, J.C. 2013 Comparison of subgrid-scale viscosity models and selective filtering strategy for large-eddy simulations. *Flow, turbulence and combustion* **91** (3), 497–518.
- BAE, J.H., YOO, J.Y. & CHOI, H. 2005 Direct numerical simulation of turbulent supercritical flows with heat transfer. *Physics of Fluids (1994-present)* **17** (10), 105104.
- BARKER, L.M. & HOLLENBACH, R.E. 1970 Shock-wave studies of pmma, fused silica, and sapphire. *Journal of Applied Physics* **41** (10), 4208–4226.
- BATTISTA, F., PICANO, F. & CASCIOLA, C.M. 2014 Turbulent mixing of a slightly supercritical Van der Waals fluid at Low-Mach number. *Physics of Fluids (1994-present)* **26** (5), 055101.
- BENZI, R., BIFERALE, L., FISHER, R.T., KADANOFF, L.P., LAMB, D.Q. & TOSCHI, F. 2008 Intermittency and universality in fully developed inviscid and weakly compressible turbulent flows. *Physical review letters* **100** (23), 234503.
- BETHE, H.A. 1942 The Theory of Shock Waves for an Arbitrary Equation of State. *Tech. Rep.* 545. Office of Scientific Research and Development.
- BLACKBURN, H.M., MANSOUR, N.N. & CANTWELL, B.J. 1996 Topology of fine-scale motions in turbulent channel flow. *Journal of Fluid Mechanics* **310**, 269–292.
- BLAISDELL, G.A., MANSOUR, N.N. & REYNOLDS, W.C. 1993 Compressibility effects on the growth and structure of homogeneous turbulent shear flow. *Journal of Fluid Mechanics* **256**, 443–485.

- BOBER, W. & CHOW, W.L. 1990 Nonideal isentropic gas flow through converging-diverging nozzles. *Journal of fluids engineering* **112** (4), 455–460.
- BODENSCHATZ, E., BEWLEY, G.P., NOBACH, H., SINHUBER, M. & XU, H. 2014 Variable density turbulence tunnel facility. *Review of Scientific Instruments* **85** (9), 093908.
- BOGEY, C. & BAILLY, C. 2004 A family of low dispersive and low dissipative explicit schemes for flow and noise computations. *Journal of Computational Physics* **194** (1), 194–214.
- BOGEY, C., DE CACQUERAY, N. & BAILLY, C. 2009 A shock-capturing methodology based on adaptative spatial filtering for high-order non-linear computations. *Journal of Computational Physics* **228** (5), 1447–1465.
- BOLMATOV, D., BRAZHNIK, V.V. & TRACHENKO, K. 2013 Thermodynamic behaviour of supercritical matter. *Nature communications* **4**.
- BORISOV, A.A., BORISOV, A.A., KUTATELADZE, S.S. & NAKORYAKOV, V.E. 1983 Rarefaction shock wave near the critical liquid–vapour point. *Journal of Fluid Mechanics* **126**, 59–73.
- BRADSHAW, P. 1977 Compressible turbulent shear layers. *Annual Review of Fluid Mechanics* **9** (1), 33–52.
- BRAZHNIK, V.V., FOMIN, Y.D., LYAPIN, A.G., RYZHOV, V.N., TSIOK, E.N. & TRACHENKO, K. 2013 “liquid-gas” transition in the supercritical region: Fundamental changes in the particle dynamics. *Physical review letters* **111** (14), 145901.
- BROWN, B.P. & ARGROW, B.M. 1998 Nonclassical dense gas flows for simple geometries. *AIAA journal* **36** (10), 1842–1847.
- BROWN, B.P. & ARGROW, B.M. 2000 Application of bethe-zel’dovich-thompson fluids in organic rankine cycle engines. *Journal of Propulsion and Power* **16** (6), 1118–1124.
- BRUN, C., BOIARCIUC, M.P., HAKERBORN, M. & COMTE, P. 2008 Large eddy simulation of compressible channel flow - arguments in favour of universality of compressible turbulent wall bounded flows. *Theoretical and Computational Fluid Dynamics* **22**, 189–212.
- BRUNNER, G. 2005 Supercritical fluids: technology and application to food processing. *Journal of Food Engineering* **67** (1), 21–33.
- BRUNNER, G. 2010 Applications of supercritical fluids. *Annual review of chemical and biomolecular engineering* **1**, 321–342.
- BUFI, E.A. & CINNELLA, P. 2015 Efficient uncertainty quantification of turbulent flows through supersonic orc nozzle blades. *Energy Procedia* **82**, 186–193.
- CANTWELL, B.J. 1993 On the behavior of velocity gradient tensor invariants in direct numerical simulations of turbulence. *Physics of Fluids A: Fluid Dynamics (1989-1993)* **5** (8), 2008–2013.
- CASATI, E., VITALE, S., PINI, M., PERSICO, G. & COLONNA, P. 2014 Centrifugal turbines for mini-organic rankine cycle power systems. *Journal of Engineering for Gas Turbines and Power* **136** (12), 122607.
- CHANG III, P.A., PIOMELLI, U. & BLAKE, W.K. 1999 Relationship between wall pressure and velocity-field sources. *Physics of Fluids (1994-present)* **11** (11), 3434–3448.

- CHEN, S., DOOLEN, G.D., KRAICHNAN, R.H. & SHE, Z.S. 1993 On statistical correlations between velocity increments and locally averaged dissipation in homogeneous turbulence. *Physics of Fluids A: Fluid Dynamics (1989-1993)* **5** (2), 458–463.
- CHERNYSHENKO, S.I. & BAIG, M.F. 2005 The mechanism of streak formation in near-wall turbulence. *Journal of Fluid Mechanics* **544** (1), 99–131.
- CHONG, M.S., PERRY, A.E. & CANTWELL, B.J. 1990 A general classification of three-dimensional flow fields. *Physics of Fluids A: Fluid Dynamics (1989-1993)* **2** (5), 765–777.
- CHONG, M.S., SORIA, J., PERRY, A.E., CHACIN, J., CANTWELL, B.J. & NA, Y. 1998 Turbulence structures of wall-bounded shear flows found using DNS data. *Journal of Fluid Mechanics* **357**, 225–247.
- CHU, B.-T. & KOVASZNAY, L.S.G. 1958 Non-linear interactions in a viscous heat-conducting compressible gas. *Journal of Fluid Mechanics* **3**, 494–514.
- CHUNG, T.H., AJLAN, M., LEE, L.L. & STARLING, K.E. 1988 Generalized multiparameter correlation for nonpolar and polar fluid transport properties. *Industrial & engineering chemistry research* **27** (4), 671–679.
- CHUNG, T.H., LEE, L.L. & STARLING, K.E. 1984 Applications of kinetic gas theories and multiparameter correlation for prediction of dilute gas viscosity and thermal conductivity. *Industrial & engineering chemistry fundamentals* **23** (1), 8–13.
- CINNELLA, P. 2006 Roe-type schemes for dense gas flow computations. *Computers & fluids* **35** (10), 1264–1281.
- CINNELLA, P. & CONGEDO, P.M. 2005 Aerodynamic Performance of Transonic Bethe-Zal’dovich-Thompson Flows past an Airfoil. *AIAA Journal* **43** (2), 370–378.
- CINNELLA, P. & CONGEDO, P.M. 2007 Inviscid and viscous aerodynamics of dense gases. *Journal of Fluid Mechanics* **580**, 179–217.
- CLERK-MAXWELL, J. 1875 On the dynamical evidence of the molecular constitution of bodies. *Nature* **11**, 357–359.
- COLEMAN, G.N., KIM, J. & MOSER, R.D. 1995 A numerical study of turbulent supersonic isothermal-wall channel flow. *J Fluid Mech* **305**, 159–183.
- COLONNA, P., CASATI, E., TRAPP, C., MATHIJSEN, T., LARJOLA, J., TURUNEN-SAARETI, T. & UUSITALO, A. 2015 Organic rankine cycle power systems: from the concept to current technology, applications, and an outlook to the future. *Journal of Engineering for Gas Turbines and Power* **137** (10), 100801.
- COLONNA, P. & GUARDONE, A. 2006 Molecular interpretation of nonclassical gas dynamics of dense vapors under the van der waals model. *Physics of Fluids (1994-present)* **18** (5), 056101.
- COLONNA, P., GUARDONE, A., NANNAN, N.R. & ZAMFIRESCU, C. 2008a Design of the dense gas flexible asymmetric shock tube. *Journal of Fluids Engineering* **130** (3), 034501.
- COLONNA, P., NANNAN, N.R. & GUARDONE, A. 2008b Multiparameter equations of state for siloxanes: $[(\text{ch}_3)_3\text{si-o}^{1/2}]_2\text{-[o-si-(ch}_3)_2]_i$ $i = 1, \dots, 3$, and $[\text{o-si-(ch}_3)_2]_6$. *Fluid Phase Equilibria* **263** (2), 115–130.

-
- COLONNA, P., NANNAN, N.R., GUARDONE, A. & LEMMON, E.W. 2006 Multiparameter equations of state for selected siloxanes. *Fluid Phase Equilibria* **244** (2), 193–211.
- COLONNA, P. & SILVA, P. 2003 Dense gas thermodynamic properties of single and multicomponent fluids for fluid dynamics simulations. *Journal of fluids engineering* **125** (3), 414–427.
- COOK, A.W. & CABOT, W.H. 2005 Hyperviscosity for shock-turbulence interactions. *Journal of Computational Physics* **203** (2), 379–385.
- CRAMER, M.S. 1989*a* Negative nonlinearity in selected fluorocarbons. *Physics of Fluids A: Fluid Dynamics (1989-1993)* **1** (11), 1894–1897.
- CRAMER, M.S. 1989*b* Shock splitting in single-phase gases. *Journal of Fluid Mechanics* **199**, 281–296.
- CRAMER, M.S. 1991*a* Nonclassical dynamics of classical gases. *Nonlinear waves in real fluids* pp. 91–145.
- CRAMER, M.S. 1991*b* On the mach number variation in steady flows of dense hydrocarbons. *Journal of fluids engineering* **113** (4), 675–680.
- CRAMER, M.S. 2006 Rayleigh processes in single-phase fluids. *Physics of Fluids (1994-present)* **18** (1), 016101.
- CRAMER, M.S. & CRICKENBERGER, A.B. 1991 The dissipative structure of shock waves in dense gases. *Journal of Fluid Mechanics* **223**, 325–355.
- CRAMER, M.S. & FRY, R.N. 1993 Nozzle flows of dense gases. *Physics of Fluids A: Fluid Dynamics (1989-1993)* **5** (5), 1246–1259.
- CRAMER, M.S. & KLUWICK, A. 1984 On the propagation of waves exhibiting both positive and negative nonlinearity. *Journal of Fluid Mechanics* **142**, 9–37.
- CRAMER, M.S., MONACO, J.F. & FABENY, B.M. 1994 Fanno processes in dense gases. *Physics of Fluids (1994-present)* **6** (2), 674–683.
- CRAMER, M.S. & PARK, S. 1999 On the suppression of shock-induced separation in Bethe–Zel’dovich–Thompson fluids. *Journal of Fluid Mechanics* **393**, 1–21.
- CRAMER, M.S. & SEN, R. 1986 Shock formation in fluids having embedded regions of negative nonlinearity. *Physics of Fluids (1958-1988)* **29** (7), 2181–2191.
- CRAMER, M.S. & SEN, R. 1987 Exact solutions for sonic shocks in van der Waals gases. *Physics of Fluids (1958-1988)* **30** (2), 377–385.
- CRAMER, M.S. & TARKENTON, G.M. 1992 Transonic flows of Bethe–Zel’dovich–Thompson fluids. *Journal of Fluid Mechanics* **240**, 197–228.
- DE BOER, J. 1948 Quantum theory of condensed permanent gases i the law of corresponding states. *Physica* **14** (2-3), 139–148.
- DEAN, R.B. 1978 Reynolds number dependence of skin friction and other bulk flow variables in two-dimensional rectangular duct flow. *Journal of Fluids Engineering* **100** (2), 215–223.
- DONZIS, D.A. & JAGANNATHAN, S. 2013 Fluctuations of thermodynamic variables in stationary compressible turbulence. *Journal of Fluid Mechanics* **733**, 221–244.

- DONZIS, D.A. & JAGANNATHAN, S. 2016 Fluctuations of thermodynamic variables in stationary compressible turbulence. *Journal of Fluid Mechanics* **733**, 221–244.
- DUAN, L., BEEKMAN, I. & MARTIN, M.P. 2010 Direct numerical simulation of hypersonic turbulent boundary layers. Part 2. Effect of wall temperature. *Journal of Fluid Mechanics* **655**, 419–445.
- DUCROS, F., FERRAND, V., NICOD, F., WEBER, C., DARRACQ, D., GACHERIEU, C. & POINSOT, T. 1999 Large-eddy simulation of the shock/turbulence interaction. *Journal of Computational Physics* **152** (2), 517–549.
- ECKERT, C.A. 1996 Supercritical fluids as solvents for chemical and materials processing. *Nature* **383**, 313–318.
- ERLEBACHER, G. & SARKAR, S. 1993 Statistical analysis of the rate of strain tensor in compressible homogeneous turbulence. *Physics of Fluids A: Fluid Dynamics (1989-1993)* **5** (12), 3240–3254.
- FERGASON, S.H., HO, T.H., ARGROW, B.M. & EMANUEL, G. 2001 Theory for producing a single-phase rarefaction shock-wave in a shock tube. *Journal of Fluid Mechanics* **445**, 37–54.
- FOYSI, H., SARKAR, S. & FRIEDRICH, R. 2004 Compressibility effects and turbulence scalings in supersonic channel flow. *Journal of Fluid Mechanics* **509**, 207–216.
- FUKAGATA, K., IWAMOTO, K. & KASAGI, N. 2002 Contribution of reynolds stress distribution to the skin friction in wall-bounded flows. *Physics of Fluids (1994-present)* **14** (11), L73–L76.
- GARNIER, E., ADAMS, N. & SAGAUT, P. 2009 *Large eddy simulation for compressible flows*. Springer Science & Business Media.
- GARNIER, E., MOSSI, M., SAGAUT, P., COMTE, P. & DEVILLE, M. 1999 On the use of shock-capturing schemes for large-eddy simulation. *Journal of Computational Physics* **153** (2), 273–311.
- GEROLYMOS, G.A., SÉNÉCHAL, D. & VALLET, I. 2010 Performance of very-high-order upwind schemes for DNS of compressible wall-turbulence. *International Journal for Numerical Methods in Fluids* **63** (7), 769–810.
- GEROLYMOS, G.A. & VALLET, I. 2014 Pressure, density, temperature and entropy fluctuations in compressible turbulent plane channel flow. *Journal of Fluid Mechanics* **757**, 701–746.
- GLOERFELT, X. & BERLAND, J. 2013 Turbulent boundary-layer noise: direct radiation at Mach number 0.5. *Journal of Fluid Mechanics* **723**, 318–351.
- GOMEZ, T., FLUTET, V. & SAGAUT, P. 2009 Contribution of reynolds stress distribution to the skin friction in compressible turbulent channel flows. *Physical Review E* **79** (3), 035301.
- GORELLI, F., SANTORO, M., SCOPIGNO, T., KRISCH, M. & RUOCCO, G. 2006 Liquidlike behavior of supercritical fluids. *Physical review letters* **97** (24), 245702.
- GUARDONE, A. & VIGEVANO, L. 2002 Roe linearization for the van der Waals gas. *Journal of Computational Physics* **175** (1), 50–78.
- GUARINI, S.E., MOSER, R.D., SHARIFF, K. & WRAY, A. 2000 Direct numerical simulation of a supersonic turbulent boundary layer at Mach 2.5. *Journal of Fluid Mechanics* **414**, 1–33.

- HARINCK, J., COLONNA, P., GUARDONE, A. & REBAY, S. 2010a Influence of thermodynamic models in two-dimensional flow simulations of turboexpanders. *Journal of turbomachinery* **132** (1).
- HARINCK, J., GUARDONE, A. & COLONNA, P. 2009 The influence of molecular complexity on expanding flows of ideal and dense gases. *Physics of Fluids (1994-present)* **21** (8), 086101.
- HARINCK, J., PASQUALE, D., PECNIK, R., VAN BUIJTENEN, J. & COLONNA, P. 2013 Performance improvement of a radial organic rankine cycle turbine by means of automated computational fluid dynamic design. *Proceedings of the Institution of Mechanical Engineers, Part A: Journal of Power and Energy* **227** (6), 637–645.
- HARINCK, J., TURUNEN-SAARETI, T., COLONNA, P., REBAY, S. & VAN BUIJTENEN, J. 2010b Computational Study of a High-Expansion Ratio Radial Organic Rankine Cycle Turbine Stator. *Journal of Gas Turbines and Power* **132** (5), 054501.
- HAYES, W.D. 1958 Fundamentals of gas dynamics. *Princeton University Press, New Jersey* **3**, 426.
- HINZE, J.O. 1975 Turbulence.
- HU, F.Q., HUSSAINI, M.Y. & MANTHEY, J.L. 1996 Low-dissipation and low-dispersion runge-kutta schemes for computational acoustics. *Journal of Computational Physics* **124** (1), 177–191.
- HUANG, P.G., BRADSHAW, P. & COAKLEY, T.J. 1993 Skin friction and velocity profile family for compressible turbulent boundary layers. *AIAA Journal* **31** (9), 1600–1604.
- HUANG, P.G., COLEMAN, G.N. & BRADSHAW, P. 1995 Compressible turbulent channel flows: DNS results and modelling. *J. Fluid Mech.* **305**, 185–218.
- INCROPERA, F.P. & DEWITT, D.P. 2007 *Fundamentals of Heat and Mass Transfer*, 6th edn. New York: Wiley.
- IVANOV, A.G. & NOVIKOV, S.A. 1961 Rarefaction shock waves in iron and steel. *Zh. Eksp. Teor. Fiz* **40** (6), 1880–1882.
- JAGANNATHAN, S. & DONZIS, D.A. 2016 Reynolds and Mach number scaling in solenoidally-forced compressible turbulence using high-resolution direct numerical simulations. *Journal of Fluid Mechanics* **789**, 669–707.
- JAMESON, A., SCHMIDT, W. & TURKEL, E. 1981 Numerical solutions of the Euler equations by finite volume methods using Runge-Kutta time-stepping schemes. *AIAA Journal* **81** (1259).
- JIANG, G.S. & SHU, C.W. 1995 Efficient implementation of weighted eno schemes. *Tech. Rep.* DTIC Document.
- JIMÉNEZ, J., WRAY, A.A., SAFFMAN, P.G. & ROGALLO, R.S. 1993 The structure of intense vorticity in isotropic turbulence. *Journal of Fluid Mechanics* **255**, 65–90.
- KAISER, C.S., RÖMPP, H. & SCHMIDT, P.C. 2001 Pharmaceutical applications of supercritical carbon dioxide. *Die Pharmazie* **56** (12), 907–926.
- KEVLAHAN, N., MAHESH, K. & LEE, S. 1992 Evolution of the shock front and turbulence structures in the shock/turbulence interaction. In *Studying Turbulence Using Numerical Simulation Databases*, , vol. 1, pp. 277–292.

- KIDA, S. & ORSZAG, S.A. 1989 Enstrophy budget in decaying compressible turbulence. *Journal of Scientific Computing* **5**, 1–34.
- KIM, J. 1989 On the structure of pressure fluctuations in simulated turbulent channel flow. *Journal of Fluid Mechanics* **205**, 421–451.
- KIM, J.W. & LEE, D.J. 2001 Adaptive Nonlinear Artificial Dissipation Model for Computational Aeroacoustics. *AIAA Journal* **39**, 810–818.
- KIM, J., MOIN, P. & MOSER, R. 1987 Turbulence statistics in fully developed channel flow at low Reynolds number. *Journal of Fluid Mechanics* **177**, 133–166.
- KIRAN, E. 1995 Supercritical fluid processing in the pulp and paper and the forest products industries .
- KIRILLOV, N. 2004 Analysis of modern natural gas liquefaction technologies. *Chemical and Petroleum Engineering* **40** (7-8), 401–406.
- KLUWICK, A. 2004 Internal flows of dense gases. *Acta mechanica* **169** (1-4), 123–143.
- KLUWICK, A. & MEYER, G. 2010 Shock regularization in dense gases by viscous–inviscid interactions. *Journal of Fluid Mechanics* **644**, 473–507.
- KLUWICK, A. & MEYER, G. 2011 Viscous–inviscid interactions in transonic flows through slender nozzles. *Journal of Fluid Mechanics* **672**, 487–520.
- KLUWICK, A. & WRABEL, M. 2004 Shock boundary layer interactions in dense gases. *PAMM* **4** (1), 444–445.
- KORTE, J.J. 2000 Inviscid design of hypersonic wind tunnel nozzles for real gas. In *Proceedings of the 38th Aerospace Sciences Meeting and Exhibit, Reno, NV, Jan*, pp. 10–13.
- KRITSUK, A.G., NORMAN, M.L., PADOAN, P. & WAGNER, R. 2007 The statistics of supersonic isothermal turbulence. *The Astrophysical Journal* **665** (1), 416.
- KUTATELADZE, S.S., NAKARYAKOV, V.E. & BORISOV, A.A. 1987 Rarefaction waves in liquid and gas-liquid media. *Annual Reviews of Fluid Mechanics* **19**, 577–600.
- KUTTA, W. 1901 Beitrag zur näherungsweise integration totaler differentialgleichungen .
- LAGHA, M., KIM, J., ELDREDGE, J.D. & ZHONG, X. 2011 A numerical study of compressible turbulent boundary layers. *Physics of Fluids (1994-present)* **23** (1), 015106.
- LAMORGESE, A.G., CAUGHEY, D.A. & POPE, S.B. 2005 Direct numerical simulation of homogeneous turbulence with hyperviscosity. *Physics of Fluids* **17** (1), 015106.
- LANDAU, L.D. & LIFSHITZ, E.M. 1959 *Fluid mechanics*. Addison-Wesley, Reading, Mass.
- LECHNER, R., SESTERHENN, J. & FRIEDRICH, R. 2001 Turbulent supersonic channel flow. *Journal of Turbulence* **2** (1), 001–001.
- LEE, J., JUNG, S.Y., SUNG, H.J. & ZAKI, T.A. 2013 Effect of wall heating on turbulent boundary layers with temperature-dependent viscosity. *Journal of Fluid Mechanics* **726**, 196–225.
- LEE, K., GIRIMAJI, S.S. & KERIMO, J. 2009 Effect of compressibility on turbulent velocity gradients and small-scale structure. *Journal of Turbulence* **10**, N9.

- LEE, M. & MOSER, R.D. 2015 Direct numerical simulation of turbulent channel flow up to $Re \approx 5200$. *Journal of Fluid Mechanics* **774**, 395–415.
- LEE, S., LELE, S.K. & MOIN, P. 1991 Eddy shocklets in decaying compressible turbulence. *Physics of Fluids A: Fluid Dynamics (1989-1993)* **3** (4), 657–664.
- LEMMON, E.W. & SPAN, R. 2006 Short fundamental equations of state for 20 industrial fluids. *Journal of Chemical & Engineering Data* **51** (3), 785–850.
- LERAT, A. & CORRE, C. 2003 *Approximations d'ordre élevé pour les écoulements compressibles*. Ecole de Printemps de mécanique des fluides, Fréjus, France.
- LESIEUR, M. 2008 *Turbulence in fluids, Fluid Mechanics and its Applications*. Springer, Dordrecht.
- LI, X., HASHIMOTO, K., TOMINAGA, Y., TANAHASHI, M. & MIYAUCHI, T. 2008 Numerical study of heat transfer mechanism in turbulent supercritical CO_2 channel flow. *Journal of Thermal Science and Technology* **3** (1), 112–123.
- LIU, X.D., OSHER, S. & CHAN, T. 1994 Weighted essentially non-oscillatory schemes. *Journal of computational physics* **115** (1), 200–212.
- MANSOUR, N.N. & WRAY, A.A. 1994 Decay of isotropic turbulence at low Reynolds number. *Physics of Fluids (1994-present)* **6** (2), 808–814.
- MARTIN, J.J. & HOU, Y.C. 1955 Development of an equation of state for gases. *AIChE Journal* **1** (2), 142–151.
- MARTÍN, J., OOI, A., CHONG, M.S. & SORIA, J. 1998 Dynamics of the velocity gradient tensor invariants in isotropic turbulence. *Physics of Fluids (1994-present)* **10** (9), 2336–2346.
- MATHIJSEN, T., GALLO, M., CASATI, E., NANNAN, N.R., ZAMFIRESCU, C., GUARDONE, A. & COLONNA, P. 2015 The flexible asymmetric shock tube (fast): a ludwig tube facility for wave propagation measurements in high-temperature vapours of organic fluids. *Experiments in Fluids* **56** (10), 1–12.
- MCHUGH, M. & KRUKONIS, V. 2013 *Supercritical fluid extraction: principles and practice*. Elsevier.
- MCMILLAN, P.F. & STANLEY, H.E. 2010 Fluid phases: Going supercritical. *Nature Physics* **6**, 479–480.
- MENIKOFF, R. & PLOHR, B.J. 1989 The Riemann problem for fluid flow of real materials. *Reviews of Modern Physics* **61**, 75–130.
- MODESTI, D. & PIROZZOLI, S. 2016 Reynolds and Mach number effects in compressible turbulent channel flow. *International Journal of Heat and Fluid Flow* **59**, 33–49.
- MOISY, F. & JIMÉNEZ, J. 2004 Geometry and clustering of intense structures in isotropic turbulence. *Journal of Fluid Mechanics* **513**, 111–133.
- MONACO, J.F., CRAMER, M.S. & WATSON, L.T. 1997 Supersonic flows of dense gases in cascade configurations. *Journal of Fluid Mechanics* **330**, 31–59.
- MONEGHAN, R.J. 1953 A review and assessment of various formulae for turbulent skin friction in compressible flow. *Aeronautical Research Council Technical Report, Current Paper* **142**.

- MORINISHI, Y., TAMANO, S. & NAKABAYASHI, K. 2004 Direct numerical simulation of compressible turbulent channel flow between adiabatic and isothermal walls. *J. Fluid Mech.* **502**, 273–308.
- MORKOVIN, M.V. 1962 Effects of compressibility on turbulent flows. *Mécanique de la Turbulence* pp. 367–380.
- NEUFELD, P.D., JANZEN, A.R. & AZIZ, R.A. 1972 Empirical equations to calculate 16 of the transport collision integrals $\omega(l, s)^*$ for the lennard-jones (12–6) potential. *The Journal of Chemical Physics* **57** (3), 1100–1102.
- NICOUD, F. & POINSOT, T. 1999 DNS of a channel flow with variable properties. *First International Symposium on Turbulence and Shear Flow Phenomena, TSFP-1*, Santa Barbara, USA .
- OKONG'O, N.A. & BELLAN, J. 2002 Direct numerical simulation of a transitional supercritical binary mixing layer: heptane and nitrogen. *Journal of Fluid Mechanics* **464**, 1–34.
- OKONG'O, N.A. & BELLAN, J. 2010 Small-scale dissipation in binary-species, thermodynamically supercritical, transitional mixing layers. *Computers & Fluids* **39**, 1112–1124.
- OOI, A., MARTIN, J., SORIA, J. & CHONG, M.S. 1999 A study of the evolution and characteristics of the invariants of the velocity-gradient tensor in isotropic turbulence. *Journal of Fluid Mechanics* **381**, 141–174.
- OUTTIER, P.Y. 2014 A new dynamic code architecture for CFD computations: application to the development of an overset-grid compact high-order solver for compressible aerodynamics. PhD thesis, Arts et Métiers ParisTech.
- OUTTIER, P.Y., CONTENT, C., CINNELLA, P. & MICHEL, B. 2013 The high-order dynamic computational laboratory for CFD research and applications. In *21st AIAA Computational Fluid Dynamics Conference*. American Institute of Aeronautics and Astronautics.
- PASQUALE, D., GHIDONI, A. & REBAY, S. 2013 Shape optimization of an organic rankine cycle radial turbine nozzle. *Journal of Engineering for Gas Turbines and Power* **135** (4), 042308.
- PASSOT, T. & POUQUET, A. 1987 Numerical simulation of compressible homogeneous flows in the turbulent regime. *Journal of Fluid Mechanics* **181**, 441–466.
- PATEL, A., PEETERS, J.W.R., BOERSMA, B.J. & PECNIK, R. 2015 Semi-local scaling and turbulence modulation in variable property turbulent channel flows. *Physics of Fluids (1994-present)* **27** (9), 095101.
- PERRY, A.E. & CHONG, M.S. 1987 A description of eddying motions and flow patterns using critical-point concepts. *Annual Review of Fluid Mechanics* **19** (1), 125–155.
- PHILLIPS, N.A. 1959 An example of non-linear computational instability. *The Atmosphere and the Sea in motion* **501**.
- PIROZZOLI, S. 2011 Numerical methods for high-speed flows. *Annual review of fluid mechanics* **43**, 163–194.
- PIROZZOLI, S. & GRASSO, F. 2004 Direct numerical simulations of isotropic compressible turbulence: Influence of compressibility on dynamics and structures. *Physics of Fluids (1994-present)* **16** (12), 4386–4407.

- POLING, B.E., PRAUSNITZ, J.M., O'CONNELL, J.P. & REID, R.C. 2001 *The properties of gases and liquids*, vol. 5. McGraw-Hill New York.
- POPESCU, M., SHYY, W. & GARBEY, M. 2005 Finite volume treatment of dispersion-relation-preserving and optimized prefactored compact schemes for wave propagation. *Journal of Computational Physics* **210** (2), 705–729.
- PORTER, D., POUQUET, A., SYTINE, I. & WOODWARD, P. 1999 Turbulence in compressible flows. *Physica A: Statistical Mechanics and its Applications* **263** (1), 263–270.
- PORTER, D.H., POUQUET, A. & WOODWARD, P.R. 1992a A numerical study of supersonic turbulence. *Theoretical and Computational Fluid Dynamics* **4** (1), 13–49.
- PORTER, D.H., POUQUET, A. & WOODWARD, P.R. 1992b Three-dimensional supersonic homogeneous turbulence: a numerical study. *Physical Review Letters* **68** (21), 3156.
- PORTER, D.H., POUQUET, A. & WOODWARD, P.R. 1994 Kolmogorov-like spectra in decaying three-dimensional supersonic flows. *Physics of Fluids (1994-present)* **6** (6), 2133–2142.
- PORTER, D., POUQUET, A. & WOODWARD, P.R. 2002 Measures of intermittency in driven supersonic flows. *Physical Review E* **66** (2), 026301.
- PORTER, D.H., WOODWARD, P.R. & POUQUET, A. 1998 Inertial range structures in decaying compressible turbulent flows. *Physics of Fluids (1994-present)* **10** (1), 237–245.
- QUARTAPELLE, L., CASTELLETTI, L., GUARDONE, A. & QUARANTA, G. 2003 Solution of the riemann problem of classical gasdynamics. *Journal of Computational Physics* **190** (1), 118–140.
- RAYLEIGH, L. 1910 Aerial plane waves of finite amplitude. *Proc. Roy. Soc. A* **84**, 247–284.
- RISTORCELLI, J.R. & BLAISDELL, G.A. 1997 Consistent initial conditions for the DNS of compressible turbulence. *Physics of Fluids (1994-present)* **9** (1), 4–6.
- ROE, P.L. 1981 Approximate Riemann Solvers, Parameter Vectors, and Difference Schemes. *Journal of Computational Physics* **43**, 357–372.
- RUNGE, C. 1895 Über die numerische auflösung von differentialgleichungen. *Mathematische Annalen* **46** (2), 167–178.
- RUSAK, Z. & WANG, C.W. 1997 Transonic flow of dense gases around an airfoil with a parabolic nose. *Journal of Fluid Mechanics* **346**, 1–21.
- RUSAK, Z. & WANG, C.W. 2000 Low-drag airfoils for transonic flow of dense gases. *Zeitschrift für angewandte Mathematik und Physik ZAMP* **51** (3), 467–480.
- SAMTANEY, R., PULLIN, D.I. & KOSOVIC, B. 2001 Direct numerical simulation of decaying compressible turbulence and shocklet statistics. *Physics of Fluids* **13** (5), 1415–1430.
- SARKAR, S. 1995 The stabilizing effect of compressibility in turbulent shear flow. *J. Fluid Mech.* **282**, 163–186.
- SARKAR, SARBEN, ERLEBACHER, G, HUSSAINI, MYJ & KREISS, HO 1991 The analysis and modelling of dilatational terms in compressible turbulence. *Journal of Fluid Mechanics* **227**, 473–493.
- SCHLICHTING, H. & GERSTEN, K. 2003 *Boundary layer theory*, 8th edn. Springer.

- SCHNERR, G.H. & LEIDNER, P. 1993 Numerical investigation of axial cascades for dense gases. In *PICAST'1 1993- Pacific International Conference on Aerospace Science and Technology, National Cheng Kung University, Tainan, Taiwan*, pp. 818–825.
- SCIACOVELLI, L. & CINNELLA, P. 2014 Numerical Study of Multistage Transcritical Organic Rankine Cycle Axial Turbines. *Journal of Gas Turbines and Power* **136** (2), 082604.
- SCIACOVELLI, L., CINNELLA, P., CONTENT, C. & GRASSO, F. 2016*a* Dense gas effects in inviscid homogeneous isotropic turbulence. *Journal of Fluid Mechanics* **800** (1), 140–179.
- SCIACOVELLI, L., CINNELLA, P. & GRASSO, F. 2016*b* Small-scale dynamics of dense gas compressible homogeneous isotropic turbulence. *Submitted in Journal of Fluid Mechanics* .
- SELLE, L. & SCHMITT, T. 2010 Large-eddy simulation of single-species flows under supercritical thermodynamic conditions. *Combustion Science and Technology* **182** (4-6), 392–404.
- SENGERS, J.V. & SENGERS, J.M.H. 1986 Thermodynamic behavior of fluids near the critical point. *Annual Review of Physical Chemistry* **37** (1), 189–222.
- SETZMANN, U. & WAGNER, W. 1989 A new method for optimizing the structure of thermodynamic correlation equations. *International Journal of Thermophysics* **10** (6), 1103–1126.
- SEWALL, E.A. & TAFTI, D.K. 2008 A time-accurate variable property algorithm for calculating flows with large temperature variations. *Computers & Fluids* **37**, 51–63.
- SHU, C.W. 1990 Numerical experiments on the accuracy of eno and modified eno schemes. *Journal of Scientific Computing* **5** (2), 127–149.
- SHU, C.W. & OSHER, S. 1989 Efficient implementation of essentially non-oscillatory shock-capturing schemes, ii. In *Upwind and High-Resolution Schemes*, pp. 328–374. Springer.
- SIEDER, E.N. & TATE, G.E. 1936 Heat transfer and pressure drop of liquids in tubes. *Industrial & Engineering Chemistry* **28** (12), 1429–1435.
- SIMEONI, G.G., BRYK, T., GORELLI, F.A., KRISCH, M., RUOCCO, G., SANTORO, M. & SCOPIGNO, T. 2010 The widom line as the crossover between liquid-like and gas-like behaviour in supercritical fluids. *Nature Physics* **6** (7), 503–507.
- SORIA, J. & CANTWELL, B.J. 1994 Topological visualisation of focal structures in free shear flows. *Applied scientific research* **53** (3-4), 375–386.
- SPAN, R. & WAGNER, W. 1996 A new equation of state for carbon dioxide covering the fluid region from the triple-point temperature to 1100 K at pressures up to 800 MPa. *Journal of Physical and Chemical Reference Data* **25**, 1509.
- SPAN, R. & WAGNER, W. 2003*a* Equations of state for technical applications. I. Simultaneously optimized functional forms for nonpolar and polar fluids. *International journal of thermophysics* **24** (1), 1–39.
- SPAN, R. & WAGNER, W. 2003*b* Equations of state for technical applications. III. Results for polar fluids. *International Journal of Thermophysics* **24** (1), 111–162.
- SPINA, E.F., SMITS, A.J. & ROBINSON, S.K. 1994 The physics of supersonic turbulent boundary layers. *Annual Review of Fluid Mechanics* **26**, 287–319.

- SPINELLI, A., DOSSENA, V., GAETANI, P., OSNAGHI, C. & COLOMBO, D. 2010 Design of a Test Rig for Organic Vapours. In *Proceedings of the ASME Turbo Expo 2010, GT2010*. June 14–18, 2010, Glasgow, UK.
- SPINELLI, A., PINI, M., DOSSENA, V., GAETANI, P. & CASELLA, F. 2013 Design, simulation, and construction of a test rig for organic vapors. *Journal of Engineering for Gas Turbines and Power* **135** (4), 042304.
- SREENIVASAN, K.R. & ANTONIA, R.A. 1997 The phenomenology of small-scale turbulence. *Annual review of fluid mechanics* **29** (1), 435–472.
- STAHL, E., QUIRIN, K.W. & GERARD, D. 2012 *Dense gases for extraction and refining*. Springer Science & Business Media.
- STRYJEK, R. & VERA, J.H. 1986 PRSV2: A cubic equation of state for accurate vapor-liquid equilibria calculations. *The Canadian Journal of Chemical Engineering* **64** (5), 820–826.
- SUTHERLAND, W. 1893 The viscosity of gases and molecular force. *The London, Edinburgh, and Dublin Philosophical Magazine and Journal of Science* **36** (223), 507–531.
- SYTINE, I.V., PORTER, D.H., WOODWARD, P.R., HODSON, S.W. & WINKLER, K.H. 2000 Convergence tests for the piecewise parabolic method and Navier–Stokes solutions for homogeneous compressible turbulence. *Journal of Computational Physics* **158** (2), 225–238.
- TAM, C.K.W. & WEBB, J.C. 1993 Dispersion-relation-preserving finite difference schemes for computational acoustics. *Journal of computational physics* **107** (2), 262–281.
- TAMANO, S. & MORINISHI, Y. 2006 Effect of different thermal wall boundary conditions on compressible turbulent channel flow at $m=1.5$. *Journal of Fluid Mechanics* **548**, 361–373.
- TANAHASHI, M., TOMINAGA, Y., SHIMURA, M., HASHIMOTO, K. & MIYAUCHI, T. 2011 Dns of supercritical carbon dioxide turbulent channel flow. In *Progress in Wall Turbulence: Understanding and Modeling*, pp. 429–436. Springer.
- TEITEL, M. & ANTONIA, R.A. 1993 Heat transfer in fully developed turbulent channel flow: comparison between experiment and direct numerical simulations. *International Journal of Heat and Mass Transfer* **36** (6), 1701–1706.
- THOMPSON, P.A. 1971 A fundamental derivative in gasdynamics. *Physics of Fluids (1958-1988)* **14** (9), 1843–1849.
- THOMPSON, P.A., CAROFANO, G.C. & KIM, Y.G. 1986 Shock waves and phase changes in a large-heat-capacity fluid emerging from a tube. *Journal of Fluid Mechanics* **166**, 57–92.
- THOMPSON, P.A., CRAVES, H., MEIER, G.E.A., KIM, Y.G. & SPECKMANN, H.D. 1987 Wave splitting in a fluid of large heat capacity. *Journal of Fluid Mechanics* **185**, 385–414.
- THOMPSON, P.A. & LAMBRAKIS, K.C. 1973 Negative shock waves. *Journal of Fluid Mechanics* **60** (01), 187–208.
- TILLNER-ROTH, R. & DIETER BAEHR, H. 1994 An international standard formulation for the thermodynamic properties of 1,1,1,2-tetrafluoroethane (HFC-134a) for temperatures from 170 K to 455 K and pressures up to 70 MPa. *Journal of Physical and Chemical Reference Data* **23** (5), 657–730.

- TRETTEL, A. & LARSSON, J. 2016 Mean velocity scaling for compressible wall turbulence with heat transfer. *Physics of Fluids (1994-present)* **28** (2), 026102.
- VAN DER WAALS, J.D. 1873 Doctoral Dissertation. PhD thesis, University of Leiden.
- VAN DRIEST, E.R. 1951 Turbulent boundary layer in compressible fluids. *Journal of the Aeronautical Sciences* **18** (3), 145–160.
- VAN LEER, B. 1979 Towards the ultimate conservative difference scheme. v. a second-order sequel to godunov's method. *Journal of computational Physics* **32** (1), 101–136.
- WAGNER, B. & SCHMIDT, W. 1978 Theoretical investigations of real gas effects in cryogenic wind tunnels. *AIAA Journal* **16** (6), 580–586.
- WALLACE, J.M. 2016 Quadrant analysis in turbulence research: History and evolution. *Annual Review of Fluid Mechanics* **48**, 131–158.
- WANG, C.W. & RUSAK, Z. 1999 Numerical studies of transonic BZT gas flows around thin airfoils. *Journal of Fluid Mechanics* **396**, 109–141.
- WANG, J., SHI, Y., WANG, L.P., XIAO, Z., HE, X. & CHEN, S. 2011 Effect of shocklets on the velocity gradients in highly compressible isotropic turbulence. *Physics of Fluids (1994-present)* **23** (12), 125103.
- WANG, J., SHI, Y., WANG, L.P., XIAO, Z., HE, X.T. & CHEN, S. 2012a Scaling and statistics in three-dimensional compressible turbulence. *Physical review letters* **108** (21), 214505.
- WANG, JIANCHUN, SHI, YIPENG, WANG, LIAN-PING, XIAO, ZUOLI, HE, XT & CHEN, SHIYI 2012b Effect of compressibility on the small-scale structures in isotropic turbulence. *Journal of Fluid Mechanics* **713**, 588–631.
- WEI, L. & POLLARD, A. 2011 Interactions among pressure, density, vorticity and their gradients in compressible turbulent channel flows. *Journal of Fluid Mechanics* **673**, 1–18.
- WHEELER, A.P.S. & ONG, J. 2013 The role of dense gas dynamics on organic rankine cycle turbine performance. *Journal of Engineering for Gas Turbines and Power* **135** (10), 102603.
- WHEELER, A.P.S. & ONG, J. 2014 A study of the three-dimensional unsteady real-gas flows within a transonic ORC turbine. In *Proceedings of the ASME Turbo Expo 2014, GT2014*. June 16–20, 2014, Dusseldorf, Germany.
- WILSON, K.G. 1983 The renormalization group and critical phenomena. *Reviews of Modern Physics* **55** (3), 583.
- ZAMFIRESCU, C. & DINCER, I. 2009 Performance investigation of high-temperature heat pumps with various BZT working fluids. *Thermochimica Acta* **488**, 66–77.
- ZAPPOLI, B., BAILLY, D., GARRABOS, Y., LE NEINDRE, B., GUENOUN, P. & BEYSENS, D. 1990 Anomalous heat transport by the piston effect in supercritical fluids under zero gravity. *Physical Review A* **41** (4), 2264.
- ZEL'DOVICH, J. 1946 On the possibility of rarefaction shock waves. *ZHURNAL EKSPERIMENTALNOI I TEORETICHESKOI FIZIKI* **16** (4), 363–364.
- ZEL'DOVICH, Y.B. & RAIZER, Y.P. 1965 Physics of shock waves and high-temperature hydrodynamic phenomena. *Tech. Rep.*. DTIC Document.

- ZEMAN, O. 1990 Dilatation dissipation: the concept and application in modeling compressible mixing layers. *Physics of Fluids A: Fluid Dynamics (1989-1993)* **2** (2), 178–188.
- ZEMAN, O. 1991 On the decay of compressible isotropic turbulence. *Physics of Fluids A: Fluid Dynamics (1989-1993)* **3** (5), 951–955.
- ZEMAN, O. & BLAISDELL, G.A. 1991 New physics and models for compressible turbulent flows. In *Advances in Turbulence 3*, pp. 445–454. Springer.
- ZEMPLÉN, G. 1905 On the possibility of negative shock waves in gas. *Comptes rendues de l'Académie des Sciences* **141**, 710–713.
- ZONTA, F. 2013 Nusselt number and friction factor in thermally stratified turbulent channel flow under Non-Oberbeck–Boussinesq conditions. *International Journal of Heat and Fluid Flow* **44**, 489–494.
- ZONTA, F., MARCHIOLI, C. & SOLDATI, A. 2012 Modulation of turbulence in forced convection by temperature-dependent viscosity. *Journal of Fluid Mechanics* **697**, 150–174.

List of Acronyms

BZT	Bethe-Zel'dovich-Thompson
CFD	Computational Fluid Dynamics
CFL	Courant-Friedrichs-Lewy
CHIT	Compressible Homogeneous Isotropic Turbulence
DG	Dense Gas
DNC	Directional Non-Compact
DNS	Direct Numerical Simulation
DRP	Dispersion-Relation Preserving
DynHoLab	Dynamic High-order Laboratory
EoS	Equation of State
HPC	High-Parallel Computing
IDRIS	Institute for Development and Resources in Intensive Scientific Computing
LES	Large-Eddy Simulation
MAH	Martin-Hou
MUSCL	Monotonic Upstream-Centered Scheme for Conservation Laws
MUSICA	MULTiscale Solver in Computational Aeroacoustics
NICFD	Non-Ideal Compressible Fluid Dynamics
ORC	Organic Rankine Cycle
PFG	Perfect Gas
RANS	Reynolds-Averaged Navier-Stokes
RK	Runge-Kutta
SWN	Span-Wagner for Non-polar fluids
SWP	Span-Wagner for Polar fluids
TCF	Turbulent Channel Flow
TVD	Total Variation Diminishing

VDW Van der Waals

List of Symbols

Roman Letters

a	Free Helmholtz energy
A_{ij}	Velocity gradient tensor
c	Speed of sound
C_f	Skin friction coefficient
$C_{a'b'}$	Correlation coefficient between a' and b'
c_p	Specific heat at constant pressure
c_v	Specific heat at constant volume
e	Specific internal energy
Ec	Eckert number
E	Turbulent kinetic energy spectrum
\mathcal{E}	Specific total energy
g	Gibbs free energy
h	Enthalpy
K	Turbulent kinetic energy
k_{bz}	Boltzmann constant
M	Mach number
\mathcal{M}	Molecular weight
M_t	Turbulent Mach number
n_c	Exponent of the isochoric ideal specific heat law
Nu	Nusselt number
O	Compressibility value of local turbulent structure
P	First invariant of A_{ij}
p	Pressure
Pr	Prandtl number
Q	Second invariant of A_{ij}
q_j	Heat flux
R	Gas constant
\mathcal{R}	Universal Gas constant
Re	Reynolds number
Re_λ	Reynolds number based on Taylor microscale
r_j^d	Bogey & Bailly dilatation-based sensor
r_j^p	Bogey & Bailly pressure-based sensor
R	Third invariant of A_{ij}
s	Entropy
S_{ij}	Strain-rate tensor
S_n	n -th order moment of velocity gradients
T	Temperature

t	Time
T_{eb}	Boiling temperature
u_i	Velocity components
u_τ	Friction velocity
V	Flow volume fraction
v	Specific volume
Z	Compressibility factor

Greek Letters

α	Reduced free Helmholtz energy
β_T	Isothermal compressibility coefficient
χ	Compressibility ratio
δ	Difference operator
δ_{ij}	Kronecker delta
ϵ_c	Cut-off parameter
ε	Dissipation of turbulent kinetic energy
η	Kolmogorov lengthscale
Γ	Fundamental derivative of gas dynamics
γ	Specific heat ratio
κ	Thermal conductivity
λ_f	Taylor microscale
λ_i	Eigenvalues of A_{ij}
μ	Dynamic viscosity
μ	Cell average operator (only in section 2.2)
ν	Kinematic viscosity
Ω	Enstrophy
ω	Vorticity
ω_{ac}	Acentric factor
Φ	Ducros sensor
Φ	Dimensionless free Helmholtz energy
ϖ	Association parameter
Ψ_j	Jameson sensor
ρ	Density
τ_{LE}	Large-eddy turnover time
θ	Velocity Divergence
ϑ	Second viscosity coefficient
τ_{ij}	Viscous stress tensor
W_{ij}	Rotation-rate tensor
ξ	Dipole moment
ζ	Bulk viscosity

Subscripts

0	Initial value
---	---------------

B	Bulk value
c	Critical point value
cl	Centerline value
r	Reduced value (normalized w.r.t. critical-point)
ref	Reference value
rms	Root-mean square value
sh	Ratio of downstream to upstream value across a shock

Superscripts

D	Dilatational component
id	Ideal contribution
S	Solenoidal component

Operator

TCF

$(\bullet)^+$	Quantity associated to focal regions
$(\bullet)^-$	Quantity associated to non focal regions
$(\bullet)^*$	Quantity associated to anisotropic part of A_{ij}
$\langle \bullet \rangle$	Volume average (on x, y, z)

CHIT

$(\bullet)^+$	Wall-scaling
$(\bullet)^*$	Semi-local scaling
$\overline{(\bullet)}$	Reynolds average (on x, z, t)
$\widetilde{(\bullet)}$	Favre average (on x, z, t)

SIMULATION NUMERIQUE D'ÉCOULEMENTS TURBULENTS DE GAZ DENSE

RÉSUMÉ : Les écoulements turbulents de gaz denses, qui sont d'un grand intérêt pour un large éventail d'applications, sont le siège de phénomènes physiques encore peu connus et difficiles à étudier par des approches expérimentales. Dans ce travail, nous étudions pour la première fois l'influence des effets de gaz denses sur la structure de la turbulence compressible à l'aide de simulations numériques. Le fluide considéré est le PP11, un fluorocarbure lourd, dont le comportement thermodynamique a été représenté à l'aide de différentes lois d'état, afin de quantifier la sensibilité des solutions aux choix de modélisation. Nous avons considéré d'abord la décroissance d'une turbulence homogène isotrope compressible. Les fluctuations de température sont négligeables, alors que celles de la vitesse du son sont importantes à cause de leur forte dépendance de la densité. Le comportement particulier de la vitesse du son modifie de manière significative la structure de la turbulence, conduisant à la formation de shocklets de détente. L'analyse de la contribution des différentes structures à la dissipation d'énergie et à la génération d'entrophie montre que, pour un gaz dense, les régions de forte dilatation jouent un rôle similaire à celles de forte compression, contrairement aux gaz parfaits, dans lesquels le comportement est fortement dissymétrique. Ensuite, nous avons mené des simulations numériques pour une configuration de canal plan en régime supersonique, pour plusieurs valeurs des nombres de Mach et de Reynolds. Les résultats confirment la validité de l'hypothèse de Morkovin. L'introduction d'une loi d'échelle semi-locale prenant en compte les variations de densité et viscosité, permet de comparer les profils des grandeurs turbulentes (contraintes de Reynolds, anisotropie, budgets d'énergie) avec ceux observés en gaz parfait. Les variables thermodynamiques, quant à elles, présentent une évolution très différente pour un gaz parfait et pour un gaz dense, la chaleur spécifique élevée de ce dernier conduisant à un découplage des effets dynamiques et thermiques et à un comportement proche de celui d'un fluide incompressible avec des propriétés variables.

Mots clés : gaz dense, simulation numérique, fluides BZT, écoulements turbulents.

NUMERICAL SIMULATION OF TURBULENT DENSE GAS FLOWS

ABSTRACT : Dense gas turbulent flows, of great interest for a wide range of engineering applications, exhibit physical phenomena that are still poorly understood and difficult to reproduce experimentally. In this work, we study for the first time the influence of dense gas effects on the structure of compressible turbulence by means of numerical simulations. The fluid considered is PP11, a heavy fluorocarbon, whose thermodynamic behavior is described by means of different equations of state to quantify the sensitivity of solutions to modelling choices. First, we considered the decay of compressible homogeneous isotropic turbulence. Temperature fluctuations are found to be negligible, whereas those of the speed of sound are large because of the strong dependence on density. The peculiar behavior of the speed of sound significantly modifies the structure of the turbulence, leading to the occurrence of expansion shocklets. The analysis of the contribution of the different structures to energy dissipation and entropy generation shows that, for a dense gas, high expansion regions play a role similar to high compression ones, unlike perfect gases, in which the observed behaviour is highly asymmetric. Then, we carried out numerical simulations of a supersonic turbulent channel flow for several values of Mach and Reynolds numbers. The results confirm the validity of the Morkovin' hypothesis. The introduction of a semi-local scaling, taking into account density and viscosity variations across the channel, allow to compare the wall-normal profiles of turbulent quantities (Reynolds stresses, anisotropy, energy budgets) with those observed in ideal gases. Nevertheless, the thermodynamic variables exhibit a different evolution between perfect and dense gases, since the high specific heats of the latter lead to a decoupling of dynamic and thermal effects, and to a behavior close to that of variable property incompressible fluids.

Keywords : dense gas, numerical simulation, BZT fluids, turbulent flows.